STUDY OF BARIUM MODIFIED BISMUTH SODIUM TITANATE/EPOXY COMPOSITES AND THEIR TRANSDUCER APPLICATIONS

WANG DAN YANG

M. PHIL.

THE HONG KONG

POLYTECHNIC UNIVERSITY

2002

ABSTRACT

Perovskite lead-free ceramics barium modified bismuth sodium titanate, 0.94 $(Bi_{1/2}Na_{1/2})$ TiO_3-$0.06BaTiO_3$ (BNBT-6), was fabricated using a mixed-oxide method. Characteristics of this ceramics, including the microstructure, ferroelectric, dielectric and piezoelectric properties were characterized. The BNBT-6 ceramics has a large remnant polarization P_r of 30.5 $\mu C/cm^2$ and electromechanical coupling coefficient k_t of 0.46 and k_p of 0.25, which are comparable to those of traditional lead zirconate titanate (PZT) ceramics. Therefore, it has good potential to replace PZT if lead-containing piezoceramics are to be phased out in the future.

BNBT-6 ceramic/epoxy 1-3 composites with different ceramic volume fractions were fabricated by the dice-and-fill technique. Characterization of these composites was carried out and found to agree with theoretical modelling. The thickness electromechanical coupling coefficient k_t of the composites can be improved to 0.5-0.6. The mode coupling theory was applied to the ceramic rods inside the 1-3 composites. When the width to thickness ratio (L/H) of the ceramic rods is close to 1.45, the 1-3 composite shows two strong resonance modes due to the coupling of the thickness and lateral mode of the rod. By using a composite with this particular aspect ratio, a dual frequency transducer with resonances at 3.8 MHz and 5.8 MHz has been fabricated and characterized.

In order to fabricate higher frequency transducers, BNBT-6 fibre/epoxy 1-3 composites were fabricated. BNBT-6 fibres were developed by two methods: one is by a sol-gel route and the other is using the viscous suspension spinning process (VSSP). After sintering with a very slow heating rate and by controlling the ambient atmosphere, dense and crack-free BNBT-6 ceramic fibres were obtained. The diameters are ~ 80 μm and 300 μm for fibres produced by the sol-gel and VSSP methods, respectively. The crystalline phase and microstructure of the ceramic fibres were checked by X-ray diffraction (XRD) and scanning electron microscopy (SEM). Some electrical properties of the ceramic fibres, such as the dielectric and ferroelectric behavior were also investigated. Most of the electrical properties were comparable to that of the bulk BNBT-6 ceramics.

BNBT-6 fibre/epoxy 1-3 composite discs were fabricated with fibre volume fractions ranging from 0.1 to 0.5 and with diameter between 2 mm to 7.5 mm. Volume fraction of the composites was determined by counting the fibre area in thé SEM micrographs. Ferroelectric and piezoelectric properties of the composites were studied. Polarization of the composites was found to be proportional to the fibre volume fraction and values of the coercive field were slightly higher than that of the bulk ceramics. Composites with resonance frequencies ranging from 8 MHz to 20 MHz were obtained by adjusting their thicknesses. Composites derived from the sol-gel fibres had higher coupling coefficients ($k_t \geq 0.60$) compared with the VSSP fibre composites which have a k_t of lower than 0.52.

High frequency transducers were fabricated using the BNBT-6 fibre/epoxy 1-3 composites and their characteristics were measured. In comparison, transducers assembled using sol-gel fibre composites possess better performance. A 15 MHz ultrasonic transducer with ~30% sol-gel fibre loading has a broad bandwidth of 80% and an insertion loss of −34.8 dB.

ACKNOWLEDGEMENT

I would first like to express appreciation to my supervisor Prof. H. L. W. Chan for her constant guidance, support, encouragement and patience throughout the period of my research study. I also would like to thank Prof. C. L. Choy, Dr. K. W. Kwok and Dr. K. H. Pang for their enlightening suggestions and discussions during these two years. Thanks are due to Mr. M. N. Yeung of the Materials Research Centre for his assistance in the SEM investigations.

My thanks are also extended to my colleagues in our department for their assistance in material preparation and measurement techniques. They include (in no particular order): Mr. K. Li, Mr. S. U. Adikary, Mr. K. C. Cheng, Mr. K. W. Tang, Mr. K. H. Lam, Mr. Y. T. Or and Mr. C. P. Chong. My study at PolyU provided many opportunities for me to meet a lot of people and make some good friends. I would like to acknowledge them for their support, help and friendship.

Most of all I would like to express my deepest appreciations to my parents and Ms. V. T. Wang for their continuous love, support, understanding and patience that inspired me to continue and grow and mature both as a person and as a professional.

TABLE OF CONTENTS

LIST OF TABLE CAPTIONS

LIST OF FIGURE CAPTIONS

LIST OF SYMBOLS

Symbol	Description	SI unit
α	attenuation coefficient	cm^{-1}
ε_0	permittivity of free space	F/m
ε_{ij}^{S}	relative permittivity under clamped condition	
ε_{ij}^{T}	relative permittivity under free condition	
θ	phase angle	degree
λ	wavelength	m
ρ	density	kg/m^3
σ^{p}	planar Poisson's ratio	
υ	velocity	m/s
ϕ	ceramic volume fraction	
A	cross-sectional area	m^2
a	radius	m
C_s	clamped capacitance	C
c_{pq}	elastic stiffness coefficient	N/m^2 or Pa
D	electric displacement	C/m^2
D (superscript)	at constant electric displacement	
d	diameter	m
d_h	hydrostatic charge coefficient	m/V or C/N
d_{ip}	piezoelectric (charge) coefficient	m/V or C/N
E	electric field	V/m
E (superscript)	at constant electric field	
e_{ip}	piezoelectric coefficient	C/m^2
f	frequency	Hz
f_r	resonance frequency	Hz
f_a	anti-resonance frequency	Hz

g_{ip}	piezoelectric (voltage) coefficient	V/N or m²/C
h_{ip}	piezoelectric coefficient	V/m or N/C
i,j,k,1,2,3	refer to directions in an orthogonal axis system	
k_{15}	shear electromechanical coupling coefficient	
k_{31}	transverse electromechanical coupling coefficient	
k_{33}	longitudinal electromechanical coupling coefficient	
k_p	planar electromechanical coupling coefficient	
k_t	thickness electromechanical coupling coefficient	
L	inductance	H
P	pressure	Pa
P_o	transmitting voltage response	Pa
P_r	remnant polarization	C/m²
Q_M	mechanical quality factor	
R	resistance	Ω
S	strain	
S (superscript)	at constant strain	
S_{pq}	elastic compliance coefficient	m²/N
T	stress	N/m²
T (superscript)	at constant stress	
T_c	Curie temperature	°C
tanδ	loss tangent	
Y	Young's modulus	N/m²
Z	electric impedance	Ω
z_L	longitudinal acoustic impedance	Rayl (kg/sm²)
z_s	shear acoustic impedance	Rayl (kg/sm²)

CHAPTER I

INTRODUCTION

1.1 Piezoelectricity and Ferroelectricity

1.1.1 Piezoelectricity

In 1880, the Curie brothers (Jacques and Pierre Curie) first discovered the piezoelectric effect in some single crystals. They noticed that, under a mechanical stress or an external electric field, some anisotropic crystals could produce a proportional electrical or mechanical displacement. The discovery of this phenomenon was the basis for establishing the physics of piezoelectrics.

Piezoelectricity is the ability of certain crystalline materials to develop an electric charge proportional to a mechanical stress. (Jaffe, 1971). In other words, piezoelectricity could be defined as a property possessed by some crystalline materials whereby application of a mechanical stress produce an electric charge (direct effect), or conversely, the changing of a size or shape when subjected to an external electric field (converse effect). Schematic diagrams illustrating both the direct and converse piezoelectric effects are shown in Figure 1.1.
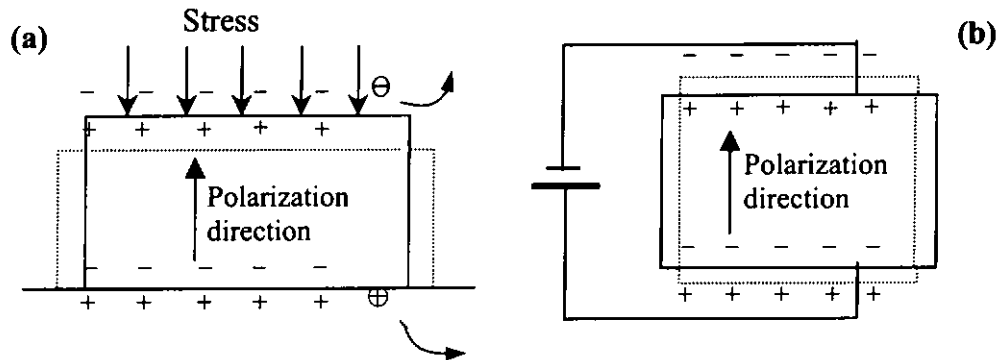
Figure 1.1 Schematic diagrams of the piezoelectric effects. (a) The direct effect and (b) the converse effect.

The relationship between the charge generated and the applied stress can be described by the following matrices (Jaffe, 1971):

$$D_m = d_{mj} T_j \quad (m=1,2,3; j=1,2, ..., 6) \tag{1.1}$$

$$S_j = d_{mj} E_m \quad (m=1,2,3; j=1,2, ..., 6) \tag{1.2}$$

The d coefficient relates the electrical displacement D (charge per unit area) to the applied stress T in the direct effect. In the converse effect, this factor relates the strain S to the applied electric field. The piezoelectric coefficient d_{mj} is numerically identical for both effects with units of coulomb/newton (C/N) in the direct effect and meter/volt (m/V) in the converse effect. Large d coefficients are desirable for materials intended for actuating motion or vibration, such as in active sonar or ultrasonic transducers.

The efficiency between the conversion of electrical to mechanical energy or vice versa is given by the square of the electromechanical coupling coefficient k.

$$k^2 = \frac{output\ mechanical\ energy}{input\ electrical\ energy} \qquad (1.3a)$$

or

$$k^2 = \frac{output\ electrical\ energy}{input\ mechanical\ energy} \qquad (1.3b)$$

Since the conversion of mechanical to electrical energy is always incomplete, k^2 is always <1, and thus k is also <1.

The definition and description for other piezoelectric constants as well as the elastic and dielectric constants of ceramics and crystals will not be described in details here as they can be found in the literature. (e.g. IEEE standards, 1978; Xu, 1991)

1.1.2 Ferroelectricity

The relationship between ferroelectrics and piezoelectrics is shown in Figure 1.2. Thus, it is seen that all pyroelectrics are piezoelectric while all ferroelectrics are pyroelectric, but the reverse may not be true. (Jaffe, 1971)
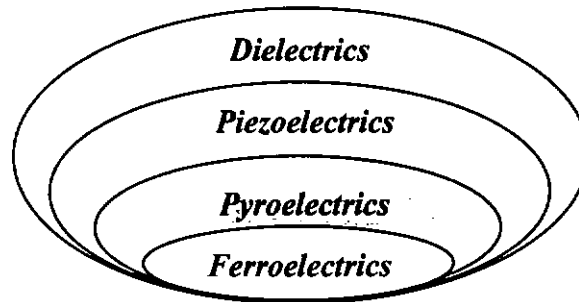
Figure 1.2 The relationship among dielectrics, piezoelectrics, pyroelectrics and ferroelectrics.

Ferroelectricity is defined as the reversibility in a polar crystal of the direction of the electric dipole by means of an applied electric field. Since it requires polarity in a crystal, it can only occur in crystal classes with spontaneous polarization. (Jaffe, 1971) A ferroelectric material exhibits a spontaneous polarization in the absence of an electric field and this polarization may be switched by the application of an external electric field. (Mitsui, 1976)

One of the important characteristics of the ferroelectrics is the ferroelectric hysteresis loop, i.e., the polarization P is a double-valued function of the applied electric field E. A typical P-E hysteresis loop in ferroelectrics is shown in Figure 1.3. The polarization is the resultant of the dipole moments per unit volume of a crystalline aggregate. In a poled ceramics or a single domain crystal there is a net remnant polarization P_r. Values of the spontaneous polarization P_s can be obtained by extrapolating the polarization at high field P_{sat} back to zero field along a tangent. The remnant polarization P_r in a crystal cannot be removed until the applied field in the opposite direction reaches a certain

value. The strength of the field required to reduce the polarization P to zero is called the

"coercive field strength" E_c.

Another important characteristics of ferroelectrics is the temperature of phase transition

called the *Curie point* T_c. At T_c a ferroelectric crystal undergoes a structural transition

from a paraelectric phase to a ferroelectric phase. Only when the temperature is below

T_c, the crystal exhibits ferroelectricity. It is generally believed that the ferroelectric

structure of a crystal is created by a small distortion of the paraelectric structure such

that the lattice symmetry in the ferroelectric phase is always lower than that in the

paraelectric phase. (Xu, 1991)
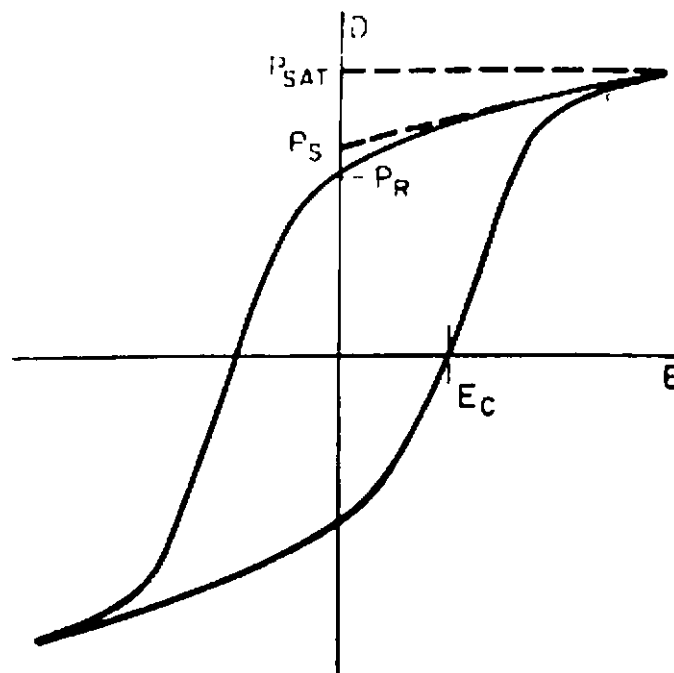
Figure 1.3 A typical P-E hysteresis loop in ferroelectrics.

1.2 Bismuth-based Lead-free Ceramic Materials

Since the discovery of excellent piezoelectric properties in lead zirconate titanate (PZT) in the early 1950's, the PZT family has become the most commonly used piezoelectric and ferroelectric materials. They have found wide applications in piezoelectric devices, including actuators, transformers, sensors and transducers, as well as in ferroelectric memory applications. However, the contamination of lead caused environmental pollution and limited the development of PZT-based devices. Therefore, the use of these lead-based materials need to be phased out and it has been necessary to search for lead-free piezoelectric materials with excellent piezoelectric or ferroelectric properties to replace the PZT system.

Many research work has been done on lead-free piezoelectric materials in the past decades. A few promising lead-free piezoelectric ceramics have been identified. These include the well-used barium titanate ($BaTiO_3$), which was discovered even early than PZT. Other systems include $KNbO_3$-$NaNbO_3$ solid solution, bismuth sodium titanate, $Bi_{1/2}Na_{1/2}TiO_3$ (abbreviated to BNT)-based solid solutions, bismuth layer-structured ferroelectrics and some piezoelectric single crystals, such as $Li_2B_4O_7$ and $La_3Ga_5SiO_{14}$. (Takenaka, 1999) Among these candidates, the bismuth-based materials have been considered to be good candidates to replace the lead-based materials in the future.

The bismuth-based materials can be roughly classified into two types according to their main applications. The first type has a perovskite phase (ABO_3), which is similar to that of the PZT family and could be used to fabricate piezoelectric devices such as ultrasonic transducers. A typical representative of this type of bismuth-based material is BNT. The other type of bismuth-based material belongs to the Aurivillius family with a layered structure and was regarded to have promising potentials for ferroelectric random access memory (FeRAM) applications. Strontium bismuth tantalate (SBT) and lanthanum modified bismuth titanate (BLT) are the two most well-studied bismuth layer-structured ferroelectrics (BLSFs) with excellent fatigue endurance against switching. The microstructures of these two types of bismuth-based materials are shown in Figure 1.4.
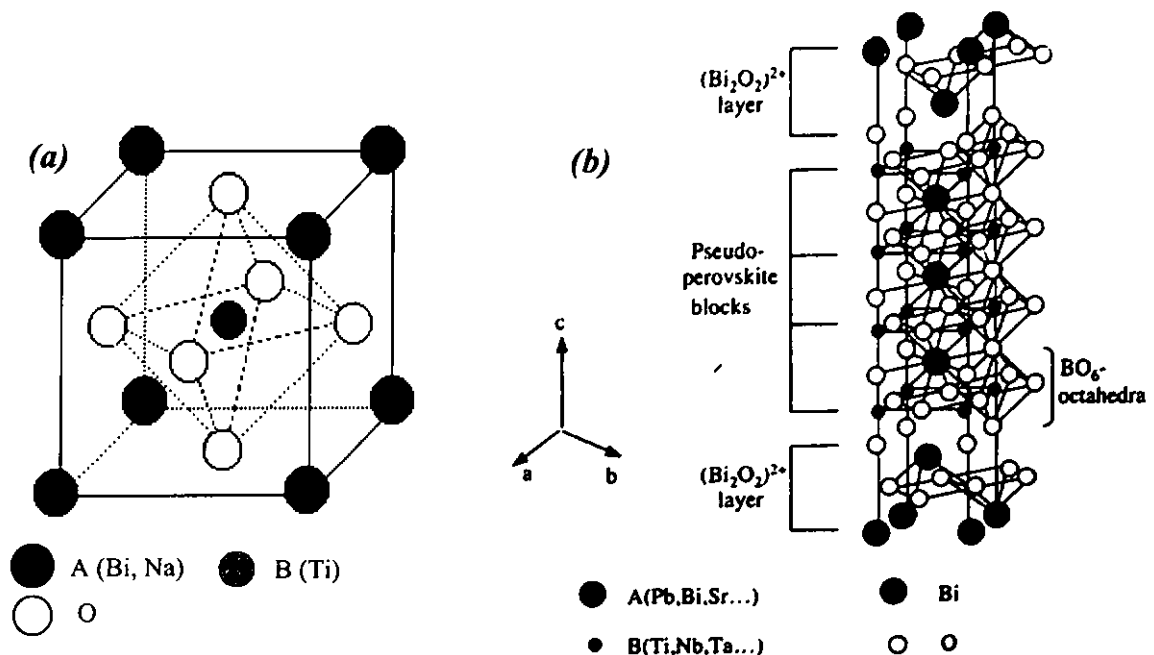
Figure 1.4 Schematic diagrams showing the crystal structures of two typical bismuth-based materials. (a) Perovskite type, and (b) bismuth layer-structured ferroelectrics (BLSFs). (Xu, 1991)

BLSFs have been studied continually by a lot of researchers since they were discovered

in 1959. (Subbarao, 1962; Smolenskii, 1962) BLSFs have a crystal structure in which

bismuth oxide layers [$(Bi_2O_2)^+$ layers] are interleaved with pseudo-perovskite blocks

along the c axis. Therefore, the BLSFs usually have a long c axis where the remnant

polarization P_r originated. SBT and BLT have been proved to be excellent candidates

for FeRAM applications. Meanwhile, this type of compounds possesses high

ferroelectric transition temperature so that they can be used as high temperature (>>

300°C) piezoelectrics, such as high temperature transducers. (Pardo, 2000)

Bismuth sodium titanate, $Bi_{1/2}Na_{1/2}TiO_3$ (BNT) is a perovskite ferroelectrics discovered

by Smolenskii et al. in 1960. (Herabut, 1997) The BNT lead-free system is of particular

interest as a new candidate to replace the lead-based perovskite materials. (Nagata, 1998)

But due to its large coercive field and relatively high conductivity, pure BNT is hard to

pole and its piezoelectric properties are not high. Barium modified BNT, (1-x)

$Bi_{1/2}Na_{1/2}TiO_3$-$xBaTiO_3$, can overcome the above drawbacks and has already attracted

much attention because of its good piezoelectric properties, which is comparable to the

PZT system. The morphotropic phase boundary (MPB) of this solid solution system is

near x=0.06. Takenaka (Takenaka, 1991) reported that the composition

$0.94Bi_{1/2}Na_{1/2}TiO_3$-$0.06BaTiO_3$ (BNBT-6), which is near the MPB, has relative good

piezoelectric properties. In this thesis, properties of BNBT-6 and BNBT-6/epoxy 1-3

composites were investigated; ultrasonic transducers based on this material were also

fabricated and characterized.

1.3 Ceramic/polymer 1-3 Composites

At present a large number of diphasic piezoelectric composites are based on piezoelectric ceramics and polymers. Connectivity is a key feature in the development of multiphase solids with the desired physical properties. Connectivity is a code used for defining the dimensions in which a particular phase within a composite is physically connected. Ten possible connectivity patterns are given by Newnham et al. (Newnham, 1978) as shown in Figure 1.5. Each phase in the composite may be self-connected in zero, one, two, or three dimensions. Using the Cartesian coordinate, for diphasic composites there are ten connectivity patterns designated as 0-0, 0-1, 0-2, 0-3, 1-1, 1-2, 1-3, 2-2, 2-3 and 3-3. For example, the commonly used composite consisted of dispersed particles embedded in a matrix would then be designated as a 0-3 composite. Another common system consisting of fibres or rods imbedded in a matrix and oriented across one of the dimensions of the sample would be known as a 1-3 composite. In a 1-3 piezoceramics/polymer composite, piezoceramic rods are embedded in a continuous polymer matrix. Under the idealized situation in which the polymer phase is far more compliant than the piezoceramics, the stress on the polymer will be transferred to the piezoceramic rods. The stress amplification on the ceramic phase along with the reduced permittivity greatly enhances the piezoelectric voltage coefficient.
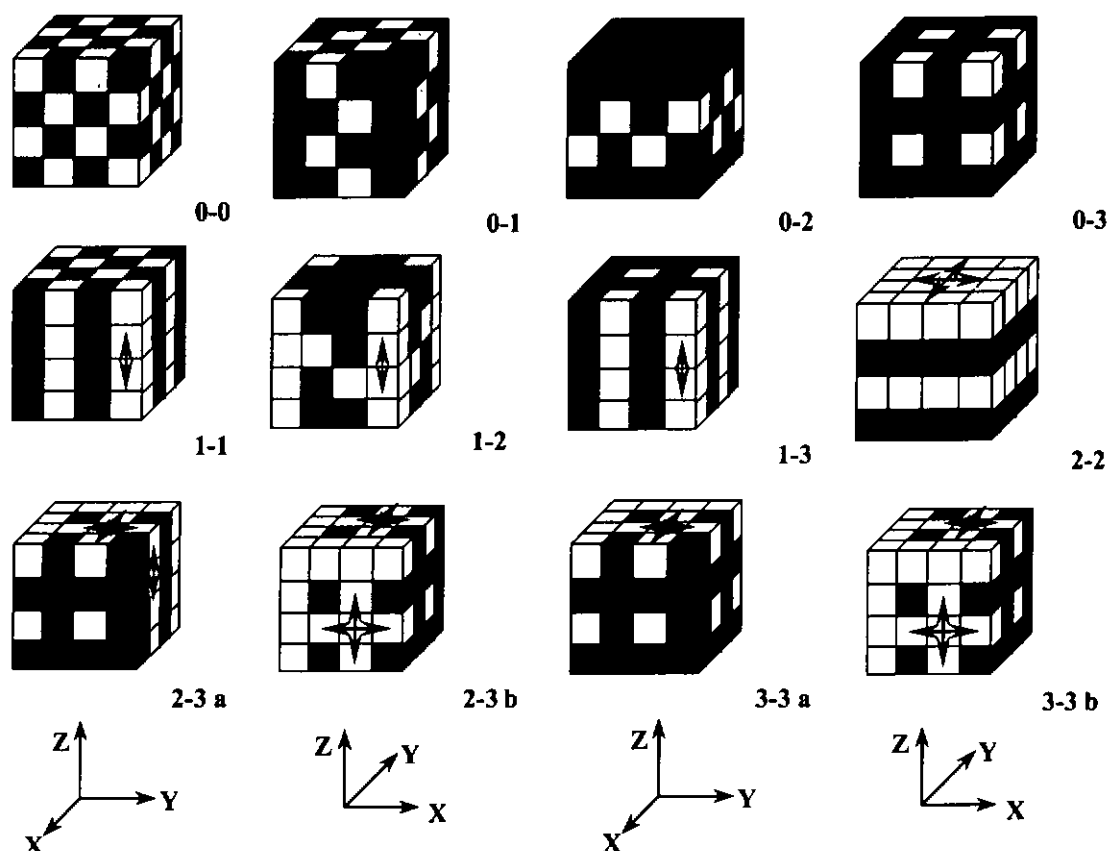
Figure 1.5. Ten different connectivity patterns for a diphasic solid. Each phase has a zero-, one-, two- or three-dimensional connectivity to itself. In the 1-3 composite, e.g., the shaded phase is three-dimensionally connected and the unshaded phase is one dimensionally connected. Arrows are used to indicate the connected directions. Two views of the 2-3 and 3-3 patterns are given because the two interpenetrating networks are difficult to visualize on paper. The views are related by 90° counterclockwise rotation about the Z-axis (after Newnham et al.).

1-3 piezoelectric ceramic/polymer composites have been successfully used in the past decades as transducers, sensors and micro-actuators for medical ultrasonic imaging applications. (Nowicki, 1995) 1-3 composites consisting of piezoelectric ceramic rods embedded in a polymer matrix have much lower acoustic impedance, hence energy can couple better to human tissue and other biological media. The 1-3 composite also

provides a broader bandwidth compared to a piezoelectric ceramics, which are beneficial

in some transducer systems. Furthermore, when used in ultrasonic arrays for medical

imaging, the 1-3 composites have good acoustic isolation between elements. Figure 1.6

shows a typical 1-3 composite material with the structure of periodically spaced ceramic

elements.

Polymer matrix

Periodicity

Thickness (d)
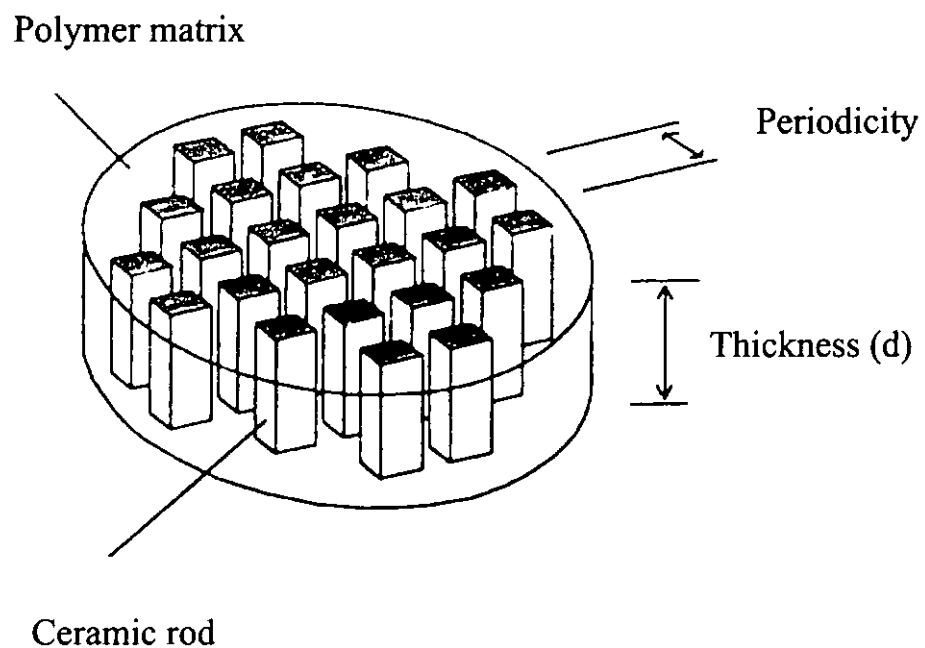
Ceramic rod

Figure 1.6 Schematic diagram of a 1-3 composite.

In 1-3 composites, the ceramic rods play an active role of conversion between the

electrical and mechanical energy, while the polymer matrix acts as a passive medium

that holds the rods together and suppresses the lateral resonance modes. Therefore, the

1-3 composite design allows for pure thickness mode operation with the advantages of a

high thickness electromechanical coupling coefficient k_t (close to k_{33} of the constituent

ceramics) over a wide range of ceramic volume fractions. (Taunaumang, 1994) Also, the

1-3 composite design dilutes the high relative permittivity characteristics of the ceramics by adding the low-permittivity polymer phase. In addition, the 1-3 composites can be fabricated, shaped and tailored to meet the needs of the application.

The conventional fabrication techniques of 1-3 composites include the dice-and-fill, injection molding and "pick and place" method. (Janas, 1995) However, as the ceramic pillar diameter is reduced, using these processes becomes increasingly difficult. The use of fine scale fibres fabricated using the sol-gel technology offers an alternative method for developing higher frequency 1-3 composite transducers. (Yoshikawa, 1992)

1.4 Principles and Designs of Piezoelectric Transducers

1.4.1 Transducer Fundamentals

Piezoelectrics are the driving components of piezoelectric transducers. They can produce electromechanical energy conversion by transmitting and receiving acoustic pulses. The basis of this electromechanical energy conversion is closely related to the crystal structure of the material. The non-centrosymmetric structure of piezoelectric materials gives rise to strains when they are subjected to electric field or can generate charges when subjected to stress. (Meyer, 1998)

The sensitivity of a transducer can be related to two piezoelectric coefficients, the piezoelectric d coefficient (piezoelectric strain constant, which has units of C/N or m/V)

and the piezoelectric g coefficient (piezoelectric voltage coefficient in V m/N) (Shung, 1996; Wells, 1977). Besides these two coefficients, the electromechanical coupling coefficient is also very important. This coefficient represents the ability of the material to convert between mechanical and electrical energy. (IEEE, 1987) Another material parameter of interest is the mechanical quality factor (Q_M). Q_M is defined as the ratio of strain in phase with the stress to strain out of phase with the stress (Jaffe, 1971). This factor indicates the mechanical loss in the material. In low Q materials, heat generation in the transducer element is more serious.

1.4.2 Transducer Design

By using piezoelectric ceramic/polymer composite, designers can overcome some of the problems dealing with either monolithic piezoceramics or piezopolymers in transducer applications (Smith, 1986). In designing 1-3 composites for ultrasonic transducer applications, several parameters including the spatial scale, pillar aspect ratio/distribution and ceramic volume fraction should be considered. These parameters can affect the operating frequencies and efficiency of the transducers.

Pure thickness-mode resonance can be achieved by adjusting the spatial scale of the composites. In 1-3 composites, the lateral periodicity of the ceramic rods must be sufficiently fine to avoid the lateral mode propagating normal to the rod axis from being coupled to the thickness mode. The lateral periodicity must be smaller than one wavelength of the transverse wave in the matrix (Gururaja, 1985). If the wavelength of

these transverse wave are at least two times larger than the periodicity of the rods, the composite can be regarded as a homogeneous medium. In this case, a composite transducer radiating ultrasound will vibrate uniformly in its thickness mode (Jadidian, 1996).

The pillar shape and aspect ratio are also important to the performance of the 1-3 composite transducer. The pillar aspect ratio affects the electromechanical coupling and the frequency of the lateral mode. Design in the aspect ratio involves additional considerations of the ceramic volume fraction and the polymer stiffness. A general rule of thumb was that the width to thickness ratio of the rod should be less than 0.25. (Hossack, 1991).

Some research work have been done to evaluate the effect of ceramic volume fraction on the transmit/receive characteristics of 1-3 composite transducers. It was found that composites with ceramic fractions between 0.4 and 0.7 had superior operating performance compared to those with lower volume fractions (Hayward, 1990).

1.5 Scope of the Present Study

The main objectives of this work are to fabricate 1-3 BNBT-6/epoxy composites and BNBT-6/epoxy composite transducers for ultrasonic imaging applications and evaluate their performance.

This thesis describes the fabrication of BNBT-6 bulk ceramics and 1-3 BNBT-6/epoxy composites. Characterization of both the ceramics and composites is also presented. Characteristics of ultrasonic transducers based on BNBT-6/epoxy 1-3 composites are discussed. The thesis is divided into seven Chapters.

Following this general introduction, the fabrication and characterization of BNBT-6 bulk ceramics are described in Chapter 2. Properties of BNBT-6 ceramics, including ferroelectric, dielectric and piezoelectric properties are given in details in this Chapter.

In Chapter 3, the dice-and-fill technique used to fabricate BNBT-6/epoxy 1-3 composites with various ceramic volume fractions are described. Properties of these composites are measured and then compared with the modelling results. Mode coupling behavior and electrical impedance as a function of frequency for the 1-3 BNBT-6/epoxy composite with different thicknesses are discussed.

In Chapter 4, the fibre processing techniques, including both the sol-gel method and viscous suspension spinning process (VSSP) for producing BNBT-6 fibres are described. Some electrical properties of the BNBT-6 fibres are also characterized.

In Chapter 5, fabrication of 1-3 BNBT-6/epoxy composites using ceramic fibres is presented. Also included is a detailed description of characterization of the 1-3 BNBT-6 fibre/epoxy composites. Elastic properties of the BNBT-6 fibres were obtained using the measured effective properties of the composites and the modified parallel and series 1-3 composite model.

Chapter 6 describes the fabrication of BNBT-6/epoxy ultrasonic transducers and their evaluation. A dual frequency transducer based on 1-3 BNBT-6/epoxy composite was constructed and evaluated using the pulse-echo technique. Fabrication and evaluation of transducers derived from 1-3 BNBT-6 fibre/epoxy composites are also given.

Each Chapter contains reviews of the relevant literature and experimental procedures, results, discussion and a summary. A final conclusion and suggestions for future work are presented in Chapter 7.

1.6 Statement of Original Contributions

To the best of my knowledge, the present work has made the following original contributions:

1. 1-3 BNBT-6/epoxy composites with various ceramic volume fractions were fabricated by the dice-and-fill technique and their properties were measured. Mode coupling behavior of the 1-3 BNBT-6/epoxy composite was studied.

2. BNBT-6 ceramic fibres were successfully produced using both the sol-gel technology and VSSP method. 1-3 composites derived from the BNBT-6 fibres were fabricated and characterized.

3. Transducers for ultrasonic imaging applications were constructed using BNBT-6/epoxy 1-3 composites. The performance of the transducers was evaluated.

CHAPTER II

FABRICATION AND CHARACTERIZATION OF
$0.94(Bi_{1/2}Na_{1/2})TiO_3$-$0.06BaTiO_3$ (BNBT-6) CERAMICS

2.1 Introduction

Due to its better piezoelectric properties compared with other lead-free systems, $0.94(Bi_{1/2}Na_{1/2})TiO_3$-$0.06BaTiO_3$ (abbreviated as BNBT-6) has attached considerable research interest recently. An important feature of this solid solution is the nearly temperature independent morphotropic phase boundary (MPB) between the rhombohedral and tetragonal phases. (Figure 2.1) The room temperature lattice constants obtained from X-ray diffraction data show that the MPB exists in compositions of x =0.06~0.07 (x is the concentration of $BaTiO_3$) (Takenaka, 1991). BNBT-6 is considered to be an excellent candidate of lead-free piezoelectric ceramics (Nagata, 1998). The only drawback of this material is its relatively high electrical conductivity, which will consequently cause some problems in poling (Herabut, 1997).

Based on the literature results (Takenaka, 1999), BNBT-6 should have potential for ultrasonic transducer applications. In this work, BNBT-6 was selected as the ceramic material to fabricate 1-3 composite transducers.
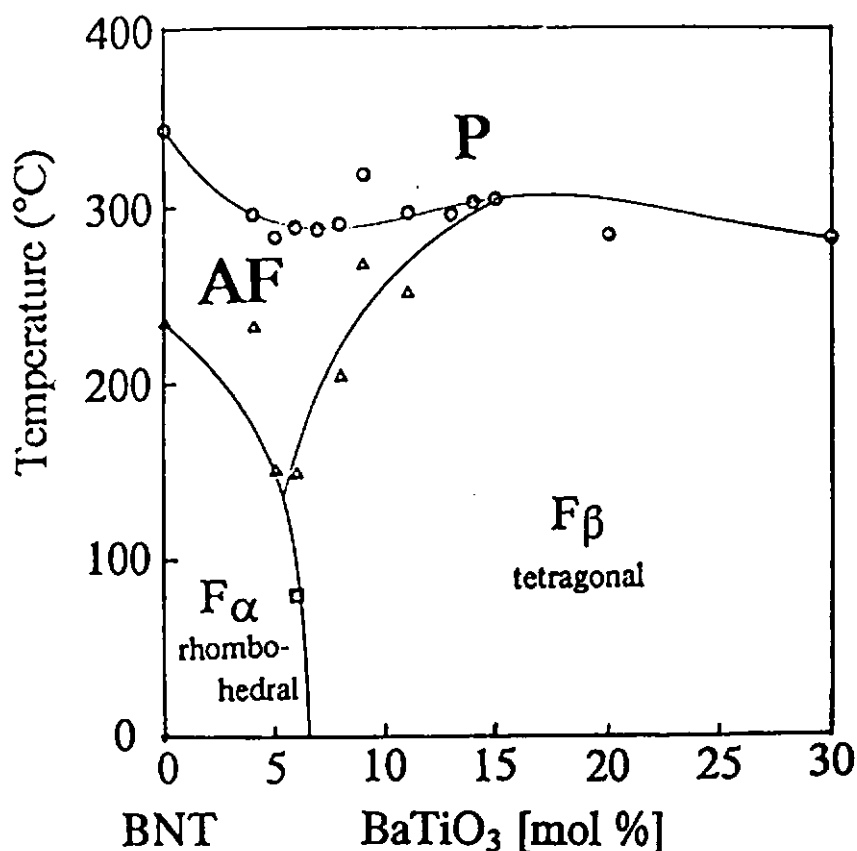
Figure 2.1 Phase relationships between $(Bi_{1/2}Na_{1/2})TiO_3$ and $BaTiO_3$ in the (1-x)$(Bi_{1/2}Na_{1/2})$ TiO_3-$xBaTiO_3$ [BNBT-100x] system. (F_α: ferroelectric rhombohedral phase, F_β: ferroelectric tetragonal phase, AF: antiferroelectric phase, P: paraelectric phase). (Takenaka, 1991)

The good properties of BNBT-6 arise from the perovskite crystal structure (Nagata, 1998). At the morphotropic phase boundary (MPB), the orientation of the spontaneous dipole can exhibit a combination of the 6 tetragonal and the 8 rhombohedral orientations for a total of 14 possible orientations. This permits easier reorientation of the dipoles during poling (Meyer, 1998).

In this Chapter, BNBT-6 ceramics were prepared by a conventional mixed-oxide method.

The ferroelectric, dielectric and piezoelectric properties of BNBT-6 ceramic were measured and presented.

2.2 Fabrication of the BNBT-6 Ceramic Samples

Four steps are included in the BNBT-6 ceramic fabrication process. These include the powder preparation, dry pressing, binder burnout and sintering. It is very important to make sure that all the equipment are clean enough to avoid any contamination by impurities, especially the presence of lead-based materials, which can affect the properties of the final ceramic samples.

2.2.1 Preparation of the BNBT-6 Powder

The conventional solid-state reaction technique was used to prepare the BNBT-6 powder. Reagent grade oxide or carbonate powders of Bi_2O_3, Na_2CO_3, $BaCO_3$ and TiO_2 with 99+% purity (ACROS Organics) were used as the starting materials. Additional Bi_2O_3 was added to 2% excess of the stoichiometric composition to compensate for the bismuth loss during the sintering process.

The powders were mixed in ethanol by ball milling for 6 h. After calcining and pre-sintering at 850°C for 1 h, the powder is ready for the ceramic fabrication. X-ray diffraction investigations of the pre-sintered powder revealed that the powder had already partially crystallized with a tetragonal structure. But there is a peak of

pyrochlore phase due to the effect of excess bismuth. The XRD pattern of BNBT-6

powder calcinated at 850°C is shown in Figure 2.2.
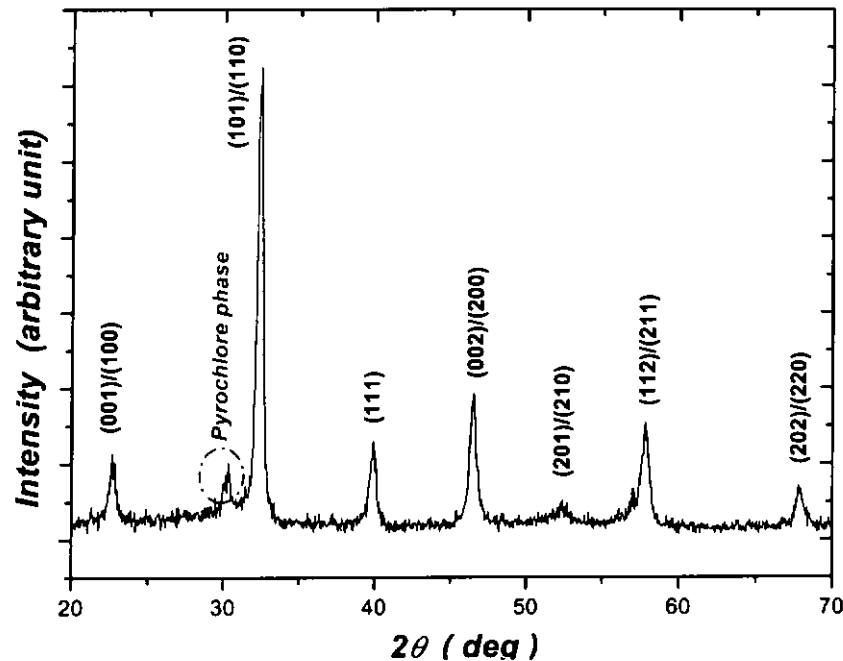
Figure 2.2 X-ray diffraction pattern of BNBT-6 powder calcinated at 850°C for 1 h.

2.2.2 Dry Pressing

Before the dry pressing step, about five weight percent polyvinyl alcohol (PVA) binder

solution (~7 wt%) was added to the ground and calcinated powder. The PVA and the

powder were mixed continuously to produce a homogeneous mixture. A required

amount of mixture was put into a stainless steel mould as shown in Figure 2.3. Before

pressing, it is necessary to make sure that the powder is distributed evenly. Then the

powder was pressed into a disc under a pressure of ~40 MPa at room temperature.

The dimensions of the green disc for dielectric and ferroelectric investigation are ~11.5 mm diameter and 1.0 mm thickness. Samples with five different shapes were prepared for piezoelectric properties measurements described in the following section.
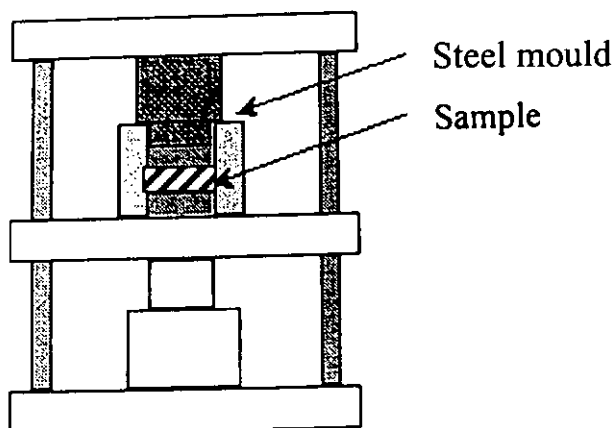
Figure 2.3 Schematic diagram of the setup for pressing the samples.

2.2.3 Binder Burnout

The green discs were placed on an alumina plate with some sintered BNBT-6 powder around the green specimens and the samples were covered by an alumina crucible (Figure 2.4). Then it was heat-treated at 550°C for 1 h with a slow heating rate of 2 °C/min in a Lindberg/blue furnace to remove the organic binder. After the binder burnout process, calcination was carried out at 850°C for 1 h. During calcination, solid-state reactions will happen to form a partially crystallized specimen. Then the samples were cooled to room temperature naturally. The crucible was then opened to let off the carbon monoxide (CO) formed during the binder burnout process. The samples must be sintered in an oxidizing atmosphere, otherwise the amount of oxygen vacancies inside

the ceramic samples will increase which results in a decrease in the piezoelectric performance.

2.2.4 Sintering

The calcinated samples were placed into a closed alumina crucible and surrounded with the sintered BNBT-6 powder and then sintered at $1150°C$ for 2 h with a heating rate of $5°C/min$. Due to the evaporation of Bi_2O_3 above $823°C$, the sintered BNBT-6 powder covering the samples can maintain a saturated Bi_2O_3 vapour in the crucible and prevent the excessive loss of bismuth content in the samples. The sintered ceramic disc has ~10.5 mm diameter and ~0.8 mm thickness.

Sintered BNBT-6 powder

Alumina crucible

BNBT-6 green samples

Alumina plate
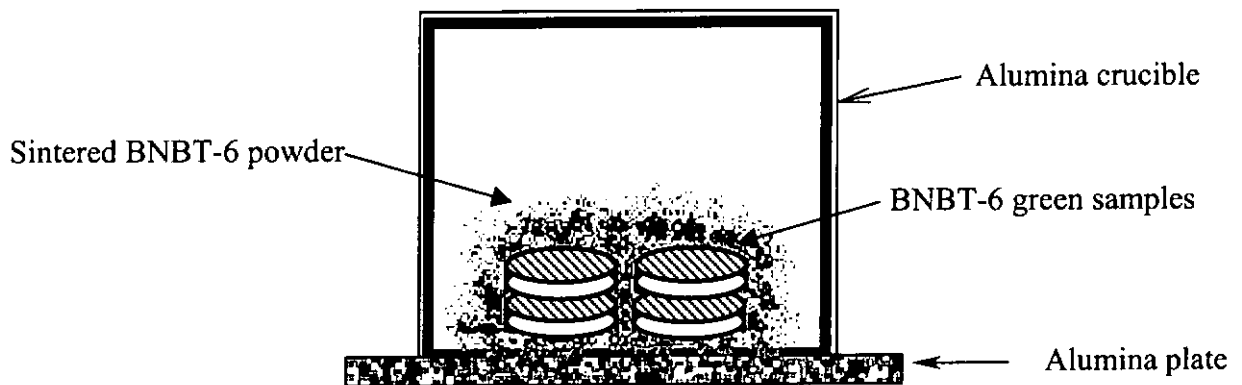
Figure 2.4 Setup for binder burnout and sintering of BNBT-6 ceramic samples.

2.2.5 Polishing and Electroding

Since the ceramics shrink during the sintering process, polishing is essential to ensure that the ceramic surfaces are flat and parallel. Wet 400# abrasive papers were used to polish the ceramic discs. After polishing, a thin layer of fired-on (at 600°C for 15 min) silver electrode was coated on both the top and bottom surfaces of the ceramic sample for subsequent measurements.

2.2.6 Poling Procedure

A sintered BNBT-6 ceramic disc does not possess any piezoelectric behavior without poling. The domains are all randomly oriented and the material is isotropic, thus no piezoelectric effect occurs. During poling, a d.c. electric field is applied on the ceramic sample to align the dipoles. After poling, the electric field is removed and a remnant polarization are maintained in the sample, and then the sample exhibits piezoelectricity (Xu, 1990). A simple illustration of the poling process is shown in Figure 2.5.

During the poling process, it is important that appropriate poling field, temperature and time be chosen. All the BNBT-6 ceramic samples were poled using the following procedure. First, the ceramic disc was heated to 100 °C in a silicone oil bath. Then based on P-E loop measurement results to be described later, (section 2.3.3) a d.c. electric field of 6.5 kV/mm was applied for 15 min. Finally, the sample was cooled to 60 °C with the electric field kept on. The d.c. poling setup is shown in Figure 2.6.
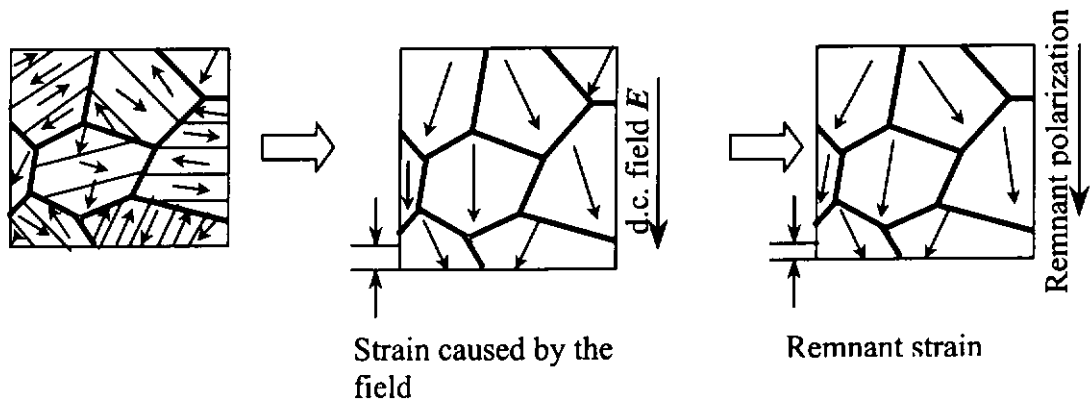
Figure 2.5 Schematic diagrams of the poling process of piezoelectric ceramics.

After poling, the domain orientation and surface charges induced on the surface caused induced stress in the sample. After a period of time, the piezoelectricity of the sample may be weakened by the stress relief. In order to eliminate the surface charges, the samples must be short-circuit. The poled samples were packed in an aluminum foil and placed at room temperature for 24 h.
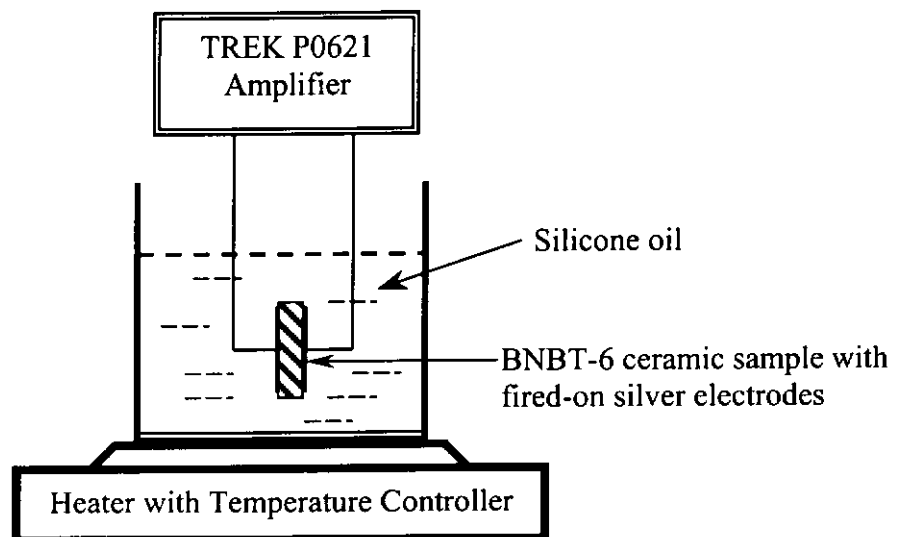
Figure 2.6 Experimental setup for poling the BNBT-6 ceramic samples.

2.3 Characterization of BNBT-6 Ceramics

2.3.1 Density Measurement

Density is an indicator of the quality of the ceramics. In this study, ceramic density was determined by the Archimedes principle. According to the Archimedes principle, dry mass of the testing sample in air (m_{dry}) and mass of the same sample suspended in water (m_{wet}) were measured using an electronic balance with a resolution of 1 mg. Sample density can be found by the following equation:

$$\rho_{ceramics} = \frac{m_{dry}}{m_{dry} - m_{wet}} \rho_{water} \tag{2.1}$$

$\rho_{ceramics}$ is density of the sample and ρ_{water} is the density of water, which is assumed to be 1000 kg/m^3.

By the Archimedes principle, density of the BNBT-6 ceramic sample sintered at 1150°C is found to be ~ 5544 kg/m^3, while the literature value is ~ 5780 kg/m^3 when sintered at 1150°C for 2 h. (Nagata, 1998)

2.3.2 Crystal Phase and Microstructure of BNBT-6 Ceramics

As H. Nagata et al. pointed out, the good piezoelectric properties of BNBT-6 arise from the perovskite crystal structure. Therefore, it is very important to make sure that the sintered BNBT-6 ceramics possess a single perovskite phase. The crystal phase of BNBT-6 ceramics was checked using an X-ray diffractometer. X-ray diffraction analysis was conducted with a Philips Analytical X-Ray Diffractometer and PC-APD Diffraction software. The sample was scanned from 20° to 70° in a step size of 0.05° with the X-Ray (alpha) wavelength of 1.54060 Å.
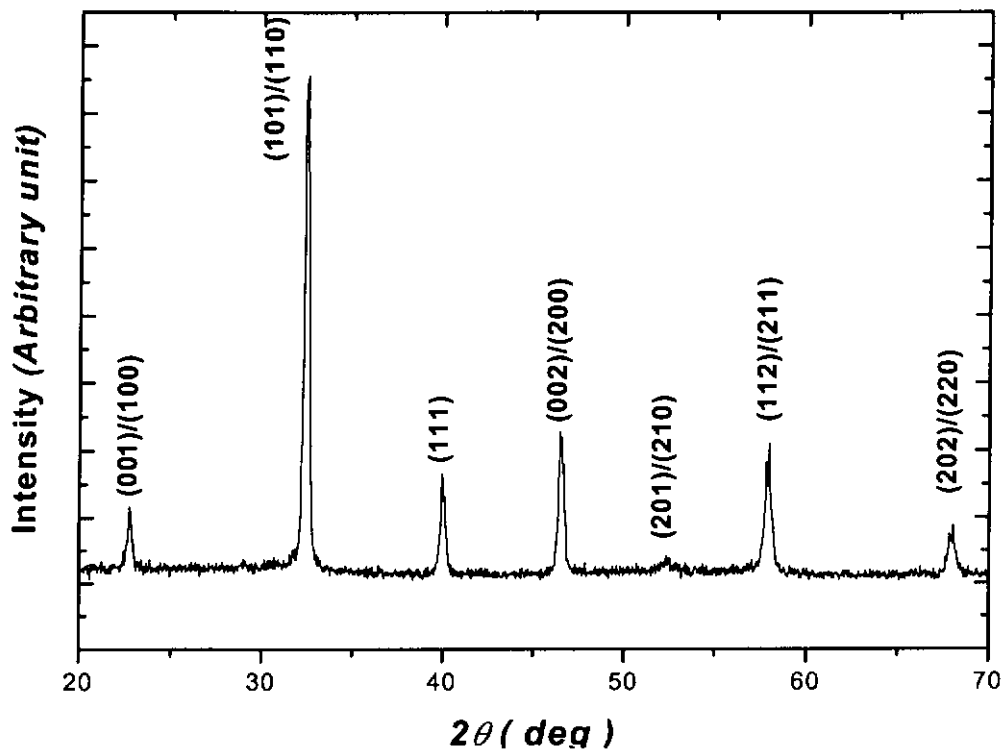
Figure 2.7 X-ray diffraction pattern of BNBT-6 ceramics sintered at 1150 °C.

As shown in Figure 2.7, the X-ray diffraction pattern of BNBT-6 ceramics shows a single perovskite phase. Compared with the XRD pattern of calcinated BNBT-6 powder, no pyrochlore phase is observed in the BNBT-6 ceramic XRD pattern. The excessive bismuth used in the starting materials had compensated for the bismuth loss during the sintering process and the ceramics regained the stoichiometric compositions. The lattice constants "a" and "c" were found to be 3.8723 Å and 3.8823 Å, respectively. The c/a ratio is ~ 1.003.

Scanning electron micrographs (SEM) of the BNBT-6 ceramics were obtained by a Leica Stereoscan 440 SEM. Both the top surface and cross sectional views of the ceramics were observed after a thin layer of gold coating was deposited.
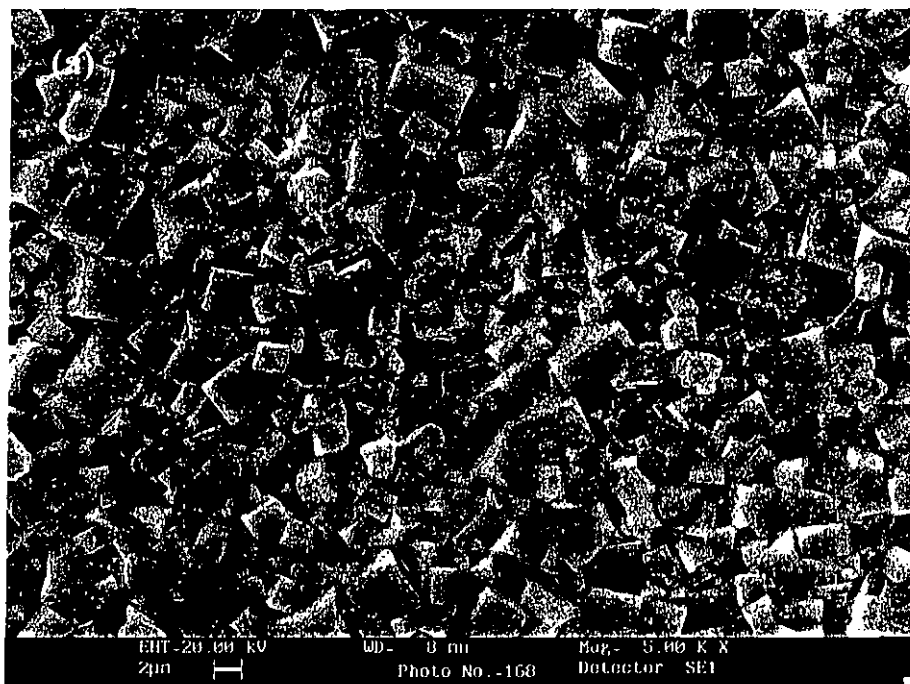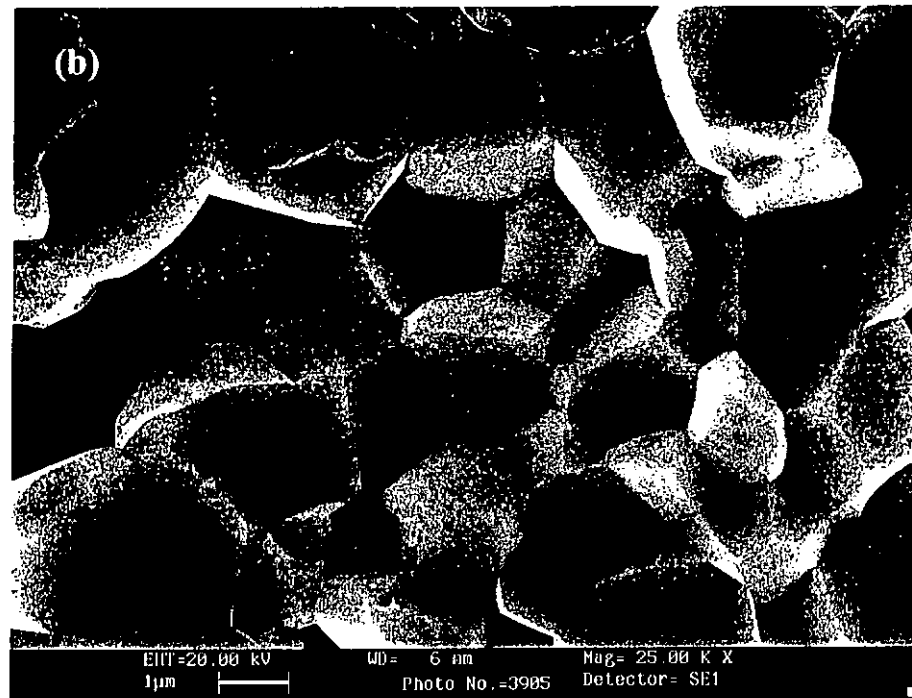
Figure 2.8 SEM micrographs of BNBT-6 ceramics sintered at 1150 °C: (a) surface view; (b) cross-sectional view.

From the SEM micrographs shown in Figure 2.8, it is found that the grain size on the surface is non-uniform due to the shrinkage and the surface stress effect during the sintering process. Large and uniform grains could be observed in the interior of the sample. The average grain size is ~ 2 μm.

2.3.3 Ferroelectric Hysteresis Measurements

For ferroelectric materials, the ferroelectric hysteresis loop is one of the most important characteristics. The definition of a ferroelectric hysteresis loop has already been described in the first Chapter. The ferroelectric hysteresis loop not only can exhibit the

ferroelectric properties of the material, but also can provide some reference information to determine the required d.c. poling electric field. Usually, we applied a poling field of two to three times the coercive field during the d.c. poling process.

In this study, ferroelectric hysteresis loops were observed by means of a Sawyer-Tower circuit (Sawyer, 1930). Figure 2.9 shows a schematic circuit of the typical Sawyer-Tower Bridge. In the circuit, the sample and the reference capacitor was connected in series, which was driven by an a.c. voltage source. Data extracted from the oscilloscope were analyzed through a computer program and a P-E loop was obtained.
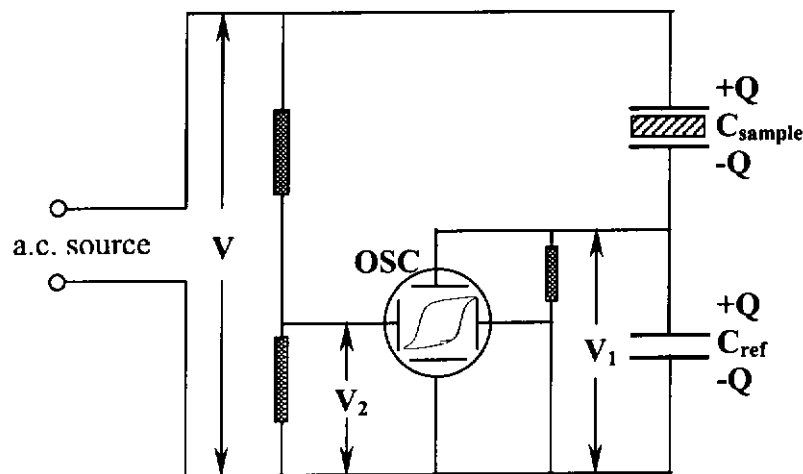
Figure 2.9 A schematic diagram of the Sawyer-Tower bridge for the observation of ferroelectric hysteresis loop (Xu, 1991).
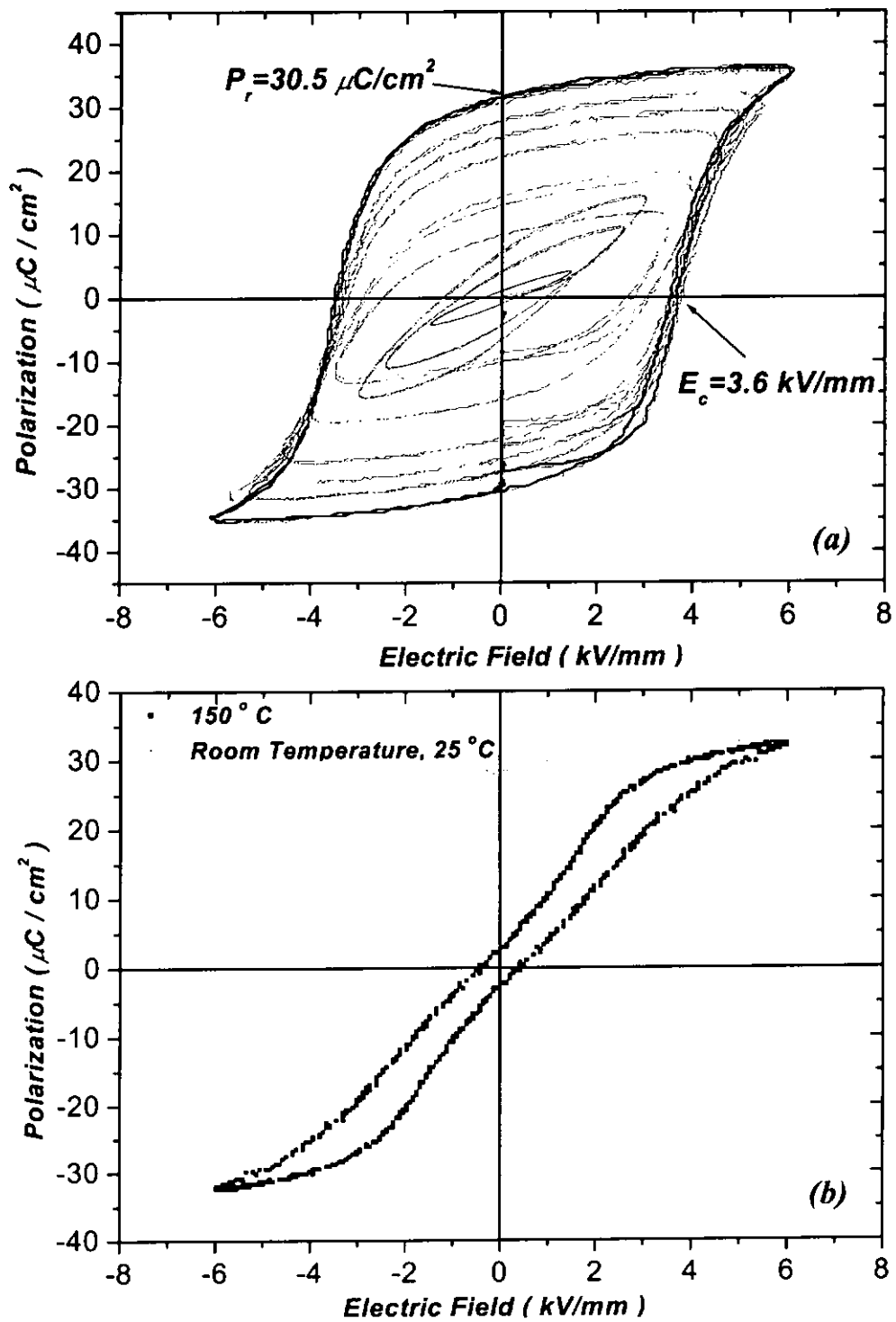
Figure 2.10 P-E hysteresis loops of BNBT-6 ceramics measured at (a) 25°C and (b) 150°C (P-E loop measured at 25°C is also shown in this graph for comparison).
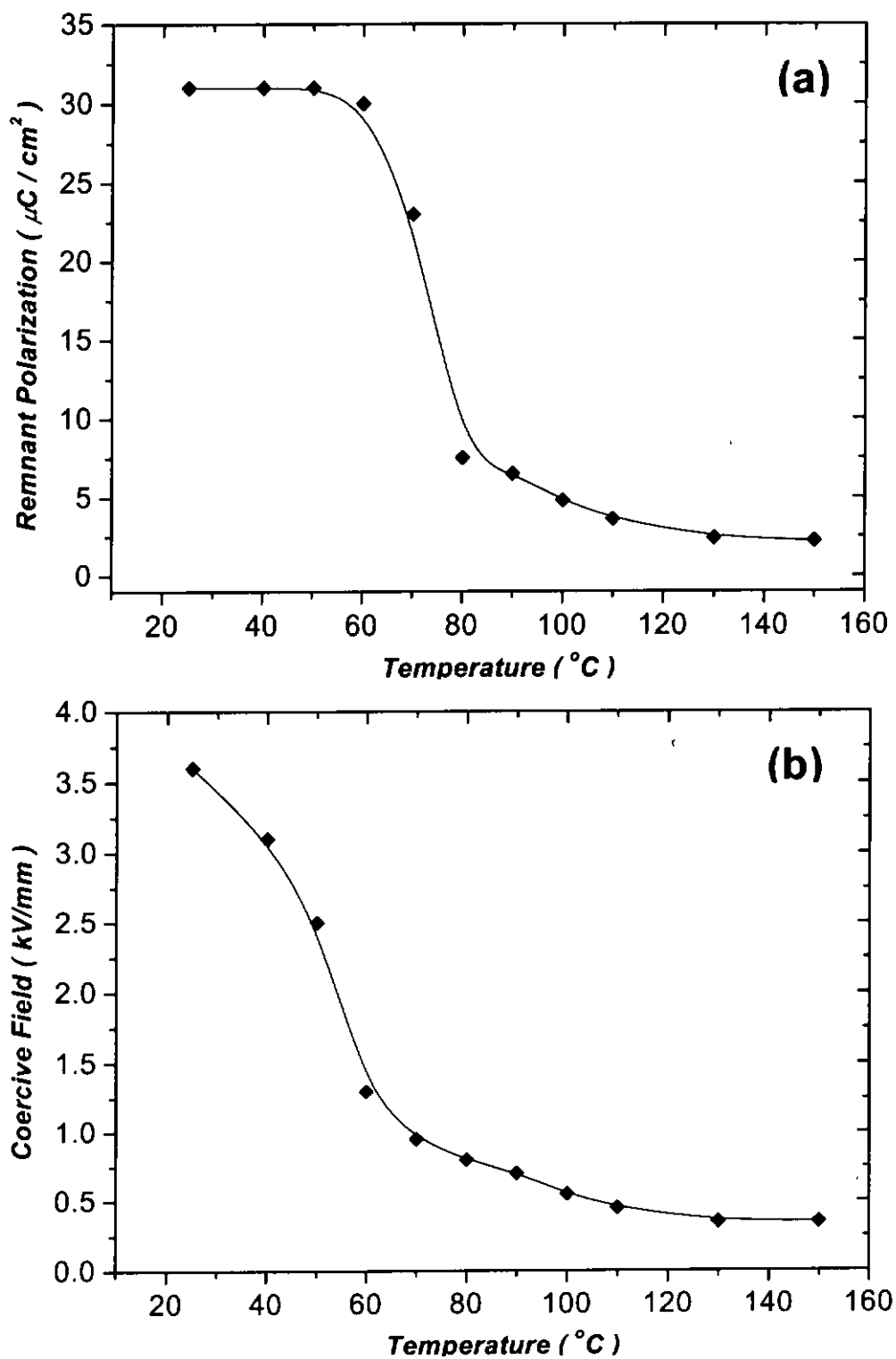
Figure 2.11 Temperature dependence of (a) remnant polarization and (b) coercive field

of BNBT-6 ceramics.

The hysteresis measurements were performed at 25°C and 150°C, respectively. The maximum applied electric field was 6.0 kV/mm at a frequency of 50 Hz. Figure 2.10 (a) is the P-E loop measured at 25°C, from which a remnant polarization P_r of 30.5 $\mu C/cm^2$ and a coercive field E_c of 3.60 kV/mm are obtained. Figure 2.10 (b) shows the P-E loop measured at 150°C, which seems quite different from the P-E loop measured at room temperature. Some researchers considered it as a "slanted" type antiferroelectric (Nagata, 1998 and Xu, 1998), while other ascribed this to a relaxor behavior. This phenomenon may not be ascribed to a single antiferroelectric or relaxor phase, but may due to a co-existing of the antiferroelectric and relaxor phases. The evolution of the P-E loop with the increase in temperature also implies that there is a phase transition between 25°C and 150°C.

The remnant polarization P_r and coercive field E_c of the BNBT-6 ceramics were plotted as functions of the measuring temperature as shown in Figure 2.11. Both the remnant polarization and coercive field decreased with the increase in measuring temperature. A sudden drop of the P_r at 70-80 °C can be found in Figure 2.11 (a), which implies a phase transition has occurred. The P_r value only changes slightly when the transition finished in a temperature range of 120 °C to 150 °C. More research work such as the microstructure investigation still need to be done to clarify the origin of this behavior.

2.3.4 Dielectric Properties

A Schering bridge-based HP4192A impedance analyzer was used to measure the relative

dielectric permittivity ε' and dielectric loss ε'' of the BNBT-6 ceramics. The

measurement setup is shown in Figure 2.12.
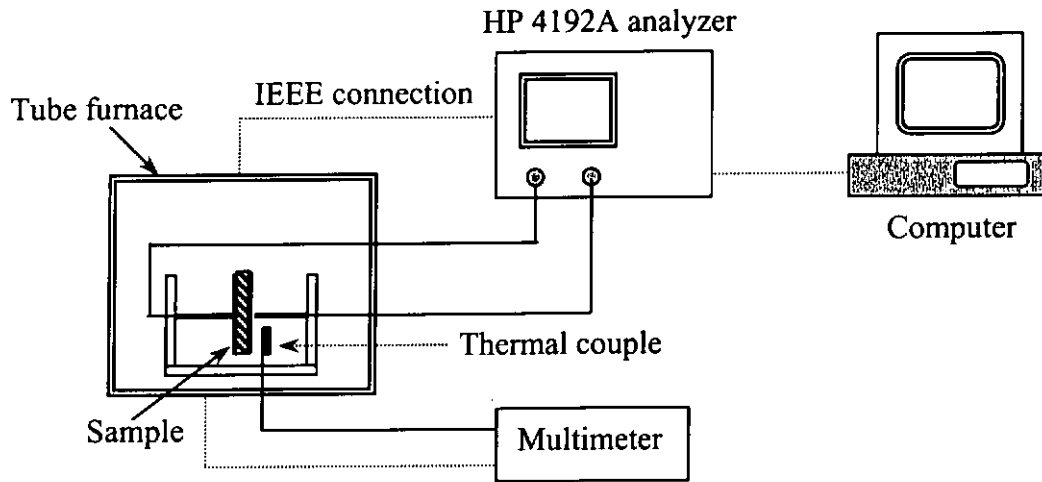
Figure 2.12 Dielectric measurement setup.

The ceramic sample was placed inside a Carbolite tube furnace so that its capacitance

could be measured in the temperature range of 25°C to 400°C. Values of capacitance and

loss tangent were saved to a computer file. Consider the BNBT-6 ceramic disc as a

parallel capacitor of thickness t, its capacitance C can be expressed as its permittimity

times the electrode area A divided by its thickness.

$$C = \frac{\varepsilon_o \varepsilon_r A}{t} \tag{2.2}$$

where ε_o is the permittivity of free space, ε_r is the relative permittivity. Since dielectric

materials would absorb electrical energy if it is subjected to an alternating electric field,

dielectric loss does exist and the relative permittivity would be in a complex form,

$$\varepsilon_r = \varepsilon' - \varepsilon''$$

(2.3)

where ε' is the real part of the permittivity and ε'' is the imaginary part of the permittivity, which is also called the dielectric loss. The relationship between ε' and ε'' can be expressed as,

$$\tan \delta = \frac{\varepsilon''}{\varepsilon'}$$

(2.4)

Thus, the relative permittivity ε' and dielectric loss ε'' can be calculated by the above equations.

Figure 2.13 shows the temperature dependence of ε' and ε'' in BNBT-6 ceramics at 1 kHz, 10 kHz and 100 kHz, respectively. The ε' vs. T curve shows a broad peak near the Curie point T_c of $\sim285^\circ C$ and a less conspicuous peak at $\sim100^\circ C$. This peak shifts to a higher temperature with the increase in measurement frequency.
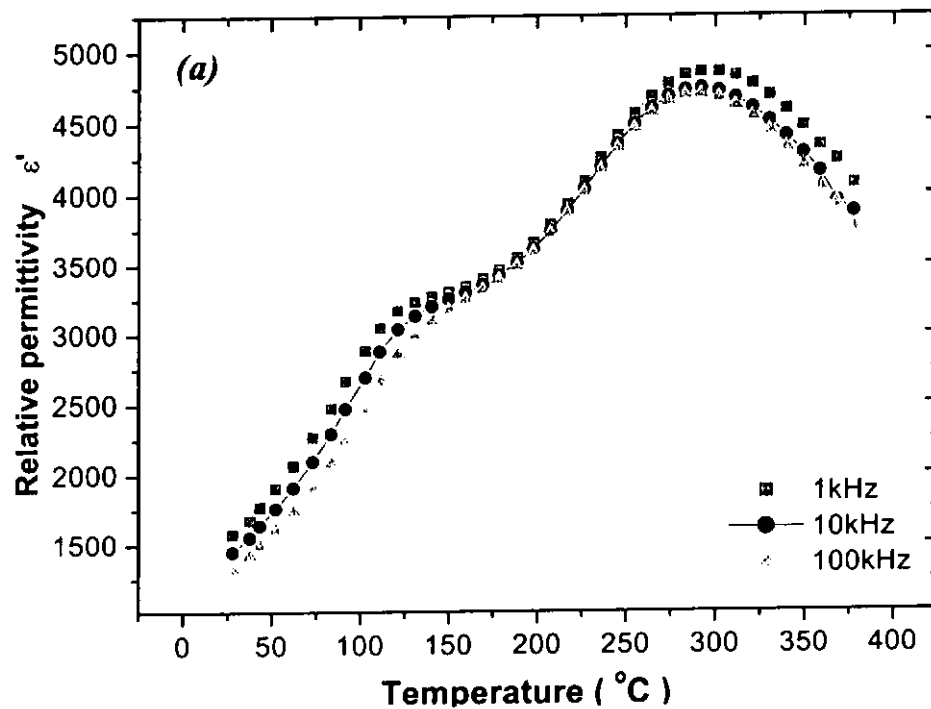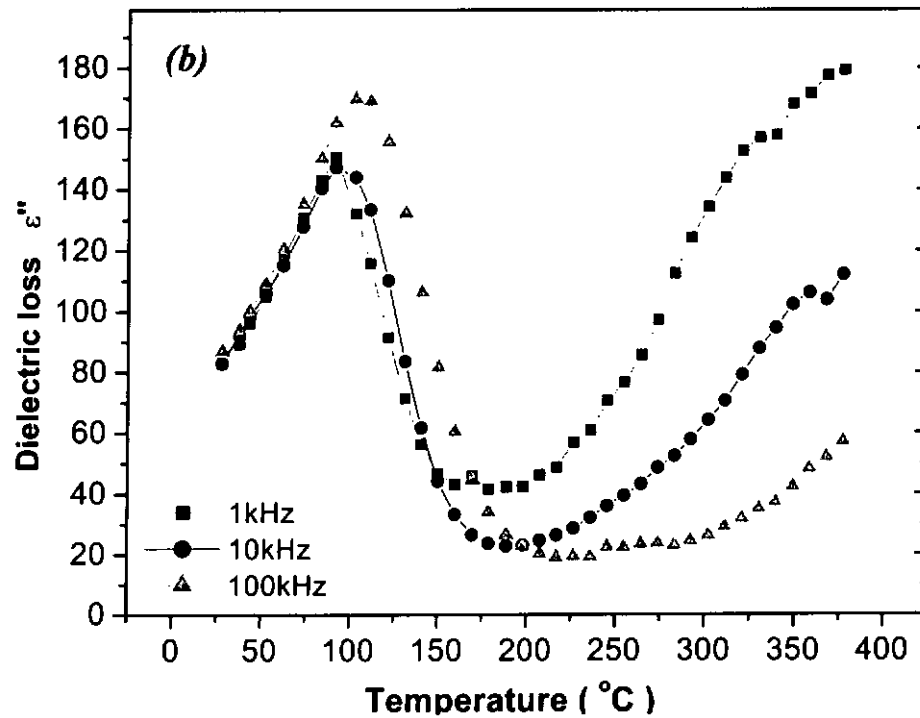
Figure 2.13 Temperature dependence of (a) relative permittivity ε' and (b) dielectric loss ε'' at 1 kHz, 10 kHz and 100 kHz.

This result implied that a second phase transition exsits at around 100-110°C in the frequency range of 1 kHz to 100 kHz (Takenaka, 1999). A peak corresponding to this transition can also be observed in the dielectric loss curves ε'' vs. T. (Figure 2.13 (b))

2.3.5 Piezoelectric Properties

Piezoelectric properties are the key properties for ultrasonic transducer applications. As fabricated, the BNBT-6 ceramics is non-piezoelectric because of the random distribution of dipoles inside the ceramics. To elicit the piezoelectric properties, an electric field must be applied (poling treatment) to align the dipoles. 6.5 kV/mm was used as the

poling field in this work.

2.3.5.1 Piezoelectric Coefficients

Assume the ceramic sample is a circular disc poled in the thickness "3" direction, and the piezoelectric properties are the same in the "1" and "2" directions. Thus, the relationship of the piezoelectric d coefficients can be expressed by (IEEE standards, 1987):

$$d_h = d_{33} + d_{31} + d_{32} \qquad (2.5)$$

or
$$d_h = d_{33} + 2d_{31} \qquad (2.6)$$

Two measurements were required to determine the piezoelectric d_{33} and d_{31} coefficients, and the hydrostatic d_h coefficient. The first one is to measure d_{33} directly by the d_{33} meter. The other is to measure d_h by applying a hydrostatic force to the sample. Then d_{31} can be deduced from the measured d_{33} and d_h.

A ZJ-3D d_{33} meter from Beijing Institute of Acoustics was used to measure the d_{33} values. The ceramic sample was placed in between the two measuring probes in the meter and magnitude of d_{33} can be obtained from the meter directly. Figure 2.14 shows the schematic diagram of the d_{33} meter.
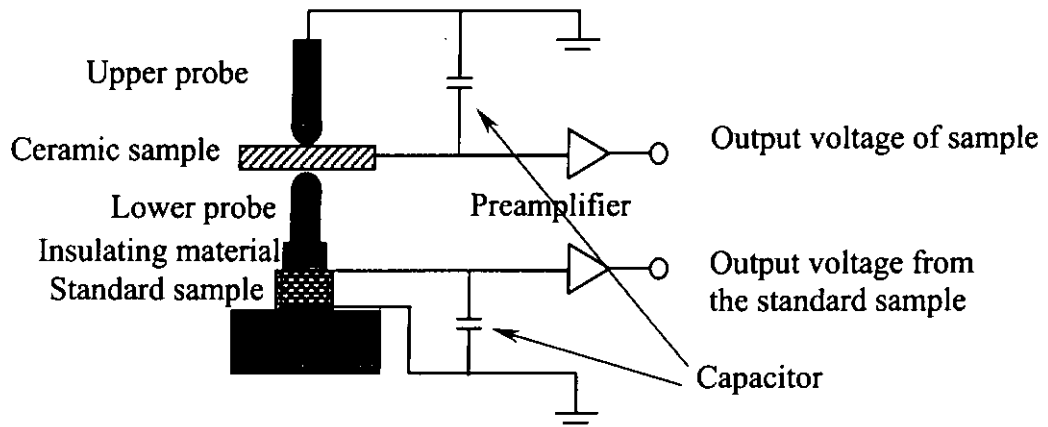
Figure 2.14 Schematic diagram of a d_{33} meter.

The hydrostatic d_h coefficient measures the charge generated when the sample is under stress applied equally in the "1", "2" and "3" directions. d_h value can be measured using a hydrostatic measurement equipment (Taunaumang, 1994) as shown in Figure 2.15. Acoustic pressure was applied to the ceramic sample by two loudspeakers. Brass gauze was used to shield the sample in order to minimize the probability of electromagnetic coupling from the loudspeakers. Frequency of the driving source is ~ 25 Hz such that the loudspeakers can generate a hydrostatic force. (Tang, 2001) Current output I_{rms} from the Stanford Research SR830 lock-in amplifier is related to d_h times the force applied F and the angular frequency ω. The applied force is equal to the rms pressure P generated by the speakers times the electroded area A of the sample. P can be measured by a calibrated hydrophone when the sample is placed in silicone oil. Thus, d_h can be calculated from:

$$d_h = \frac{\sqrt{2}I_{rms}}{A\omega P} \tag{2.8}$$

Then d_{31} can be calculated from Equation (2.7).
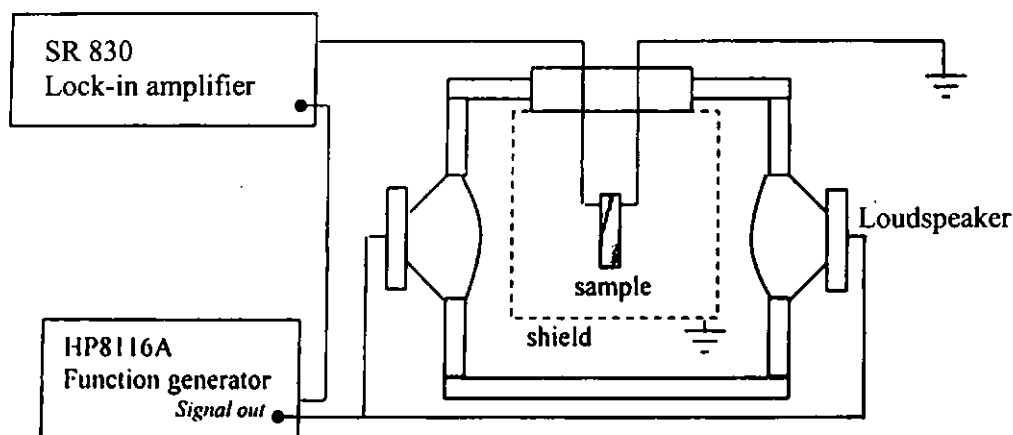
Figure 2.15 Setup for the hydrostatic d_h coefficient measurement.

2.3.5.2 Impedance Measurements

The impedance vs. frequency spectrum of a piezoelectric ceramic sample can be used to estimate the electromechanical coupling coefficients, which shows how efficient the material can transform mechanical energy into electrical energy and vice versa. The impedance/phase vs. frequency curves were obtained by an HP 4294A impedance/gain phase analyzer. A resonance method introduced by the IEEE Standards on Piezoelectricity (IEEE Standard, 1987) was used to evaluate the piezoelectric properties of BNBT-6 ceramics. Five samples with different geometries, including a circular disc, a long bar, a thin square plate, a thin shear plate and a thin rod as shown in Figure 2.16 were fabricated and used to evaluate the piezoelectric properties. The piezoelectric parameters related to these geometries are listed in Table 2.1.

Circular disc   Long bar   Shear plate

Square plate   Thin rod
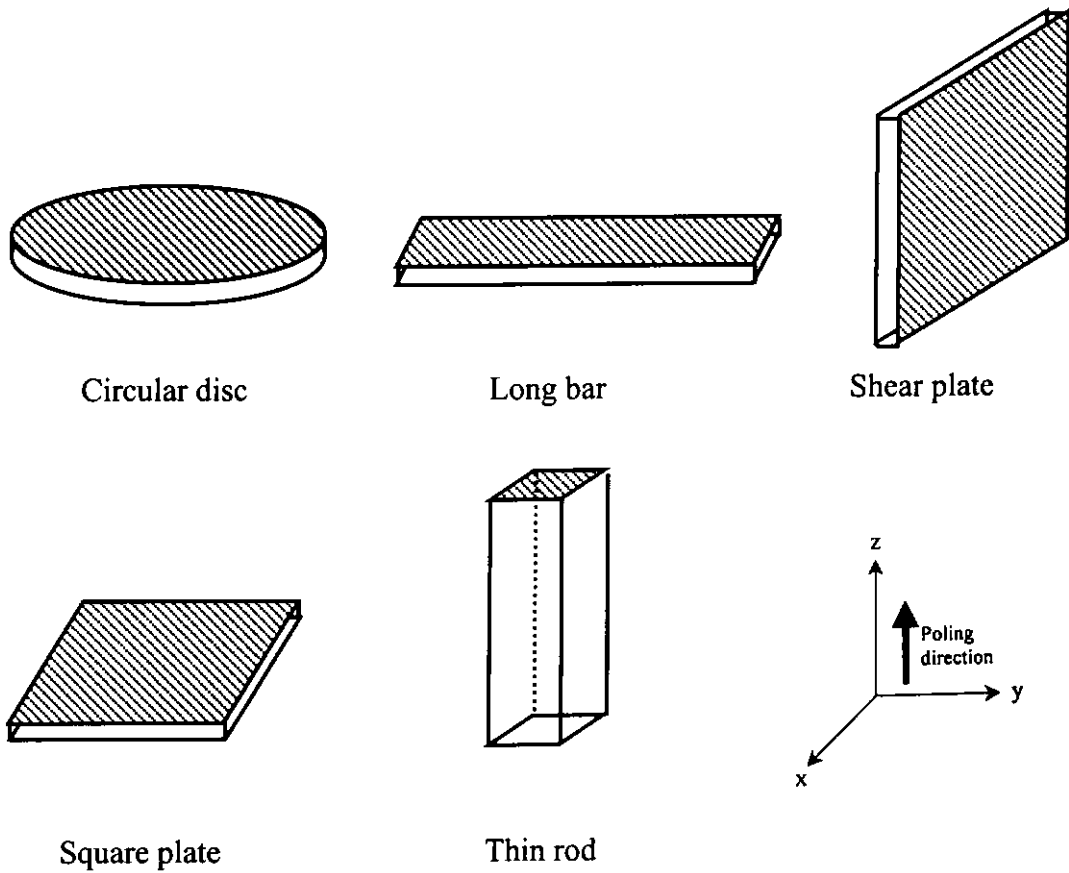
Figure 2.16 Various BNBT-6 samples for the piezoelectric properties measurements. (Detail dimensions of the samples are listed in Table 2.2)

The planar electromechanical coupling coefficient k_p was obtained from the k_p versus $(f_a-f_r)/f_r$ curves in the IEEE Standard on Piezoelectricity (IEEE Standard, 1987). The thickness electromechanical coupling coefficient k_t was calculated according to the equation:

$$k_t^2 = \frac{\pi}{2}\frac{f_r}{f_a}\tan(\frac{\pi}{2}\frac{f_a-f_r}{f_a})$$

(2.8)

Equations for calculating other electromechanical coupling coefficients are listed below:

$$\frac{k_{31}^2 - 1}{k_{31}^2} = \frac{\tan(\frac{\pi}{2}\frac{f_a}{f_r})}{\frac{\pi}{2}\frac{f_a}{f_r}} \tag{2.9}$$

$$k_{15}^2 = \frac{\pi}{2}\frac{f_r}{f_a}\tan(\frac{\pi}{2}\frac{f_a - f_r}{f_a}) \tag{2.10}$$

$$k_{33}^2 = \frac{\pi}{2}\frac{f_r}{f_a}\tan(\frac{\pi}{2}\frac{f_a - f_r}{f_a}) \tag{2.11}$$
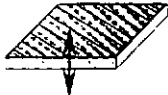
where f_r and f_a are the resonace and antiresonance frequencies of the correspoding resonance modes.

Details for calculation of other material parameters, including elastic compliance constants s^E and s^D, elastic stiffness constant c^E and c^D, piezoelectric voltage constant g, piezoelectric stress constant e, piezoelectric stiffness constant h and frequency constant N, are described in Appendix I. It is noted that parameters with a superscript D and E represent the open and short circuit conditions, respectively.

Table 2.1 Resonance modes of the five geometries and their related piezoelectric parameters.

Geometry	Resonance modes	Related piezoelectric parameters
	Planar Resonance	k_p, σ^P, s_{12}^{E}
	Thickness Resonance	k_t, c_{33}^{E}, c_{33}^{D}, ε_{33}^{T}, ε_{33}^{S}
	Length Extensional Resonance	k_{33}, s_{33}^{E}, s_{33}^{D}
	Length Extensional Resonance	k_{31}, d_{31}, s_{11}^{E}
	Thickness Shear Resonance	k_{15}, d_{15}, c_{44}^{E}, c_{44}^{D}, s_{44}^{E}, ε_{11}^{T}, ε_{11}^{S}

Mechanical quality factor Q_M is the ratio of the reactance to the resistance in the series equivalent circuit. Therefore, it can be determined by the equivalent circuit analysis function built in to the HP 4294A impedance/gain phase analyzer. Figure 2.17 shows the equivalent circuit for determining Q_M.
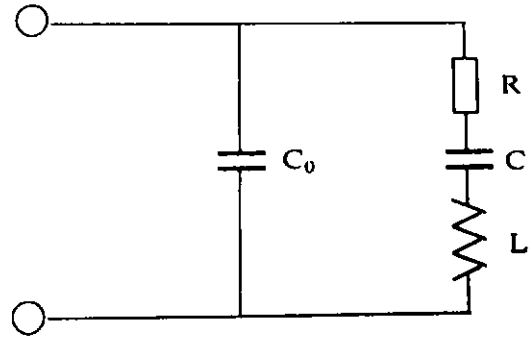
Figure 2.17 Equivalent circuit of a piezoelectric device.

C_o is the free electrical capacitance (at 1 kHz). L, C_1 and R are the inductance, electrical capacitance and resistance, respectively, which represent the converted mechanical properties-effective mass, compliance and mechanical loss. Thus, the mechanical Q factor Q_M can be calculated by,

$$Q_M = \frac{\omega L}{R} \qquad (2.12)$$

where ω is the angular frequency.

Electrical Q factor Q_E is the inverse of the dissipation factor $\tan\delta$, where $\tan\delta$ can be measured at 1 kHz by the impedance analyzer.

$$Q_E = \frac{1}{\tan\delta} \qquad (2.13)$$

2.3.5.3 Results

With the measured resonance data of BNBT-6 ceramics (Table 2.2), their elastic, piezoelectric and dielectric constants were determined by the resonance technique. In Table 2.3, the measured material parameters of the BNBT-6 samples are listed together with some literature data for comparison.

Table 2.2. Data of the BNBT-6 samples.

Test Samples	Dimensions (mm)			Frequency (kHz)	
	Length (L)	Width (w)	Thickness (t)	Resonance f_r	Anti-resonance f_a
Disc	Diameter=10.45		0.565	292.25	299.00
Square plate	7.250	7.400	0.610	4060.0	4500.0
Shear plate	7.870	2.020	0.710	2025.0	2161.25
Long bar	7.050	1.710	0.615	327.50	331.25
Thin rod	2.020	0.650	0.650	1026.60	1195.75

Table 2.3. Elastic, piezoelectric, dielectric constants and electromechanical coupling coefficients for test samples measured by the resonance technique at room temperature.

Material parameters	BNBT-6 ceramics	Literature data ([#] and [*])	
Electromechnical coupling coefficient			
k_{33}	0.552	0.55[#]	
k_{31}	-0.167	-0.192[#]	
k_{15}	0.382	0.498[#]	
k_t	0.460	0.40[*]	
k_p	0.250	0.29[*]	
Constant electric field elastic compliance $(10^{-12} m^2/N)$			
s_{11}^E	8.46	8.59[#]	
s_{12}^E	-2.39	--	
s_{13}^E	-1.08	--	
s_{33}^E	11.12	10.0[#]	
s_{44}^E	22.43	23.3[#]	
s_{66}^E	21.70	--	
Constant electric displacement elastic compliance $(10^{-12} m^2/N)$			
s_{11}^D	8.22	--	
s_{12}^D	-2.63	--	
s_{13}^D	-0.303	--	
s_{33}^D	7.73	--	
s_{44}^D	19.16	--	
s_{66}^D	21.70	--	
Constant stress dielectric constant			
$\varepsilon_{33}^T / \varepsilon_0$ at 1kHz	680	580[#]	601[*]
$\varepsilon_{11}^T / \varepsilon_0$ at 1kHz	907	733[#]	
Constant strain dielectric constant			
$\varepsilon_{33}^S / \varepsilon_0$ at $2*f_p$	441	--	
$\varepsilon_{11}^S / \varepsilon_0$ at $2*f_p$	595	--	

Cont.

Table 2.3 Elastic, piezoelectric, dielectric constants and electromechanical coupling coefficients for test samples measured by the resonance technique at room temperature.

Material parameters	BNBT-6 Ceramics	Literature data ($^{\#}$ and *)	
Constant electric field elastic stiffness (10^{10}N/m^2)			
c_{11}^{E}	13.14	--	
c_{12}^{E}	3.92	--	
c_{13}^{E}	5.58	--	
c_{33}^{E}	13.02	--	
c_{44}^{E}	4.46	--	
c_{66}^{E}	4.61	--	
Constant electric displacement elastic stiffness (10^{10}N/ m^2)			
c_{11}^{D}	13.60	--	
c_{12}^{D}	4.37	--	
c_{13}^{D}	3.97	--	
c_{33}^{D}	16.69	--	
c_{44}^{D}	5.22	--	
c_{66}^{D}	4.61	--	
Piezoelectric strain constant (10^{-12}C/N)			
d_{33}	124	125$^{\#}$	122*
d_{31}	- 37.7	-40$^{\#}$	
d_{h}	48.6	45$^{\#}$	
d_{15}	140.3	194$^{\#}$	
Piezoelectric voltage constant (10^{-3}m^{2}C^{-1})			
g_{33}	20.60	--	
g_{31}	-6.26	--	
g_{15}	23.31	--	
Mechanical quality factor			
Q_{M}	30~300	--	
Q_{E}	25	77$^{\#}$	56*

Cont.

Table 2.3 Elastic, piezoelectric, dielectric constants and electromechanical coupling coefficients for test samples measured by the resonance technique at room temperature.

Material parameters	**BNBT-6 Ceramics**	Literature data ([#] and [*])	
Piezoelectric voltage constant (C/m^2)			
e_{33}	11.94	--	
e_{31}	-5.25	--	
Piezoelectric stiffness constant ($10^8 N/C$)			
h_{33}	29.41	--	
h_{31}	-3.07	--	
h_{15}	12.17	--	
Frequency constant (Hz-m)			
N_p	3054	2975[#]	3000[*]
N_{31}	2309	2264[#]	
N_{33}	2074	2507[#]	2522[*]
N_{15}	1438	1586[#]	
Density ρ (kg/m^3)	5544	5780[#]	
Poisson ratio σ	0.28	0.25[*]	
Young's modulus Y ($10^{10}Pa$)	8.99	--	

Data with superscript # are from reference (Takenaka, 1999) and superscript * are from

reference (Chu, 2000).

2.4 Summary

Dense piezoelectric BNBT-6 ceramics with a grain size of approximately 2 μm has been prepared by sintering the BNBT-6 powder derived from the mixed-oxide method at 1150°C. The microstructure, ferroelectric and piezoelectric properties of the ceramics were investigated.

The result shows that the ceramics has perovskite crystal structure with a remnant polarization of 30 $\mu C/cm^2$ and a coercive field of 3.6 kV/mm at room temperature. At 150°C the ceramics exhibits a relaxor-like hysteresis loop. A Curie temperature of 285°C was observed from the dielectric measurement. At ~100-110°C, there exists a phase transition in the ceramics.

Piezoelectric properties of BNBT-6 ceramics were systematically characterized. The piezoelectric coefficient d_{33} (~124 pC/N) and thickness electromechanical coupling coefficient k_t (~0.46) are larger than those of other lead-free ceramics. Also BNBT-6 ceramics has a low k_p (~0.25), which is beneficial to ultrasonic transducer applications. However, the mechanical quality factor Q_M shows a wide dispersion ranged from 30 to 300, which depends on the quality of the ceramic samples.

CHAPTER III

STUDY OF BNBT-6/EPOXY 1-3 COMPOSITES FABRICATED BY THE DICE-AND-FILL TECHNIQUE

3.1 Introduction

The use of piezoelectric composites is an important attempt to overcome the disadvantages of ceramics (Newnham, 1978). In the past two decades, piezoelectric ceramic/polymer 1-3 composites have been widely used in medical ultrasonic transducer applications because they could offer both fabrication and performance advantages. (Gururuja, 1984; Chan, 1987) These advantages include higher electromechanical coupling coefficient k_t, lower acoustic impedance z_0 and lower mass. (Fiore, 1996; Smith, 1996) Propeties of the ceramic/polymer composites can be tailored to suit different applications by changing the volume fraction (Smith, 1985) and spatial distribution of the ceramic phase. (Gururaja, 1985)

A number of methods have been developed to prepare 1-3 composites: 1) the pick-and-place method (Klicker, 1981; Meyer, 1998); 2) the dice-and-fill technique (Newhnam, 1978; Chan, 1987); 3) the lamination technique (Taunaumang, 1993); 4) the lost wax/mold technique (Lubitz, 1993); and 5) the injection molding technique (Bowen,

1993). In the pick-and-place method, the ceramic rods or fibres are first prepared by extrusion and then imbedded into a polymer matrix. This method will be discussed in detail in Chapter IV and V. The dice-and-fill technique is one of the most commonly used ways to fabrication 1-3 composites. The smallest dimensions for the ceramic rods depend on the mechanical properties and grain size of the ceramic materials. For a PZT ceramics, the dicing operation is feasible for rod dimension down to 50 μ m. (Kwok, 1997) In this Chapter, BNBT-6/epoxy 1-3 composites with various ceramic volume fractions were fabricated using the dice-and-fill technique. Then the composites were characterized by the resonance technique. The experimental results were then compared with the theoretical modelling.

The 1-3 composites may exhibit a complex resonance behavior due to the coupling of the thickness and lateral modes. This behavior can be predicted using the mode-coupling theory. (Onoe, 1963; Chan, 1987) In this Chapter, by progressively thinning a composite, the mode coupling behavior of BNBT-6/epoxy 1-3 composites with 0.52 volume fraction of BNBT-6 were studied. The experimental data show good agreement with the theoretical predictions.

3.2 Selection and Characterization of the Polymer Matrix

A passive polymer matrix plays an important role in stress transfer to the ceramics and in interaction between elements. The polymer can isolate each rod and reduce the vibration of the ceramic rods along the planar direction. On the other hand, the compressional force impinging on the polymer matrix can be transferred to the ceramic rods so that the deformation and the charges generated from the ceramic rods increase. Consequently, the composite has a k_t value higher than the bulk ceramics. In general, a softer polymer allows the pillars to expand and contract more freely resulting in a larger electromechanical coupling coefficient close to the k_{33} of the ceramics (Smith, 1992). The low density and soft polymer matrix also lead to lower acoustic impedance $\bar{z}$ and longitudinal velocity which aids matching considerations to tissue yielding a better $\bar{k}_t - \bar{z}$ trade-off (Smith, 1991).

Epoxy type Araldite LY5138-2 with hardener HY5138 (mixed in a weight ratio of 1:0.23 and cured at 40°C for 12 h) from Ciba Geigy Pty Ltd. was selected as the matrix material in this study. Acoustic velocity of the epoxy was measured by using an ultrasonic immersion method (Read, 1978) and elastic constant was calculated by density times (velocity) ^{2}. Relative dielectric permittivity and dissipation loss of the epoxy were also measured.

3.2.1 Ultrasonic Wave Velocity and Acoustic Impedance Measurements
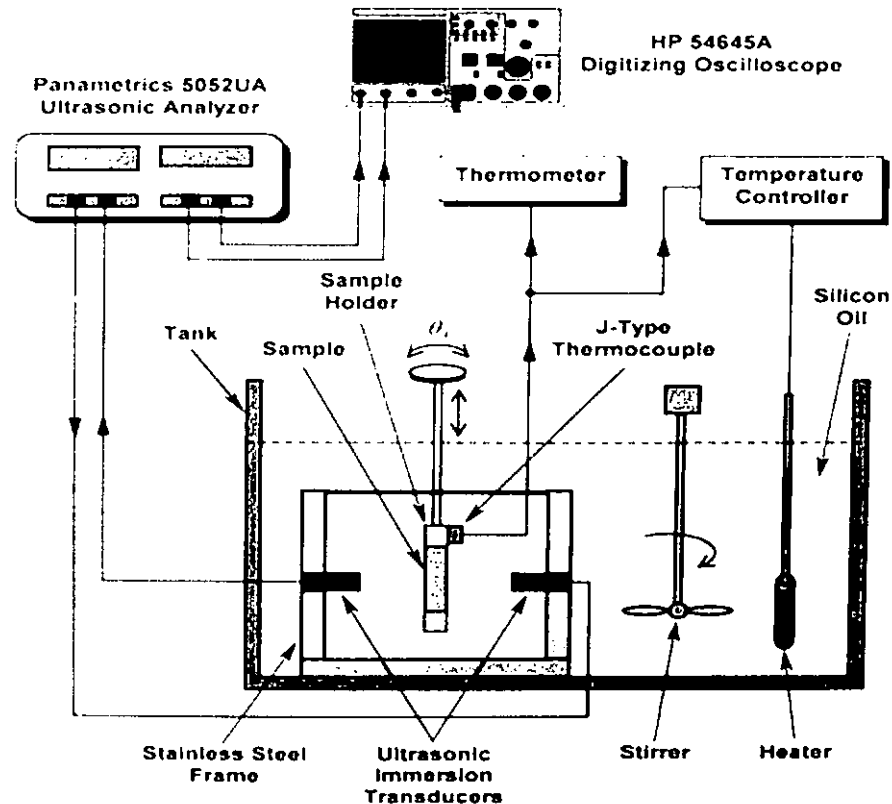
Figure 3.1 Schematic setup of the ultrasonic immersion method (Or, 2001).

In an unbounded isotropic solid, two types of ultrasonic waves can propagate, namely the longitudinal and shear waves. The schematic experimental setup of the ultrasonic immersion method is shown in Figure 3.1. A sample immersed in a silicone oil bath was mounted in a holder which was located between a pair of 10 MHz ultrasonic transducer of 10 mm diameter. One of the transducers acted as the transmitter P_1 and the other acted

as the receiver P_2. The distance between P_1 and P_2 was 31.45 mm. P_1 was driven by a broadband excitation which was a sharp pulse generated by a Panametrics 5052UA ultrasonic analyzer.

Four epoxy samples with 31.6 mm diameter and thicknesses of 0.868 mm, 0.812 mm, 0.968 mm and 0.907 mm, respectively, were used in the measurements.

3.2.1.1 Longitudinal Wave Velocity Measurements

The method for measuring the longitudinal velocity was described as follows. (Read, 1978) When the wave consisting of several pulses or a tone burst passed through the epoxy sample, both longitudinal and transverse waves may be generated in the sample depending on the angle of incidence. For the measurement of longitudinal wave velocity, the ultrasonic wave incident normally on the sample and was picked up by the receiver after passing through the sample. Since the velocity of sound in silicone oil is less than the longitudinal wave velocity of the epoxy sample, the ultrasonic pulse will take a shorter time to reach the receiver and the signal will shift forward in time. This shift in the transit time $\Delta\tau_L$ is related to the longitudinal wave velocity in the sample υ_L by:

$$\Delta\tau_L = t(\frac{1}{v_L} - \frac{1}{v_{oil}}) \tag{3.1}$$

where t is the sample thickness. υ_{oil} is the velocity of sound in oil which can be calculated from the arrival time in the absence of the sample. The acoustic impedance z_L is given by

$$z_L = v_L \rho \qquad\qquad (3.2)$$

Density of the sample ρ was determined using the Archimedes principle.

3.2.1.2 Shear Wave Velocity Measurements

The measurement setup is essentially the same as that in Figure 3.1 for the immersion method. The sample was rotated to a critical angle such that total reflection of the longitudinal wave took place and only the shear wave can propagate through the sample as shown in Figure 3.2. By rotating the sample slowly, the shear wave would appear at a later time than the longitudinal wave and increase in amplitude until it attains a maximum value. At the same time, the longitudinal wave decreases in amplitude until it disappears.
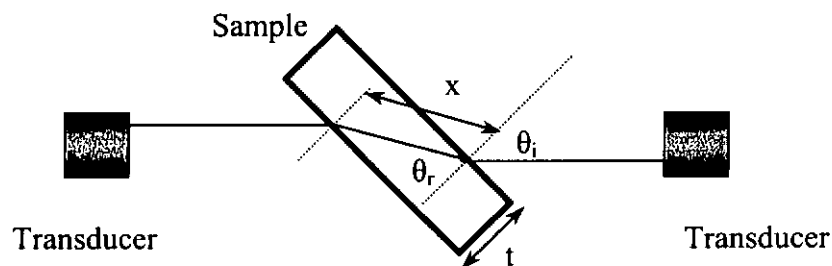
Figure 3.2 Geometry of the shear wave propagation.

To calculate the shear wave velocity υ_s, according to Snell's law,

$$\frac{\sin\theta_i}{\sin\theta_r} = \frac{v_{oil}}{v_S} \quad (3.3)$$

where θ_i is the angle of incidence, θ_r is the angle of refraction, x is the path length through the sample.

$$x = \frac{t}{\cos\theta_r} = t(1 - (\frac{v_S \sin\theta_i}{v_{oil}})^2)^{-1/2} \quad (3.4)$$

By solving equation (3.4), x can be determined. The time shift $\Delta\tau_S$ was measured from an oscilloscope, the shear wave velocity can be calculated by

$$\Delta\tau_S = x(\frac{1}{v_S} - \frac{1}{v_{oil}}) \quad (3.5)$$

The shear acoustic impedance z_S is given by

$$z_S = v_S\rho \quad (3.6)$$

3.2.2 Attenuation Coefficient and Mechanical Quality Factor Measurements

Several epoxy samples with the same cross sectional area but different thicknesses were used to measure the wave amplitude in this experiment. Thus, the amount of surface reflection and diffraction can be assumed to be the same in the measurements, and if absorption in oil is neglected, the difference in amplitude observed in two samples is only due to the absorption accruing in a thickness equal to the difference in the thickness of the two samples. Attenuation coefficient α is given by (Hartmann, 1980)

$$\alpha(dBm^{-1}) = \frac{20\log(\frac{A_1}{A_2})}{(t_2 - t_1)} \tag{3.7}$$

where A_1 and A_2 are the amplitudes measured in samples of thickness t_1 and t_2.

To convert α (dBm^{-1}) to α (m^{-1}), the following equation can be used:

$$\alpha(m^{-1}) = \frac{1}{2}\ln(10^{\frac{\alpha(dBm^{-1})}{10}}) \tag{3.8}$$

The mechanical Q factor of the polymer can be calculated using:

$$Q_L = \frac{\pi f}{v_L \alpha} \tag{3.9}$$

where f is the frequency of ultrasonic wave and v_L is the longitudinal wave velocity of the sample.

3.2.3 Elastic Properties of Epoxy

For an isotropic material, only two independent stiffness coefficients are needed to specify its elastic properties, they are c_{11} and c_{66}. For the two types of elastic waves propagating through an isotropic material of density ρ, their velocities, v_L and v_S, are related to the stiffness coefficients by the following equations (Hartmann, 1980):

$$c_{11} = c_{22} = c_{33} = \rho v_L^2 \tag{3.10}$$

$$c_{44} = c_{55} = c_{66} = \rho v_S^2 \tag{3.11}$$

$$c_{12} = c_{21} = c_{13} = c_{31} = c_{23} = c_{32} = \rho(v_L^2 - 2v_S^2) = c_{11} - 2c_{44} \tag{3.12}$$

where c_{11}, c_{66}, c_{12} are the longitudinal, shear, and cross-plane stiffness, respectively.

Once c_{pq} is known, the elastic compliances s_{pq} can be obtained by inverting the stiffness

matrix, given by (Auld, 1973)

$$s_{11} = s_{22} = s_{33} = \frac{c_{11} + c_{12}}{(c_{11} - c_{12})(c_{11} + 2c_{12})} \tag{3.13}$$

$$s_{44} = s_{55} = s_{66} = \frac{1}{c_{44}} \tag{3.14}$$

$$s_{12} = s_{21} = s_{13} = s_{31} = s_{23} = s_{32} = \frac{-c_{12}}{(c_{11} - c_{12})(c_{11} + 2c_{12})} \tag{3.15}$$

Then the Poisson's ratio σ can be calculated by the following relation (Auld, 1973):

$$\sigma = -\frac{s_{12}}{s_{11}} \tag{3.16}$$

3.2.4 Results

Table 3.1 Material properties of epoxy type Araldite LY5138-2 with hardener HY5138 measured at room temperature.

Density	ρ	(kg/m^3)	1150
Relative dielectric permittivity	$\varepsilon/\varepsilon_o$		5.048
Dissipation loss factor	$\tan\delta$		0.0225
Longitudinal wave velocity	υ_L	(m/s)	2450
Shear wave velocity	υ_S	(m/s)	1123
Longitudinal acoustic impedance	z_L	(Mrayl)	2.817
Shear acoustic impedance	z_S	(Mrayl)	1.291
Longitudinal stiffness	c_{11}	$(10^{10}\ N/m^2)$	0.6911
Shear stiffness	c_{44}	$(10^{10}\ N/m^2)$	0.1460
Stiffness in x-y plane	c_{12}	$(10^{10}\ N/m^2)$	0.3991
Longitudinal compliance	s_{11}	$(10^{-12}\ m^2/N)$	257.7
Shear compliance	s_{44}	$(10^{-12}\ m^2/N)$	705.3
Compliance in x-y plane	s_{12}	$(10^{-12}\ m^2/N)$	-94.92
Attenuation coefficient at 10 MHz	α	(dBm^{-1})	4610
		(m^{-1})	531
Mechanical Q factor	Q_M		21.2
Poisson's ratio	σ		0.365

3.3 Fabrication of BNBT-6/Epoxy 1-3 Composites by the Dice-and-Fill Technique

1-3 composites were fabricated using the dice-and-fill technique. BNBT-6 ceramics with 10.5 mm diameter and various thicknesses, and Araldite LY5138-2 / HY5138 epoxy described in the previous section were used as the active and matrix materials, respectively. A Disco DAD 341 automatic dicing saw equipped with a flange type diamond saw blade of 75 μm thickness (Disco NBC-Z 2050) was used to perform the dicing operation. In order to avoid breakage of the sample, an appropriate blade rotation rate of 40000 rpm was set and this resulted in a cutting speed of 0.5 mm/s. Distilled water was used as the coolant and lubricant during dicing.

The ceramics were poled before they are cut. Since the BNBT-6 ceramics is very fragile, the reticulated cuts cannot be made in both directions in one go, otherwise, the sample will break. After cleaning in an ultrasonic bath, the sample was firstly cut in a direction parallel to the diameter and epoxy was filled into the grooves. Subsequently, the sample was degassed in a vacuum chamber for 30 min and then placed into a 40°C oven for 30 min to cure the epoxy. After the epoxy had cured, a second set of cuts was made to the sample in a direction perpendicular to the first set of cuts. Then epoxy was filled into the grooves. To obtain the optimum properties of the epoxy, the sample should be cured at 40°C for 12 h. But as the BNBT-6 ceramics cannot withstand a heat treatment for a long period of time due to its low phase transition temperature (~ 100°C), hence, the samples were placed at room temperature for one day to cure the epoxy.

Then the samples was ground and polished to desired thicknesses using abrasive papers

(400# and 800#). A thin layer of air-dried silver paint was applied on both surfaces of

the discs as electrodes. The composite samples were repoled under the same conditions

as that of BNBT-6 ceramics before the electrical properties measurements.

A series of composites sample with different ceramic volume fractions ϕ ranging from

0.56 to 0.83 were fabricated and shown in Figure 3.3. Information of the composites was

given in Table 3.2. It was found that the epoxy grooves were about 80-82 μm (7%-9%

wider than the blade thickness) due to the vibration of the blade. The ceramic volume

fraction was calculated by the following equation:

$$\bar{\rho} = \phi\rho + (1-\phi)\bar{\bar{\rho}} \tag{3.17}$$

where the $\bar{\rho}$, ρ and $\bar{\bar{\rho}}$ are the density of the composite, ceramics and epoxy,

respectively. Density of the samples was determined by applying the Archimedes

principle.
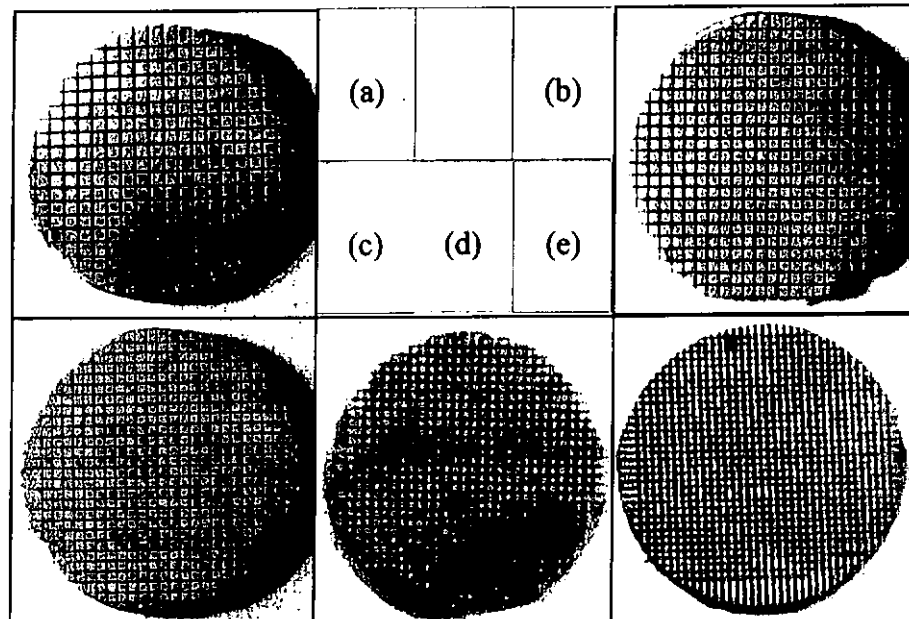
Figure 3.3 BNBT-6/epoxy 1-3 composites with different ceramic volume fractions.

Table 3.2 Description of BNBT-6 /epoxy 1-3 composites.

Sample	Ceramic width (L) (μ m x μ m)	Epoxy Groove width (μ m)	Ceramic volume fraction ϕ	Thickness (H) (mm)	BNBT-6 Element Configuration (L/H)
a	400x400	82	0.83	0.76	0.526
b	350x350	80	0.76	0.68	0.515
c	300x300	80	0.67	0.64	0.469
d	250x250	80	0.63	0.50	0.500
e	200x200	82	0.56	0.47	0.426

3.4 Characterization of BNBT-6/epoxy 1-3 Composites with Different Ceramic Volume Fractions

3.4.1 Experimental Results

Characterization of BNBT-6/epoxy 1-3 composites is based on the resonance technique and IEEE Standards on Piezoelectricity, which has been described in the previous Chapter. The piezoelectric and dielectric properties of the five BNBT-6 /epoxy 1-3 composites are shown in Table 3.3.

Table 3.3. Piezoelectric and dielectric properties of BNBT-6/epoxy 1-3 composites of 10.4 mm diameter.

	a (ϕ=0.83)	b (ϕ=0.76)	c (ϕ=0.67)	d (ϕ=0.63)	e (ϕ=0.56)
d_{33}(pC/N)	103	103	108	105	100
d_{31}(pC/N)	-33.3	-34.4	-34.8	-32.5	-31.2
d_h(pC/N)	36.4	34.3	38.4	40.0	37.6
k_p	0.23	0.21	0.18	0.18	0.17
k_t	0.55	0.52	0.53	0.50	0.51
Q_M	15.4	25.5	29	7.3	17.9
N_t(Hz m)	1847	1822	1856	1820	1642
$\varepsilon_{33}^T/\varepsilon_0$ (1kHz,RT)	554.8	499.3	416.7	386.6	350.2
tan δ (1kHz,RT)	0.046	0.045	0.050	0.043	0.046
g_{33} (10^{-3} Vm/N)	20.9	23.3	29.3	30.7	32.2

The ceramic volume fraction (ϕ) has a significant effect on the piezoelectric properties

of the 1-3 composite. The d_{33} and the d_{31} values of the composites are lower than that of

the bulk ceramics. A 1-3 composite also has a lower planar coupling and lower k_p and

d_{31} values compared to the BNBT-6 ceramics. The thickness electromechanical coupling

factor k_t of the BNBT-6/epoxy 1-3 composite increased by about 9-20% compared to the

bulk BNBT-6 ceramics. In a 1-3 composite the ceramic rods are vibrating quite freely as

the relatively soft epoxy cannot impose strong clamping on the ceramic rods. Hence, the

k_t of a composite is close to the k_{33} of the ceramics. (Taunaumang, 1994)

The relative dielectric permittivity of the 1-3 composites decreased almost linearly with

the decrease in ceramic volume fraction. As the ceramic and epoxy phases are in parallel,

both electrically and mechanically, the dielectric permittivity of a composite could be

estimated by the following relationship (Chan, 1994):

$$\overline{\varepsilon_{33}^S} = \phi[\varepsilon_{33}^S + \frac{2(e_{31})^2}{C(\phi)}] + (1-\phi)\overline{\overline{\varepsilon_{11}}} \qquad (3.18)$$

where ϕ is the ceramic volume fraction and

$$C(\phi) = c_{11}^E + c_{12}^E + \frac{\phi(\overline{\overline{c_{11}}} + \overline{\overline{c_{12}}})}{1-\phi} \qquad (3.19)$$

In Equation (3.19), the influence of the piezoelectric contribution (2nd term in the

parentheses) is relatively small and the dielectric permittivity is roughly proportional to

the ceramic volume fraction ϕ (Taunaumang, 1994). The electrical impedance and

phase angle of the composites were measured using an HP 4294A impedance/gain phase

analyzer and the impedance spectra are shown in Figure 3.4.
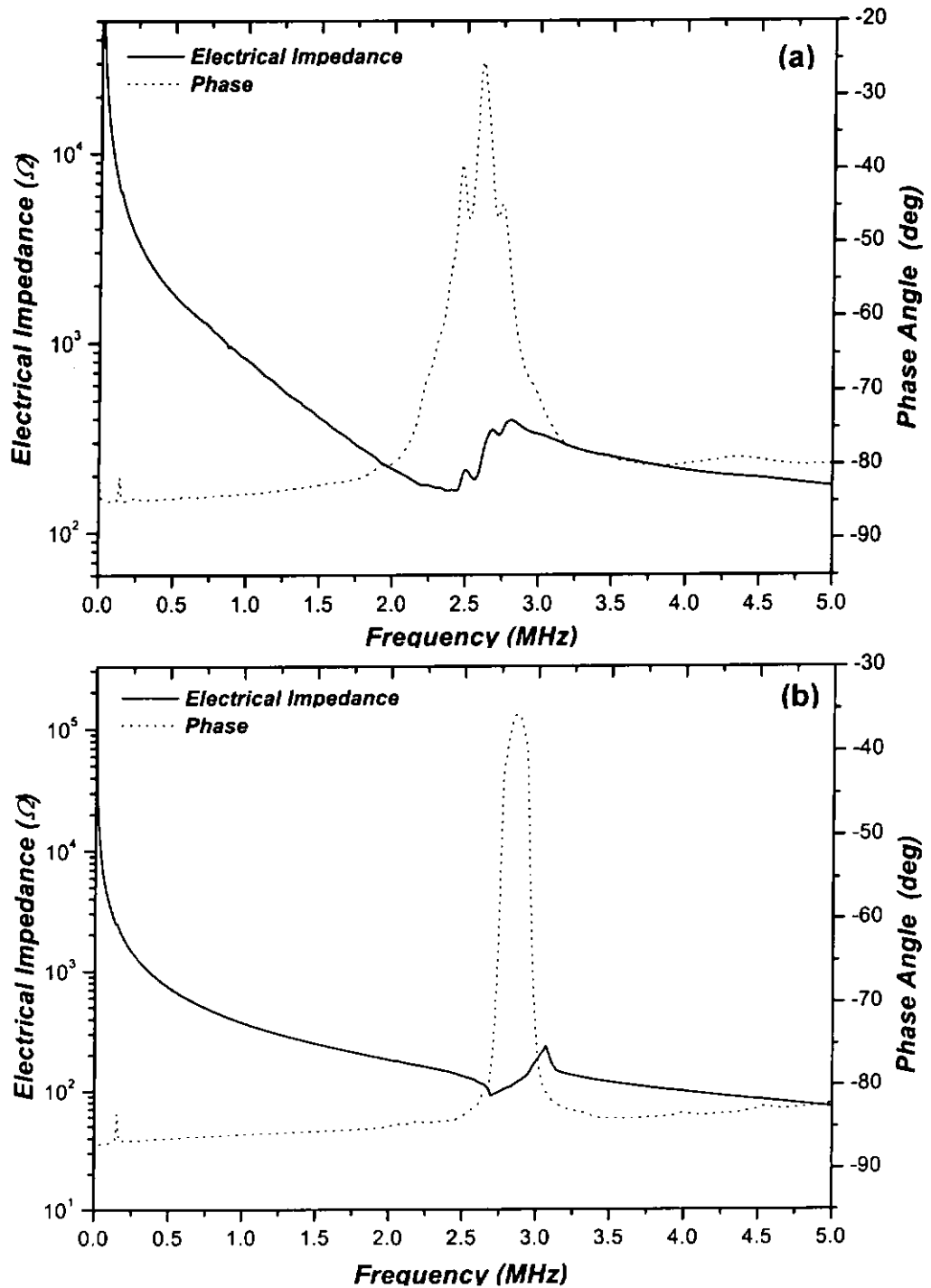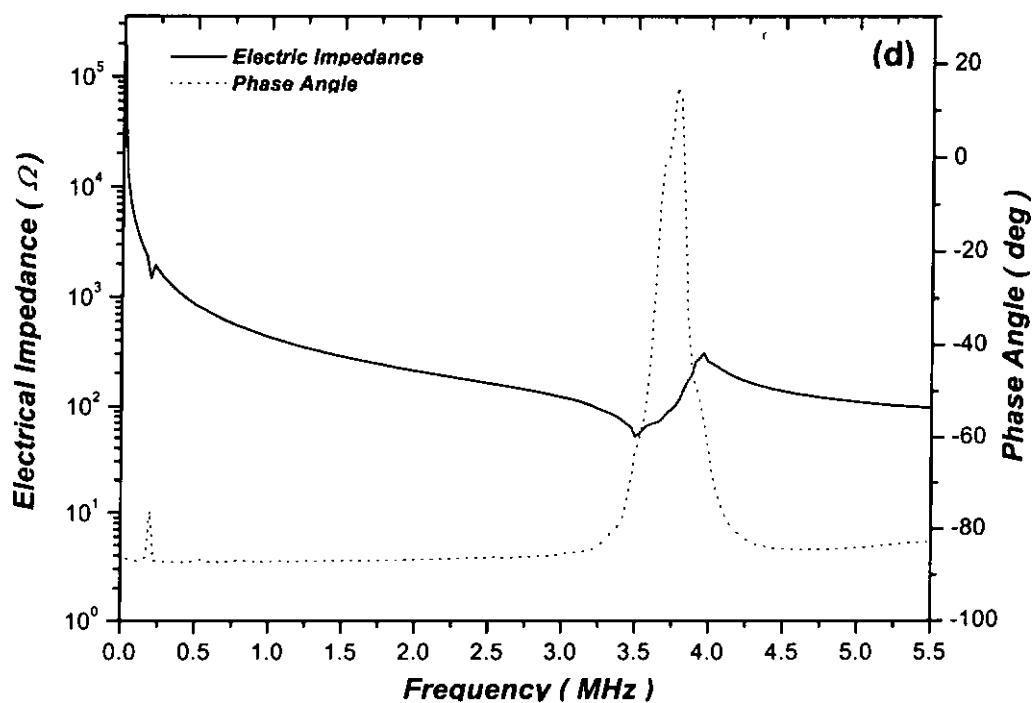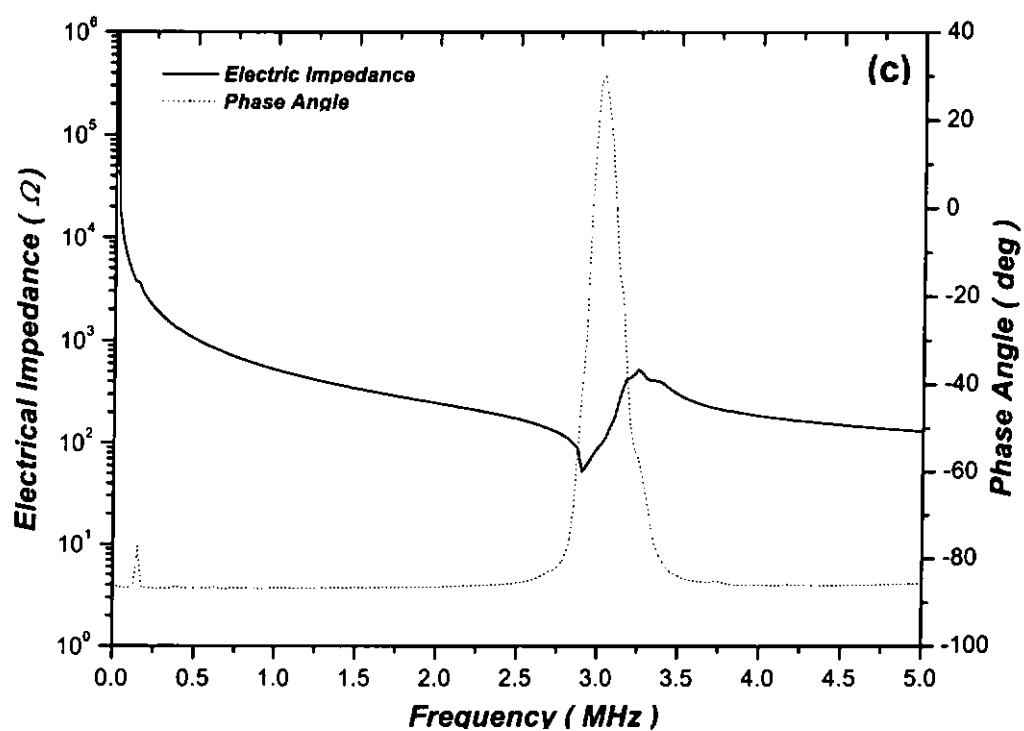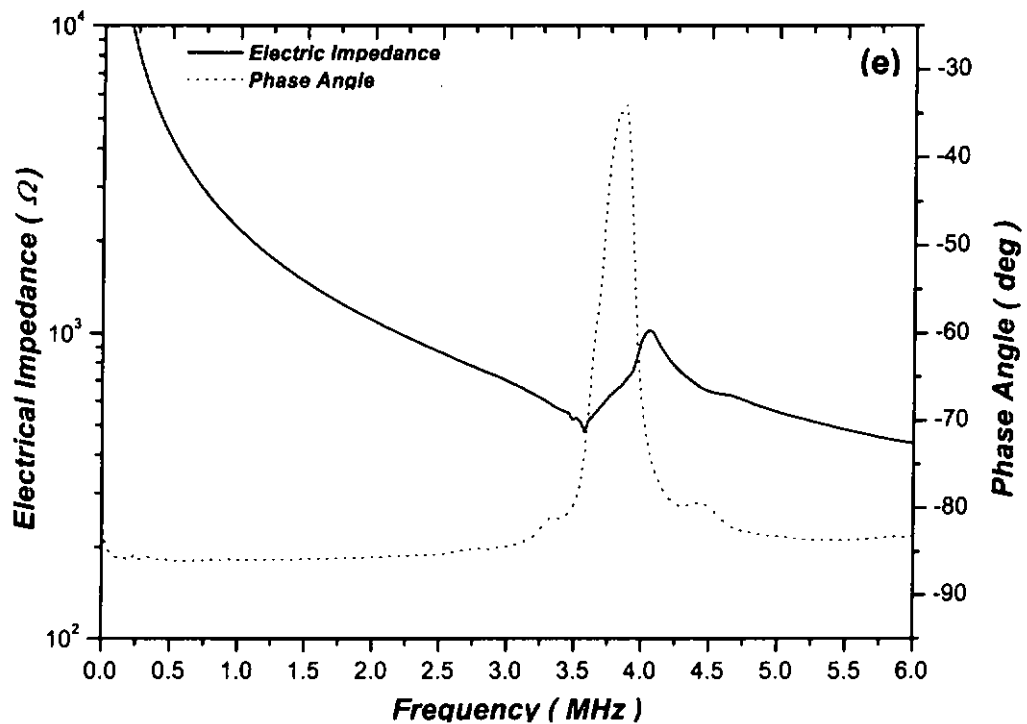
Figure 3.4 Electrical impedance and phase angle versus frequency plots for BNBT-6/epoxy 1-3 composites with various ceramic volume fractions.

3.4.2 A Model for 1-3 Composites

3.4.2.1 The Modified Parallel and Series Model

To evaluate the overall performance of the BNBT-6/epoxy 1-3 composites, a modified parallel and series model was used in this study. This model was used to calculate the material parameters of BNBT-6/epoxy 1-3 composites and then compared with the experimental data.

In this analysis, the material parameters of epoxy was denoted by a double bar on the top of the parameters and the effective material parameters of the composites was denoted with a bar. Consider a 1-3 composite with the major faces covered with uniform electrodes as shown in Figure 1.6. The thickness direction of the poled BNBT-6 rods are aligned parallel to the z-axis. The following assumptions were adopted in the model (Smith, 1991; Chan, 1987; Chan, 1989):

1) The mechanical displacements are parallel to the coordinate axes so that all shear components vanish in the x-y plane,

$$T_4 = T_5 = T_6 = \overline{\overline{T_4}} = \overline{\overline{T_5}} = \overline{\overline{T_6}} = 0 \qquad (3.20a)$$

$$S_4 = S_5 = S_6 = \overline{\overline{S_4}} = \overline{\overline{S_5}} = \overline{\overline{S_6}} = 0 \qquad (3.20b)$$

2) All fringing fields anywhere inside the materials are zero, giving:

$$E_1 = E_2 = \overline{\overline{E_1}} = \overline{\overline{E_2}} = 0 \qquad (3.21a)$$

$$D_1 = D_2 = \overline{\overline{D_1}} = \overline{\overline{D_2}} = 0 \qquad (3.21b)$$

3) The composite can be treated as an effective homogenous medium, both the BNBT-6 and epoxy move together in a uniform thickness oscillation and the vertical strains are the same in both phases (isostrain), giving:

$$\overline{S_3} = S_3 = \overline{\overline{S_3}} \qquad (3.22a)$$

This leads to an effective total stress in the z direction given by averaging over the contributions of the constituent phases,

$$\overline{T_3} = \phi T_3 + (1 - \phi)\overline{\overline{T_3}} \qquad (3.22b)$$

4) Electric fields are the same in both the BNBT-6 and epoxy phases in the z direction,

$$\overline{E_3} = E_3 = \overline{\overline{E_3}}$$ (3.23a)

Thus, the effective total electric displacement is the average over the contributions of the two phases,

$$\overline{D_3} = \phi D_3 + (1 - \phi)\overline{\overline{D_3}}$$ (3.23b)

5) The composite as a whole is laterally clamped but not for the individual elements,

$$\overline{T_1} = T_1 = \overline{\overline{T_1}}$$ (3.24a)

$$\overline{T_2} = T_2 = \overline{\overline{T_2}}$$ (3.24b)

$$\overline{S_1} = \phi S_1 + (1 - \phi)\overline{\overline{S_1}}$$ (3.24c)

$$\overline{S_2} = \phi S_2 + (1 - \phi)\overline{\overline{S_2}}$$ (3.24d)

The thickness mode parameters are derived from the following approach used by Smith *et al.* Both BNBT-6 and epoxy, and hence the 1-3 composites are considered as isotropic in the x-y plane so that all lateral components are equal, $T_1 = T_2$, $\overline{\overline{T_1}} = \overline{\overline{T_2}}$, $S_1 = S_2$, $\overline{\overline{S_1}} = \overline{\overline{S_2}}$.

If S and E are chosen as independent variables, some composite parameters can be derived,

$$\overline{c_{33}^E} = \phi[c_{33}^E - \frac{2(c_{13}^E - \overline{\overline{c_{12}}})^2}{C(\phi)}] + (1-\phi)\overline{\overline{c_{11}}} \tag{3.25}$$

$$\overline{e_{33}} = \phi[e_{33}^E - \frac{2e_{31}(c_{13}^E - \overline{\overline{c_{12}}})^2}{C(\phi)}] \tag{3.26}$$

$$\overline{c_{33}^D} = \overline{c_{33}^E} + \overline{h_{33}}\,\overline{e_{33}} \tag{3.27}$$

$$\overline{h_{33}} = \frac{\overline{e_{33}}}{\overline{\overline{\varepsilon_{33}^S}}} \tag{3.28}$$

$$\overline{k_t} = \sqrt{1 - \frac{\overline{\overline{c_{33}^E}}}{\overline{\overline{c_{33}^D}}}} \tag{3.29}$$

$$\overline{\upsilon_{3t}^D} = \sqrt{\frac{\overline{\overline{c_{33}^D}}}{\rho}} \tag{3.30}$$

$$\overline{\upsilon_{3t}^E} = \sqrt{\frac{\overline{\overline{c_{33}^E}}}{\rho}} \tag{3.31}$$

$$\overline{Z} = \sqrt{\overline{\overline{\rho c_{33}^D}}} = \overline{\rho}\,\overline{\upsilon_{3t}^D} \tag{3.32}$$

On the other hand, if T and E are taken as independent variables, some composite parameters are given:

$$\overline{d_{31}} = \phi d_{31} - \frac{\phi(1-\phi)d_{33}(s_{13}^E - \overline{\overline{s_{12}}})}{S(\phi)} \tag{3.33}$$

$$\overline{d_{33}} = \frac{\phi d_{33}\overline{\overline{s_{11}}}}{S(\phi)} \tag{3.34}$$

$$\overline{\varepsilon_{33}^T} = \phi\varepsilon_{33}^T + (1-\phi)\overline{\overline{\varepsilon_{11}}} - \frac{\phi(1-\phi)\overline{d_{33}^2}}{S(\phi)} \tag{3.35}$$

$$S(\phi) = \phi\overline{\overline{s_{11}}} + (1-\phi)s_{33}^E \tag{3.36}$$

$$\overline{k_{33}} = \frac{\overline{d_{33}}}{\sqrt{\overline{\varepsilon_{33}^T s_{33}^E}}} \tag{3.37}$$

$$\overline{k_{31}} = \frac{\overline{d_{31}}}{\sqrt{\overline{\varepsilon_{33}^T s_{11}^E}}} \tag{3.38}$$

$$\overline{g_{33}} = \frac{\overline{d_{33}}}{\overline{\varepsilon_{33}^T}} \tag{3.39}$$

Calculations for other composite parameters will be presented in detail in Appendix II.

To determine the mechanical quality factor $\overline{Q_M}$, it was assumed that the composite has very fine epoxy width so that the isostrain condition in assumption 3 holds true. Then the effective total longitudinal attenuation coefficient of the composite $\overline{\alpha}$ (in m^{-1}) is the average over the contributions of the two phases and can be estimated using the parallel connectivity approach (Hayward, 1990),

$$\overline{\alpha} = \phi\alpha + (1-\phi)\overline{\overline{\alpha}} \tag{3.40}$$

where the values of α and $\overline{\overline{\alpha}}$ can be deduced from the corresponding quality factors. Thus, $\overline{Q_M}$ of the composite can be calculated as $\overline{\alpha}$ in Equation (3.40) is known.

$$\overline{Q}_M = \frac{\pi f}{\overline{\alpha v_{3t}^E}}$$

(3.41)

3.4.2.2 Comparison Between Predicted and Experimental Results

Using the equations derived above and substituting the material parameters of BNBT-6 ceramics and Araldite LY5138-2/HY5138 epoxy from Tables 2.3 and 3.1, respectively, the effective material parameters of BNBT-6/epoxy 1-3 composites as functions of BNBT-6 volume fraction ϕ can be calculated. The theoretical prediction curves including the density $\overline{\rho}$, piezoelectric charge coefficients $\overline{d_{33}}$ and $\overline{d_{31}}$, relative permittivity $\overline{\varepsilon_{33}^T}$, dielectric loss tangent $\overline{\tan \delta}$, electromechanical coupling coefficient $\overline{k_t}$, mechanical quality factor $\overline{Q_M}$ and piezoelectric voltage constant $\overline{g_{33}}$, were plotted (Figure 3.5) together with the experimental data for comparison.
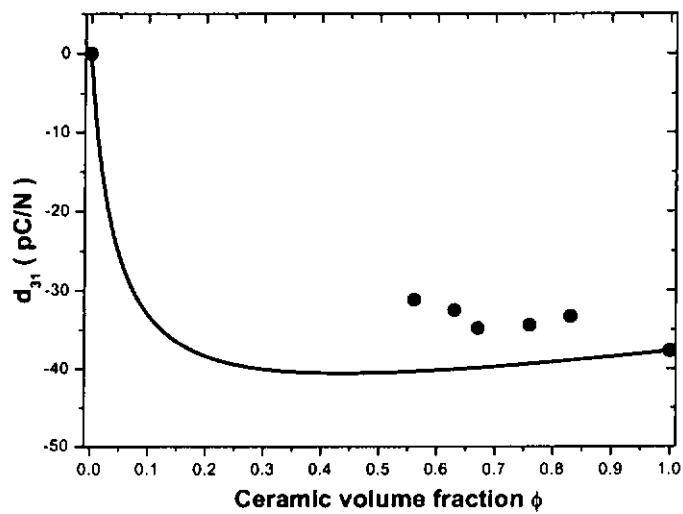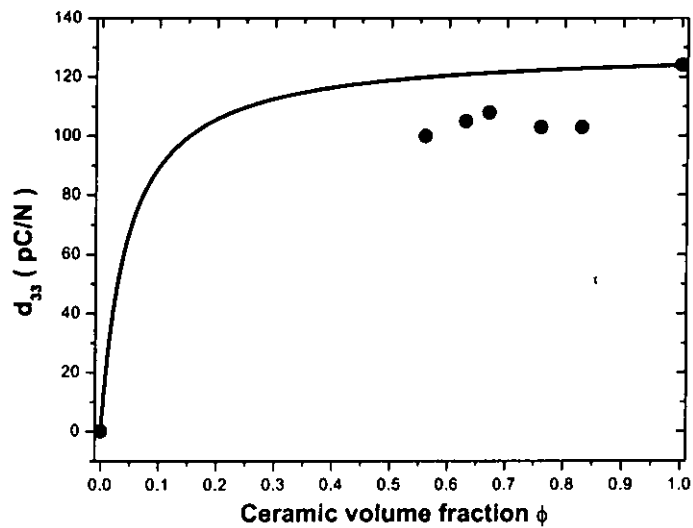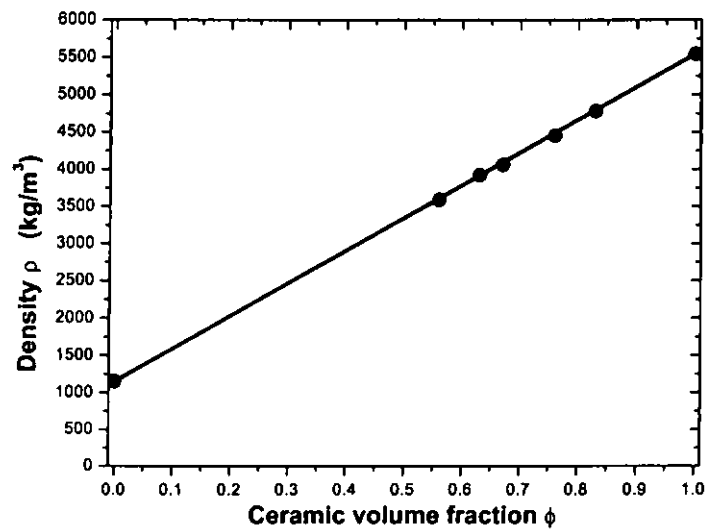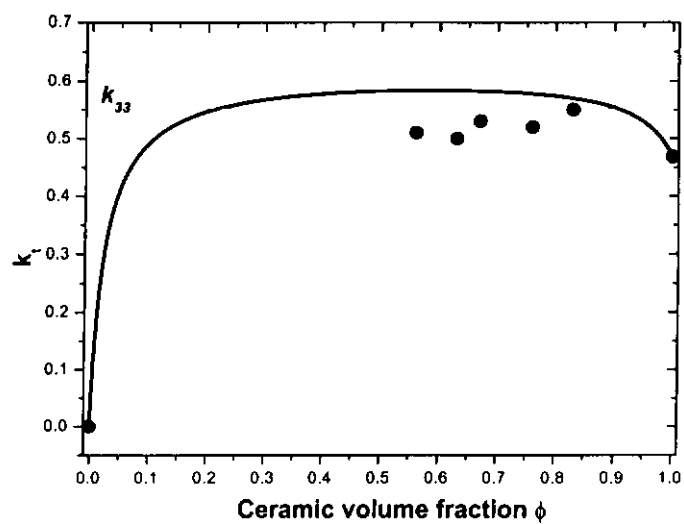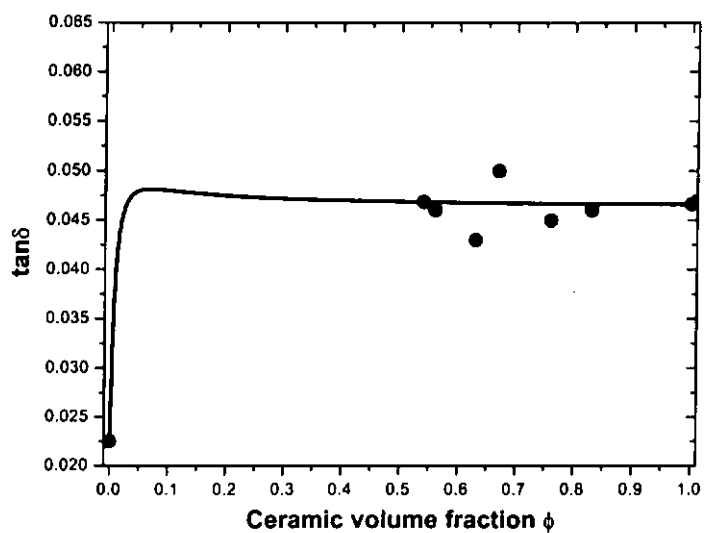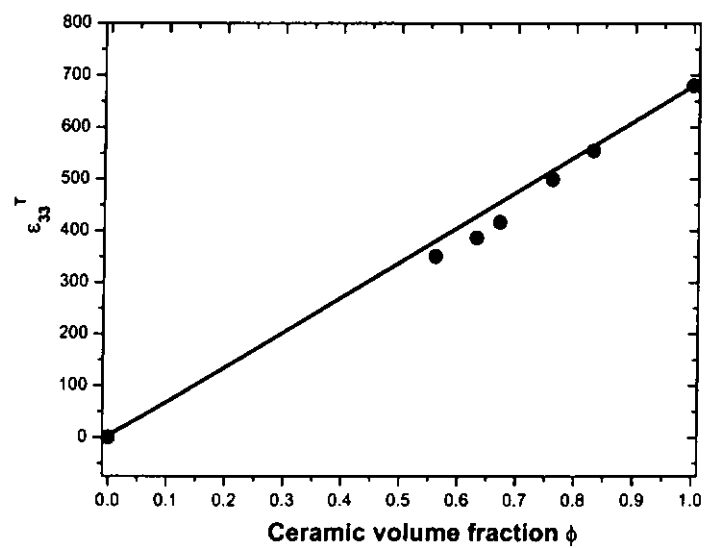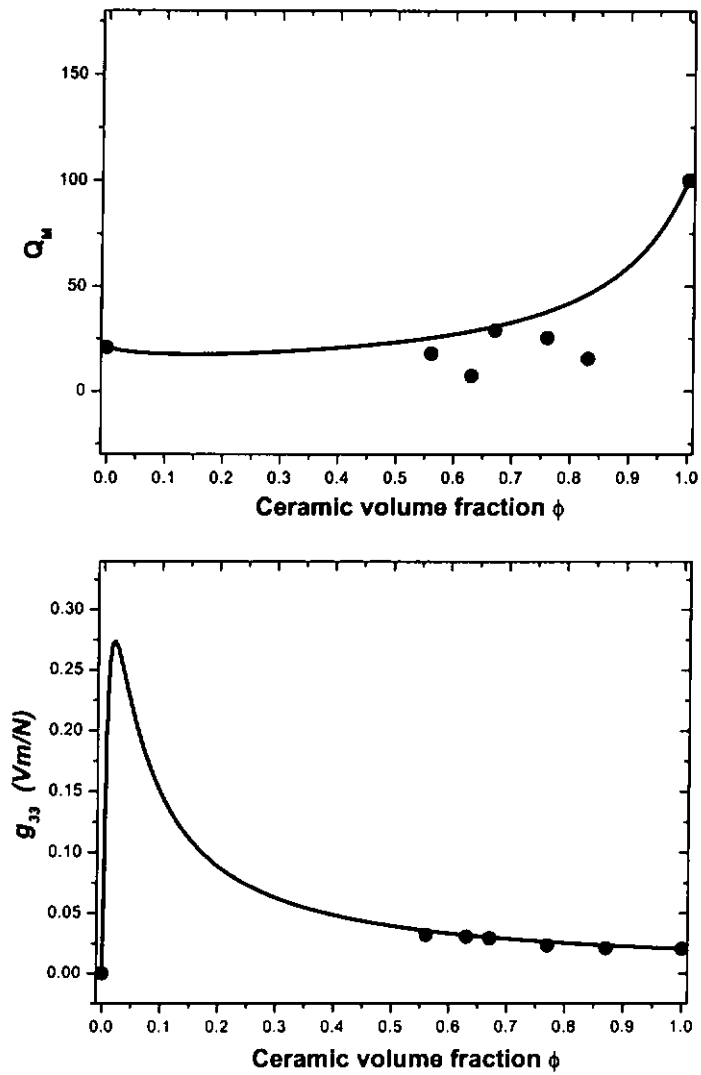
Figure 3.5 Variation of effective material parameters of the BNBT-6/epoxy 1-3
composites with the volume fraction ϕ of BNBT-6.

As shown in Figure 3.5, the calculated $\overline{\rho}$ is a linear function of ϕ and agrees well with

the measured values. Also the relative permittivity $\overline{\varepsilon_{33}^T}$ varies almost linearly with

increasing ϕ except at both ends. The measured $\overline{\varepsilon_{33}^T}$ has good agreement with the theoretical values.

It is observed that the measured $\overline{d_{33}}$ values are lower than the calculated data. This is probably due to cracks inside the ceramic rods induced by the vibration of the dicing saw blade in the cutting process. Since BNBT-6 ceramics is very fragile, it is likely that cracks have been induced. These fine cracks may adversely affect the piezoelectric properties of the composites especially in lowering the Q_M values. Thus, in the mechanical quality factor $\overline{Q_M}$ vs. ϕ graph, lower measured data were found. $\overline{Q_M}$ of the composites is dominated by the low $\overline{\overline{Q_M}}$ value of the polymer. The measured $\overline{k_t}$ are lower than the calculated results, presumably also due to the micro cracks inside the ceramic rods.

3.5 The Mode Coupling Theory and Thinning Test Results

In this study, a BNBT-6/Araldite LY5138-2/HY5138 epoxy 1-3 composite with 0.52 ceramic volume fraction was fabricated using the dice-and-fill technique for mode coupling investigation. This composite sample is 10.4 mm diameter and has 0.575 mm ceramic width and 0.225 mm epoxy width as shown in Figure 3.6. An HP 4294A impedance analyzer was used to measure the electric impedance as a function of

frequency and Figure 3.7 shows the electric impedance versus frequency spectrum of this composite.
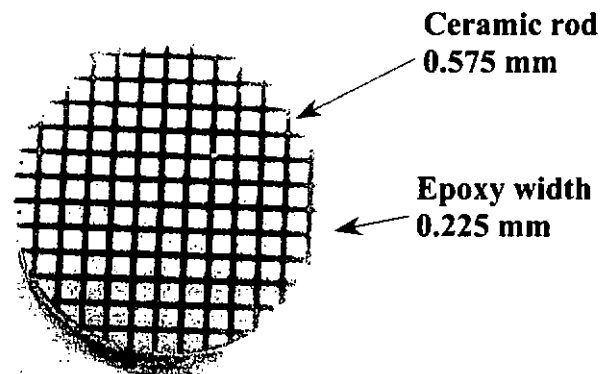
Figure 3.6 Photograph of the BNBT-6/epoxy 1-3 composite with ϕ =0.52.
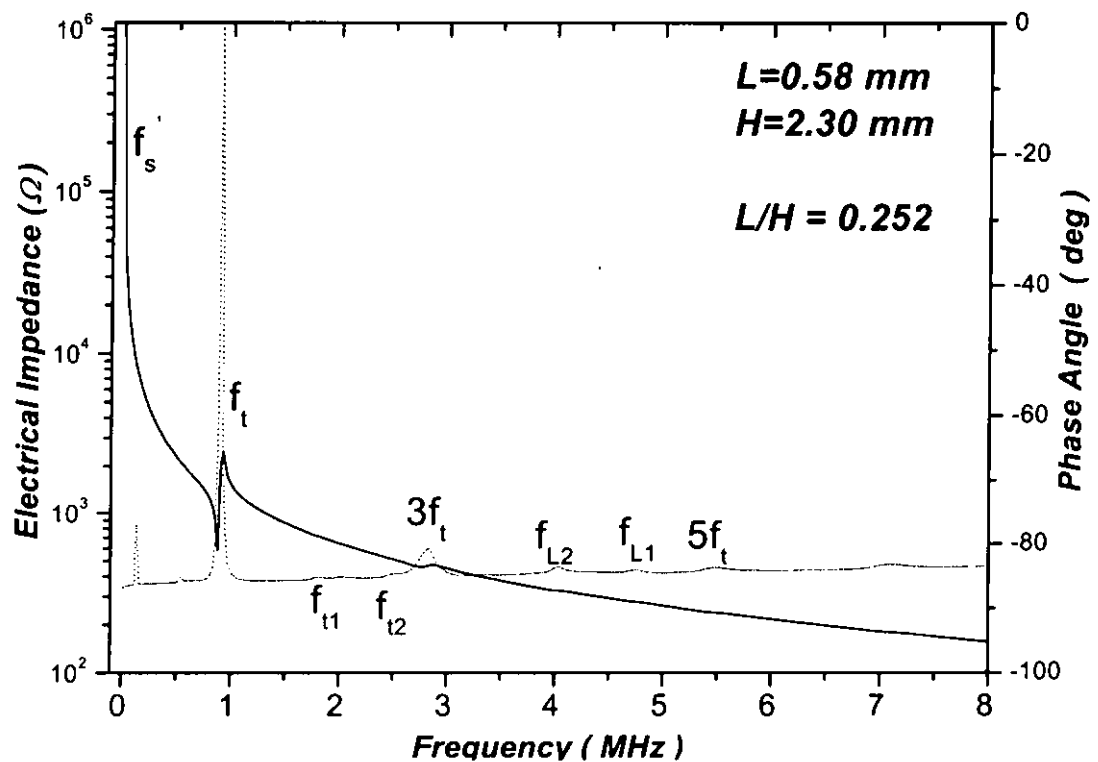
Figure 3.7 Electrical impedance and phase versus frequency of BNBT-6/epoxy 1-3 composite with ϕ =0.52.

3.5.1 Resonance Modes in a BNBT-6/epoxy 1-3 Composites

As shown in Figure 3.7, the 1-3 composite exhibits a series of resonance peaks. They can be classified into two main kinds (Gururaja, 1985; Chan, 1994): 1) Cooperative resonance, which includes the planar mode resonance f_s, and stopband mode f_{t1} and f_{t2}; 2) Characteristic resonance of the individual piezoelectric rods, which includes the thickness mode resonance f_t and lateral mode resonance f_{L1} and f_{L2}.

3.5.1.1 Planar Mode Resonance

The planar mode vibration in a thin circular disc, as illustrated in Figure 3.8, involves mechanical vibration of the whole specimen in the x-y plane when driven by an electric field in the z direction (poling direction). Since the diameter is the largest dimension so that the planar mode is located at the lowest frequency.
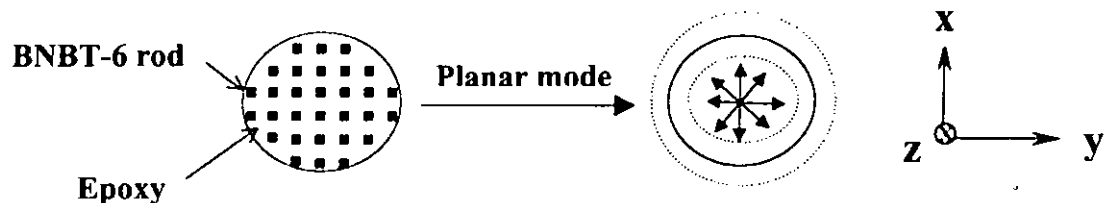
Figure 3.8 Planar mode in a BNBT-6/epoxy 1-3 composite.

3.5.1.2 Thickness Mode Resonance

The thickness mode resonance is the important mode for pulse-echo type transducer applications as it is used in transmitting and receiving the longitudinal ultrasonic waves. In the thickness mode resonance, BNBT-6 rods vibrate in the fundamental length longitudinal 33 mode along the z direction as shown in Figure 3.9. Since BNBT-6 rods embedded in the epoxy matrix are considered to be an integral part of the composite, the thickness mode resonance of the composite corresponds to the 33 mode of the BNBT-6 rods.
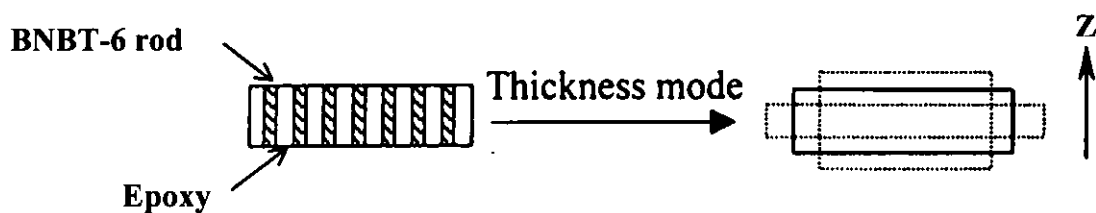
Figure 3.9 Thickness mode in a BNBT-6/epoxy 1-3 composite.

3.5.1.3 Stopband Resonances

In a 1-3 composite, when the BNBT-6 rods vibrate at their thickness mode resonance, they also generate shear wave in the polymer propagating in the x-y plane as shown in Figure 3.10. The shear wave interacts with neighboring rods to an extent depending on the wavelength across the polymer matrix and the lateral periodicity d. The existence of

stopbands is related to Bragg-scattering from the neighboring elements in the periodic

lattice. The stopband resonances occur at frequencies near where Bragg reflections occur

in the x-y plane. For a fully electroded disc, the piezoelectrically coupled stopband

resonances are the upper band edges of the second stopband for which one periodicity

d=(1 polymer width +1 ceramic width)=1 shear wavelength λ (Auld, 1986).
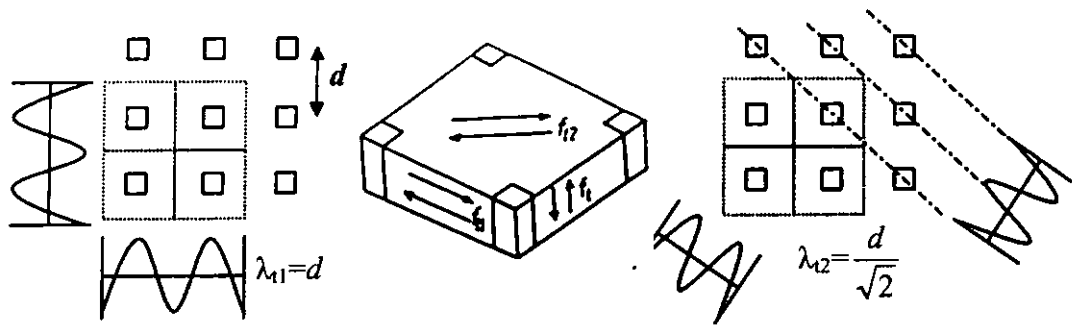
Figure 3.10 Stopband resonances due to Bragg reflection in x-y plane. (Chan, 1987)

3.5.1.4 Lateral Resonances

Lateral mode resonances are independent of thickness of the composite but are related to

the lateral dimensions of the BNBT-6 rods inside the composite. If there were no mode

coupling, the lateral modes would have the same frequency f_L because of symmetry.

However, due to the existence of mode coupling between the two lateral modes and

thickness mode, f_L split into two lateral modes f_{L1} and f_{L2}.
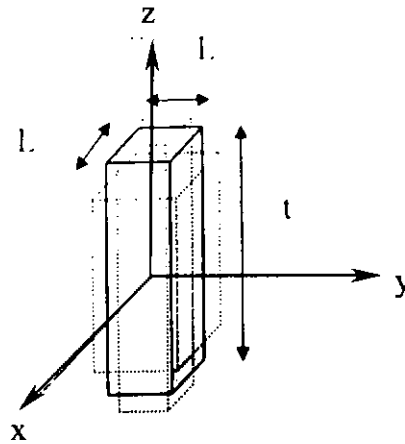
Figure 3.11 A pillar-shaped BNBT-6 element inside a BNBT-6/epoxy 1-3 composite.

3.5.2 Thinning Test Results

Thinning tests were performed on the BNBT-6/epoxy 1-3 composite (Figure 3.6) to study the mode coupling behavior. The thinning test results are shown in Figure 3.12. When thickness of the composite sample decreased, the thickness mode resonance frequency f_t increases linearly. If f_t is comparable with the stopband mode or lateral mode frequencies, it will couple with them to form some complex resonance peaks.

The stopband resonance f_{t1} and f_{t2} do not change with the thickness. However, if the thickness mode resonance f_t is closed to them, the stopband mode couples with the thickness mode and forms a wide resonance range from 1.75 MHz to 2.80 MHz as shown in Figure 3.12 (a). When f_t is situated between the stopband and the lateral mode frequency, a clear and strong thickness resonance can be observed as shown in Figure

3.12 (b). As the thickness is reduced further, the thickness mode then starts to couple

with the lateral mode and forms a wide and double-peak resonance range between 3.20

MHz and 6.80 MHz when the L/H ratio is increased to 1.45. The main properties of

these two resonances are shown in Table 3.4.

Table 3.4 Main properties of the double resonances.

	Resonance frequency (MHz)	Minimum impedance (Ω)	Electromechanical coupling coefficient k_t	Q_M
I	3.8	75.8	0.51	3.1
II	5.8	55.6	0.48	4.8

Following results from the thinning test, desirable thickness of the BNBT-6/epoxy 1-3

composite can be chosen to meet the specific device requirements. A dual frequency

ultrasonic transducer was fabricated using the ϕ=0.52 composite with a L/H ratio of

1.45, details of this transducer will be presented in Chapter VI.
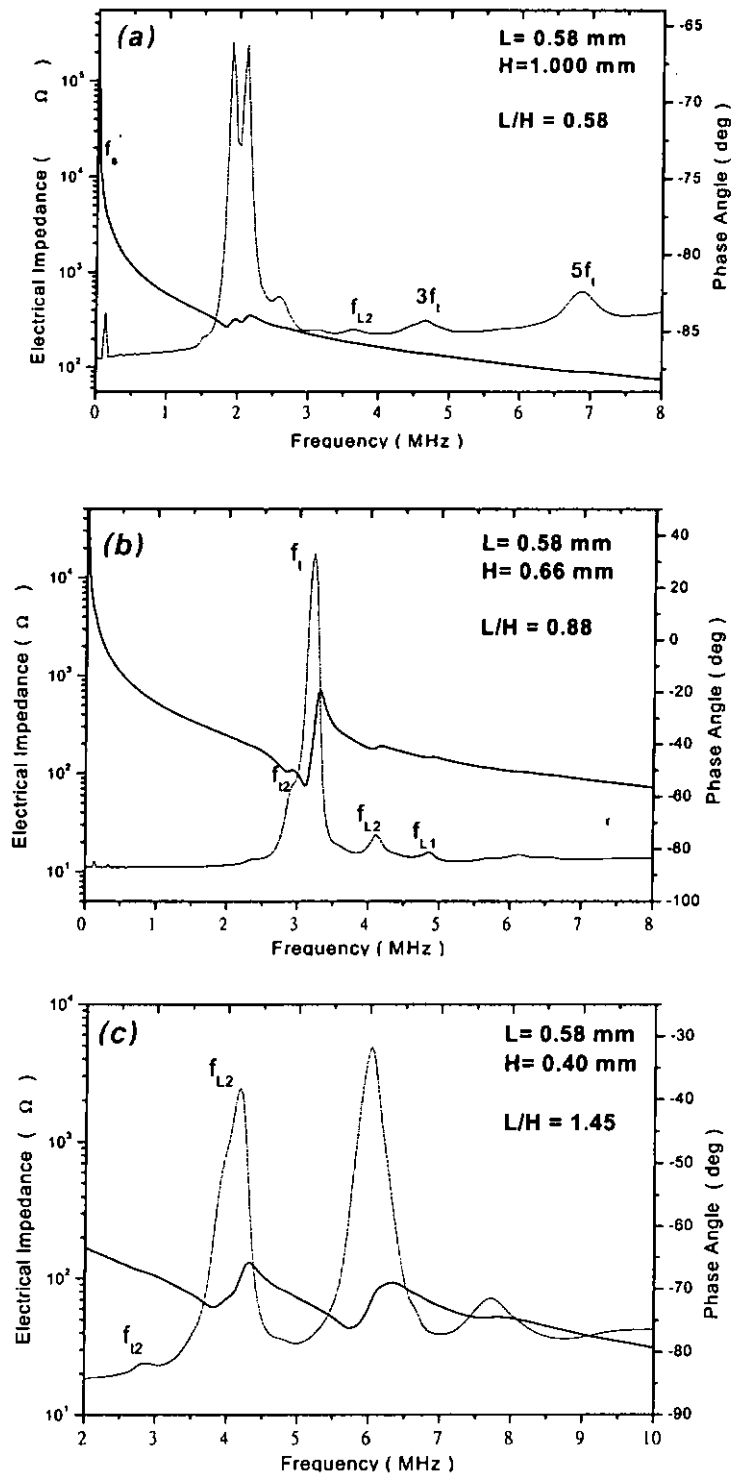
Figure 3.12 Thinning test results of the ϕ =0.52 BNBT-6/epoxy 1-3 composite.

3.5.3 Mode Coupling Theory

Thickness mode resonance is the mode of particular interest for ultrasonic imaging. If the composite sample is thick enough and the ceramic element is a tall thin rod, the thickness and lateral mode are well separated. But when the width and thickness of the ceramic element are comparable, the lateral and thickness mode will couple. This behavior can be analyzed using the mode coupling theory.

Assume the piezoelectric ceramic rod is a square pillar with width L and height H, the frequency equation is given by (Bui, 1988):

$$\{f^2 - f_a^2(1-\gamma)\}\{f^4 - [f_a^2(1+\gamma)+f_b^2)]f^2 + f_a^2 f_b^2(1+\gamma-2\alpha^2)\} = 0 \qquad (3.42)$$

where f_a is the uncoupled lateral resonance frequency and f_b is the uncoupled thickness resonance frequency. α And γ are the coupling constants,

$$f_a = \frac{1}{2L}\sqrt{\frac{c_{11}}{\rho}} \qquad (3.43)$$

$$f_b = \frac{1}{2H}\sqrt{\frac{c_{33}}{\rho}} \qquad (3.44)$$

$$\alpha = \frac{c_{13}}{\sqrt{c_{11}c_{33}}} \qquad (3.45)$$

$$\gamma = \frac{c_{12}}{c_{11}} \qquad (3.46)$$

c_{11}, c_{12}, c_{13} and c_{33} are the elastic stiffness constants of the ceramic material and ρ is the density. Equation (3.42) can be factorized into

$$f^2 - f_a^2(1 - \gamma) = 0 \qquad\qquad (3.47)$$

$$f^4 - [f_a^2(1+\gamma) + f_b^2]f^2 + f_a^2 f_b^2(1+\gamma - 2\alpha^2) = 0 \qquad (3.48)$$

The lateral resonance frequencies can be calculated from the above equations. f_{L1} is a solution of Equation (3.48) and $f_{L2} = f_a(1-\gamma)^{1/2}$.

The required ceramic constants for solving Equations (3.47) and (3.48) can be found in Table 2.3, and then the theoretical data can be calculated from these two equations. Under an open circuit condition, constants with superscript D are used to solve the frequency equations and the corresponding experimental data are the anti-resonance frequencies. Constants with superscript E and the resonance frequencies are used in the calculation for the short-circuit case. The theoretical values derived from Equations (3.47) and (3.48) for both the open-circuit and short-circuit cases are plotted in Figure 3.13 together with the experimental data for comparison. It is found that the experimental values have good agreement with the theoretical curves. The coupling constants α and γ of BNBT-6/epoxy 1-3 composites are small because of the ceramic anisotropy (Chan, 1987).
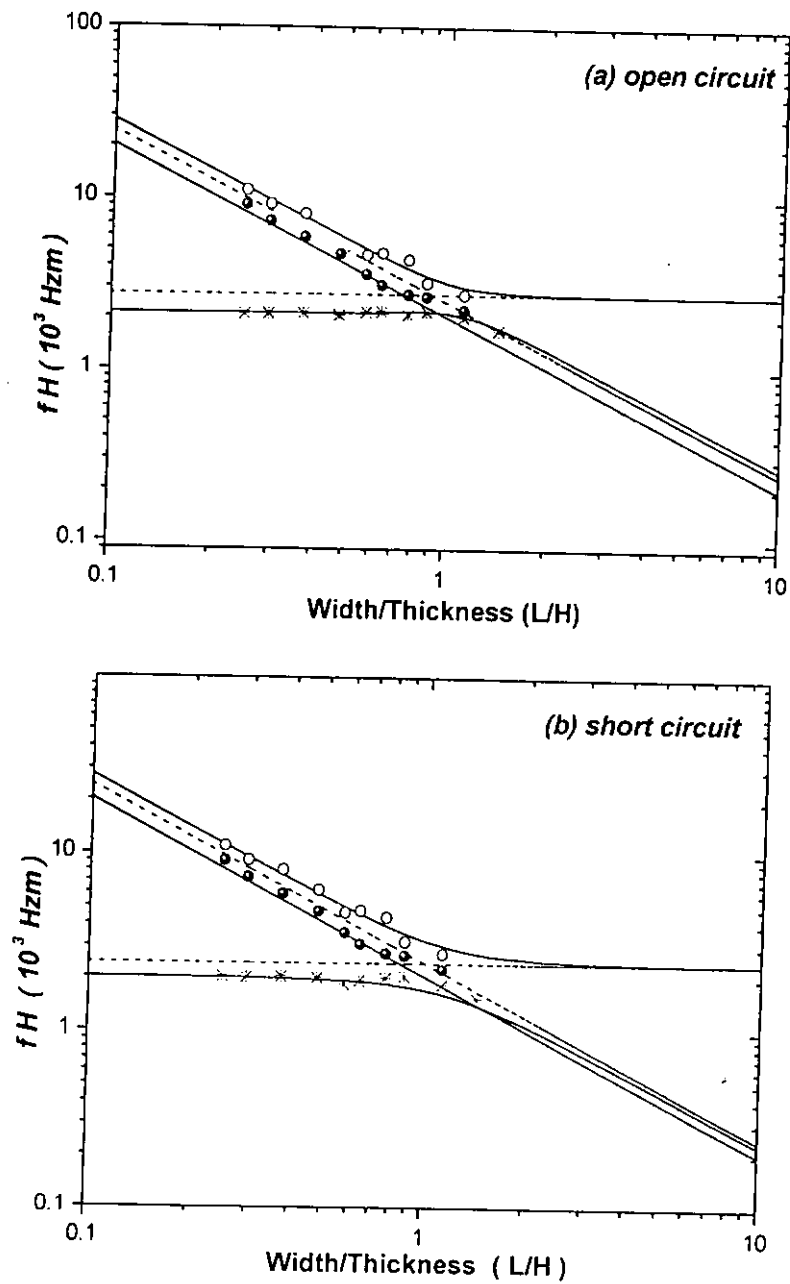
Figure 3.13 Frequency constant (f·H) of BNBT-6/epoxy 1-3 composite as a function of the width to thickness ratio of the ceramic rod. (log-log plot), - - -: uncoupled resonance, ——: theoretical calculations, o,* ,•: experimental results.

3.6 Summary

BNBT-6/epoxy 1-3 composites with various ceramic volume fractions were fabricated using the dice-and-fill technique. Araldite epoxy LY5138-2/HY5138 was used as the matrix material in this study and the epoxy was characterized using the immersion method. Characterization of the BNBT-6/epoxy 1-3 composites were based on the resonance technique and IEEE standards. The ceramic volume fraction ϕ affects most of the composite properties. The electromechnical coupling coefficients k_t of the composites improved by about 9~20% compared with the constituent ceramics, which is beneficial to ultrasonic transducer applications. A physical model was employed to simulate the composite parameters. It was found that most of the experimental data agreed well with the theoretical calculations.

Thinning tests were performed to observe the mode coupling behavior of BNBT-6/epoxy 1-3 composites. This behavior can be analyzed using the mode-coupling theory. The experimental results showed good agreement with the theoretical prediction. Aspect ratio (L/H) is a key factor which affects the mode coupling behaviour of the composite. Therefore, it is important to adjust the L/H ratio to meet the specific requirements for certain devices.

CHAPTER IV

FABRICATION AND CHARACTERIZATION
OF BNBT-6 FIBRES

4.1 Introduction

Advances in 1-3 composite ultrasonic transducer technology have led to the development of finer scale and piezoelectric materials with special geometries as the active elements because the thinner the element the higher the resonance frequency (Meyer, 1998). For high frequency 1-3 composite applications, conventional methods for fabricating pillars, such as the dice-and-fill and injection molding etc. are limited typically >70 μm in diameter. Therefore, Many researchers have focussed their attention on the processing of fine scale piezoelectric fibres. Several methods have been developed to prepare ceramic fibres. Fabrication of BNBT-6 ceramic fibres has been achieved in two different routes in this work. Both the viscous suspension spinning process (VSSP) and sol-gel (Meyer, 1996) process offer the ability to produce continuous green or gel fibres. The objective of this work is to produce fine scale BNBT-6 fibre and develop 1-3 fibre composites and ultrasonic transducers.

Fine scale BNBT-6 ceramic fibres between 60 and 100 μm were prepared using a sol-gel process. This method offers the advantage of chemical homogeneity in multi-component systems and ease of compositional adjustments (Yoshikawa, 1992). One disadvantage to

this type of processing is the large organic content (~60 wt%) in the gel fibres. Removal

of the organics during the gel to ceramic conversion results in large shrinkage and

cracking of the fibres. Therefore, in order to produce dense and crack-free fibres, it is

necessary to adjust the heating rates and control the atmosphere during binder burnout.

The other route for BNBT-6 preparation (VSSP) in this study is a powder-based

extrusion technique. The VSSP fibres have thicker diameters around 300 μm and much

more easier to handle. Moreover, the properties of single VSSP BNBT-6 ceramic fibre

can be measured.

4.2 Fibre Processing Review

For high frequency 1-3 composite ultrasonic transducers, recent interest in passive

vibration damping has prompted the investigation into the processing of fine scale

fibrous shaped piezoelectric elements. Some fibre processing techniques have been well

developed in recent years.

4.2.1   Sol-Gel Fibres Based on Carboxylates

A typical application of this method is the production of PZT fibres using alcoholates

sol-gel precursors and propionic acid (Glaubitt, 1997). This chemistry provided a stable

sol both for storage and during spinning. The viscosity of the sol can be controlled

through adjusting the temperature for fibre drawing. One disadvantage of this precursor

route was the extraordinarily high volume fraction of organics (>60%) in the gel fibre. Shrinkage during pyrolysis was reported to be as high as 85 vol% (Meyer, 1998). So the gel to ceramic conversion has to be performed using low heating rates and aided with the use of inert or reducing atmosphere at low temperature.

4.2.2   Sol-Gel Fibres Based on Alkoxides

Due to the rapid change in viscosity near the gel point, this method can be utilized to develop fibres. But some chemical additives and the solution curing temperature should be investigated to improve the workability or fibre drawing time of the sol for reproducibility. This method shows that variations in the processing conditions of the precursor solution and thus optimum conditions should be chosen to give improvements in the spinnability of the sol.

Increase in temperature were found to significantly reduce the time to gelation and the contents of acids could improve the gel structure, allowing for longer fibre drawing time (Meyer, 1998). However, the acid concentration of the must be controlled to avoid the precipitation of the precursors and dilution of the solid content of the gels. Pyrolysis of the gel fibres in this method needs to be performed under the guidance of thermogravimetric analysis (TGA) results.

4.2.3   Viscous Suspension Spinning Process (VSSP)

In the viscous suspension spinning process (VSSP), slurry of ceramic powder is mixed with a rayon precursor (regenerated cellulose-viscose) and extruded through a spinnerette into an aqueous acid/acid solution. After a number of additional chemical treatments, the end product is a continuous green fibre that can be produced at a rate of approximately 20 m/min. The green fibres have a solid loading between 50 and 90 wt%. The diameter of the fibre depends on the size of pinhole on the spinnerette.

4.3   Fabrication of BNBT-6 Fibres Through the Sol-Gel Route

The sol-gel technique offers a unique approach to the creation of ceramic powders, films and fibres. This technology is based on the chemistry of metal ions in the solution in which networks of metal-oxygen-metal bonds are produced. The process by which the solution converts to gel can be utilized to form ceramics and ceramic composites by dip-coating, impregnation, spinning and fibre drawing. For this reason, the sol-gel technology has received enormous attention in the last decade. The sol-gel route to ceramics offers excellent control of homogeneity in multi-components systems by the mixing of metal cations at a molecular level. Therefore, the sol-gel technique was employed in this study to prepare BNBT-6 fibres.

4.3.1   Gel Fibre Preparation

Gel fibres of BNBT-6 were fabricated using sol-gel technique. The detail procedure was shown in the flow diagram in Figure 4.1. Solutions were produced using bismuth 2-ethylhexanoate (Strem, 72% in mineral spitrits), titanium n-butoxide (Acros, 99% pure), sodium methoxide (Acros, 30% in methanol) and barium acetate (Acros, 99% pure) as starting precursors with 2-ethylhexanoic acid and acetic acid as solvents. The stoichiometric raw materials were used except that bismuth was excessive by 2% to compensate the bismuth loss during the subsequent sintering process.
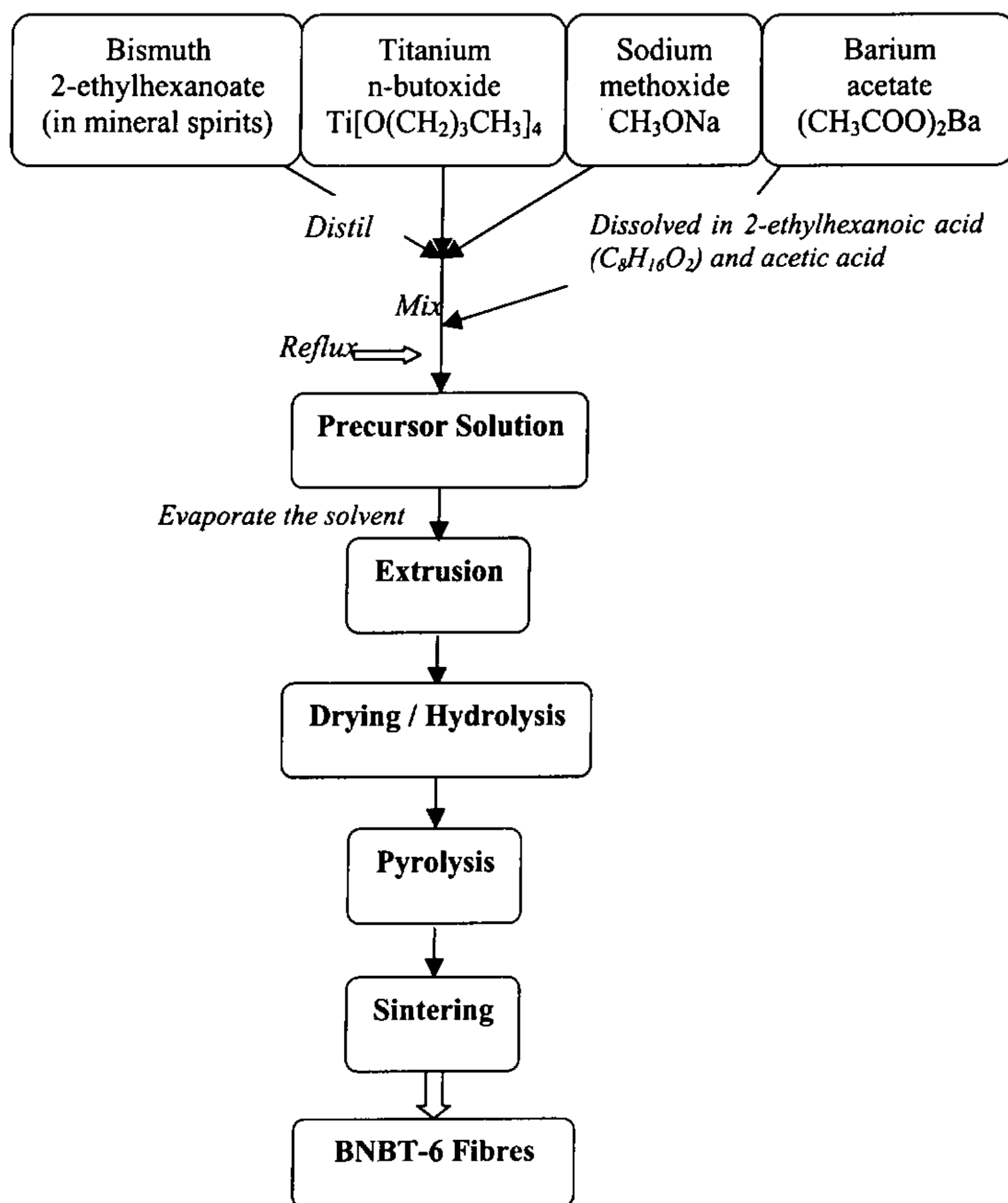
Figure 4.1 Flow diagram for the production of BNBT-6 fibres through a sol-gel route.

Initially, barium acetate was dissolved in a mixture of 2-ethylhexanoic acid and acetic acid, and then bismuth 2-ethylhexanoate was added into this solution. Since the bismuth 2-ethylhexanoate contains mineral spirits, the mixture was distilled for about 1 h to eliminate the mineral spirits and the acetic acid which might cause the titanium n-butoxide to hydrolyze in subsequent procedures. The other two chemicals were mixed into the solution and after refluxing at 125 °C for ~1 h, a uniform and transparent precursor solution was prepared. Then the solution was filtered and concentrated by heating in a rotatable evaporator. When most of the solvent was removed, suitable amount of water/propionic acid mixture was added to adjust the viscosity. The solution was refluxed for 30 min more at about 140°C and then evaporated until it became honey-like.
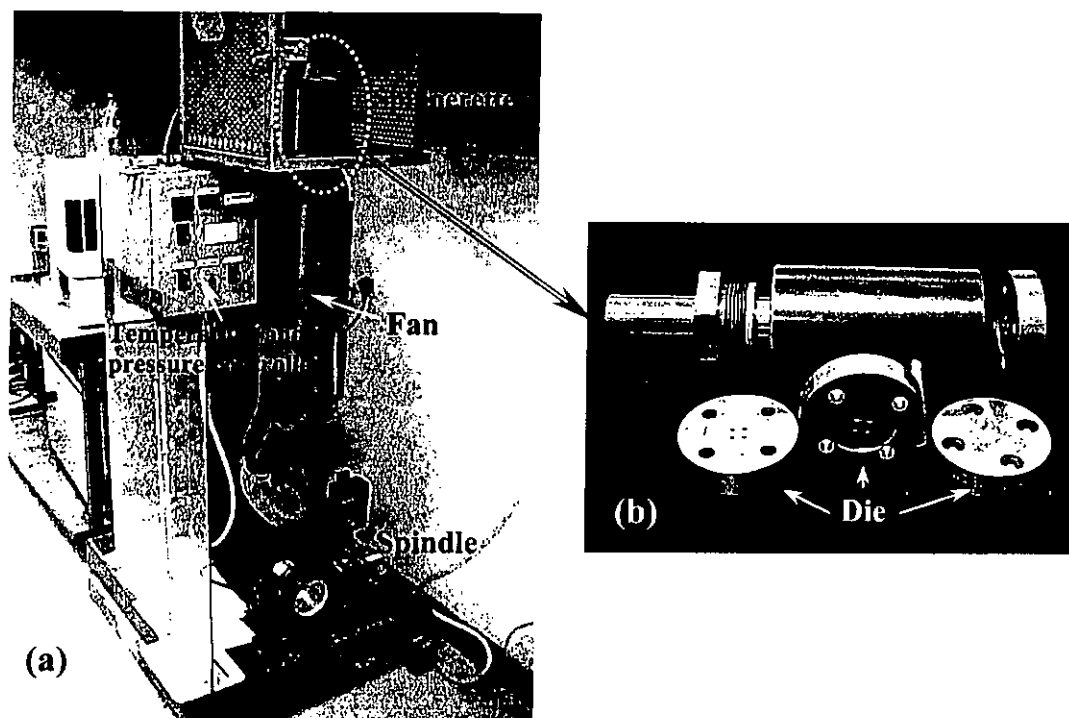
Figure 4.2 Photograph of the fibre extrusion machine and the spinnerette with different dies.

Fibre extrusion was performed near the gel point of the solution. The solution was poured into a metal spinnerette and extruded into fibres using a gel-spun fibre machine (OneShot III from Alex James & Assoc., Inc.) at 40°C as soon as possible. The spinnerette was equipped with a die of 150 μ m pinholes. The fibres were collected on a spindle. After drying and hydrolysis, pyrolysis of the gel fibres were carried out using a very low heating rate and reducing (CO) atmosphere control to prevent fibre cracking.

4.3.2 X-ray Diffraction Analysis of BNBT-6 Sol-gel Powder
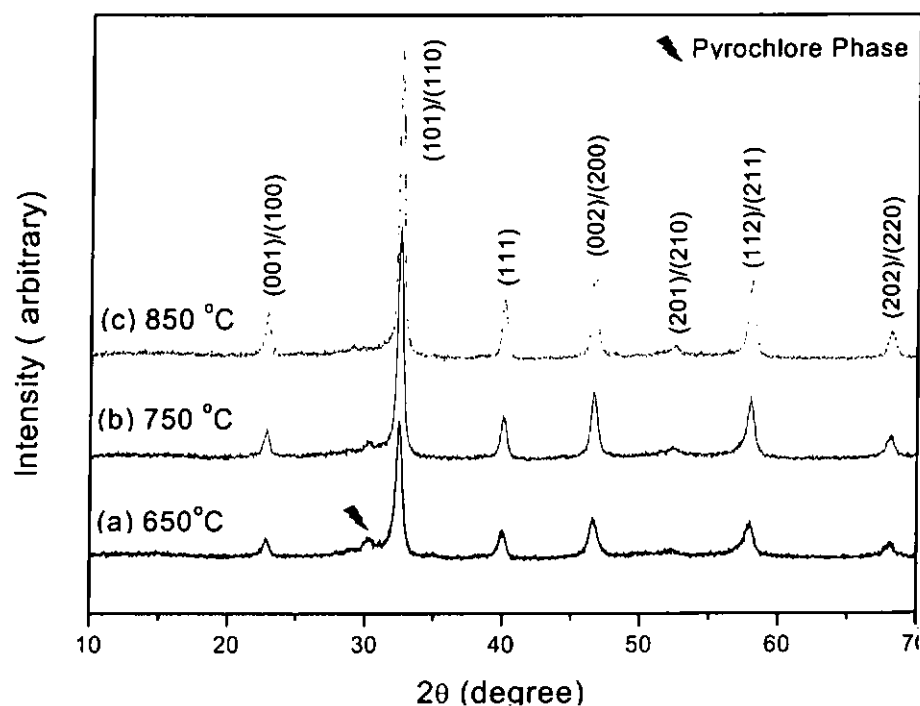
Figure 4.3 X-ray diffraction analysis of BNBT-6 calcined powder obtained after the fibre extrusion process (sol-gel).

To evaluate whether the fibres fabricated by this sol-gel method have the same phase structure as the bulk ceramics derived from mixed-oxide method, X-ray diffractometry was used to check the crystal phase of the gel fibre. Figure 4.3 shows the XRD patterns of sol-gel powder sintered at different temperatures. When the powder was sintered at a lower temperature of 650°C, the pattern shows some pyrochlore phase. With the increase in sintering temperature, the patterns become a pure perovskite phase as shown in the pattern of (c). So it is proved that the BNBT-6 fibres produced by the sol-gel method can have the same phase structure and composition as those of bulk ceramics fabricated by the mixed-oxide technique.

4.3.3   Pyrolysis

Since the gel fibres contained high organic contents, a pyrolysis process was required to remove the organics. In the previous work on PZT fibres, pyrolysis consisted of a 2°C/min heating rate to 600°C in air with a 10 min dwell time (Meyer, 1995). But it was found that if BNBT-6 fibres were produced by the above-described method, pyrolysis in air at heating rates even as low as 0.5°C/min resulted in fibre cracking. This cracking, as shown in Figure 4.4, stems from the large shrinkage associated with the organic removal and was described as "onion skin" cracking (Meyer, 1998).

In order to prevent fibre cracking, the heating procedure should be adjusted. From the thermogravimetric analysis (TGA) profile shown in Figure 4.5, the thermal events that occur during calcination of the BNBT-6 fibres were found to include solvent

evaporation at 250°C, decomposition of some acetate groups between 200-375°C (Meyer,

1998) and carbon removal up to 450-550°C.
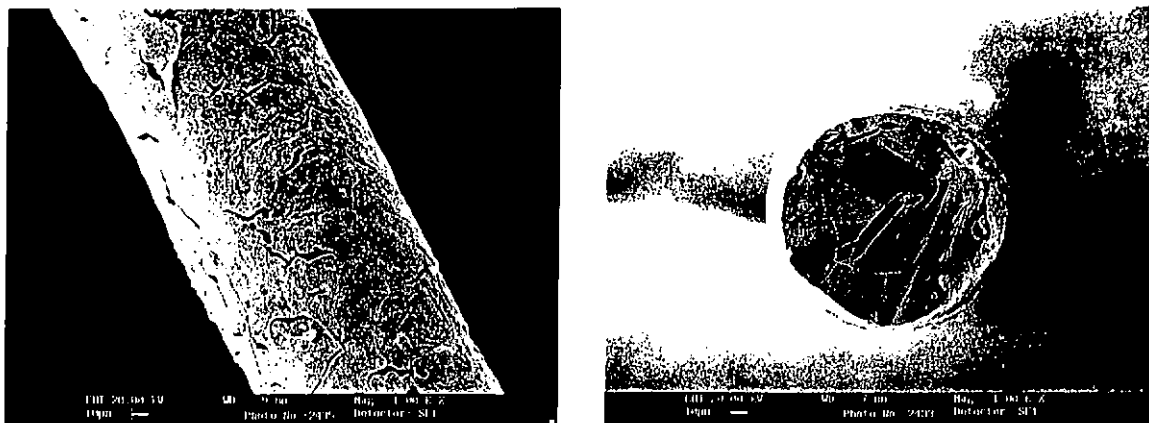
Figure 4.4 SEM micrograph of a cracked fibre obtained using an air atmosphere during

pyrolysis at 550°C at a heating rate of 0.5 °C/min.
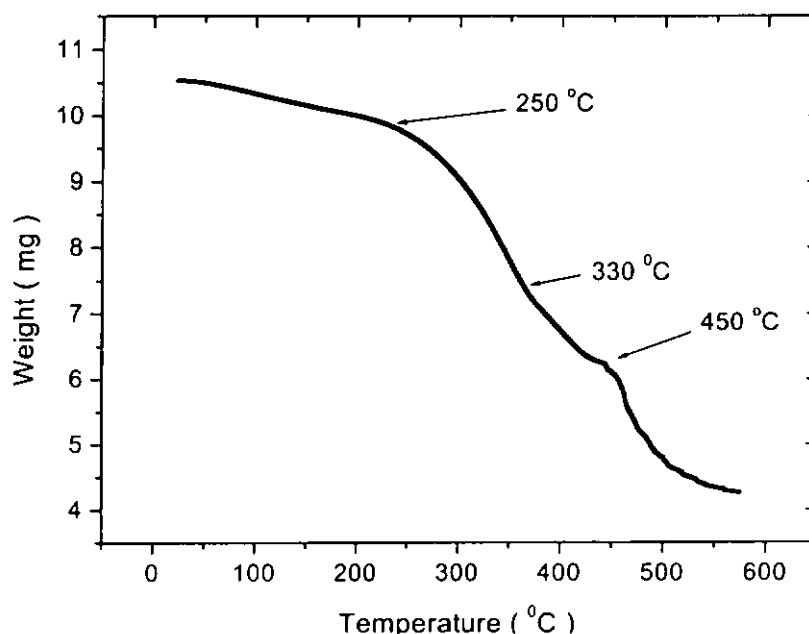
Figure 4.5 TGA curve of gel BNBT-6 fibre generated using a heating rate of 20°C/min

in air.

According to the TGA results, a heating procedure was worked out as shown in Figure

4.6. Steps to avoid cracking involved slower heating rates as 0.5 °C/min and using

reducing atmosphere (CO) at later stages of the pyrolysis. The use of atmosphere control

has been utilized in this work and is commonly used in the processing of materials

containing high organic contents such as in injection molding and extrusion (Meyer,

1998). By using a CO atmosphere as shown in Figure 4.7, the carbon burnout rate can be

decreased so that the cracks were reduced.
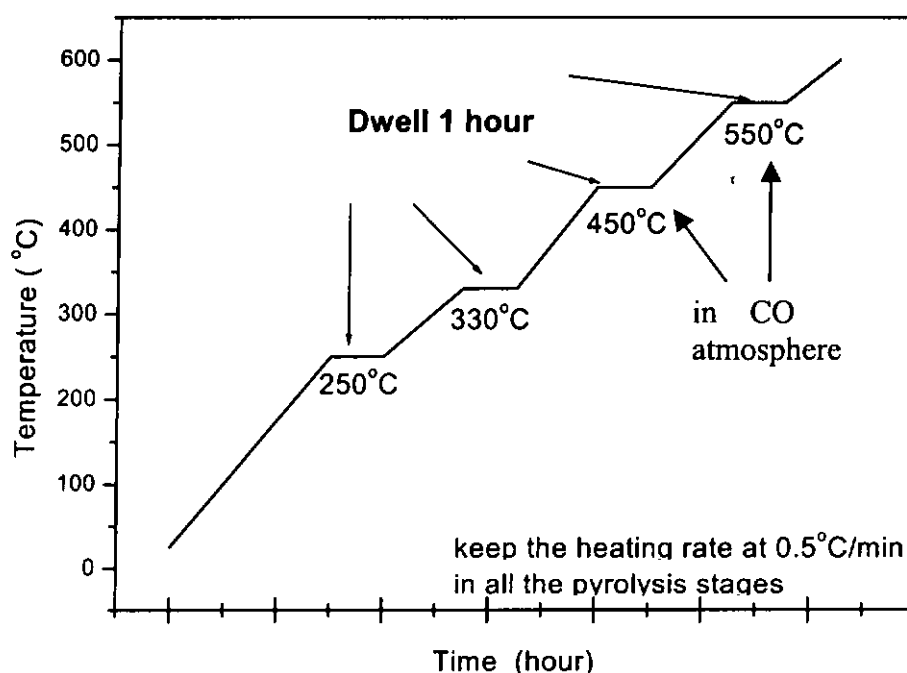
Figure 4.6 Pyrolysis profile of BNBT-6 gel fibres.
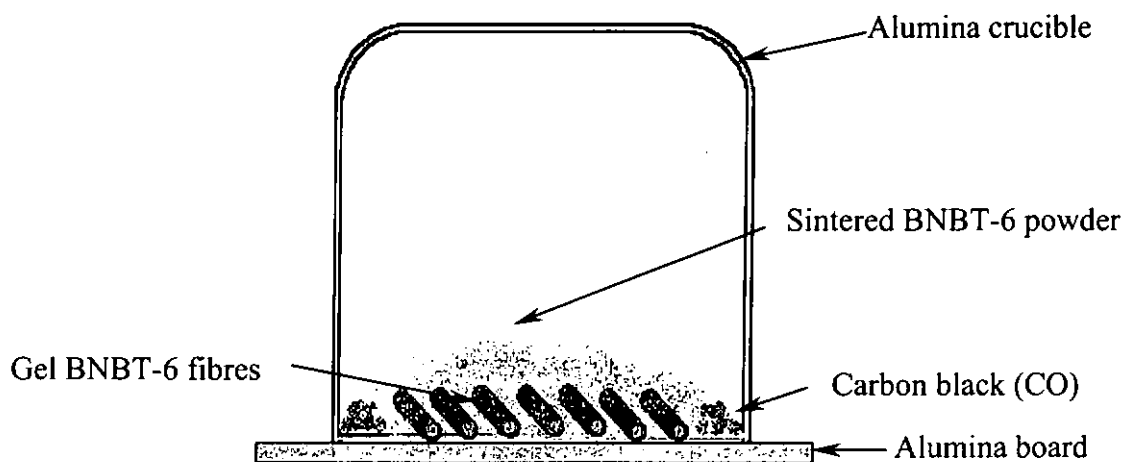
Figure 4.7 Setup for pyrolysis of BNBT-6 gel fibres.
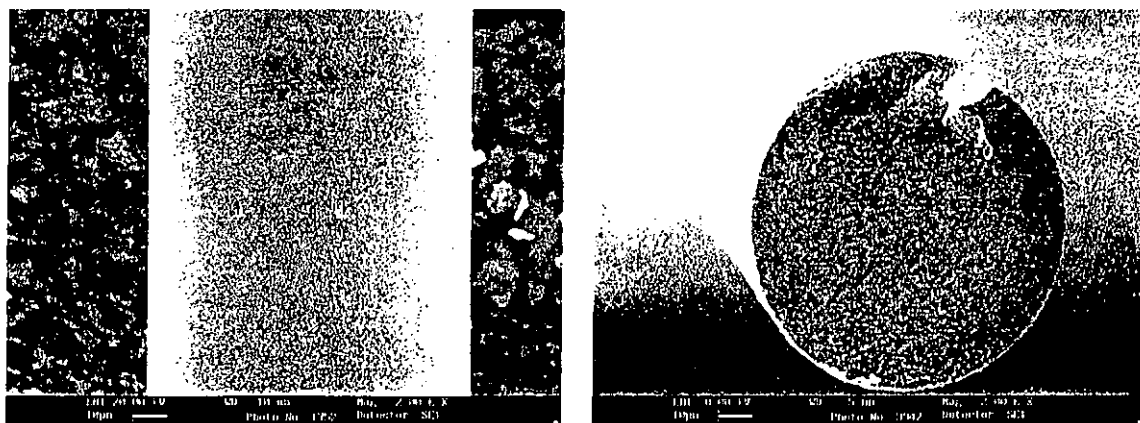
Figure 4.8 SEM image of a BNBT-6 fibre pyrolyzed in a CO atmosphere at 550°C with a heating rate of 0.5 °C/min.

Figure 4.8 shows the SEM micrographs of a pyrolyzed fibre using the above (Figure 4.6)

burnout profile. The fibre was crack-free with a diameter of approximately 100 μm.

4.3.4   Sintering

The pyrolyzed fibres were cooled to room temperature and then transferred to a sealed crucible where they were sintered under a bismuth atmosphere (covered with sintered BNBT-6 powder). A sintering temperature of 1150°C was used with 90 min dwell time at a heating rate of 2-3°C/min. The length of the fibre produced were between several millimeters and a few centimeters. SEM images of the fibre surface and cross-section are depicted in Figures 4.9 and 4.10, respectively.
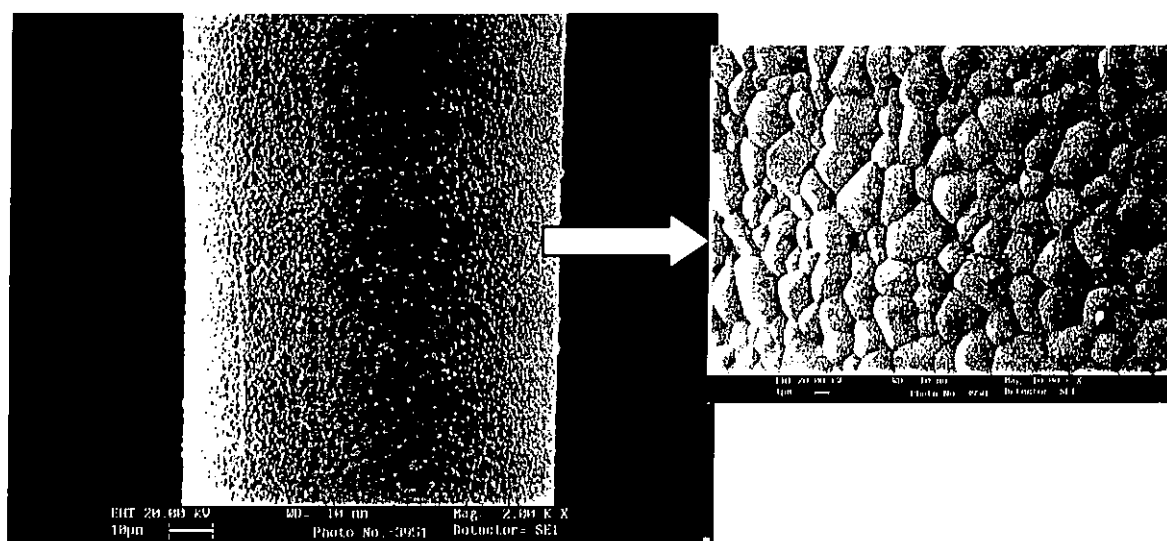
Figure 4.9 SEM micrographs of BNBT-6 sol-gel fibres (surface) sintered at 1150 °C for 90 min.
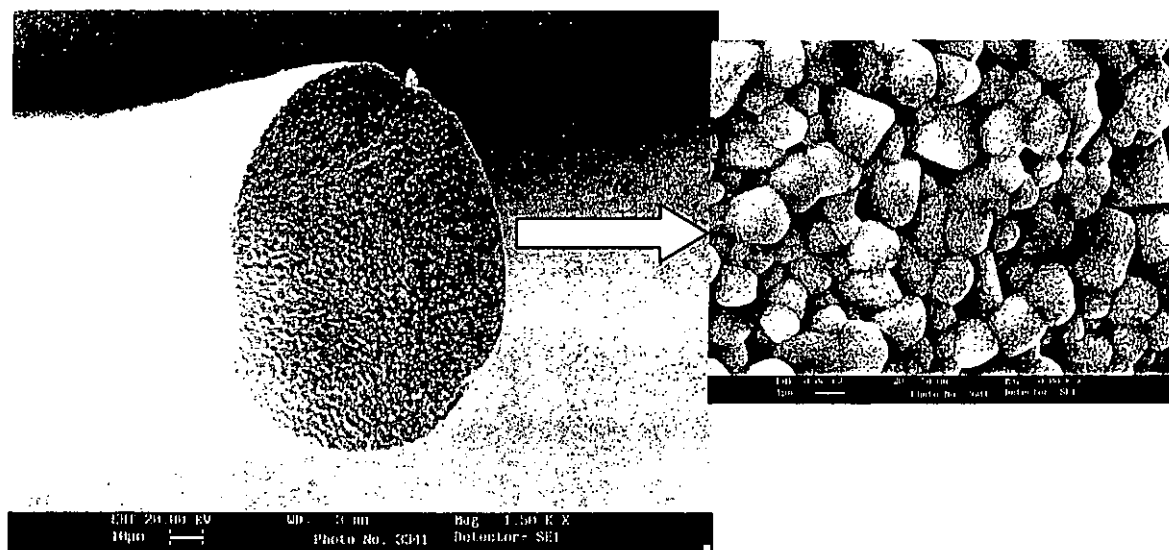
Figure 4.10 SEM micrographs of BNBT-6 sol-gel fibres (cross-section) sintered at 1150°C for 90 min.

It was observed from Figures 4.9 and 4.10 that the sintered fibre was dense and crack-free with a diameter of 90 μm. An average grain size of 2-3 μm can be seen clearly in the magnification in the SEM micrographs of both the fibre surface and cross-section. For structural stability, there should be at least ten grains across the diameter (Meyer, 1998). The fibre can meet the requirement and have a stable performance. The close examination of the sintered fibres in Figures 4.9 and 4.10 also revealed the differences in the grain structure from the surface to the interior. The surface of the fibre was much denser than the interior. It is probably due to the difference in organic burnout rate of the fibre surface and the interior. During the later stages of the pyrolysis, CO gas was employed to lower the carbon burnout rate. But this might cause some residual carbon inside the fibre when the CO or CO_2 vapor pressure saturated in the crucible. Thus,

when the temperature continued to increase in the sintering process, the removal of these residual carbon will leave some holes or even some slight cracks inside the fibre.

4.4 Fabrication of BNBT-6 Fibres Through a Powder-based Extrusion Technique

4.4.1 Green Fibres Preparation

Fibre preparation in this route was based on the viscous solution-mixed presintered BNBT-6 powder suspensions. The presintered BNBT-6 powder mixed with proper binder was used as the precursor for fibre extrusion. The procedure is shown in the flow diagram in Figure 4.11. The BNBT-6 powder is prepared by a solid-state reaction as described in Chapter II. Then the BNBT-6 powder was calcined at 850°C for 1 h to form a crystalline phase. The calcinated BNBT-6 powder was ball-milled using ethanol as the medium for 10 h. Zirconium oxide balls with a diameter of 1 mm were used as the milling medium to obtain a powder with fine scale particle size. After ball milling, the average particle size of the presintered BNBT-6 powder can be reduced to several hundred nanometers as measured by a particle size analyzer (Horiba CAPA-700). Poly (acrylic acid) (PAA, 25% aqueous solution) was used as the viscous solution (binder) in this work and the powder to binder weight ratio is 1: 0.25. Then the mixture was stirred using a magnetic stirrer until it became a uniform slurry. After curing at 50°C for 30 min, the slurry was poured into a metal spinnerette and extruded into fibres at room temperature using a gel-spun fibre machine (OneShot III from Alex James & Assoc., Inc.), which is the same as the sol-gel fibre extrusion (Figure 4.2). The spinnerette was

equipped with a die of 500 μm pinholes. The subsequent fibre drawing procedures are similar to the sol-gel fibre preparation.
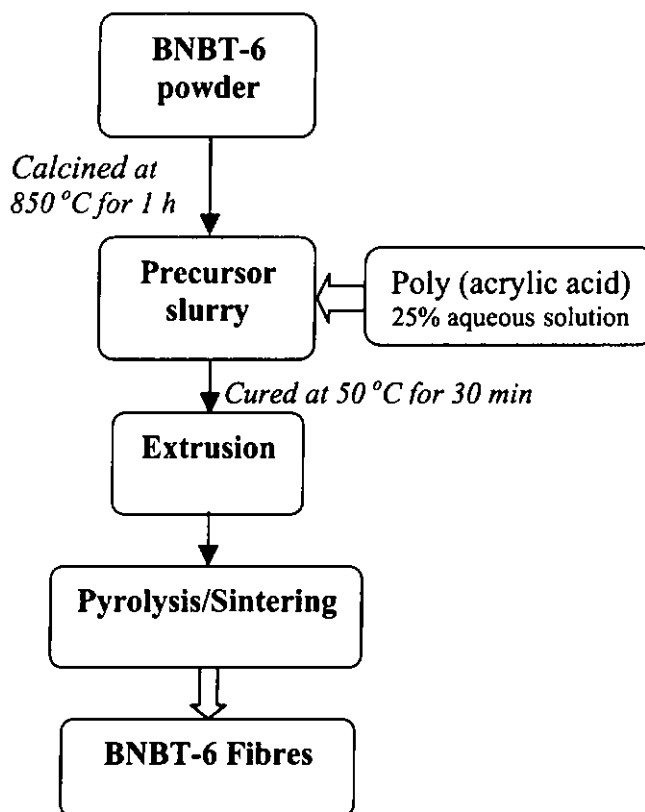
Figure 4.11 Flow diagram for the production of BNBT-6 fibres through the VSSP route.

4.4.2 Pyrolysis and Sintering

In order to prevent fibre cracking during the pyrolysis process, TGA was also employed to monitor the weight loss during pyrolysis up to 600°C. Thermal events that occur during pyrolysis were quite similar to that of the gel fibres and the TGA result is shown in Figure 4.12. Since less solvent was used, unlike the gel fibres there was no sudden drop at around 200°C in the TGA curve. Decomposition of the PAA binder occurred

between 200-400°C and carbon removal took place at 450-550°C.
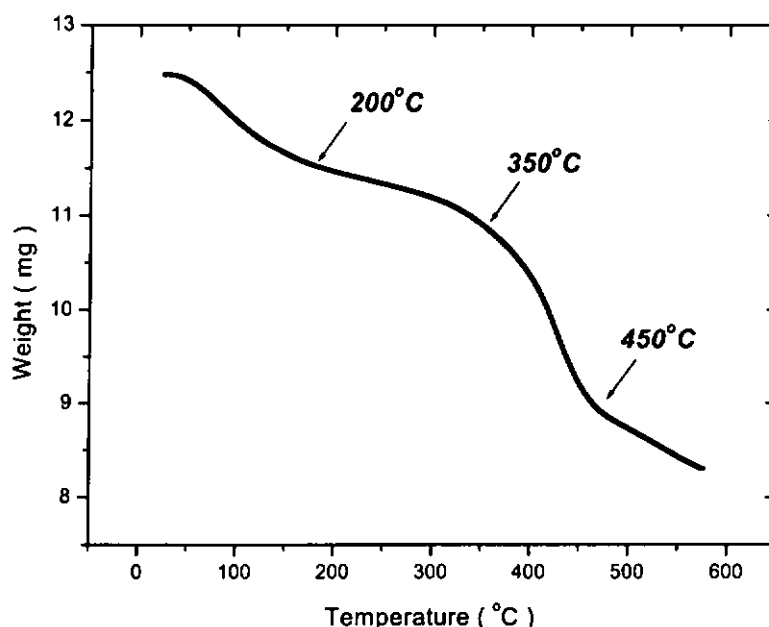
Figure 4.12 TGA profile of VSSP BNBT-6 fibre generated using a heating rate of 20 °C/min in air.

According to the TGA results, a heating profile was worked out as shown in Figure 4.13 under the guidance of the pyrolysis process. Since there was only about 30% of organic contents in the VSSP green fibre, the heating rate can be slightly faster than that of the gel fibre. Reducing atmosphere (CO) was still needed at later stages of the pyrolysis to control the carbon burnout rate.
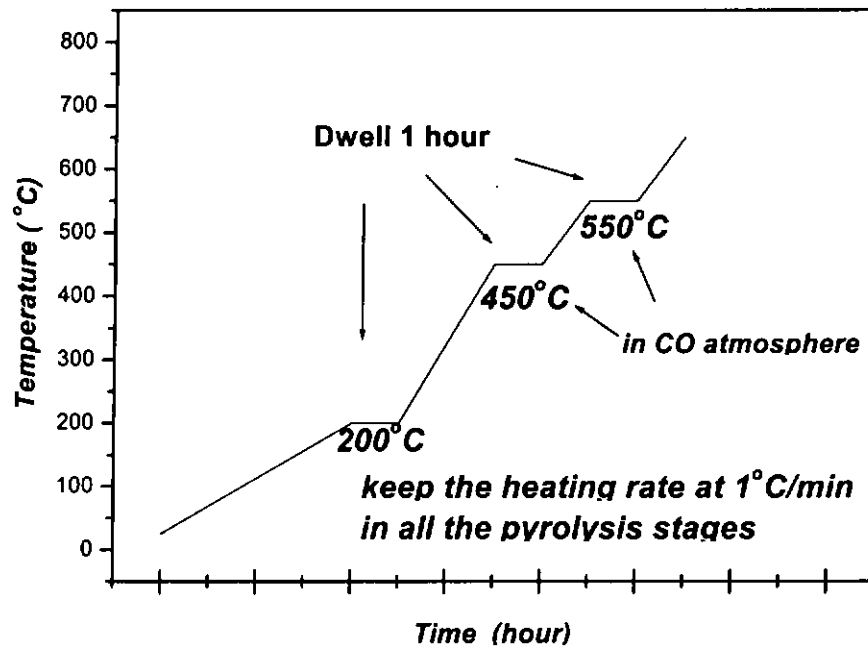
Figure 4.13 Pyrolysis profile of BNBT-6 VSSP green fibres.

After pyrolysis, sintering of the VSSP green fibres was performed using the same setup as that of gel fibres. The fibres were sintered at 1150°C for 120 min with a heating rate of 5°C/min. The sintered fibre exhibits crack-free and dense structure with diameter of around 300 μm as shown in Figures 4.14 and 4.15.
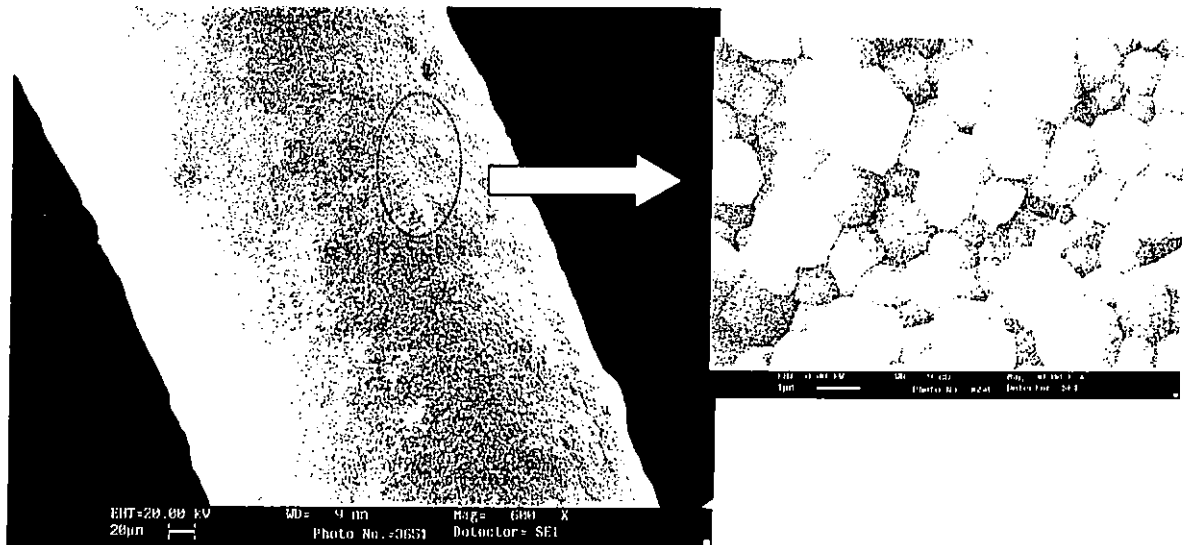
Figure 4.14 SEM micrographs of BNBT-6 VSSP fibres (surface) sintered at 1150°C for 120 min.
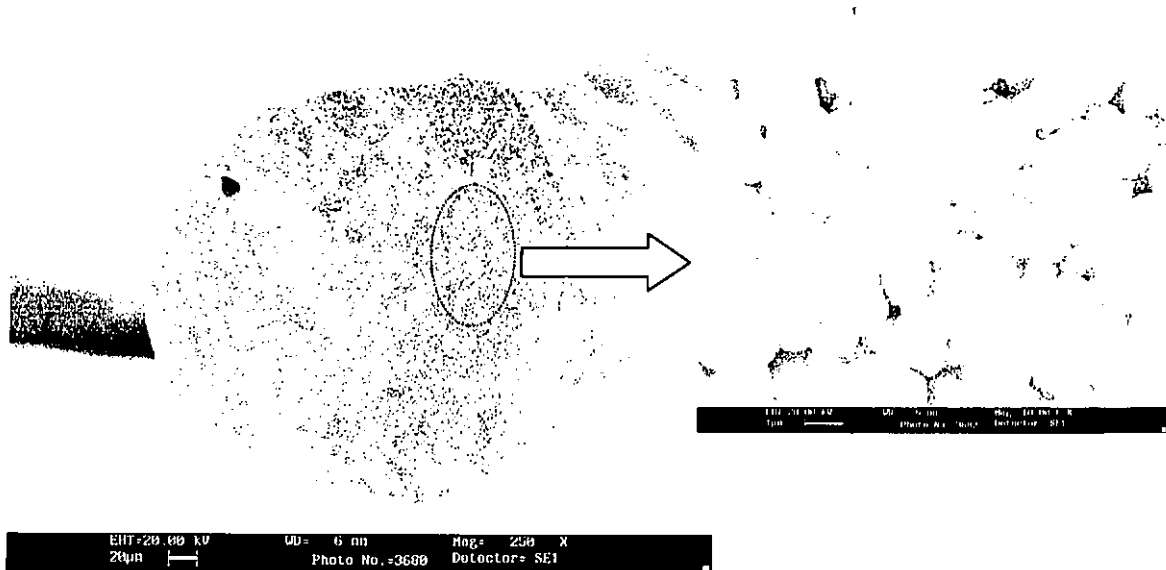
Figure 4.15 SEM micrographs of BNBT-6 VSSP fibres (cross-section) sintered at 1150°C for 120 min.

From the SEM photos, grain size of about 1-2 μm can be observed clearly in both the fibre surface and cross-sectional views. However, some large holes with diameter around several microns were found inside some fibre. The holes were probably induced by the trapped air in the precursor slurry. After fibre extrusion, the trapped air inside the fibre cannot escape during the pyrolysis and sintering processes, which gives rise to some holes inside the fibre. These large holes will adversely affect the fibre properties.

4.4.3 Characterization of A Single BNBT-6 VSSP Fibre

Since the VSSP fibre has a large diameter, it is much easier to handle than the sol-gel fibres and characterization of a single fibre becomes possible. We immersed the single fibre into an epoxy matrix and sliced this composite into thin discs. Gold electrodes were only coated on the fibre area with the help of a shadow mask. Then a series of measurements, including P-E hysteresis measurement and piezoelectric measurement, can be performed using such a "single fibre sample". The schematic graph of the sample is shown in Figure 4.16.
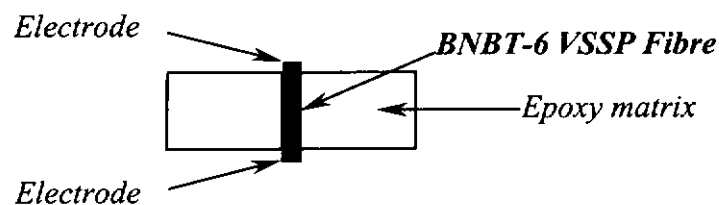
Figure 4.16 Schematic diagram of a VSSP BNBT-6 "single fibre" sample.

4.4.3.1 P-E Hysteresis Loop Measurement

The P-E hysteresis loop of the VSSP BNBT-6 single fibre was measured at room temperature using a Sawyer-Tower circuit with a maximum a.c. electric field of 6.0 kV/mm. Hysteresis loop of VSSP BNBT-6 single fibre is shown in Figure 4.17. P-E loop of bulk BNBT-6 ceramics was also plotted in this graph for comparison. Both the P_r and coercive field E_c of the single fibre are almost the same as those of the bulk sample but the shape of the fibre P-E loop of the fibre became slightly slanted. This may be due to the clamping effect of the epoxy.
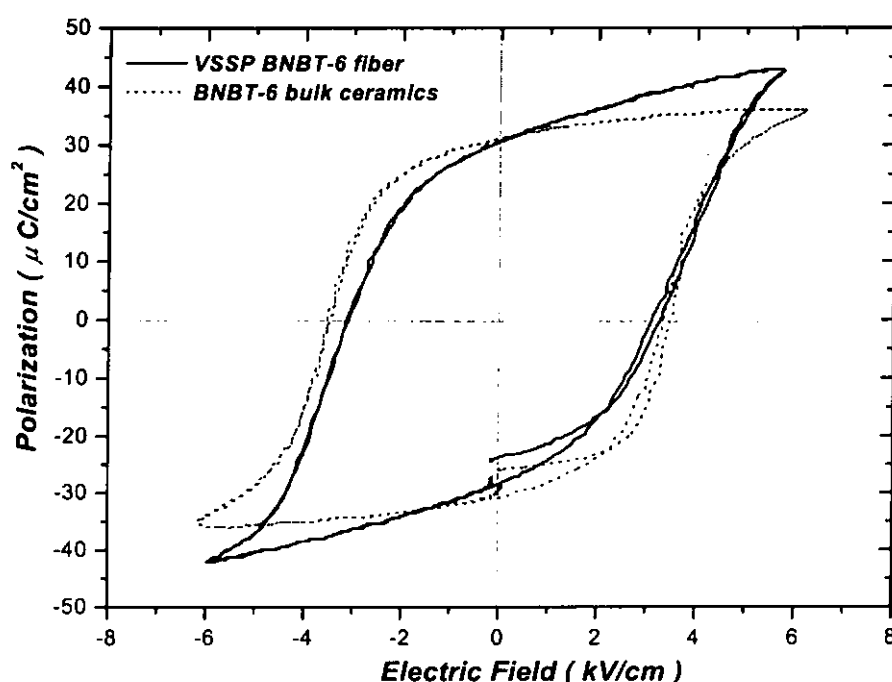
Figure 4.17 P-E hysteresis loop of the VSSP BNBT-6 single fibre sample.

4.4.3.2 Piezoelectric Properties Measurement

The fibre for piezoelectric measurement was poled under the same condition as the bulk ceramics. The characterization method is also based on the IEEE standards on Piezoelectricity, which has been described in Chapter II. The impedance characteristics were observed using an HP4294 impedance analyzer as shown in Figure 4.18 and d_{33} was directly measured using a d_{33} meter. Table 4.1 summarized the main piezoelectric properties of the VSSP BNBT-6 fibre. The piezoelectric properties are lower than the bulk ceramics especially for the relative permittivity $\varepsilon_{33}^T / \varepsilon_0$ and mechanical quality factor Q_M presumably due to the existence of holes inside the fibre.
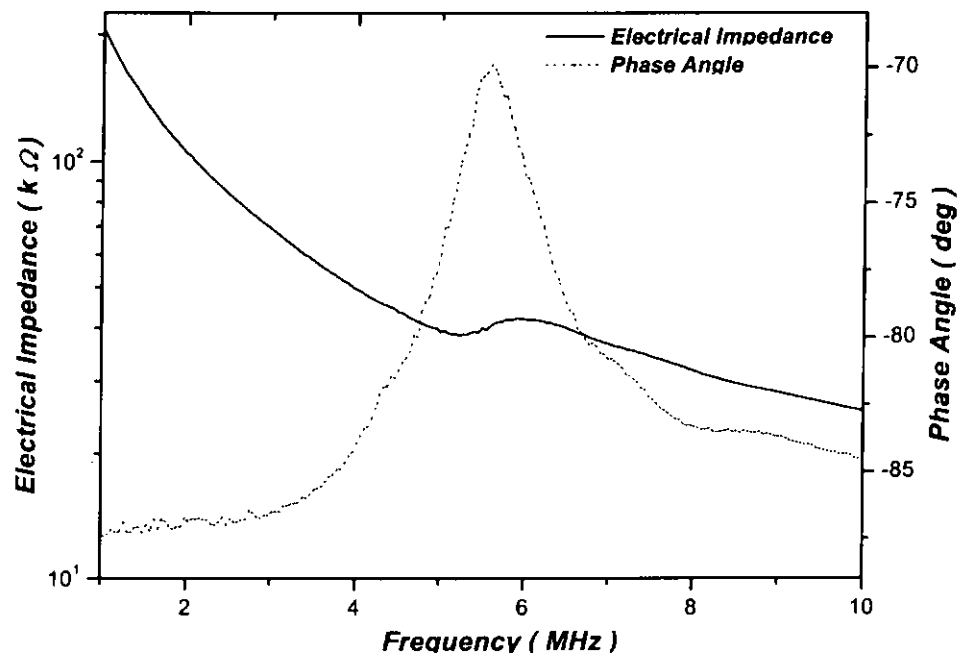
Figure 4.18 Electrical impedance and phase angle against frequency plots of the VSSP BNBT-6 single fibre sample with a thickness of 370 μm.

Table 4.1 Piezoelectric properties of VSSP BNBT-6 single fibre (300 μm diameter and 370 μm thickness)

	VSSP BNBT-6 single fibre	BNBT-6 ceramics
d_{33} (pC/N)	101	124
k_{33}	0.49	0.55
$\varepsilon_{33}^{T}/\varepsilon_0$	580	680
Q_M	5.6	30~300

4.5 Summary

BNBT-6 fibres derived from both the sol-gel and VSSP processes for 1-3 composite transducer applications were fabricated in this study.

Through adjustment of the sol-gel chemical precursors and solvents, BNBT-6 gel fibres with required diameters of 150~200 μm can be developed successfully. Due to the high organic contents in the gel fibre, the pyrolysis of gel fibre must be carried out under some inert or reducing atmosphere with a very low heating rate. The heating profile should be designed according to the TGA results of the gel fibre. CO was used as the protection vapor during the later stage of pyrolysis and resulted in dense and crack-free BNBT-6 fibres with diameters betweens 80 and 100 μm.

The viscous suspension spinning process (VSSP) provides a powder extrusion based technique of fibre fabrication. Pyrolysis of the green VSSP fibre is easy to succeed with the guidance of TGA results and atmosphere control. The final VSSP BNBT-6 fibre products are dense and crack-free with approximately 300 μm diameter. Some holes induced by the trapped air were found inside some fibres. Properties of the VSSP BNBT-6 single fibres can be measured by encapsulating the single fibre into an epoxy matrix. Most of the properties of the VSSP fibre are lower than those of the bulk ceramics due to the adverse effect caused by the holes inside the fibre.

As described in Chapter V, both the sol-gel and VSSP BNBT-6 fibres are fabricated into 1-3 composites and applied in ultrasonic transducers.

CHAPTER V

FABRICATION AND CHARACTERIZATION
OF BNBT-6 FIBRE/EPOXY 1-3 COMPOSITES

5.1 Introduction

1-3 composites are useful transducer materials due to their high electromechnical
coupling which approaches the k_{33} of the ceramics when operated in the thickness or
"33" mode. (Gururaja, 1981; Smith, 1991) They also have the advantages of having low
acoustic impedance, wide bandwidth, minimized lateral mode coupling and have
adjustable dielectric constants. In recent development of medical ultrasound, the desire
for higher resolution imaging used in ophthalmology, dermatology and intravascular
ultrasound has created the need for transducers capable of operating at very high
frequencies. (Foster, 1991)

Increase in operating frequencies and functional properties like a higher bandwidth can
be achieved by further downscaling of the diameter of the piezoceramic rods in 1-3
composites. Conventional fabrication methods of 1-3 composites have limited the
ceramic pillar diameters to larger than 70 μm (~15 MHz). (Janas, 1995). By using fine
PZT fibres as the pillars, frequency range of the 1-3 composites has been expanded up to

70 MHz. (Meyer, 1998) By maintaining fibre aspect ratios in a suitable range, using a random distribution of fibre diameters and using a random fibre arrangement, lateral vibration modes of the ceramics can be suppressed resulting in pure thickness oscillation, which is beneficial to pulse-echo type ultrasonic transducer applications.

In this Chapter, the fabrication and characterization of BNBT-6 fibre/epoxy 1-3 composites were described. BNBT-6 fibres derived from both the sol-gel and VSSP routes were used in producing 1-3 composites. Ferroelectric, piezoelectric and dielectric properties of the BNBT-6 fibre composites were measured. Moreover, a simple model derived by R. Steinhausen based on the modified series and parallel model was employed to evaluate the elastic properties of a single fibre through the measured properties of the composites.

5.2 Fabrication of BNBT-6 Fibre/Epoxy 1-3 Composites

Sintered BNBT-6 fibres were prepared for composite fabrication by selecting straight 0.5 - 2.5 cm long fibres. The fibres were put into a plastic tube with diameter of 5 mm to maintain alignment. Araldite LY5138-2/HY5138 epoxy was filled into this tube to encapsulate the fibre bundles. Then the composite was degassed under vacuum for about 30 min. The epoxy was cured at 40°C overnight to obtain the optimum property. The fabrication procedure described above is shown in Figure 5.1.

Next, the composite rod was sliced into ceramic fibre/epoxy 1-3 composite discs with

thickness ranging between 200 μm and 300 μm using an ISOMET 2000 (BUEHLER)

diamond saw. A 150 μm thick blade was used to minimize the wastage. Figure 5.2

shows the SEM photos of the BNBT-6 fibre/epoxy 1-3 composite samples derived from

sol-gel fibres and VSSP fibres, respectively. It could be seen that most of the fibres

aligned well and were perpendicular to the face. However, some holes inside the fibres

can be seen clearly from the SEM photos. Therefore, the composite discs should be

refilled with epoxy to prevent break down during subsequent poling processes.
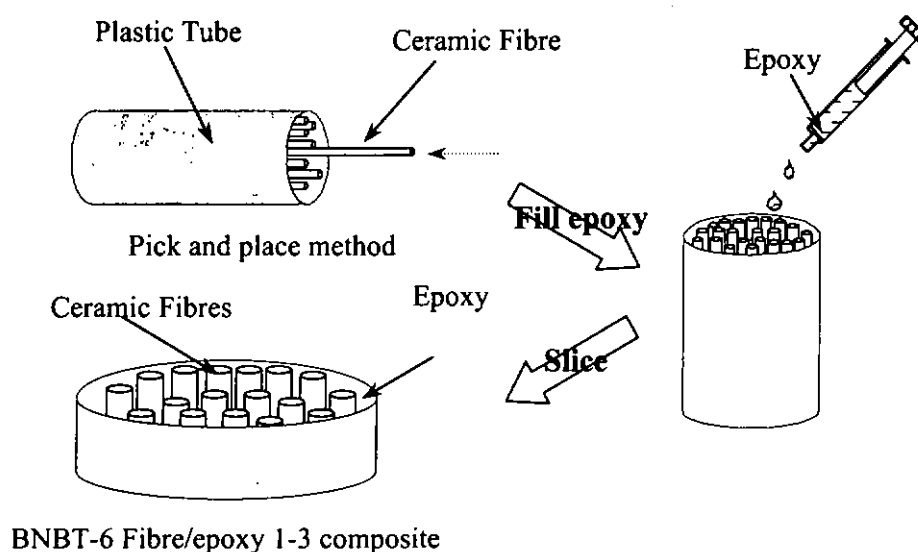
Figure 5.1 Fabrication procedure of BNBT-6 fibre/epoxy 1-3 composite.

After refilling of epoxy, the composites were polished to desired thicknesses using an

ECOMET 3 (BUEHLER) polishing machine with 800# and 1200# abrasive paper. With

this setup, composites could be polished down to 150 μm thick with a flatness of ± 1μm

from edge to edge. Chromium and gold were evaporated as electrodes on both surfaces

of the composites for electrical characterization. Poling of the composites was

performed under the same condition as that for BNBT-6 bulk ceramics.
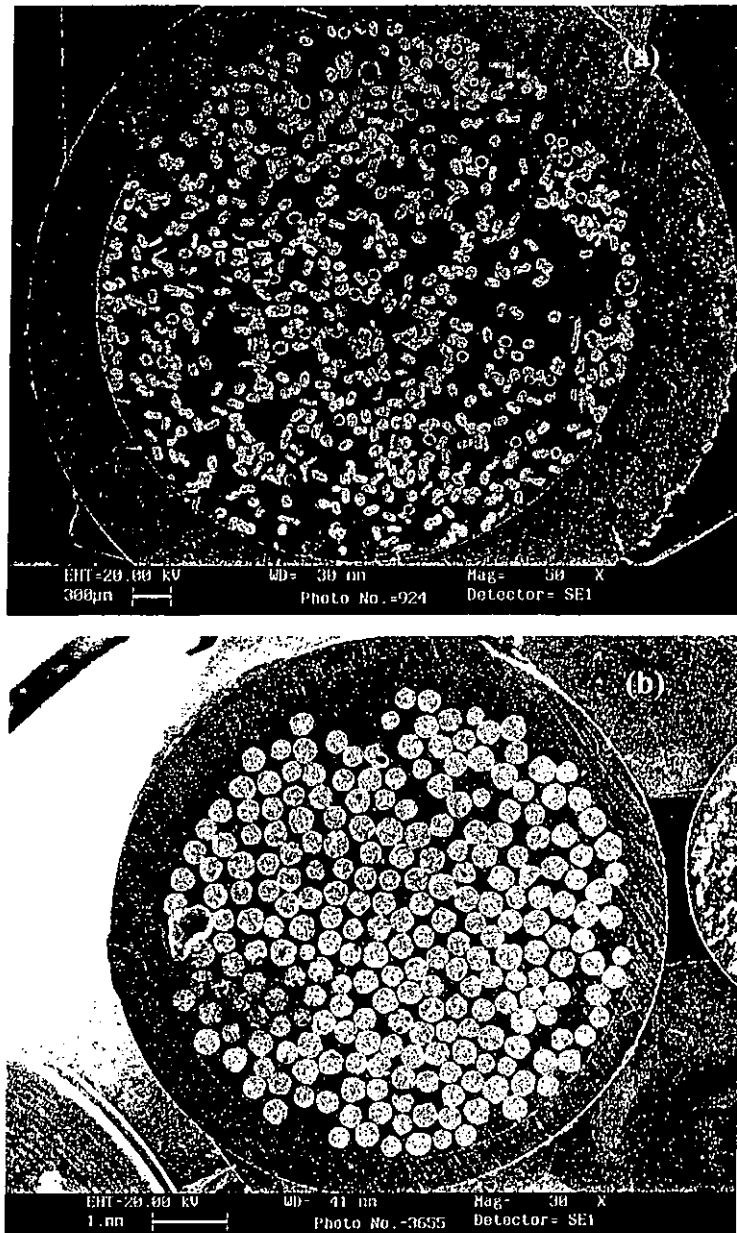
Figure 5.2 SEM micrographs of BNBT-6 fibre/epoxy 1-3 composites: (a) A sol-gel fibre

composite ($\phi = \sim 0.30$); (b) A VSSP fibre composite ($\phi = \sim 0.50$).

Fibre volume fractions ϕ of the composites can be obtained by density measurements. But since there are holes inside some fibres, it is hard to determine the density of the fibres. Therefore, ϕ cannot be calculated accurately by this way. Volume fractions could also be found by scanning the SEM photos into a computer and converting the pictures into black and white. Software such as NIH image, Digital micrograph and Adobe Photoshop can be used to calculate the fraction of white vs. black.

Ferroelectric P-E loops of the composites were measured using a Sawyer-Tower circuit (Figure 2.8). Resonance characteristics and dielectric properties were measured using an HP 4294A impedance/gain phase analyzer with an HP 16034E test fixture.

5.3 Characterization of BNBT-6 Sol-Gel Fibre/Epoxy 1-3 Composites

Before characterizing the BNBT-6 sol-gel fibre/epoxy 1-3 composites, BNBT-6 ceramics were also fabricated by the sol-gel method for comparison with the composites. The fabrication procedures are the same as that of the solid-state reaction route but with the sol-gel powder replaced the mix-oxide powder. Sol-gel BNBT-6 powder was obtained by calcining the gel at 550°C for 1h. Then some of the required properties were measured. The P-E hysteresis loop (Figure 5.3) measured at room temperature exhibits a remnant polarization P_r of 30 $\mu C/cm^2$ and a coercive field E_c of about 3.0 kV/mm.
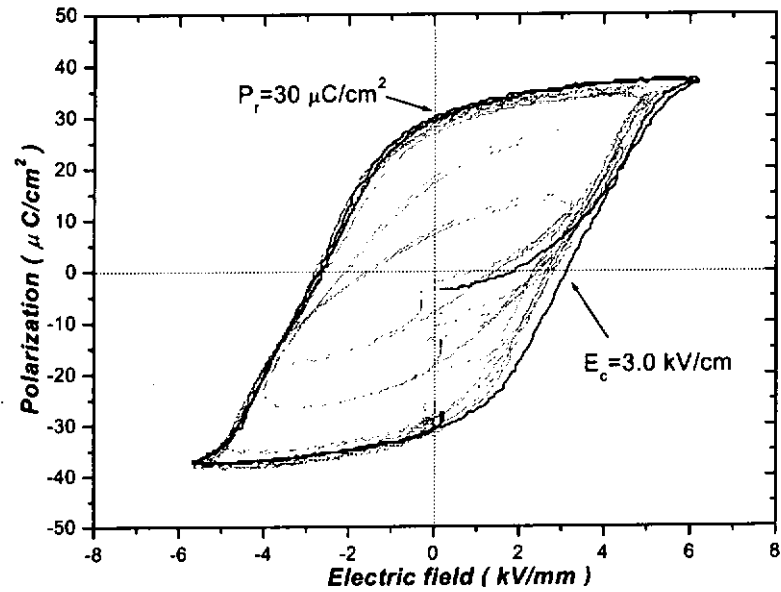
Figure 5.3 P-E hysteresis loops of BNBT-6 ceramics derived from the sol-gel method measured at room temperature.

Other necessary properties of the sol-gel BNBT-6 ceramics are listed in Table 5.1.

Table 5.1 Properties of BNBT-6 ceramics derived from the sol-gel method. For comparison, parameters of the BNBT-6 ceramics fabricated by the mixed-oxide method are also listed.

	Sol-gel	Mixed-oxide
ρ (kg/m^3)	5766	5544
d_{33} (pC/N)	98	124
k_p	0.180	0.250
k_t	0.406	0.460
s_{11}^E (10^{-12}m^2/N)	8.13	8.46
s_{12}^E (10^{-12}m^2/N)	-2.27	-2.39
s_{13}^E (10^{-12}m^2/N)	-1.04	-1.08
s_{33}^E (10^{-12}m^2/N)	9.90	11.12
$\varepsilon_{33}^T/\varepsilon_0$	955	680
Q_M	20~100	30~300
P_r (μC/cm^2)	30.0	30.5
E_c (kV/mm)	3.0	3.6

5.3.1 Ferroelectric Measurements

Ferroelectric hysteresis loops of the BNBT-6 sol-gel fibre/epoxy 1-3 composites were observed by driving the composites with an alternating electric field. The polarization behavior of the composites with various volume fractions is plotted in Figure 5.4. The remnant polarization values for the composites are roughly proportional to the ceramic remnant polarization times the volume fraction ϕ. (Figure 5.5) For the composite with about 30% fibre loading as shown in Figure 5.4 (b), the observed P_r value is 10 $\mu C/cm^2$, which is closed to 1/3 of the P_r of the ceramics. The coercive fields E_c of the composites are almost the same as that of the bulk ceramics. (Table 5.1)

Figure 5.5 shows the average values for composite polarization as a function of volume fraction for BNBT-6 sol-gel fibre/epoxy 1-3 composites. The calculated values are also shown and they are lower than the measured values at large ϕ. It is due to effect of leakage current. So the observed "P_r" from the P-E loop is the sum of remnant polarization and leakage current.
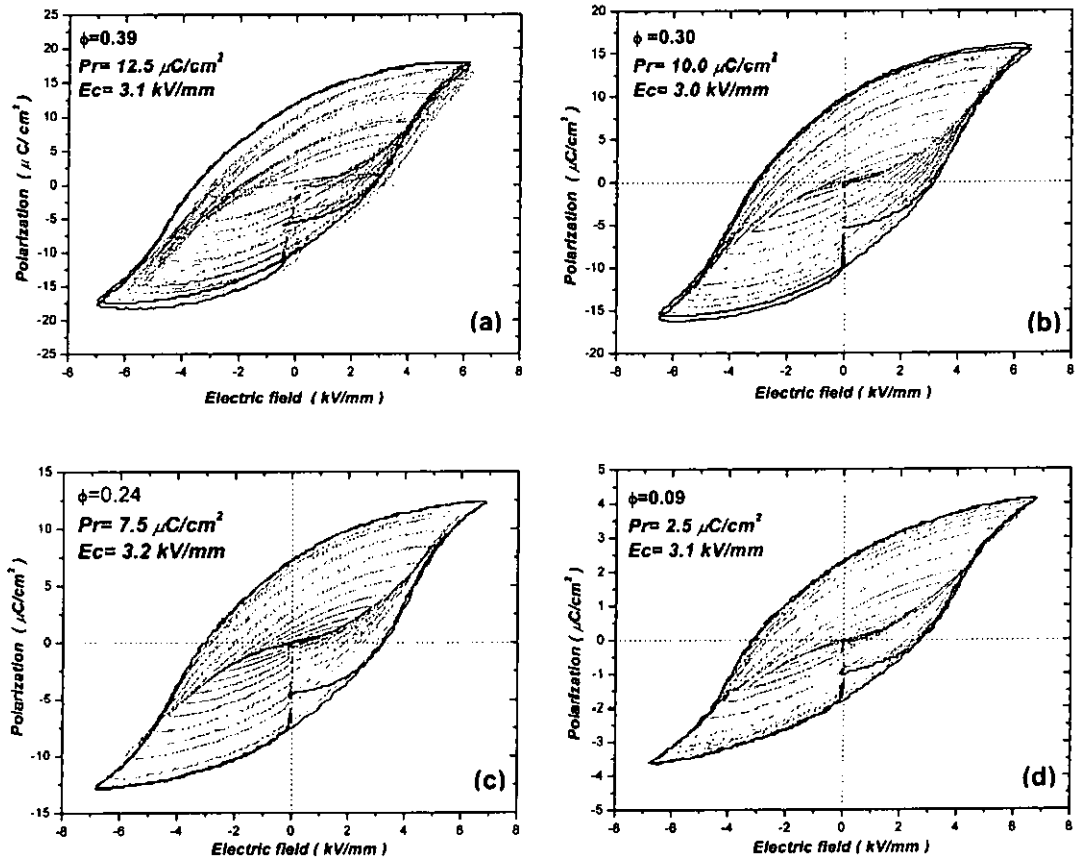
Figure 5.4 P-E hysteresis loops of BNBT-6 sol-gel fibre/epoxy 1-3 composites with various volume fraction of fibres.
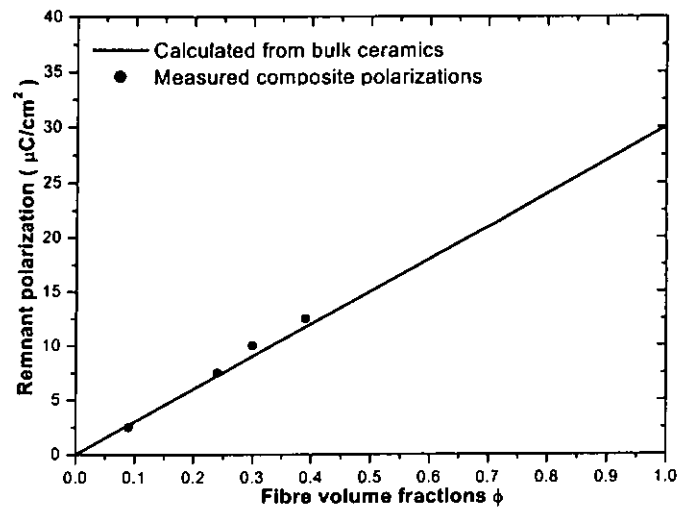
Figure 5.5 Measured remnant polarization values for BNBT-6 sol-gel fibre/epoxy 1-3 composites plotted as a function of volume fraction of fibres.

5.3.2 Piezoelectric Properties

Piezoelectric properties of the BNBT-6 sol-gel fibre/epoxy 1-3 composites were measured based on the resonance technique. Composite samples were thinned down to obtain higher resonance frequencies. But unfortunately, many samples were broken during grinding, only two good ones were left. Since the amount of sample is limited and the composite sample will be used to fabricate transducers, no other experiments were carried out on these samples besides resonance measurements. Table 5.2 summarized the main properties of the BNBT-6 sol-gel fibre/epoxy 1-3 composites. Impedance spectra of these composites are shown in Figure 5.6.

Table 5.2 Properties of BNBT-6 sol-gel fibre/epoxy 1-3 composites.

	A	B
Thickness (μm)	215	170
Fibre volume fraction ϕ	~0.39	~0.30
d_{33} (pC/N)	72	64
Resonance frequency f_r (MHz)	9.596	11.525
Impedance at f_r (Ω)	278.5	152.9
k_t	0.635	0.690
Q_M	2.7	2.0
Dielectric permittivity $\varepsilon_{33}^{T}/\varepsilon_o$	488	409
tanδ	0.041	0.044
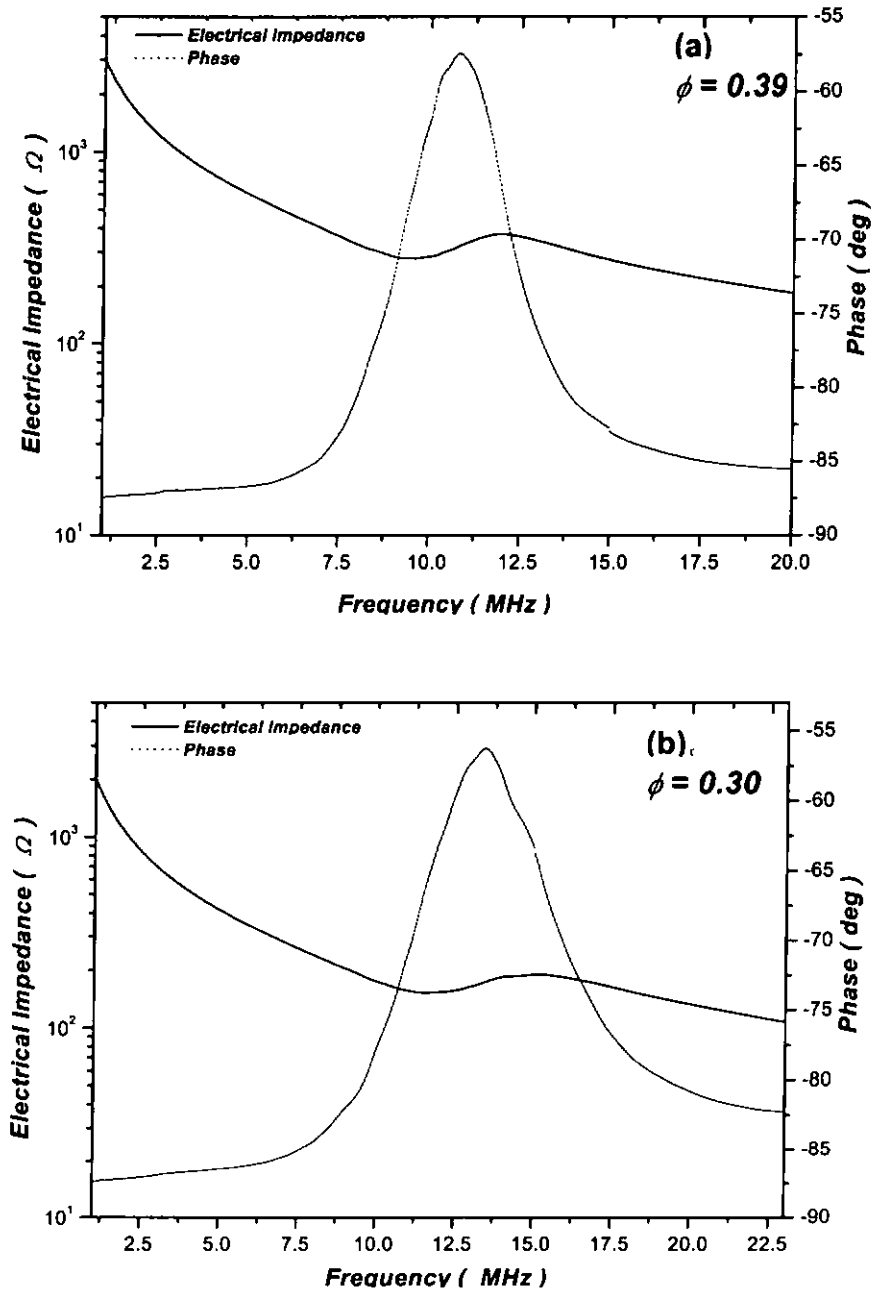
Figure 5.6 Electrical impedance and phase angle versus frequency plots for BNBT-6 sol-gel fibre/epoxy 1-3 composites. (a) ϕ =0.39; (b) ϕ =0.30.

Very broad resonance could be observed from the impedance spectrum, which resulted in high electromechnical coupling coefficient k_t (>0.60) in comparison with that of the bulk ceramics. The d_{33} value of the composites measured by the d_{33} meter is about 60% of that of the bulk ceramics and mechanical quality factor Q_M is quite low as calculated by the equivalent circuit. The overall properties of the BNBT-6 sol-gel fibre composites seem good for ultrasonic transducer applications.

5.4 Characterization of BNBT-6 VSSP Fibre/Epoxy 1-3 Composites

5.4.1 Ferroelectric Measurements

P-E hysteresis loops of BNBT-6 VSSP fibre/epoxy 1-3 composites were measured using the Sawyer-Tower circuit. Loops of the composites with different fibre volume fractions are shown in Figure 5.7. P_r values of the composites also depend on the fibre volume fractions. The shape of the P-E loops is square and quite similar to that of the bulk BNBT-6 ceramics prepared by the mixed-oxide technique. In case of the VSSP fibre composites, the fibre loading can go up to over 50%, thus the observed P_r value in the loop of a composite with ϕ =0.52 was around 15.2 $\mu C/cm^2$. Values for polarization as a function of volume fraction for the BNBT-6 VSSP fibre/epoxy 1-3 composites are plotted in Figure 5.8. It was found that the measured P_r fitted well with the calculated curves, which implied that the ferroelectric property of the VSSP fibre was quite closed to the bulk ceramics and agreed with results obtained for the single VSSP fibre P-E hysteresis measurement shown in Figure 4.17.
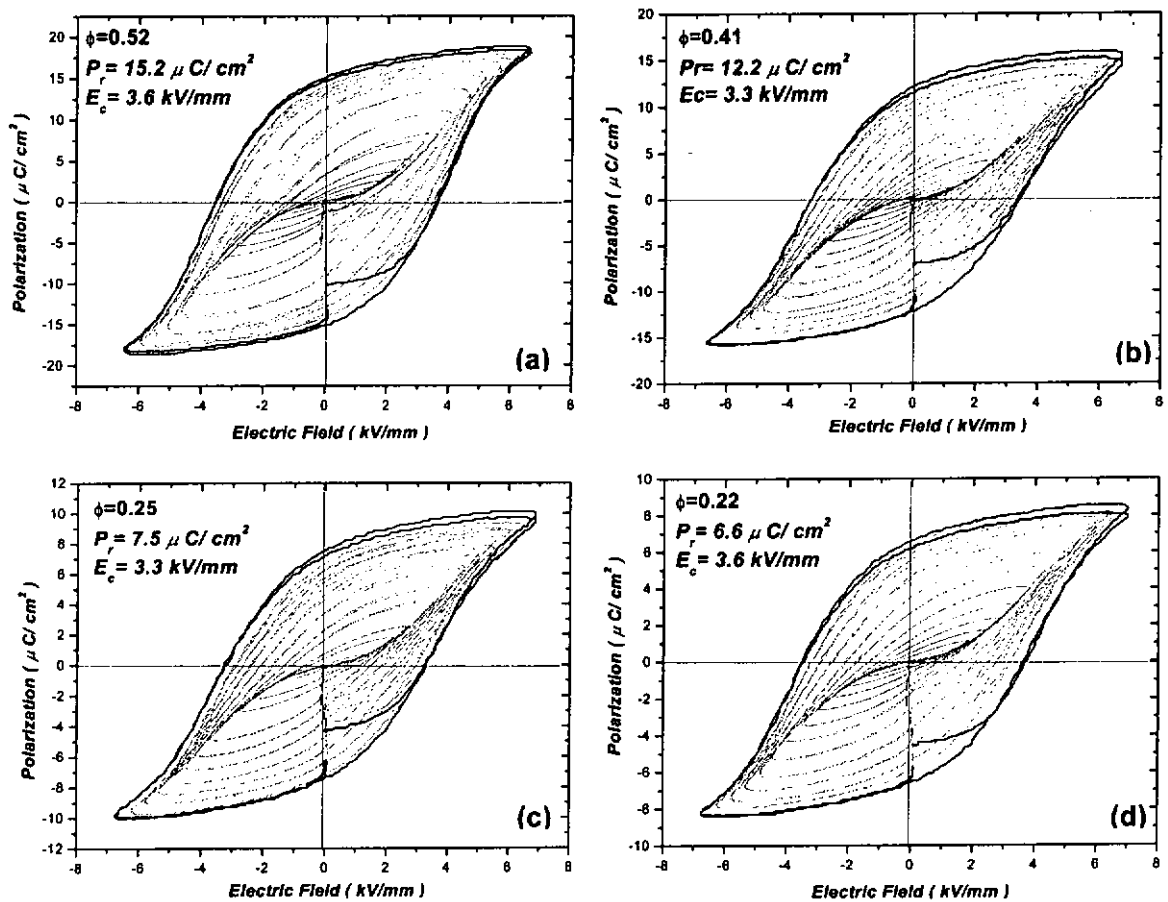
Figure 5.7 P-E hysteresis loops of BNBT-6 VSSP fibre/epoxy 1-3 composites with various volume fraction of fibres.
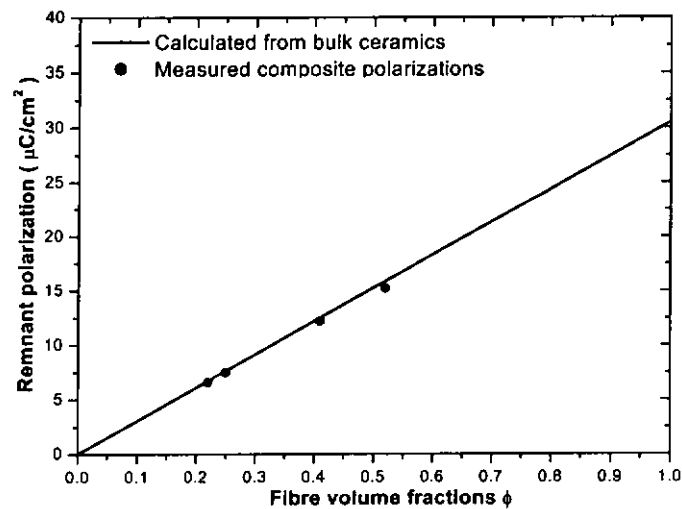
Figure 5.8 Measured remnant polarization values for BNBT-6 VSSP fibre/epoxy 1-3 composites plotted as a function of volume fraction of fibres.

5.4.2 Piezoelectric Properties

Piezoelectric measurements of BNBT-6 VSSP fibre/epoxy 1-3 composites were carried out as described in the previous section. Table 5.3 shows the piezoelectric properties of the VSSP fibre composites with various fibre volume fractions.

Table 5.3 Properties of BNBT-6 VSSP fibre/epoxy 1-3 composites.

	A	B	C	D
Thickness (μm)	213	220	217	225
Fiber volume fraction ϕ	~0.52	~0.41	~0.25	~0.22
d_{33} (pC/N)	75	83	73	71
Resonance frequency f_r (MHz)	8.427	8.270	8.271	7.980
Impedance at f_r (Ω)	34.30	42.80	64.35	76.60
k_t	0.47	0.45	0.45	0.52
Q_M	3.2	2.3	2.5	3.0
Dielectric permittivity $\varepsilon_{33}^T / \varepsilon_o$	487	451	309	258
tanδ	0.049	0.054	0.050	0.052

Most properties of these composites were comparable to that of the sol-gel fibre composites except for the thickness electromechanical coupling coefficient. For a particular sample of ϕ =0.4 fibre filling, the k_t value could be 0.64 for a sol-gel fibre composite but only ~0.45 for the VSSP fibre composite. If we investigated the orientation of fibres inside the composites from the SEM pictures, it was noticed that almost all the fibres were perpendicular to the surface for a VSSP fibre composite while in the case of sol-gel fibre composite, fibres arranged rather randomly, there existed a

small tilt angle between the fibre and the sample surface. In 1-3 composites, randomly

oriented active elements can enhance the thickness electromechanical coupling because

the effective thickness of each fibre is slightly different. (Turcu, 2002) This gives rise to

a slightly different resonance frequency for each fibre which results in a broadening of

the resonance peak of the composites and hence a higher k_t. Therefore, the sol-gel fibre

composites should have better transducer performance. On the other hand, the holes

existed in the VSSP fibre also affected the composite properties. Resonance

characteristics of the VSSP fibre composites are shown in Figure 5.9.

All the spectra show two main resonance peaks. It is due to the coupling of the lateral

and thickness modes of the fibres. Thinning test of a 1-3 composite made by the dice-

and-fill method presented in Chapter III has proved both from experimental results and

theoretical calculation that when the aspect ratio is larger than 1.3, the thickness mode

and lateral mode will couple to form two strong resonance modes. In the case of these

VSSP fibre composites, the fibre diameters are about 300 μm and the thickness of the

samples are about 200-220 μm, so the aspect ratios are between 1.36 to 1.5, which are in

the range where coupling occurs. Therefore, the spectrum has a double peak resonance.
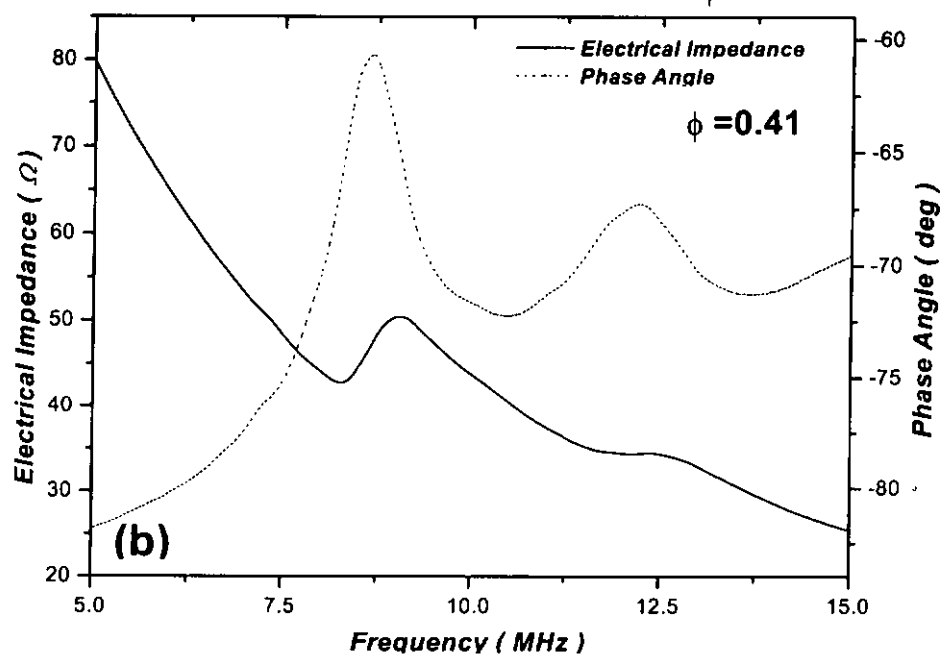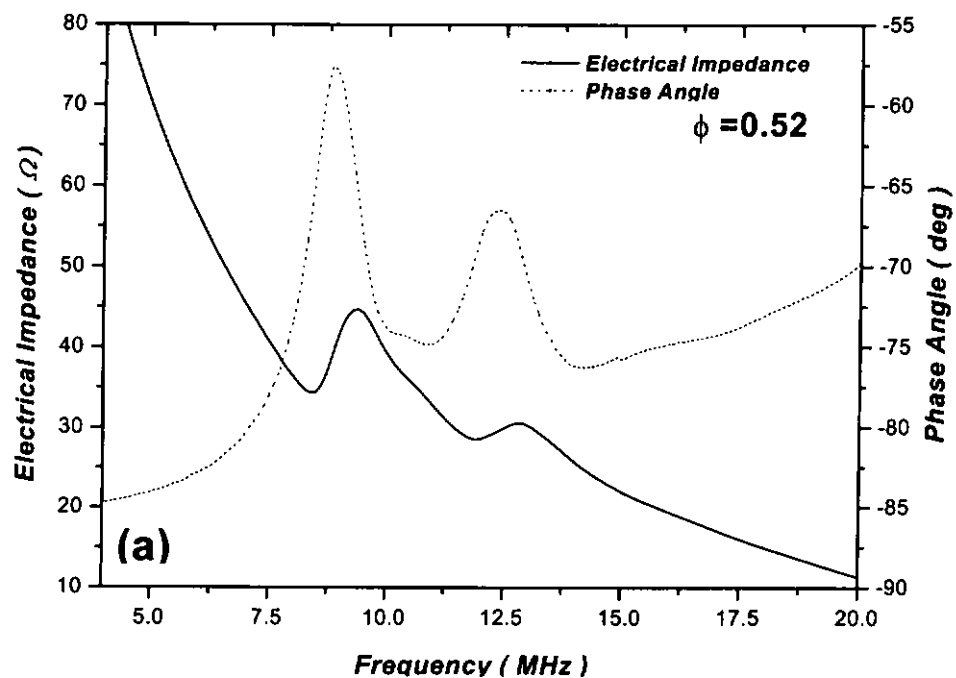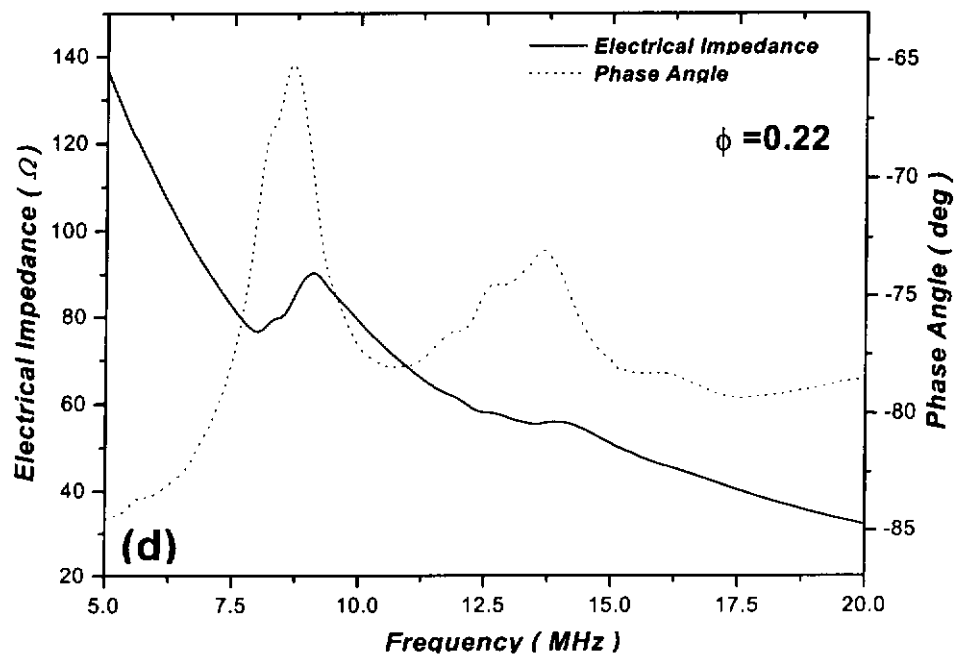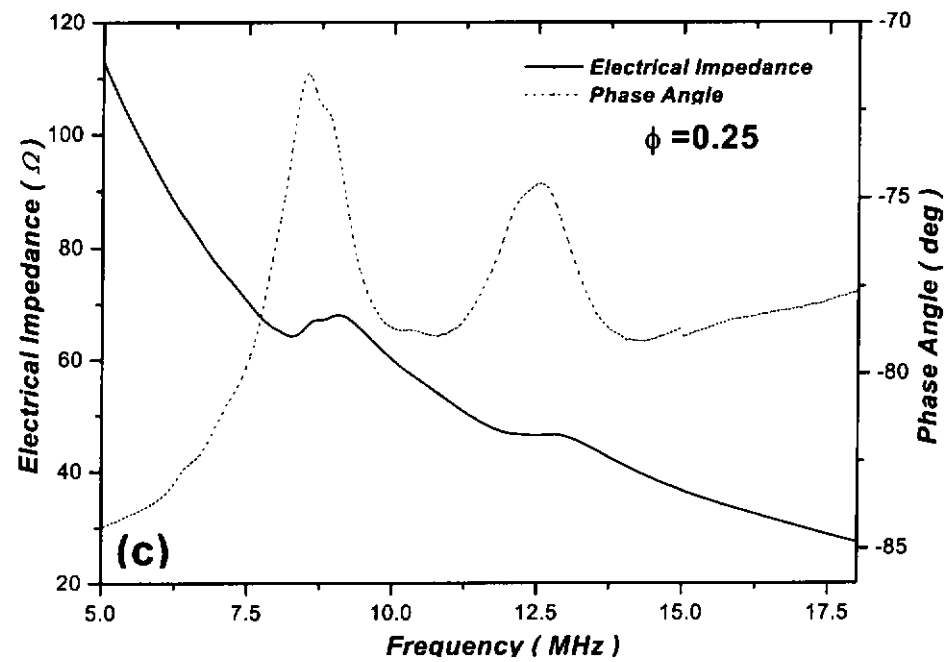
Figure 5.9 Electrical impedance and phase angle versus frequency plots for BNBT-6

VSSP fibre/epoxy 1-3 composites. (a) ϕ =0.52; (b) ϕ =0.41; (c) ϕ =0.25;

(d) ϕ =0.22.

In order to reveal how high the resonance frequency of VSSP fibre composite can be achieved, thinning test was performed using a composite with about 40% fibre loading (electrode area= ~33.2 mm^2) to find out the change of resonance characteristics. Real part of the impedance was plotted as a function of frequency as shown in Figure 5.10. As the thickness of the sample was reduced, the lateral mode resonance dose not change but the thickness mode resonance increases and separates from the lateral mode gradually. When the sample was thinned down to about 123 μm, the lateral mode and thickness mode are well separated and the thickness resonance frequency could be up to over 20 MHz. When the thickness was reduced to below 100 μm, although resonance frequency can increase closed to 30 MHz, the resonance peak becomes very broad. Therefore, it is better to use the VSSP fibre composites below 30 MHz for ultrasonic transducer applications.
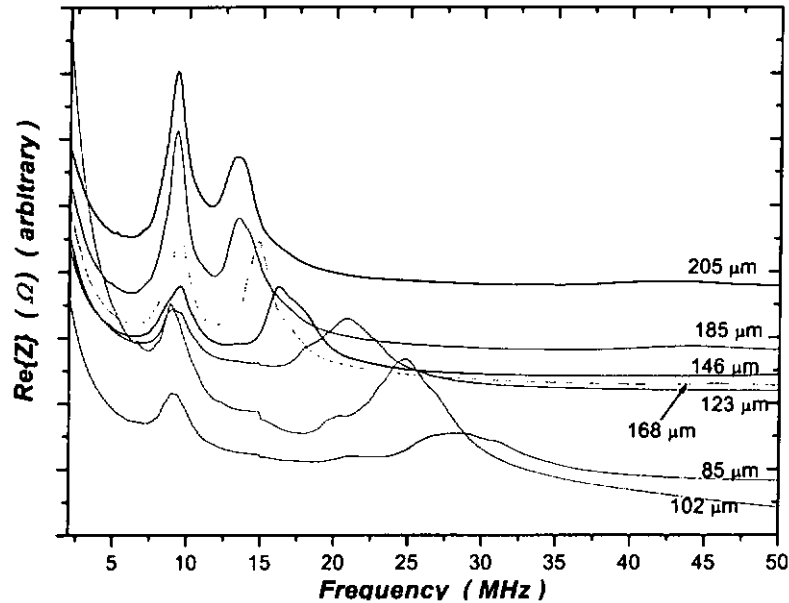
Figure 5.10 The real part of impedance plotted as a function of frequency for a BNBT-6
VSSP fibre/epoxy 1-3 composite with ~40% fibre loading and 6.5 mm
diameter of various thicknesses.

5.5 Characterization of A Single BNBT-6 Fibre

5.5.1 Evaluation Models

For the optimization of the ceramic fibre performance, it is necessary to determine their

dielectric, elastic and piezoelectric properties. Conventional measurement methods

cannot be applied to evaluate a single fibre because they are too thin and brittle. A

method for characterizing single fibres has been described in Chapter IV. However, if

the fibre is too thin, even this method cannot be used to measure the fibre properties

directly. However, the elastic coefficient $s^E_{33,f}$ of the fibres can be calculated from the

effective coefficients $c^E_{33,\textit{eff}}$ and $s^E_{33,\textit{eff}}$ of 1-3 composites containing such fibres. Then

piezoelectric strain coefficient $d_{33,f}$ and relative permittivity $\varepsilon^T_{33,f}$ of the single fibres

could be derived from the calculated $s^E_{33,f}$.

The effective elastic compliance $s^E_{33,\textit{eff}}$ is related to the elastic coefficient of the

components and their volume fraction v, according to: (Steinhausen, 2001)

$$s^E_{33,\textit{eff}} = \frac{s^E_{33,a}}{v_p s^E_{33,a} Y_p + v_a} \tag{5.1}$$

where Y is the Young's modulus. The subscripts "a" and "p" represent the active

(BNBT-6 ceramics) and the passive (epoxy) material, respectively. From Equation (5.1),

the elastic compliance $s^E_{33,f}$ of the BNBT-6 fibres becomes

$$s^E_{33,f} = \frac{v_a s^E_{33,\textit{eff}}}{1 - v_p s^E_{33,a} Y_p} \tag{5.2}$$

Then, it is possible to extract the piezoelectric coefficient and dielectric permittivity of

single fibres by using the analytical approximations. In this calculation, the experimental

results obtained from measurements of the effective properties of the 1-3 composites

were used. The piezoelectric modulus $d_{33,f}$ of the fibre can be calculated directly from

the measured effective piezoelectric modulus $d_{33,\textit{eff}}$ of the composites by:

$$d_{33,f} = d_{33,eff}(1 + \frac{v_p}{v_f} s_{33,f}^E Y_p) \tag{5.3}$$

The dielectric permittivity $\varepsilon_{33,f}^T$ of the fibre can be calculated by the formula:

$$\varepsilon_{33,f}^T = \frac{\varepsilon_{33,eff} - v_p \varepsilon_p}{v_f} + \frac{d_{33,f}^2}{s_{33,f}^E + \frac{v_f}{v_p} \frac{1}{Y_p}} \tag{5.4}$$

where v_f is the volume fraction of fibres, $s_{33,f}^E$ is the elastic coefficient of the fibres

which can be derived from Equation (5.2), $\varepsilon_{33,eff}$ and ε_p are the dielectric permittivity of

the composite and epoxy matrix, respectively.

5.5.2 Results and Discussion

Both the sol-gel and VSSP BNBT-6 fibres were evaluated using the model described

above. Effective composite parameters $s_{33,eff}^E$ can be measured directly using BNBT-6

fibre/epoxy 1-3 composites with various fibre volume fractions. Actually, the optimum

sample for $s_{33,eff}^E$ measurement is a tall thin rod with thickness to lateral dimension of

10:1. But since there are no extra composites samples to prepare the suitable geometry

for $s_{33,eff}^E$ measurement, disc shaped BNBT-6 fibre/epoxy 1-3 composites with aspect

ratio of 0.5 -1.5 were used in this experiment to obtain the approximate $s_{33,eff}^E$ values.

Material parameters needed in this calculation can be found in Tables 2.3, 3.1 and 5.1.

Figure 5.11 shows the modelled and measured effective elastic compliance $s_{33,eff}^E$ of the

sol-gel and VSSP fibre composites.
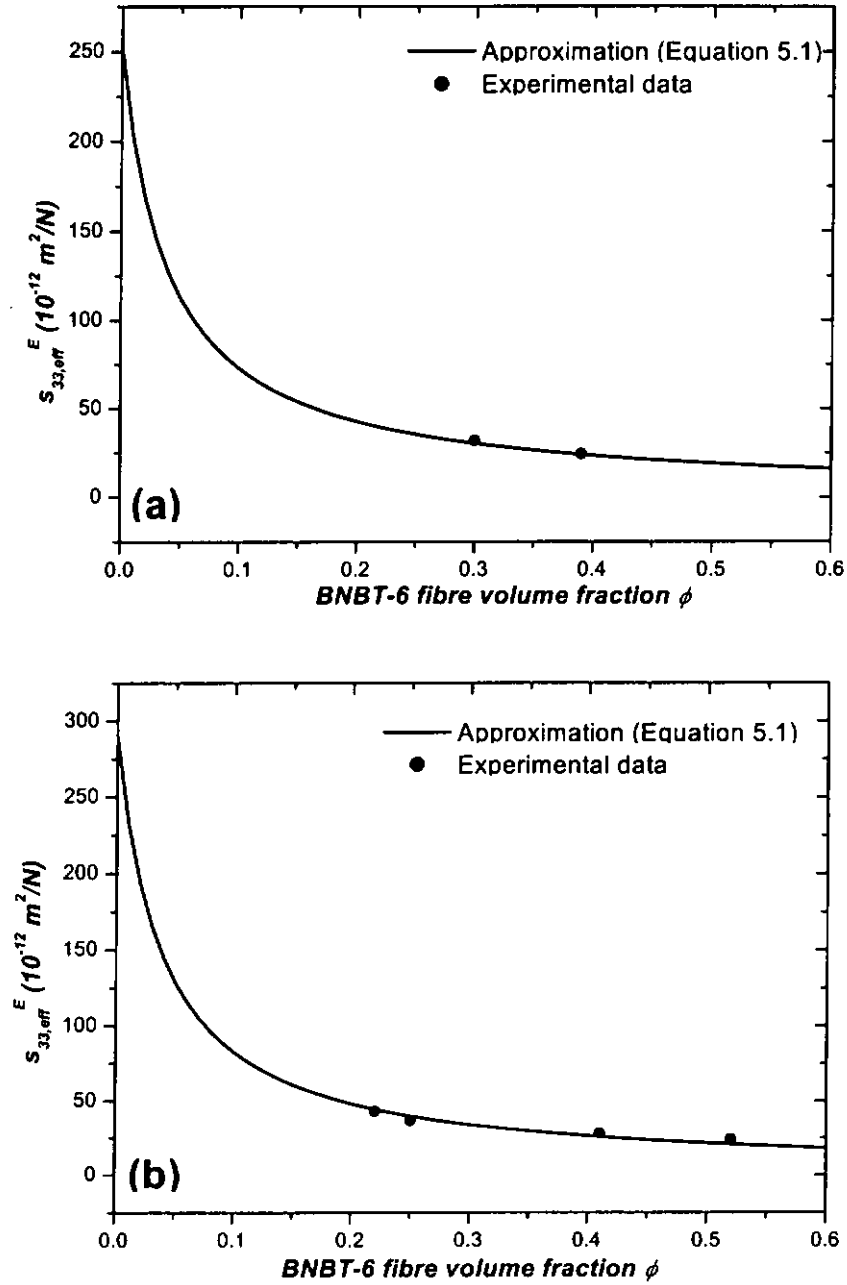
Figure 5.11 Effective elastic compliance $s^E_{33,\mathit{eff}}$ of BNBT-6 fibre/epoxy 1-3 composites:

(a) sol-gel fibre composites; (b) VSSP fibre composites.

The measured data coincided well with the modelling curves and the elastic compliance

$s_{33,f}^E$ of the BNBT-6 single fibre was calculated using Equation (5.2) and the results were

presented in Figure 5.12. Each data point is an average of values measured at different

positions on the same sample. Average values of $s_{33,f}^E$ for the sol-gel and VSSP fibre are

10.27×10^{-12} m²/N and 11.69×10^{-12} m²/N, respectively. It was noticed that $s_{33,f}^E$ was

slightly higher than the corresponding value of the bulk ceramics for both the sol-gel and
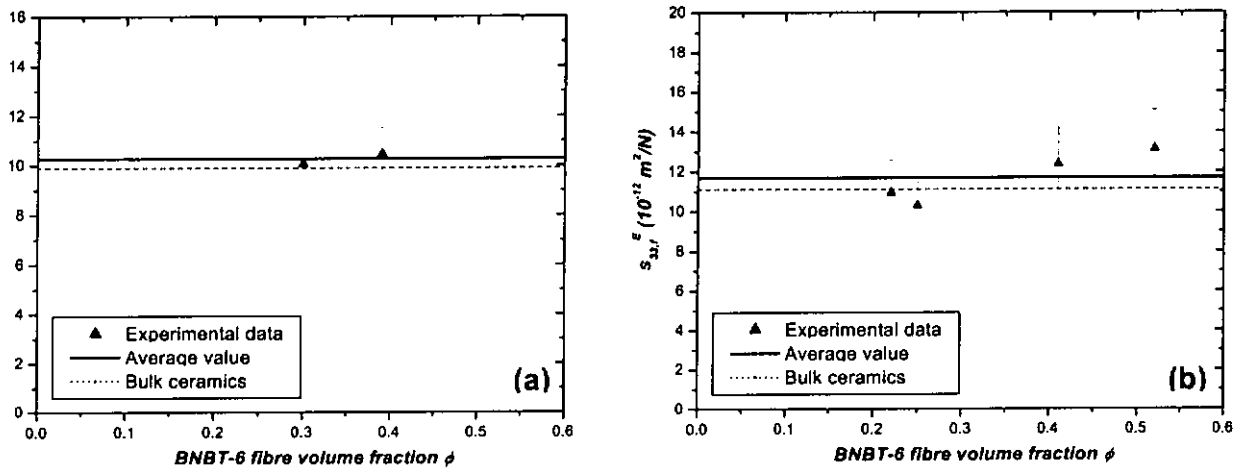
VSSP fibres.

Figure 5.12 Elastic compliance coefficient $s_{33,f}^E$ of the BNBT-6 single fibres: (a) sol-gel
fibre; (b) VSSP fibre.

The piezoelectric strain coefficient $d_{33,f}$ and dielectric permittivity $\varepsilon_{33,f}^{T}$ of BNBT-6 single fibre were then calculated using Equations (5.3) and (5.4). Effective composite parameters $d_{33,eff}$ and $\varepsilon_{33,eff}^{T}$ were measured using a d_{33} meter and an HP 4294A impedance/gain phase analyzer, respectively. $s_{33,f}^{E}$ derived from Equation (5.2) was used in the calculation of $d_{33,eff}$ and $\varepsilon_{33,eff}^{T}$. The calculation results are shown in Figure 5.13 and 5.14. For both the sol-gel and VSSP fibres, $d_{33,f}$ and $\varepsilon_{33,f}^{T}$ are lower than the values of bulk ceramics.
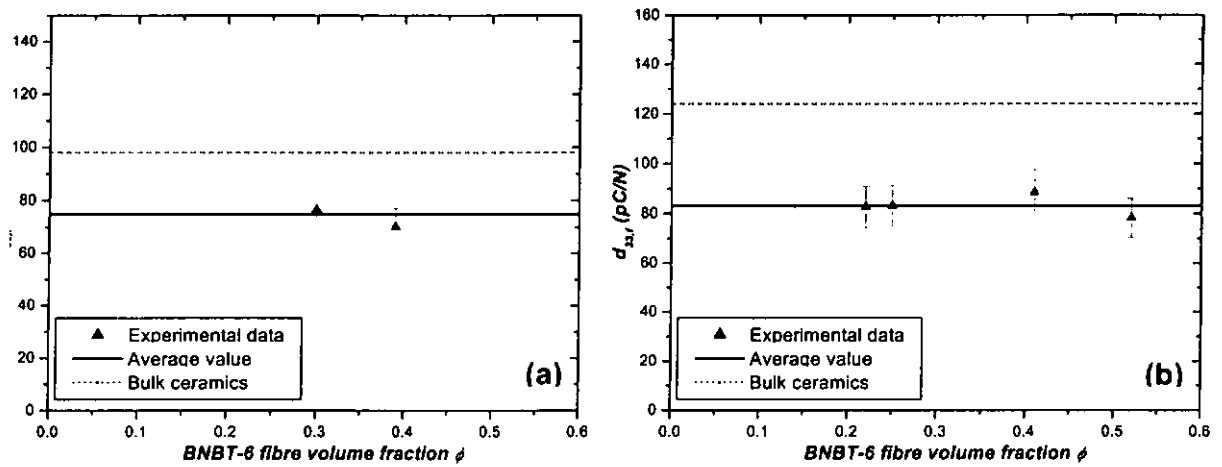
Figure 5.13 Piezoelectric strain coefficient $d_{33,f}$ of the BNBT-6 single fibres: (a) sol-gel fibre; (b) VSSP fibre.
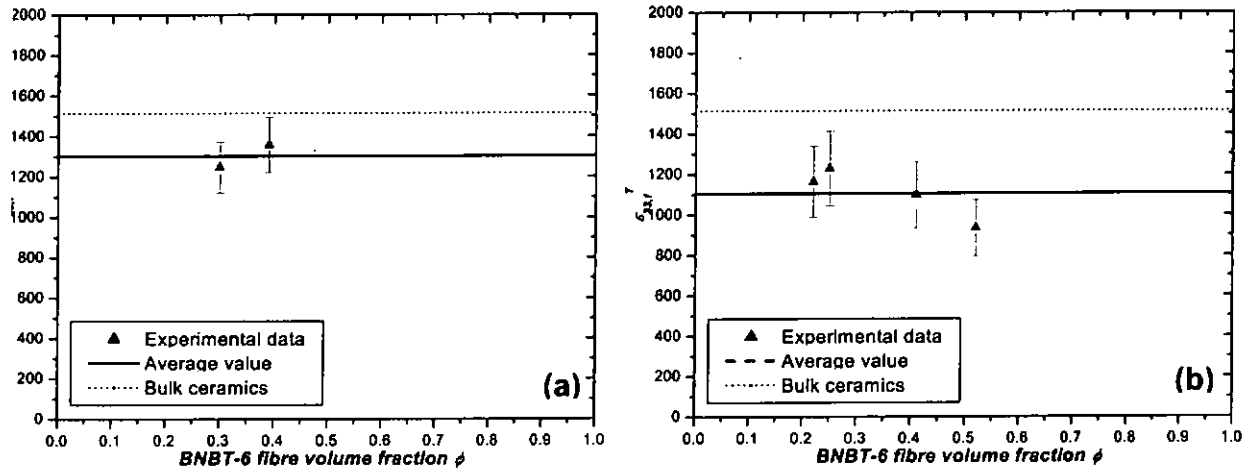
Figure 5.14 Dielectric permittivity $\varepsilon^T_{33,f}$ of the BNBT-6 single fibre: (a) sol-gel fibre; (b) VSSP fibre.

5.6 Summary

BNBT-6 fibre/epoxy 1-3 composites were fabricated by encapsulating fibres into an epoxy matrix. Both sol-gel and VSSP fibres were used to develop 1-3 composites in this work. SEM photos revealed the microstructure of the fibre composites and can be used to estimate the fibre volume fraction with the help of some image analysis softwares. P-E hysteresis loops of the composites with various fibre volume fractions were measured. The P_r value of the composite depends on the fibre volume fraction. Characterization of the fibre composites was also based on the resonance technique. In comparison, sol-gel

fibre composites have larger thickness electromechanical coupling coefficient k_t of nearly 0.70 due to the random arrangement of some fibres inside the composite.

A model was employed to evaluate the properties of BNBT-6 single fibres. The elastic compliance coefficient $s_{33,f}^E$ of a single BNBT-6 fibre was calculated from the effective compliance of the composites $s_{33,eff}^E$. The calculated $s_{33,f}^E$ was quite closed to the bulk ceramic values for both the sol-gel and VSSP fibres. Then, the piezoelectric strain coefficient $d_{33,f}$ and dielectric permittivity $\varepsilon_{33,f}^T$ of the single fibres were derived from the calculated $s_{33,f}^E$. Calculated $d_{33,f}$ and $\varepsilon_{33,f}^T$ were lower than the bulk values presumably due to the low $d_{33,eff}$ of the composites caused by pores in the fibres.

CHAPTER VI

ULTRASONIC TRANSDUCERS BASED ON BNBT-6/EPOXY 1-3 COMPOSITES

6.1 Introduction

Ultrasound, defined as mechanical vibrations with frequency higher than 20 kHz, has found lots of applications since its inception in the late 1940's. The most important applications of ultrasound include finding defects in materials and parts, imaging and therapy of human body as well as underwater surveillance and guidance systems. (Meyer, 1998) Moreover, Ultrasonic imaging has currently become the second largest diagnostic imaging technique in medicine after X-ray. (Shung, 1992)

The advantages of ultrasonic imaging techniques have attracted a wide range of interest in ultrasonic transducer design, improvement and applied research. Development in high-resolution ultrasonic imaging, e.g. in the imaging of arteries, dermatology and ophthalmology, have called for the fabrication of high performance transducers with operation frequencies above 15 MHz. Resolution is a critical feature of ultrasonic transducers. Resolution increases as operating frequency increases but at the expense of penetration depth. Resolution can also be improved through transducer design, which includes varying the aperture size and shape, acoustic backing and matching layers.

Design and evaluation of single element pulse-echo type transducers have been investigated by many scientists and engineers. (Zipparo, 1997; Foster, 1991; Lukacs, 1997) Transducers fabricated using 1-3 piezoelectric composites take advantage of the variable acoustic impedance and dielectric permittivity, high electromechanical coupling and low mechanical quality factor. Piezocomposites with 1-3 connectivity have been shown to have 4-8 dB improvements in sensitivity over monolithic transducers. (Meyer, 1996) Besides, the operating frequencies of 1-3 composite transducers could be increased to over 15 MHz by downscaling the piezoelements inside the composites. A number of fine scale PZT based fibres have been used in developing ultrasonic transducers and very high operating frequencies (30 MHz ~ 70 MHz) as well as excellent transducer performance were obtained. (Li, 2001; Meyer, 1998)

This Chapter begins with a description of the evaluation method of pulse-echo type ultrasonic transducer. BNBT-6/epoxy 1-3 composites developed from both the dice-and-fill technique and by encapsulating fibres in a polymer matrix were used to fabricate ultrasonic transducers. A discussion on the fabrication and characterization of ultrasonic transducers made by these BNBT-6/epoxy 1-3 composites was presented.

6.2 Evaluation of Pulse-Echo Type Ultrasonic Transducers

1-3 composite pulse-echo type transducer performance is characterized by its transmit

efficiency and receiving sensitivity as well as the bandwidth and energy lost on

transmission and reception (round-trip insertion loss). Bandwidth is a measure of the

frequency response of the transducer and is defined as the frequency range over which

the amplitude of the response is within 6 dB of the peak response. (NEMA Standards,

1982) Bandwidth can be improved with modifications in the transducer fabrication by

adding backing and matching layers to reduce ringing. Round-trip insertion loss is a

function of the ability of the material to convert energy, the energy lost due to mismatch

between the transducer and the electronics and the energy lost due to the energy

absorbed in the backing materials.

Transducers were tested in a water bath in pulse-echo mode by reflecting the signal off a

flat and smooth stainless steel target. The testing setup is illustrated in Figure 6.1. The

transducer is immersed in a tank with degassed water at 20 ± 5 °C. The transducer is

mounted on a holding device capable of independent angular adjustments in two

orthogonal planes containing the acoustical axis. (NEMA Standard, 1982) The

transducer beam is reflected from the interface at the standard test distance Z_0. The

standard test distance Z_0 for plane interface pulse-echo measurements is the distance

from the face of the transducer assembly to the point of maximum acoustical intensity

on the acoustic axis. In the case of circular nonfocussed transducer, $Z_0 \cong a^2 / \lambda_c$, where

a is the radius of the transducer and λ_c is the acoustic wavelength in water at the centre

frequency of the transducer. For a focussed transducer, it was placed at the focal point of

the transducer. Excitation was achieved using a Panametrics model 5900 PR pulser-

receiver. The reflected waveform was received and digitized on an HP Infiniium

54820A oscilloscope.
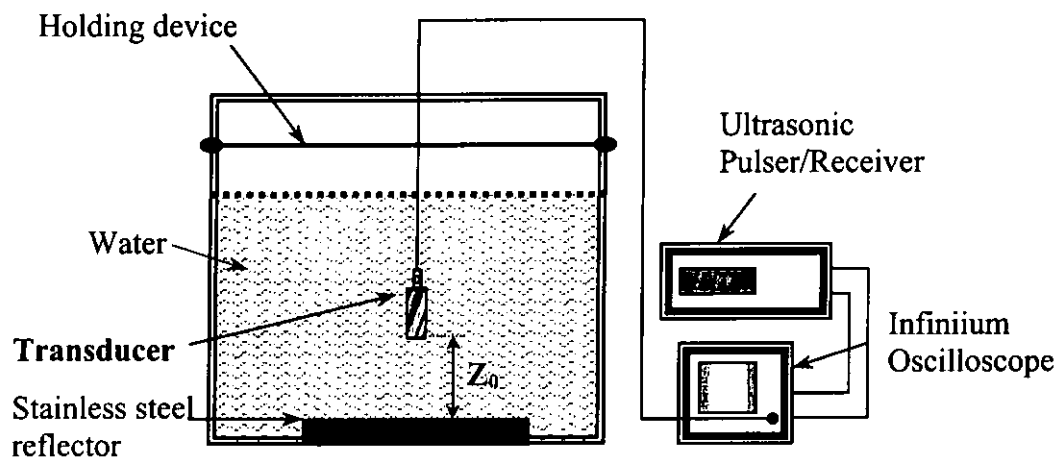
Figure 6.1 Setup for testing the pulse-echo response of a transducer.

6.2.1   Frequency Spectrum and Bandwidth Determination

Frequency spectrum of the transducer was obtained by the Fast Fourier Transform (FFT)

method, which is a built-in function of the Origin software. The centre frequency of a

transducer is a key factor which affects the axial resolution. Increasing the frequency of

a transducer results in an improved axial resolution. But increasing the frequency will

decrease the penetrating ability of the beam because high frequencies are more quickly

attenuated by body tissues. Therefore, high frequency transducers will provide high-

resolution image where penetration is not a critical requirement.

Bandwidth is an important parameter to evaluate transducer performance. A higher

bandwidth means the transducer can be used in a wider frequency range. In addition,

bandwidth is also an indicator of the damping factor. Wide bandwidths are the

characteristics of highly damped transducers, while narrow bandwidths indicate lower

degrees of damping. There are several methods to obtain the bandwidth of a transducer

as described in the NEMA Standard. The spectrum analyzer method was employed in

this study to determine the bandwidth characteristics of a transducer in its frequency

domain.

Figure 5.2 shows a schematically diagram of the frequency spectrum for bandwidth

determination. Several parameters should be measured: 1) frequency of maximum pulse-

echo response, (f_p); 2) frequencies (f_l and f_u) at which the pulse-echo response is one half

(-6 dB) the maximum response. Thus, the centre frequency (f_c) of the transducer is

defined as,

$$f_c = \frac{f_u + f_l}{2} \qquad (6.1)$$

Subsequently, the −6 dB bandwidth (BW) of a transducer in percentage form can be

calculated by:

$$BW = \frac{f_u - f_l}{f_c} \times 100\% \qquad (6.2)$$
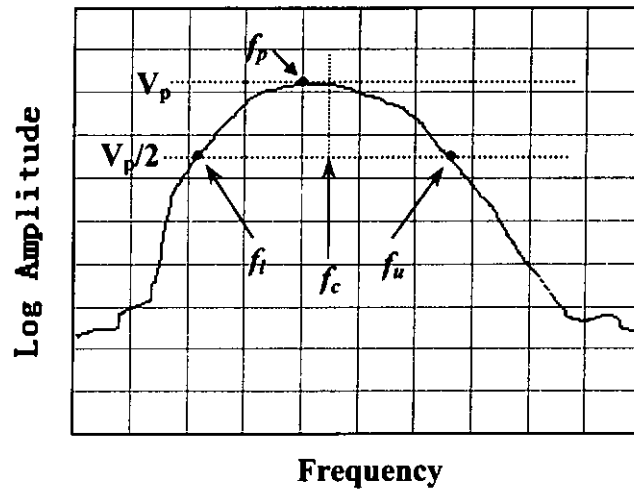
Frequency

Figure 6.2 Illustration of the frequency spectrum of a transducer for bandwidth determination.

6.2.2 Insertion Loss Measurements

The insertion loss (or the relative pulse-echo sensitivity) of the transducer is another key parameter affecting the imaging quality. It is defined as the ratio of power of the received transducer echo power P_r divided by the power of the excitation pulse power P_t delivered into the transducer. The insertion loss (IL) of a transducer can be expressed in dB form as,

$$IL = 10\log(\frac{P_r}{P_t})$$

(6.3)

To measure the insertion loss, an HP 8116A function generator (which is a 50 ohm output impedance gated-sinewave signal generator) was adjusted to produce a toneburst of 15 or 20 cycles with an amplitude of 1 V peak to peak at the centre frequency f_c of the transducer as measured by the Infiniium oscilloscope that has been set to a 50-Ω

termination. With the transducer mounted in the water tank, it was connected to the

function generator and the oscilloscope was set to 1 MΩ termination to ensure that all

the energy from the function generator is channeled to the transducer. The transducer

then was adjusted to give a maximum echo from the steel reflector. The maximum peak-

to-peak amplitude V_r of the first received echo was recorded. The measurement is

shown schematically in Figure 6.3. V_s is the open circuit voltage of the function

generator, which is twice V_t, the voltage transmitted into a matched 50 Ω load. P_t can be

calculated by

$$P_t = V_t(\frac{V_s}{2R}) = \frac{V_t^2}{R} \tag{6.4}$$

Therefore, the insertion loss of the transducer can be calculated by the following

equation:

$$IL = 10\log\frac{P_r}{P_t} = 10\log(\frac{V_r^2/R}{V_t^2/R}) = 20\log(\frac{V_r}{V_t}) \tag{6.5}$$
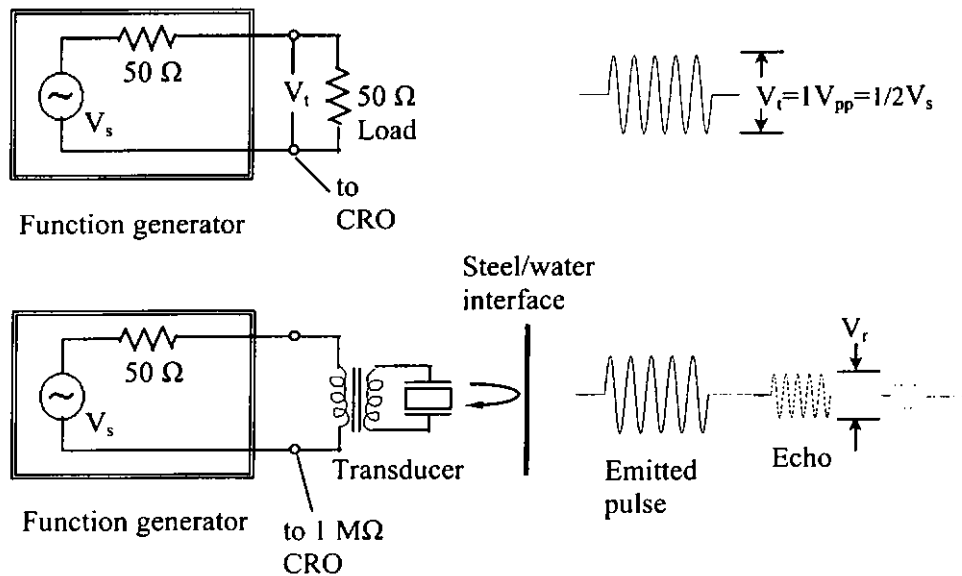
Figure 6.3 Schematic diagram of the insertion loss measurement.

6.3 Transducer Fabrication

Two kinds of pulse-echo type ultrasonic transducers were fabricated in this study. The first type is a dual frequency transducer based on BNBT-6/epoxy 1-3 composite fabricated by the dice-and-fill method. The second type is high frequency transducers based on the BNBT-6 fibre/epoxy 1-3 composites. Both the sol-gel and VSSP fibre composites were used in fabricating the high frequency transducers.

6.3.1   Fabrication of the Dual Frequency Transducer

As mentioned in Chapter III, the thinning test results of BNBT-6/epoxy 1-3 composite revealed that the composite showed two resonance peaks due to the coupling of lateral mode and thickness mode when the aspect ratio of the ceramic rod inside the composite was adjusted to around 1.45. A dual resonance frequency transducer was fabricated using this particular configuration. The 1-3 BNBT-6/epoxy composite used in the transducer has a L/H ratio of 1.45 with 0.40 mm thickness. A thin layer of air-dried silver paint was applied as the electrodes and coaxial wires were attached using silver epoxy. The composite was housed in a steel housing with air backing and had no front-face matching layer. The diameter of the plane transducer was 10.4 mm. The schematic structure of this transducer is shown in Figure 6.4.
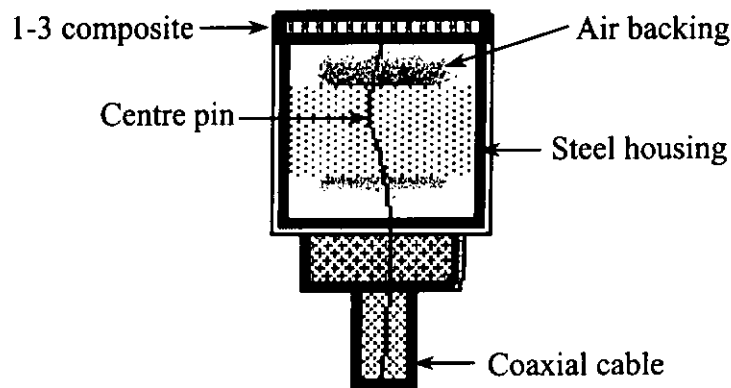
Figure 6.4 Schematic structure of the dual frequency transducer based on BNBT-6/epoxy 1-3 composite.

6.3.2   Fabrication of High Frequency Ultrasonic Transducers

To fabricate high frequency ultrasonic transducers, factors which will affect the transducer performance must be considered. This includes the electrical impedance and the selection of backing materials. Since common electronic equipments have a 50 ~ 80 Ω impedance, thus the transducer should match this impedance so that the energy transmission efficiency from the power supply to the transducer can be increased. Backing materials are quite essential for high frequency transducers. They can give a mechanical support to the very thin composite samples and absorb the ultrasonic waves reflection from the back of the housing. A piezoelectric disc will emit ultrasonic waves in both the forward and backward directions. If the disc does not have a backing with sufficient damping, reflection from the back will overlap with the echo from the front of the transducer and cause a long ring-down time. Therefore, a common way to reduce the

ringing is to use a soft polymer backing which greatly increases the absorption of the

reflected waves.

BNBT-6 fibre/epoxy 1-3 composites with various thicknesses were used to fabricate

high frequency ultrasonic transducers. A schematic diagram of the transducer is shown

in Figure 6.5. Chromium and gold was evaporated on the top surface of the transducer

and served as the ground terminal. The composite samples were polarized before they

were fabricated into transducers. UHF connectors were used as the housings and they

were filled with silicone rubber as the backing material with a composite sample

attached on the top surface. To form a spherical shaped surface, a steel ball with

diameter of 25 mm was used to press on the surface of the transducer for 24 hours. After

the silicone rubber has dried, the steel ball was removed and a focussed ultrasonic

transducer with slightly was produced.
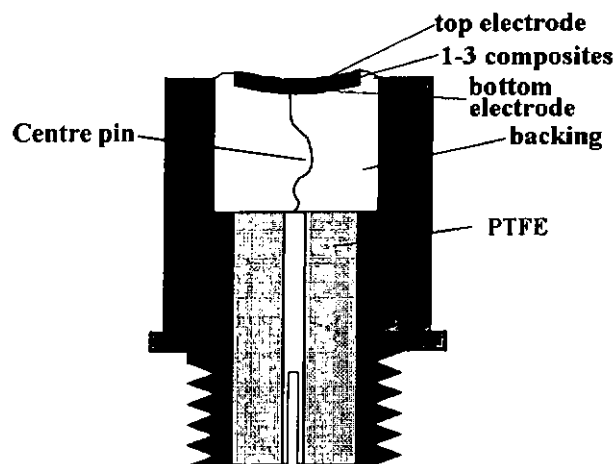
Figure 6.5 Schematic structure of a high frequency transducer based on BNBT-6
          fibre/epoxy 1-3 composite. (Li, 2001)

6.4 Results and Discussion

6.4.1 The Dual Frequency Transducer

The electrical impedance of the dual frequency transducer was measured using the HP

4294 impedance analyzer as shown in Figure 6.6. The impedance shows two main

resonances at around 3.8 MHz and 5.8 MHz, which is very similar to that of the

constituent composite.
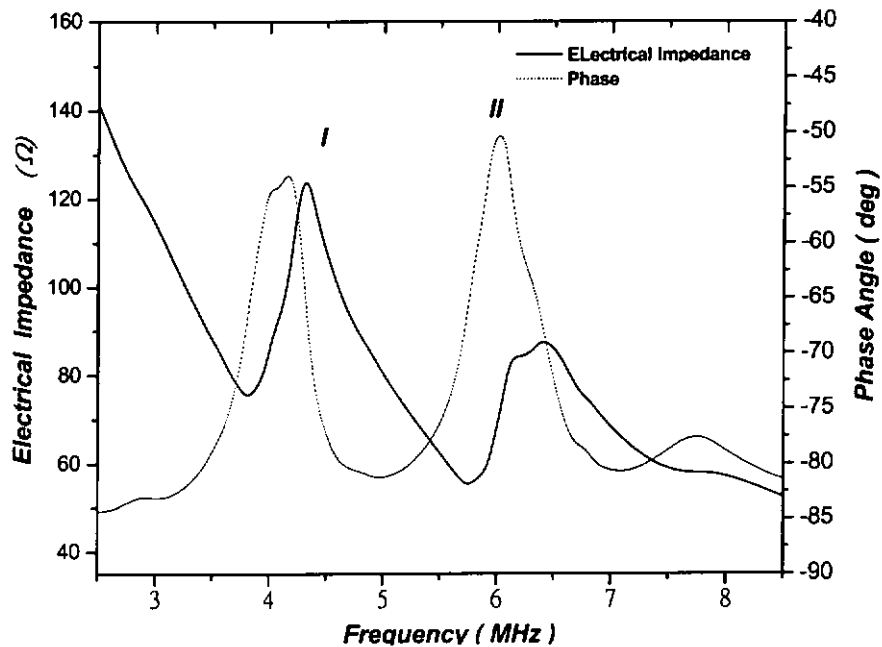
Figure 6.6 Electrical impedance of the dual frequency ultrasonic transducer based on
BNBT-6/epoxy 1-3 composite. (ϕ=0.52,diameter=10.4 mm, thickness=0.40
mm)

Pulse-echo characteristics of the transducer were measured using the setup shown in

Figure 6.1. The pulse-echo response was obtained by placing a flat stainless steel target

at a^2 / λ_c from the transducer. An HP pulse/function generator was used to emit a tone

burst of 3 cycles. The transducer was then driven at 3.8 and 5.8 MHz and an HP

Infiniium oscilloscope was used to record the echos at these two frequencies and the

frequency spectra of the transducer were measured using the FFT function. The pulse-

echo responses of the dual frequency transducer are shown in Figure 6.7. It was

observed that the transducer has long ring down times at both 3.8 and 5.8 MHz. Since air

backing was used in this transducer, the transducer is not very well damped.
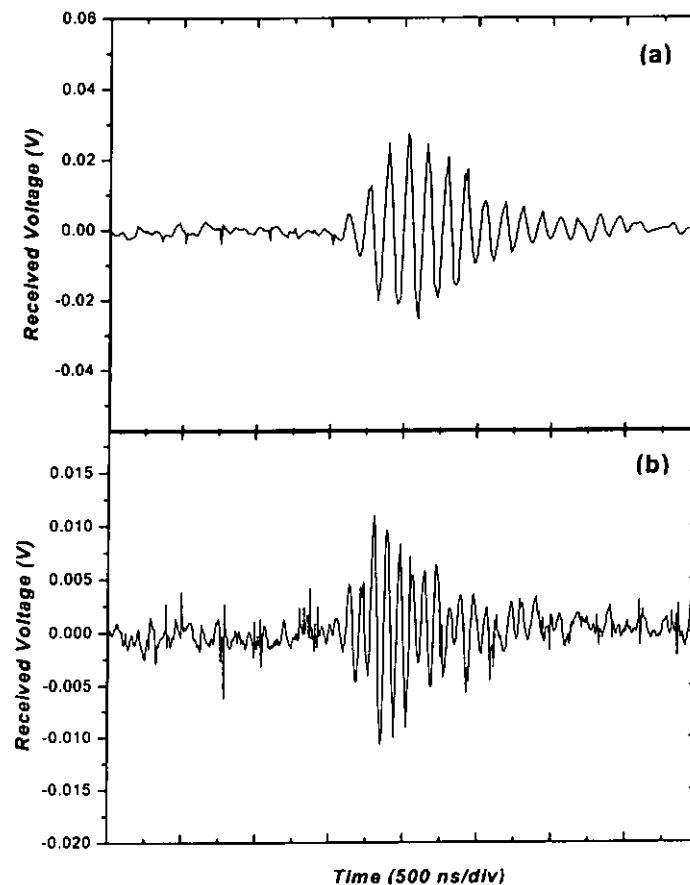
Figure 6.7 Pulse-echo response of the dual frequency transducer based on BNBT-
6/epoxy 1-3 composite at (a) 3.8 MHz; (b) 5.8 MHz.

The frequency spectrum of the dual frequency transducer is shown in Figure 6.8. The

frequency spectrum also exhibits two resonance peaks at around 3.9 MHz and 6.0 MHz,

respectively. Bandwidth of these two resonance peaks can be calculated from this

spectrum using Equation (6.2). The bandwidths of the two resonance peaks (at 3.9 MHz

and 6 MHz) are found to be 21% and 16%, respectively. The low bandwidth values

indicated that this dual frequency transducer was not well damped. Transducers for

diagnostic imaging should have bandwidths of at least 40%, therefore, the dual

frequency transducers based on BNBT-6/epoxy 1-3 composite needs to be further

improved before it can be used for imaging applications. It is possible to use a

nonuniform 1-3 composite disc to broaden the bandwidth of the transducer, but this will

be left for future work.
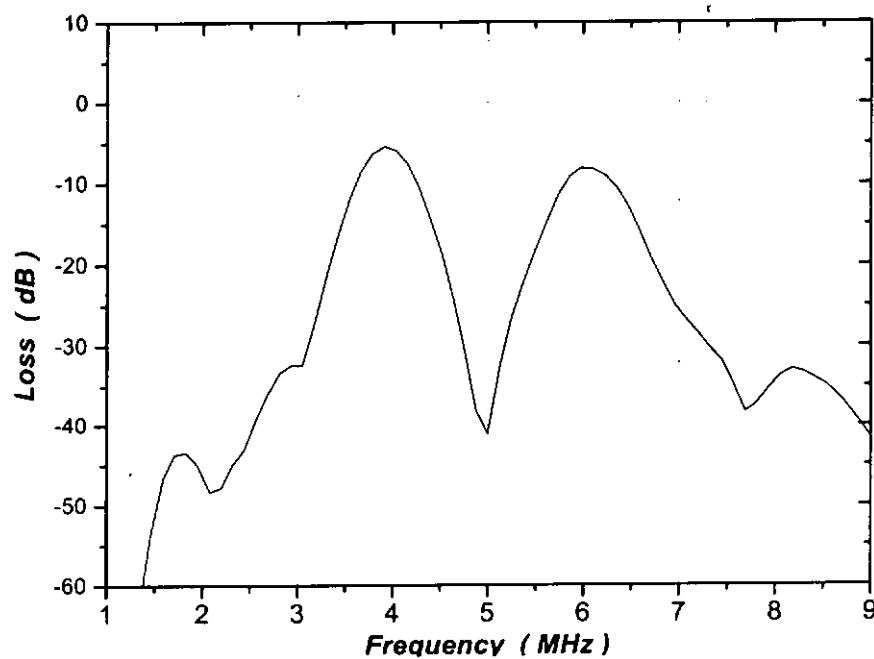
Figure 6.8 Frequency spectrum of the dual frequency ultrasonic transducer based on
BNBT-6/epoxy 1-3 composite.

The insertion loss was measured using the setup shown in Figure 6.3. An HP

pulse/function generator, which has a 50 Ω output impedance gated-sinewave signal

generator, was used to produce a tone burst of 20 cycles with an amplitude of 1V peak-

to-peak at the centre frequency of the transducer. Then the Infiniium oscilloscope

recorded the echo amplitude in the peak-to-peak mode. The measured insertion losses at

these two resonance frequencies are –25.9 dB and –30.7 dB, respectively. A summary of

the properties of this dual frequency transducer is shown in Table 6.1.

Table 6.1 Summary of the dual frequency transducer parameters.

	Resonance Peak I	Resonance Peak II
Resonance frequency f_r (MHz)	3.8	5.8
Electromechanical coupling coefficient k_t	0.51	0.48
Centre frequency f_c (MHz)	3.9	6.0
Electrical impedance at f_c, Z (Ω)	75.6	55.1
-6 dB Bandwidth (%)	21	16
Insertion loss (dB)	-25.9	-30.7

6.4.2 High Frequency Transducers

Both the sol-gel and VSSP fibre BNBT-6/epoxy 1-3 composites were used to develop high frequency transducers. The impedance spectra of these high frequency transducers are shown in Figures 6.9-6.12. Figures 6.9 and 6.10 are the impedance spectra of the transducers derived from the sol-gel fibres. The spectra show broad resonances which result in high thickness electromechanical coupling. For transducers derived from the VSSP fibres, the transducers show good resonance spectra below 10 MHz. However, when the resonance frequency of the transducer was increased up to around 27 MHz, the frequency resonance became rather weak as shown in Figure 6.12 and the impedance drops to ~20 Ω.

Pulse-echo responses of these transducers were recorded using the HP Infiniium oscilloscope. Figures 6.13-6.16 show the echo responses of the 1-3 composite transducers and Figures 6.17-6.20 show the corresponding frequency spectra obtained by FFT. Bandwidths were calculated using Equation (6.2). It was noticed that these high frequency transducers had much shorter ringdown time and broader bandwidth compared with the dual frequency transducer described in the previous section. Silicone rubber was used as the backing materials for the high frequency transducers, it can absorb the ultrasonic waves radiated into the backing and the transducers were well damped. In comparison, transducers derived from the sol-gel fibre possess broader bandwidth due to the higher thickness electromechanical coupling coefficient k_t.
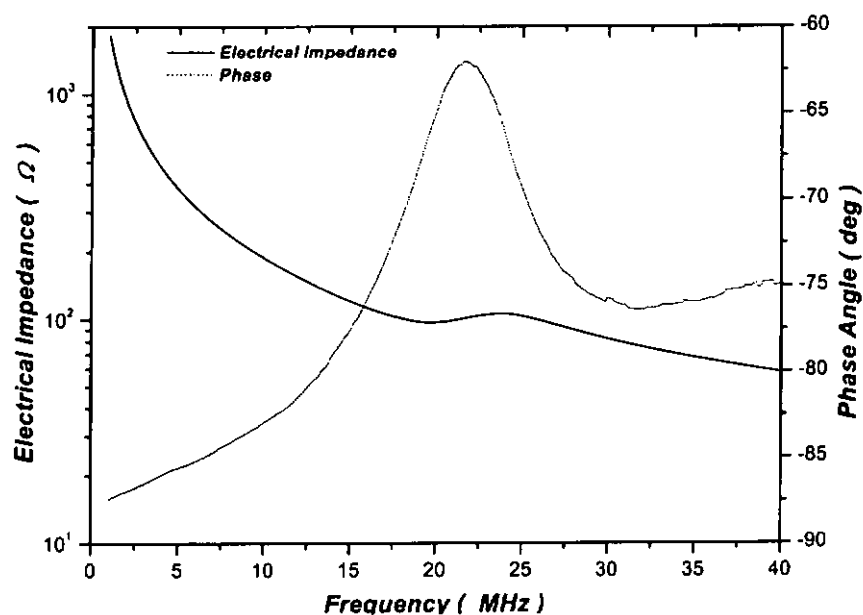
Figure 6.9 Electrical impedance and phase spectra of ultrasonic transducer S1 derived from BNBT-6 fibre/epoxy 1-3 composite. The active element of this transducer is a ϕ =0.39, 4.20mm diameter composite disc with BNBT-6 sol-gel fibres.

Figure 6.10 Electrical impedance and phase spectra of ultrasonic transducer S3 derived from BNBT-6 fibre/epoxy 1-3 composite. The active element of this transducer is a ϕ =0.30, 3.95 mm diameter composite disc with BNBT-6 sol-gel fibres.

Figure 6.11 Electrical impedance and phase spectra of ultrasonic transducer T6 derived from BNBT-6 fibre/epoxy 1-3 composite. The active element of this transducer is a ϕ =0.41, 7.50 mm diameter composite disc with BNBT-6 VSSP fibres.

Figure 6.12 Electrical impedance and phase spectra of ultrasonic transducer T2 derived from BNBT-6 fibre/epoxy 1-3 composite. The active element of this transducer is a ϕ =0.25, 7.30 mm diameter composite disc with BNBT-6 VSSP fibres.

Insertion losses of these transducers were measured using the technique presented in Section 6.2.2. The high insertion losses implied that the silicone rubber backing had absorbed substantial ultrasonic energy and lowered the efficiency of the transducers. Silicone rubber absorbed most of the ultrasonic energy radiated into the backing, so only approximately half of the input energy can be delivered in the forward direction. The overall properties of these high frequency ultrasonic transducers are summarized in Table 6.2. The setting on the Panametrics 5900 ultrasonic transducer analyzer for all the measurements were as follows: mode=P/E, rep rate=10 kHz, energy=2 μJ, damping=50 Ω, low pass filter=100 MHz, high pass filter=1 MHz, attenuation= 25 dB, gain=54 dB.

Figure 6.13 Pulse-echo response of ultrasonic transducer S1 derived from BNBT-6 fibre/epoxy 1-3 composite. The active element of this transducer is a ϕ =0.39, 4.20 mm diameter composite disc with BNBT-6 sol-gel fibres.
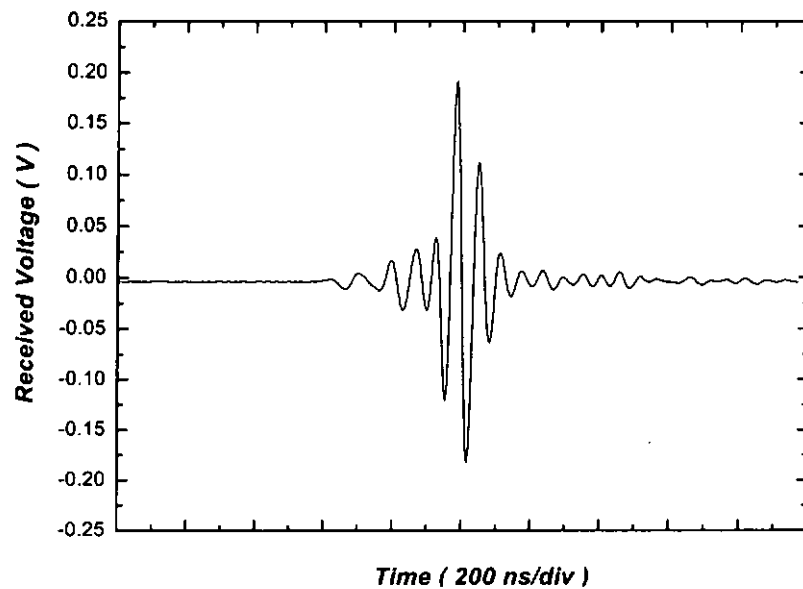
Figure 6.14 Pulse-echo response of ultrasonic transducer S3 derived from BNBT-6 fibre/epoxy 1-3 composite. The active element of this transducer is a ϕ =0.30, 3.95 mm diameter composite disc with BNBT-6 sol-gel fibres.
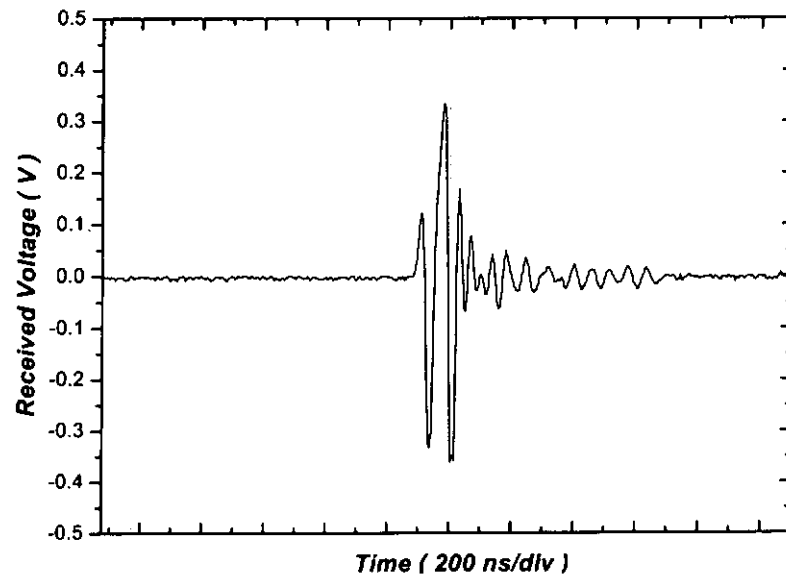
Figure 6.15 Pulse-echo response of ultrasonic transducer T6 derived from BNBT-6 fibre/epoxy 1-3 composite. The active element of this transducer is a ϕ =0.41, 7.50 mm diameter composite disc with BNBT-6 VSSP fibres.
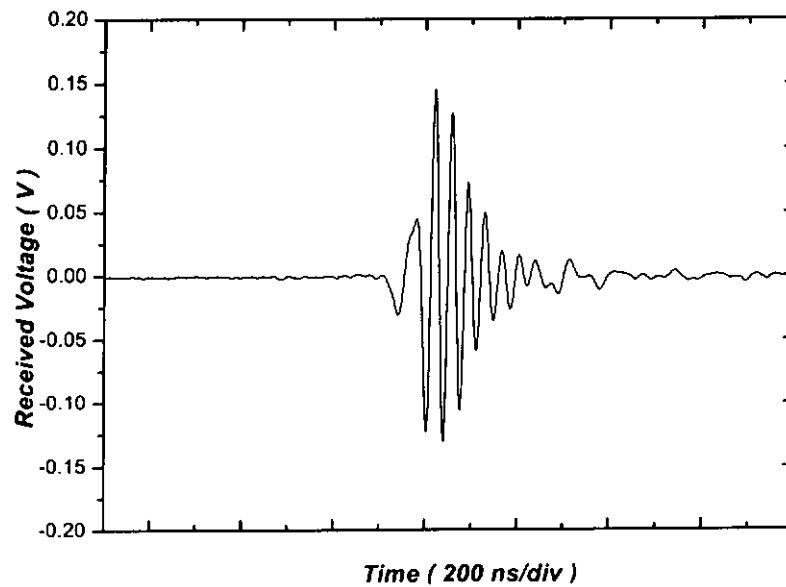
Figure 6.16 Pulse-echo response of ultrasonic transducer T2 derived from BNBT-6 fibre/epoxy 1-3 composite. The active element of this transducer is a ϕ =0.25, 7.30 mm diameter composite disc with BNBT-6 VSSP fibres.
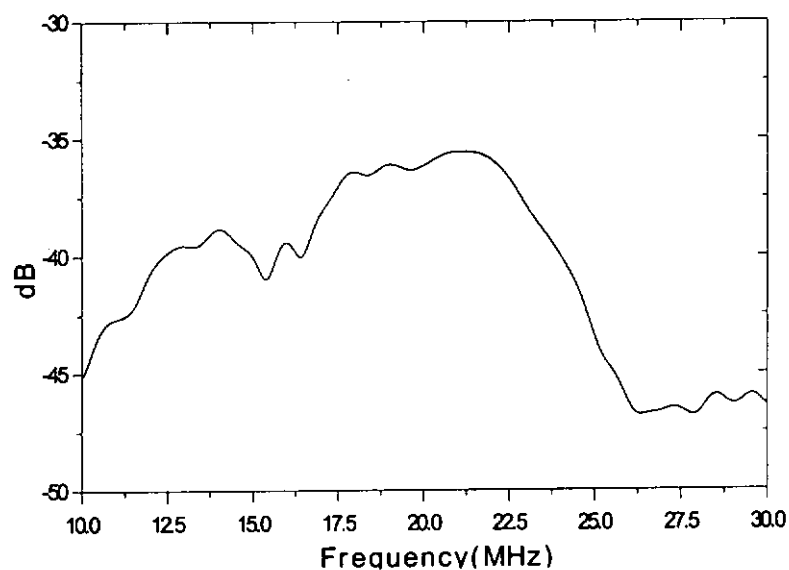
Figure 6.17 Frequency spectrum of ultrasonic transducer S1 derived from BNBT-6 fibre/epoxy 1-3 composite. The active element of this transducer is a ϕ =0.39, 4.20 mm diameter composite disc with BNBT-6 sol-gel fibres.
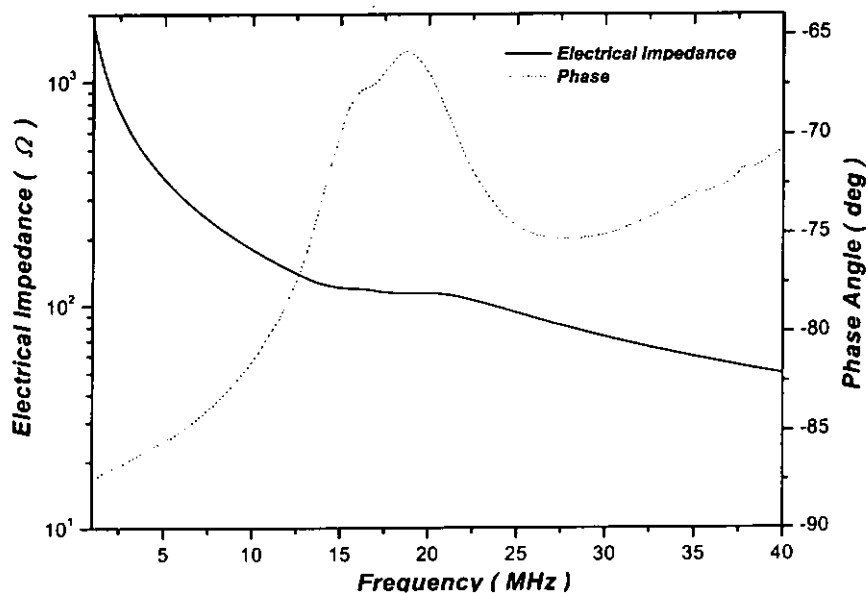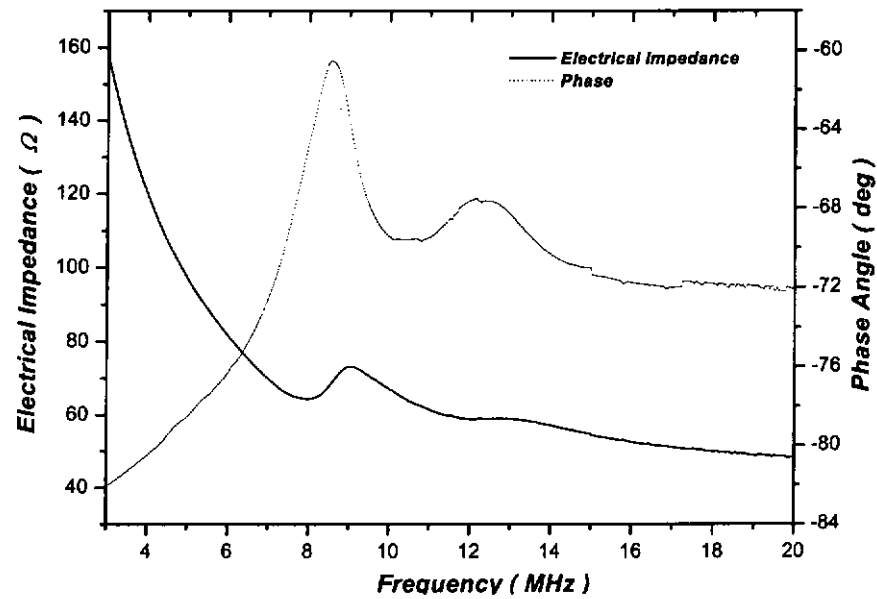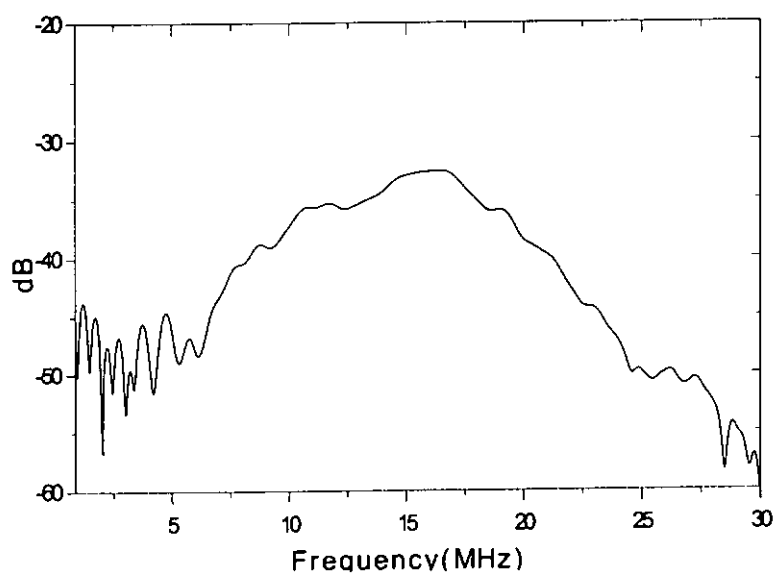

Figure 6.18 Frequency spectrum of ultrasonic transducer S3 derived from BNBT-6 fibre/epoxy 1-3 composite. The active element of this transducer is a ϕ =0.30, 3.95 mm diameter composite disc with BNBT-6 sol-gel fibres.
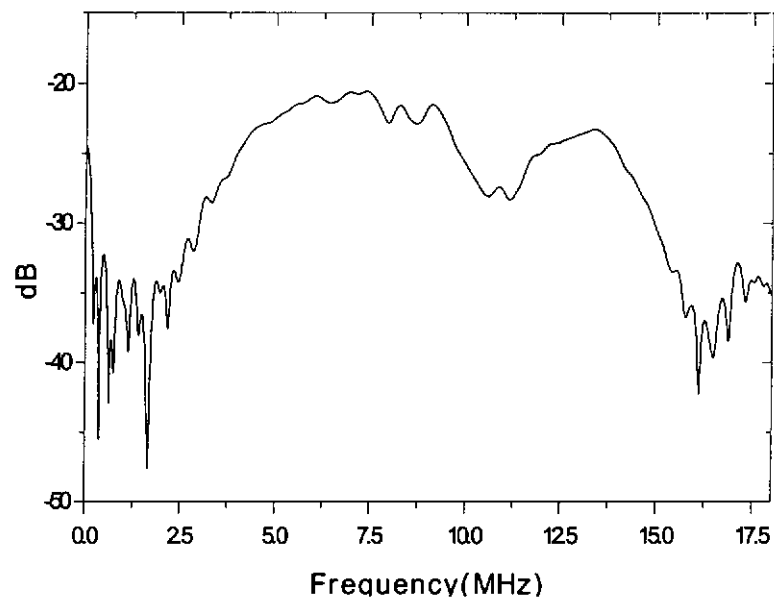
Figure 6.19 Frequency spectrum of ultrasonic transducer T6 derived from BNBT-6 fibre/epoxy 1-3 composite. The active element of this transducer is a ϕ =0.41, 7.50 mm diameter composite disc with BNBT-6 VSSP fibres.
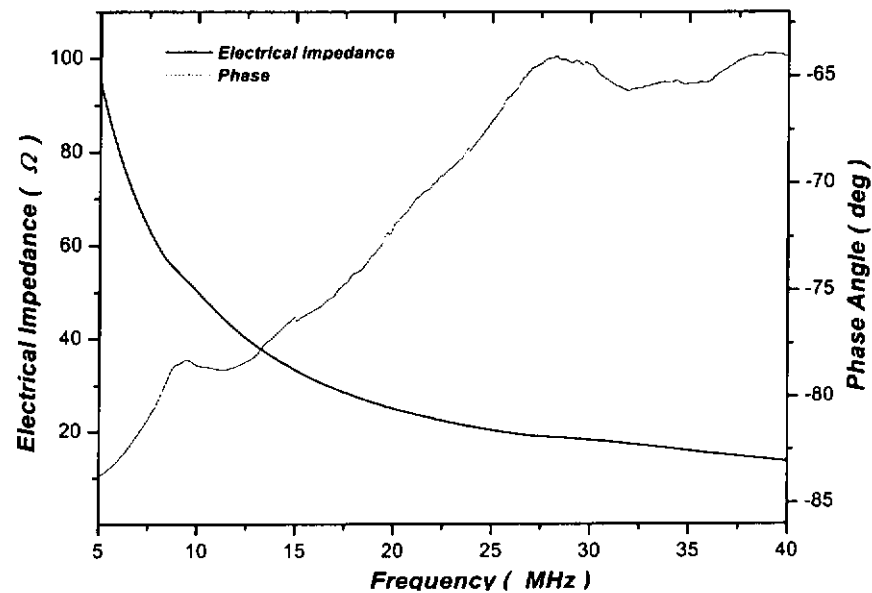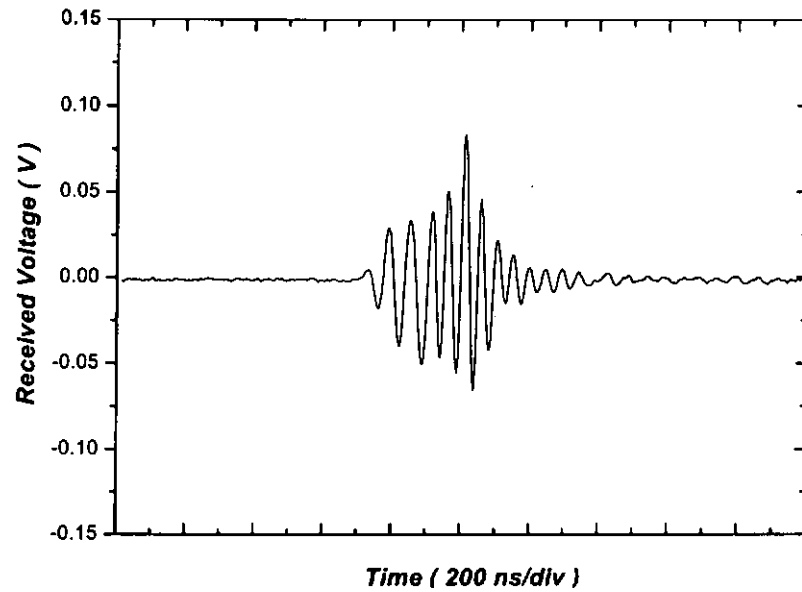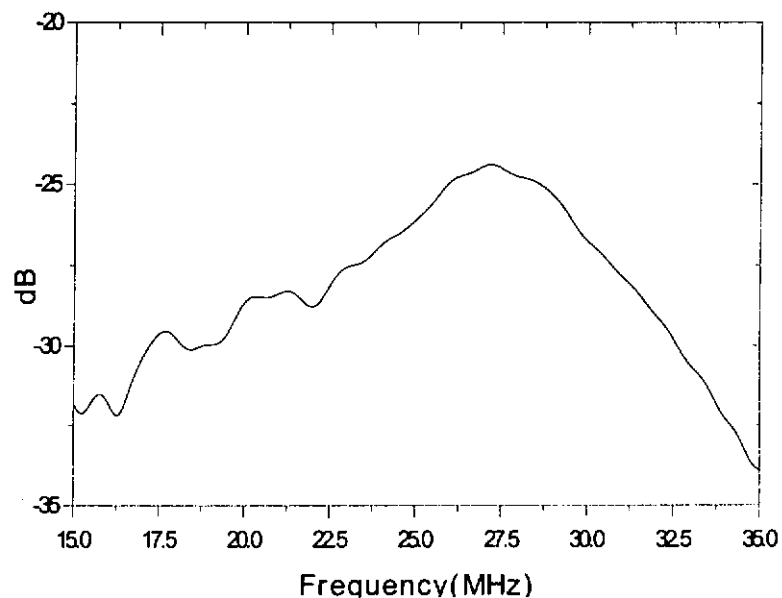

Figure 6.20 Frequency spectrum of ultrasonic transducer T2 derived from BNBT-6 fibre/epoxy 1-3 composite. The active element of this transducer is a ϕ =0.25, 7.30 mm diameter composite disc with BNBT-6 VSSP fibres.

Table 6.2 Summary of overall properties of ultrasonic transducers derived from the BNBT-6 fibre/epoxy 1-3 composites.

	S1	S3	T6	T2
Fibre type	Sol-gel	Sol-gel	VSSP	VSSP
Composite thickness (μm)	120	143	213	85
Composite diameter (mm)	4.20	3.95	7.50	7.30
Fibre volume fraction ϕ	0.39	0.30	0.41	0.25
Backing material	Silicone rubber	Silicone rubber	Silicone rubber	Silicone rubber
Resonance frequency f_r (MHz)	19.75	15.03	7.96	26.83
Electromechnical coupling coefficient k_t	0.61	0.71	0.52	0.49
Centre frequency f_c (MHz)	18.00	14.30	6.95	27.20
Electrical impedance at f_c (Ω)	101.2	124.0	70.3	19.1
−6dB Bandwidth (%)	34	80	88	22
Insertion loss (dB)	-36.5	-34.8	-32.8	-40.2

6.5 Summary

1-3 composites using both the BNBT-6 bulk ceramics and fibres were fabricated into ultrasonic transducers to evaluate their responses. Methods introduced by NEMA were employed to measure the transducer characteristics which include the pulse-echo response, bandwidth and insertion loss.

A dual frequency ultrasonic transducer was fabricated based on the coupling behavior of BNBT-6/epoxy 1-3 composites when the aspect ratio is closed to 1.45. The impedance spectrum of this transducer shows two strong resonances at 3.8 and 5.8 MHz with high electromechanical coupling coefficients. But since air backing was used in this transducer, it has a long ring-down time and low bandwidth values of 21% and 16% at the two resonance frequencies, respectively. The results implied that this transducer need to be further optimized before it can be used for imaging applications.

Both the sol-gel and VSSP fibre composites were assembled into transducers with silicone rubber backing. In comparison, transducers derived from the sol-gel fibre composites possess better properties. A 15 MHz transducer with about 30% sol-gel fibre loading can have a broad bandwidth of 80%. High insertion loss was found due to the absorption of ultrasonic energy in the silicone rubber backing.

CHAPTER VII

CONCLUSIONS AND RECOMMENDATIONS FOR FUTURE WORK

7.1 Conclusions

A lead-free piezoelectric ceramics, barium modified bismuth sodium titanate, with a formula of $0.94(Bi_{1/2}Na_{1/2})TiO_3-0.06BaTiO_3$ (BNBT-6), was fabricated and characterized in this work. The mixed-oxide method was used to fabricate bulk BNBT-6 ceramics. It is found that BNBT-6 ceramics had superior properties among lead-free piezoelectric ceramics. Ceramics sintered at 1150°C was observed to have an average grain size of 2 - 3 μm. BNBT-6 ceramics has a perovskite phase with a large remnant polarization P_r of 30.5 μC/cm^2 at room temperature. Dielectric measurement revealed that there existed two phase transitions in BNBT-6 ceramics at around 100°C and 285°C, respectively. Piezoelectric properties of this ceramics were measured using the IEEE standards. Electromechanical coupling coefficients k_p and k_t were found to be 0.25 and 0.46, respectively.

BNBT-6/epoxy 1-3 composites with various ceramic volume fractions were fabricated using the dice-and-fill technique. Epoxy was used as the polymer matrix for the 1-3 composites and its properties were determined using the ultrasonic immersion method.

The thickness electromechnical coupling coefficients k_t of the 1-3 composites increased to over 0.5. Ceramic volume fraction affects most of the composite properties. The modified series and parallel model was used to describe the composite properties with various ceramic volume fractions. The experimental results agree well with the theoretical modelling. Resonance characteristics of BNBT-6/epoxy 1-3 composites were studied by thinning down a composite sample with 0.52 ceramic volume fraction. Mode coupling theory was used to predict the resonance behavior. The experimental data have good agreement with the theoretical predictions. When the aspect ratio (width to thickness) of the ceramic rods is close to 1.45, the 1-3 composite shows two strong resonance modes due to the coupling of the thickness and lateral modes of the ceramic rods inside the composite.

BNBT-6 ceramic fibres for high frequency transducer applications were prepared through both the sol-gel and VSSP routes. By adjusting the heating rate and sintering ambience, dense and crack-free BNBT-6 ceramic fibres can be obtained. The diameters are ~ 80 µm and 300 µm for fibres made from the sol-gel and VSSP methods, respectively. Microstructure of the fibre was checked by SEM and an average grain size of 2 µm was observed. Some electrical properties of VSSP fibres can be measured by inserting the fibres into an epoxy matrix. Most of the properties of the VSSP fibres are comparable to bulk BNBT-6 ceramics.

BNBT-6 fibre/epoxy 1-3 composites were fabricated by encapsulating a fibre bundle into the epoxy matrix. Fibre volume fractions of the composites were obtained by

counting the fibre areas in SEM photos. Ferroelectric properties of the composites were measured. Polarization of the fibre composites was found to depend on the fibre volume fraction and their coercive field was slightly higher than that of the bulk ceramics due to clamping of the epoxy matrix. For sol-gel fibre composite with fibre volume fraction of ~ 0.3, the k_t was found to be nearly 0.7. The composites derived from VSSP fibres possess k_t values ranging from 0.45 to 0.52 which varied with different fibre volume fractions. A model introduced by R. Steinhausen was used to evaluate the elastic properties $s_{33,f}^E$ of a single fibre through the measured effective composite parameters. Furthermore, piezoelectric strain coefficient $d_{33,f}$ and dielectric permittivity $\varepsilon_{33,f}^T$ of a single BNBT-6 fibre could be determined by using the calculated $s_{33,f}^E$. Properties of the single fibre are close to those of the constituent BNBT-6 ceramics.

Two kinds of pulse-echo type ultrasonic transducers were fabricated based on the BNBT-6/epoxy 1-3 composites. Methods introduced by NEMA were used to evaluate the transducer characteristics. The first kind is a dual frequency transducer using a 1-3 composite with 1.45 ceramic aspect ratio. The transducer has two resonance frequencies at 3.8 MHz and 5.8 MHz. High frequency transducers were assembled using BNBT-6 fibre/epoxy 1-3 composites. These transducers have shorter ring-down time and higher operating frequencies ranging from 7 MHz to 27 MHz. In comparison, the transducers developed from sol-gel fibre composites possess better properties. A 15 MHz transducer with about 30 % sol-gel fibre loading can have a broad bandwidth of 80% and an insertion loss of −34.8 dB.

7.2 Recommendations For Future Work

Study of lead-free piezoelectric ceramic composites and their application in ultrasonic transducers is an original work. Some useful results have been obtained in this work, but there are still room for improvement, especially in varying the dopants to further enhance the ceramic properties.

7.2.1 Properties of BNBT-6 Bulk Ceramics

BNBT-6 ceramics has proved to possess excellent piezoelectric and ferroelectric properties among lead-free ceramics and some properties are even comparable to traditional PZT ceramics. However, the properties of the BNBT-6 ceramics are not stable, especially in the mechanical quality factor Q_M and relative permittivity ε. On one hand, their properties strongly depend on the sample fabrication process. Purity of the starting materials, pressure for dry pressing and even the grinding and polishing process will affect the properties of the final ceramics. On the other hand, aging exists in BNBT-6 ceramics. The piezoelectric properties of fully poled BNBT-6 ceramics will drop after some time even when placed at room temperature. In addition, there is a second order phase transition at around 100°C in BNBT-6 ceramics. All the piezoelectric and ferroelectric effects will disappear when the temperature goes above this transition point. Thus, this ceramics is quite easy to depolarize and cannot be used in a high temperature environment.

Based on the above discussion, the BNBT-6 ceramics should be improved to overcome the above mentioned drawbacks. Some high valent ions such as Nb^{5+} can be considered to dope for A site substitution to suppress the activity of Na^+. This may enhance the Q_M factor and increase the phase transition temperature of this ceramics without affecting other properties.

7.2.2 BNBT-6 Fibre Fabrication and Properties

Two different techniques were used in this work to fabricate BNBT-6 ceramic fibres. But the quality of the fibres still needs to be improved. In the sol-gel route, selection of the precursors is a critical step for gel viscosity control, which will affect the fibre quality. A high viscosity bismuth precursor was used in this work, which resulted in the difficulty in fibre extrusion and high organic content in the gel fibres. Some bismuth ethoxides with low viscosity such as bismuth 2-methoxyethanol and bismuth triethoxide can be used as the precursors to improve the fibre properties. But the cost for using ethoxides is high. Therefore, to find suitable bismuth precursor has become the most important step for obtaining better quality fibres through the sol-gel route. For the VSSP technique, if the particle size of the starting powder can be reduced, thinner fibre can be fabricated. Moreover, different binders may be tried to increase the powder loading fractions of the green fibres so the density of the sintered fibres can be improved.

7.2.3 Composite Transducers

The 1-3 composites derived from BNBT-6 bulk ceramics and the fibres have been assembled into ultrasonic transducers. By changing the backing materials, the pulse-echo characteristics of the transducers could be improved. Fibre composites with different volume fractions will be used in transducer applications. Higher operation frequencies, shorter ring-down time and broader bandwidth are the aims in the future transducer work.

Although the backing is important for reducing the ring-down time of transducers, but the expense is the lost of approximately half of the input ultrasonic energy. Therefore, it is also important to have a front-face matching layer. One or more layers can be used between the transducer material (e.g. piezoelectric ceramics or composites) and the load (water or human tissues). This will broaden the frequency response characteristics, giving higher efficiency than transducers only damped by a matched backing. Usually, layers with a thickness of a quarter of the acoustic wavelength $\lambda/4$ are used to improve the transmission and bandwidth properties of the transducers. The advantages of quarter wave matching layers have been established in optical, RF, and μ-wave devices, as well as in ultrasonic transducers (Souquet, 1979).

Kossoff made an assessment of $\lambda/4$ matching layer of the transducers (Kossoff, 1966). For example, when a matching layer with an intermediate impedance z and a thickness

of λ/4 was bonded to the front surface of the transducer, an improved beam transmission was observed. The theoretical optimum value of z was based on the equation,

$$z = \sqrt{z_T z_W}$$ (7.1)

where z_T is the acoustic impedance of the transducer material and z_W is the acoustic impedance of water or human tissues. More completed theoretical and experimental analysis of the transducer with multiple matching layers have also been proposed (Desilets, 1978).

If the matching layer is properly selected, transducers could have broad bandwidth even with air backing. Parylene is a commonly used front-matching layer material for high frequency transducers. It has an acoustic impedance z of 2.85 Mralyl. The use of proper matching layers was not included in this work and this will be left for future work.

REFERENCES

Auld, B.A. *Acoustic Fields and Waves in Solids*, Vol. I and II, John Wiley and Sons, (1973)

Auld, B.A. "High frequency piezoelectric resonators". *Proceedings of the 10th IEEE International Symposium on applications of Ferroelectrics*, Vol. 2, pp.288-295 (1996)

Berlincourt, D.A., Curran, D.R. and Jaffe, H. "Piezoelectric and piezomagnetic materials and their function in transducers". Physical Acoustics, Vol. 1, Part A, Academic Press, New York, pp.169-270 (1964)

Bowen, L.J., Gentilman, R.L. Pham, H.T., Fiore, D.F. and French, K.W. "Injection molded fine-scale piezoelectric composite transducers". *Proceedings of 1993 IEEE Ultrasonics Symposium*, pp.499-503 (1993)

Bui, T., Chan, H. L. W. and Unsworth, J. "A multifrequency composite ultrasonic transducer system". *Proceedings of 1988 IEEE Ultrasonics Symposium*, pp.627-630 (1988)

Chan, H.L.W. "Piezoelectric ceramic/polymer 1-3 composites for ultrasonic transducer applications". *Ph. D. Thesis*, Macquarie University, (1987)

Chan, H. L. W. and Unsworth, J. "Effect of ceramic anisotropy on the properties of ceramic/polymer piezoelectric composites". *Proceedings of 1987 IEEE Ultrasonics Symposium*, pp.651-654 (1987)

Chan, H. L. W. and Unsworth, J. "Simple model for piezoelectric ceramic/polymer 1-3 composites used in ultrasonic transducer applications". *IEEE Transactions on Ultrasonics, Ferroelectrics and Frequency Control.* Vol. 36, pp.434-441 (1989)

Chan, H. L. W. and Guy, I.L. "Piezoelectric ceramic/polymer composites for high frequency applications". *Key Engineering Materials,* Trans. Tech. Publications, Switzerland, Vol. 92-93, pp.275-300 (1994)

Chu, B.J., Chen, D. R., Li, G.R. and Yin, Q.R. "Electrical properties of $Na_{1/2}Ba_{1/2}TiO_3$-$BaTiO_3$ ceramics". *Journal of the European Ceramic Society*, Vol. 22, pp.2115-2121 (2002)

Desilets, C. S., Fraser, J.D. and Kino, G.S. "The design of efficient broad-band piezoelectric transducers". *IEEE Transaction on Sonic and Ultrasonics*, Vol. SU-25, pp.115-125 (1978)

Fiore, D., Gentilman, R., Pham, H., Serwatka, W., McGuire, P. and Bowen, L. "Recent developments in 1-3 piezocomposite transducer fabrication", *Proceedings of the 10th IEEE International Symposium on Applications of Ferroelectrics*, Vol. 2, pp.531-534 (1996)

Foster, F.S., Ryan, L.K. and Turnbull, D.H. "Characterization of lead zirconate titanate ceramics for use in miniature high-frequency transducers". *IEEE Transactions on UFFC*, Vol. 38, pp.446-453 (1991)

Glaubitt, W., Sporn, D. and Rainer, J. "Sol-gel processing of functional and structural ceramic oxide fibers". *Journal of the Sol-gel Science and Technology*, Vol.8, pp.29-33 (1997)

Gururaja, T.R., Schulze, W.A., Shrout, T.R. Safari, A., Webster, L. and Cross, L.E. "High frequency applications of PZT/polymer composite materials". *Ferroelectrics*, Vol. 39, pp.1245-1248 (1981)

Gururaja, T.R. "Piezoelectric composite materials for ultrasonic transducer applications". *Ph. D. Thesis*, The Pennsylvania State University, (1984)

Gururaja, T. R., Schulze, W. A., Cross, L.E., Newnham, R.E., Auld, B.A. and Wang, Y. J. "Piezoelectric composite materials for ultrasonic transducer applications". *IEEE Transactions on Sonics and Ultrasonics*, Vol. SU-32 [4], pp.481-498 (1985)

Gururaja, T. R., Schulze, W. A., Cross, L.E. and Newnham, R.E. "Piezoelectric composite materials for ultrasonic transducer applications. Part II: Evaluation of ultrasonic medical applications". *IEEE Transactions on Sonics and Ultrasonics*, Vol. SU-32, pp.499-523 (1985)

Hartmann, B. "Ultrasonic measurements". *Method of Experimental Physics*, Vol. 16C, Academic Press, NY, USA, pp.59-90 (1980)

Hayward, G. and Hossack, J.A. "Unidimensional modeling of 1-3 composite transducers". *Journal of the Acoustical Society of America*, Vol. 88[2], pp.599-608 (1990)

Herabut, A. and Safari A. "Processing and electromechanical properties of $(Bi_{0.5}Na_{0.5})_{(1-1.5x)}La_xTiO_3$ ceramic". *Journal of the American Ceramic Society*, Vol. 80[11], pp.2954-2958 (1997)

Hossack, J.A. and Hayward, G. "Finite element analysis of 1-3 composite transducers". *IEEE Transactions on Ultrasonics, Ferroelectricc and Frequency Control*, Vol. 38[6], pp.618-629 (1991)

IEEE standard on piezoelectricity, ANSI/IEEE Std. 176-1987

IEC Standard, "Guide to dynamic measurements of piezoelectric ceramics with high electromechanical coupling", (1964)

Ikeda, T. "Fundamentals of piezoelectricity", Oxford University Press-Tokyo, pp.119-121 (1990)

Jadidian, B., Janas, V. and Safari, A. "Development of fine scale piezoelectric ceramic/polymer composite via incorporation of fine PZT fibers". *Proceeding of IEEE 10th international symposium on the application of ferroelectrics*, Vol. 1, pp.31-34 (1996)

Jaffe, B, Cook, W.R.Jr. and Jaffe, H. "The piezoelectric effect in ceramics". In Roberts, J.P. and Popper, P., eds., *Piezoelectric ceramics*, Academic Press, London and New York, pp.7-23 (1971)

Janas, V. F. and Safari, A. "Overview of fine-scale piezoelectric ceramic/polymer composite processing", *Journal of the American Ceramic Society*, Vol. 78[11], pp.2945-2955 (1995)

Klicker, K.A., Bigger, J.V. and Newnham, R.E. "Composites of PZT and epoxy for hydrostatic transducer applications". *Journal of the American Ceramic Society*, Vol. 64, pp.5-8 (1981)

Kossoff, G. "The effects of backing and matching on the performance of piezoelectric ceramic transducers". *IEEE Transaction on Sonic and Ultrasonics*, Vol. SU-13, pp.20-30 (1966)

Kwok, K.W. "Piezoelectric ceramic/piezoelectric polymer composites for ultrasonic applications". *Ph. D. Thesis*, The Hong Kong Polytechnic University, (1997)

Kwok, K.W., Chan, H.L.W. and Choy, C.L. "Evaluation of the material parameters of piezoelectric materials by various methods". *IEEE Transactions on Ultrasonics, Ferroelectrics and Frequency Control*, Vol. 44, pp.733-742 (1997)

Kwok, K.W., Chan, H.L.W. and Choy, C.L. "Lead zirconate titanate/poly(vinylidene fluoride-trifluoroethylene) 1-3 composites for ultrasonic transducer applications". *IEEE Transactions on Ultrasonics, Ferroelectrics and Frequency Control*. Vol. 46, pp.626-637 (1999)

Li, K., Lam, K.H., Wang, D.Y., Chan, H.L.W. and Choy, C.L. "Studies of Li, Nb and Mn doped PZT ceramic fibres and ceramic fibre/epoxy 1-3 composites". *Proceeding of 4th Pacific Rim International Conference on Advanced Materials and Processing (PRCIM4)*, Vol. 2, pp.1583-1586, (2001)

Li, K., Wang, D.Y., Lam, K.H., Chan, H.L.W. and Choy, C.L. "Samarium and manganese doped lead titanate ceramic fibre/epoxy 1-3 composites for high frequency transducer applications". *Proceeding of 4th Pacific Rim International Conference on Advanced Materials and Processing (PRCIM4)*, Vol. 2, pp.1603-1606, (2001)

Lubitz, K., Wolff, A. and Peru, G. "Microstructure technology". *Proceedings of 1993 IEEE Ultrasonics Symposium*, pp.515-524 (1993)

Lukacs, M., Sayer, M. and Foster, F.S. "Single element and linear array PZT ultrasound biomicroscopy transducers". *Proceedings of the IEEE Symposium on UFFC*, Toronto, Canada, Vol. 2 pp.1709-1712 (1997)

Lukacs, M., Sayer, M. and Foster, F.S. "Single element high frequency (>50 MHz) PZT sol-gel composite ultrasound transducers". *IEEE Transactions on Ultrasonics, Ferroelectrics, and Frequency Control*, Vol. 47, pp.148-159 (2000)

Meyer, R.J.Jr. "Fabrication of perovskite lead zirconate titanate and barium strontium titanate fibers using sol-gel technology". *MSc Thesis*, The Pennsylvania State University, (1995)

Meyer, R. J. Jr, Shrout, T. R. and Yoshikawa, S. "Development of ultra-fine scale piezoelectric fibres for use in high frequency 1-3 transducers". *Proceedings of the 10th IEEE International Symposium on Applications of Ferroelectrics*, Vol. 2, pp.547-550 (1996)

Meyer, R.J. Jr. "High frequency (15-70MHz) 1-3 PZT fiber/polymer composites: fabrication and characterization". *Ph.D. Thesis*, The Pennsylvania State University, (1998)

Mitsui, T., Tatsuzaki, I., and Nakamura, E. "An Introduction to the Physics of Ferroelectrics". London: Gordon and Breach Science Publishers, Ltd, pp.1-7 (1976)

Nagata, H. and Takenaka, T. "$(Bi_{1/2}Na_{1/2})$ TiO_3-based non-lead piezoelectric ceramics". *Journal of Korean Physics Society*, Vol. 32, pp.1298-1300 (1998)

Nagata, H. and Takenaka, T. "Additive effects on electrical properties of $(Bi_{1/2}Na_{1/2})TiO_3$ ferroelectric ceramics". *Journal of the European Ceramic Society*, Vol. 21, pp.1299-1302 (2001)

NEMA Standard methods for testing single –element pulse-echo ultrasonic transducers, *Journal of ultrasound in medicine*, Vol. 1, (1982)

Newnham, R.E., Skinner, D.P. and Cross, L.E. "Connectivity and piezoelectric-pyroelectric composites". *Materials Research Bulletin*, Vol. 13, pp.525-536 (1978)

Nowicki, A., Kycia, K., Iien, T. D., Gaji, O. and Klciber, M. "Numerical calculations of the acoustic properties of the 1-3 composite transducers for medical applications". *IEEE Ultrasonics Symposium*, pp.1041-1044 (1995)

Nye, J.F. *Phycical properties of crystals*, Oxford at the Clarenoon Press, pp.322 (1967)

Onoe, M., Tiersten, H. F. and Meitzler, A.H. "Shift in the location of resonance frequencies caused by large electromechanical coupling in thickness-mode resonators". *Journal of the Acoustical Society of America*, Vol.35, pp.36-42 (1963)

Or, S.W. "High frequency transducer for ultrasonic bonding". *Ph. D. Thesis*, The Hong Kong Polytechnic University, (2001)

Pardo, L., Castro, A., Millan, P., Alemany, C., Jimenez, R. and Jimenez, B. "$(Bi_3TiNbO_9)_x(SrBi_2Nb_2O_9)_{1-x}$ Aurivillius type structure piezoelectric ceramics obtained from mechanochemically activated oxides". *Acta Materialia*, Vol. 48, pp.2421-2428 (2000)

Read, B.E. and Dean, G.D. "The ultrasonic immersion method". *The Determination of Dynamic Properties of Polymers and Composite*, Adam Hilger, Bristol, UK, (1978)

Subbarao, E.C. "Ferroelectricity in mixed bismuth oxides with layer-type structure". *Journal of the American Ceramic Society*, Vol. 45[4], pp.166-169 (1962)

Sawyer, C.B. and Tower, C.H. "Rochelle salt as a dielectric". *Physical Review*, Vol. 35, pp.269-273 (1930)

Shung, K.K., Smith, M.B. and Tsui, B. "Principles of medical imaging". Academic Press, Inc., San Diego, CA, USA, (1992)

Shung, K.K. and Zipparo, M. "Ultrasonic Transducers and Arrays". *IEEE Engineering in Medicine and Biology*, Nov-Dec. pp.20-30 (1996)

Smith, S. W., Davidsen, R. E., Emery, C. D., Goldberg, R. L., Light, E. D., and Mills, D. M. "2-D array transducers for medical ultrasound at Duke University: 1996".

Proceedings of the 10th IEEE International Symposium on Applications of Ferroelectrics, Vol. 1, pp.5-11 (1996)

Smith, W.A., Shaulov, A. and Auld, B.A. "Tailoring the properties of composite piezoelectric materials for medical ultrasonic transducers". *Proceedings of 1985 IEEE Ultrasonics Symposium*, pp.642-647 (1985)

Smith, W.A. "Composite piezoelectric materials for medical ultrasonic imaging transducer-A review". *Proceeding of IEEE 6th international symposium on the application of ferroelectrics, Bethlehem,PA*, pp.249-56 (1986)

Smith, W.A. and Auld, B.A. "Modeling 1-3 composite piezoelectrics: thickeess-mode oscillations". *IEEE Transactions on Ultrasonics, Ferroelectrics, and Frequency Control*, Vol. 38, pp.40-47 (1991)

Smith, W. A. "New opportunities in ultrasonic transducers emerging from innovations in piezoelectric materials". *New Developments in Ultrasonic Transducers and Transducer Systems, SPIE Proceedings*, Vol. 1773, San Diego, CA, pp.3-26 (1992)

Smolenskii, G.A., Isupov, V.A., Agranovskaya, A.I. and Krainik, N.N. "New ferroelectrics of complex composition". *Soviet Physics. –Solid State (Engl. Transl)*, Vol. 2[11] pp.2651-2654 (1961)

Smolenskii, G.A., Isupov, V.A., Agranovskaya, A.I. "Ferroelectric of the oxygen-octahedral type with layer-structure". *Soviet Physics. –Solid State*, Vol. 3, pp.651-655 (1962)

Souquet, J., Defranould, P. and Desbois, J. "Design of low-loss wide-band ultrasonic transducers for noninvasive medical application". *IEEE Transaction on Sonic and Ultrasonics*, Vol. SU-26, pp.75-81 (1979)

Steinhausen, R., Hauke, T., Seifert, W., Beige, H., Watzka, W., Seifert, S., Sporn, D., Starke, S. and Schonecker, A. "Finescaled piezoelectric 1-3 composites: properties and modeling". *Journal of European Ceramic Society*, Vol. 19, pp.1289-1293 (1999)

Steinhausen, R., Hauke, T., Beige, H., Watzka, W., Lange, U., Sporn, D., Gebhardt, S. and Schonecker, A. "Proerties of fine scale piezoelectric PZT fibers with different Zr content". *Journal of European Ceramic Society*, Vol. 21, pp.1459-1462 (2001)

Steinhausen, R., Hauke, T., Seifert, W., Beige, H., Lange, U., Sporn, D., Gebhardt, S. and Schonecker, A. "A new method for the determination of elastic properties of the thin piezoelectric PZT fibers". *Proceedings of the 10th International Meeting on Ferroelectricity, (IMF) 2001 - Madrid, Spain - special edition of Ferroelectrics*, (2001)

Takenaka, T., Maruyama, K. and Sakata, K. "$(Bi_{1/2}Na_{1/2})TiO_3$-$BaTiO_3$ system for lead-free piezoelectric ceramics". *Japanese Journal of Applied Physics*, Vol. 30, pp.2236-2239 (1991)

Takenaka, T. and Nagata, H. " Present status of non-Lead-Based piezoelectric ceramics". *Ceramic Society of Japan*, Vol. 1, pp.57-63 (1999)

Tang, K.W. "Piezoelectric actuators for ultrasonic wire bonding applications". *MPhil. Thesis*, The Hong Kong Polytechnic University, (2001)

Taunaumang, H. "Electromechanical properties of 1-3 piezoelectric ceramic/piezoelectric polymer composites". *MSc Thesis*, Macquarie University, (1993)

Taunaumang, H., Guy, I. L. and Chan, H. L. W. "Electromechanical properties of 1-3 piezoelectric ceramic/piezoelectric polymer composites". *Journal of Applied Physics*, Vol. 76[1], pp.484-489 (1994)

Turcu, S., Jadidian, B., Danforth, S.C. and Safari, A. "Novel piezoelectric ceramic/polymer composite transducers". *International Joint Conference on the Applications of Ferroelectrics (IFFF)* (2002)

Wells, P.N.T. "Biomedical Ultrasonics". Academic Press-London, (1977)

Xu, B.M., Moses, P., Pai, N.G. and Cross, L.E. "Charge release of lanthanum-doped lead zirconate titanate stannate antiferroelelctric thin films", *Applied Physics Letters*, Vol. 72[5], pp.593-595 (1998)

Xu, B.M., Pai, N.G., Wang, Q.M. and Cross, L.E. "Antiferroelectric thin and thick films for high-strain microactuators". *Integrated Ferroelectrics*, Vol. 22, pp.545-557 (1998)

Xu, Y.H. "Introduction: Characteristics of ferroelectrics". *Ferroelectrics Materials and Their Applications*, North-Holland, Elsevier Science Publishers, Amsterdam and New York, pp.1-36 (1991)

Xu, Y.H. "Perovskite-type ferroelectrics: part I". *Ferroelectrics Materials and Their Applications,* North-Holland, Elsevier Science Publishers, Amsterdam and New York, pp.101-162 (1991)

Xu, Y.H. "Other ferroelectric crystal materials". *Ferroelectrics Materials and Their Applications,* North-Holland, Elsevier Science Publishers, Amsterdam and New York, pp.301-327 (1991)

Yoshikawa, S., Selvaraj, U., Brooks, K. and Kurtz, S. "Piezoelectric PZT tubes and fibers for passive vibration damping", *Proceeding of 8th IEEE International Symposium on Applied Ferroelectrics.* pp.269-272 (1992)

Zipparo, M.J., Shung, K.K. and Shrout, T.R. "Piezocaramics for high frequency (20-100 MHz) transducers and arrays". *IEEE Ultrasonics Symposium,* pp.1663-1667 (1997)

LIST OF PUBLICATIONS

Journal Papers

1. <u>D.Y. Wang</u> and H. L. W. Chan, "A Dual Frequency Transducer Based on BNBT-6/epoxy 1-3 Composite". *Materials Science and Engineering: B* (in press)

2. J. S. Zhu, <u>D. Y. Wang</u>, H. L. W. Chan, K. H. Wong and C. L. Choy, "Ferroelectric Properties of $Bi_{3.25}La_{0.75}Ti_3O_{12}$-$SrBi_4Ti_4O_{15}$ Thin Films Fabricated by Pulsed Laser Deposition". *Thin Solid Films* (in press)

3. J. S. Zhu, <u>D. Y. Wang</u>, D. Su, X. M. Lu, H. X. Qin, Y. N. Wang, H. L. W. Chan and C. L. Choy, "La-doped Effect on the Ferroelectric Properties of $Bi_4Ti_3O_{12}$-$SrBi_4Ti_4O_{15}$ Thin Film Fabricated by Pulsed Laser Deposition". *Journal of Applied Physics* (in press)

Conference Paper

4. <u>D.Y. Wang</u>, K. Li, H. L. W. Chan and C. L. Choy, "Characterization of $0.94(Bi_{0.5}Na_{0.5})TiO_3$-$0.06BaTiO_3$ (BNBT-6) Lead-free Ceramics and BNBT-6/epoxy 1-3 Composites". *Proceeding of Fourth Pacific Rim International Conference on Advanced Materials and Processing (PRCIM4)*, Vol. 2, pp.2845-2849 (2001)

5. K. Li, <u>D.Y. Wang</u>, K. H. Lam, H. L. W. Chan and C. L. Choy "Samarium and Manganese Doped Titanate Ceramic Fibre/epoxy 1-3 Composites for High Frequency Transducer Applications". *Proceeding of Fourth Pacific Rim International Conference on Advanced Materials and Processing (PRCIM4)*, Vol. 2, pp1603-1606 (2001)

APPENDIX I

CHARACTERIZATION OF BNBT-6 CERAMICS BY THE RESONANCE TECHNIQUE

In Appendix I, a resonance technique described in IEEE standards (ANSI/IEEE Std. 176-1987) was used to determine the material parameters of BNBT-6 ceramics. Five BNBT-6 ceramic samples with specific geometry shown in Figure 2.14 were used in the measurements. In the resonance method, some specific resonance modes are excited by applying an a.c. electric field to a piezoelectric material of specific shape, aspect ratio and polarization direction. Impedance spectra of these geometries were recorded using the HP 4292A impedance/gain phase analyzer and the corresponding resonance and anti-resonance frequencies of different resonance modes were used to determined the electromechnical coefficients. The elastic, piezoelectric and dielectric matrices for the BNBT-6 ceramics are shown in Figure A 1.1.

A 1.1 Constitutive Equations and Matrix Notation

The fundamental resonance mode of the five samples with different geometries can be described by sets of constitutive equations, which are related by the intrinsic variable stress T and electric field E with extrinsic variables strain S and electric displacement D. (ANSI/IEEE Std. 176-1987). Generally, two of the variables (one electrical and one mechanical) are considered as independent variables in writing the constitutive

equations for a system while the other two are dependent variables. For example, if the

components of stress T and electric displacement D are taken as dependent variables, the

equations with mechanical and electrical boundary conditions are given by: (ANSI/IEEE

Std. 176-1987)

$$T_{ij} = c^E_{ijkl} S_{kl} - e_{kij} E_k \qquad \text{(A1.1)}$$

$$D_i = e_{ikl} S_{kl} + \varepsilon^S_{ik} E_k \qquad \text{(A1.2)}$$

where c^E_{ijkl} is the elastic stiffness coefficient at constant electric field, e_{kij} is the

piezoelectric coefficient and ε^S_{ik} is the dielectric permittivity under clamped condition.

Elastic stiffness matrix:
$$\begin{pmatrix} c_{11} & c_{12} & c_{13} & 0 & 0 & 0 \\ c_{21} & c_{11} & c_{13} & 0 & 0 & 0 \\ c_{13} & c_{13} & c_{33} & 0 & 0 & 0 \\ 0 & 0 & 0 & c_{44} & 0 & 0 \\ 0 & 0 & 0 & 0 & c_{55} & 0 \\ 0 & 0 & 0 & 0 & 0 & c_{66} \end{pmatrix}$$

Piezoelectric matrix:
$$\begin{pmatrix} 0 & 0 & 0 & 0 & d_{15} & 0 \\ 0 & 0 & 0 & d_{15} & 0 & 0 \\ d_{31} & d_{31} & d_{33} & 0 & 0 & 0 \end{pmatrix}$$

Dielectric matrix:
$$\begin{pmatrix} \varepsilon_{11} & 0 & 0 \\ 0 & \varepsilon_{11} & 0 \\ 0 & 0 & \varepsilon_{33} \end{pmatrix}$$

Figure A 1.1 Elastic, piezoelectric and dielectric matrices of a tetragonal crystal with 4 mm and for a hexagonal structure of 6 mm point group symmetries. (Nye, 1967)

For simplicity, it is customary to use an abbreviated matrix notation in the IEEE standards in place of the full tensor notation. The following scheme is used:

Tensor notation	11	22	33	23, 32	31, 13	12, 21
Matrix notation	1	2	3	4	5	6

in which the symmetry of S_{ij} and T_{ij} with respect to exchanging subscripts is employed. Then, the piezoelectric constitutive equations become:

$$T_p = c_{pq}^E S_q - e_{kp} E_k \qquad (A1.3)$$

$$D_i = e_{ip} S_q + \varepsilon_{ik}^S E_k \qquad (A1.4)$$

The shear strain components S_4, S_5 and S_6 are redefined as $S_4 = S_{23} + S_{32} = 2S_{23}$, $S_5 = S_{31} + S_{13} = 2S_{13}$, and $S_6 = S_{12} + S_{21} = 2S_{12}$.

Since any mechanical and electrical variables can be chosen as independent variables, the piezoelectric constitutive equations can be expressed in other forms:

$$T_p = c_{pq}^D S_q - h_{kp} D_k \qquad (A1.5)$$

$$E_i = -h_{iq} S_q + \beta_{ik}^S D_k \qquad (A1.6)$$

or

$$S_p = s_{pq}^E T_q + d_{kp} E_k \qquad (A1.7)$$

$$D_i = d_{iq} T_q + \varepsilon_{ik}^T E_k \qquad (A1.8)$$

or

$$S_p = s_{pq}^D T_q - g_{kp} D_k \qquad (A1.9)$$

$$E_i = -g_{iq} T_q + \beta_{ik}^T D_k \qquad (A1.10)$$

where c_{pq}^D and c_{pq}^E are the elastic stiffness coefficients at constant electric displacement and electric field, respectively, s_{pq}^D and s_{pq}^E are the elastic compliance coefficients at constant electric displacement and electric field, respectively, β_{ik}^T and β_{ik}^S are the impermittivity at constant stress (free) and strain (clamped), respectively. ε_{ik}^T and ε_{ik}^S are the dielectric permittivity at constant stress (free) and strain (clamped), respectively. d_{iq} is the piezoelectric charge coefficient, e_{iq} the piezoelectric coefficient, g_{iq} the piezoelectric voltage coefficient and h_{iq} is the piezoelectric coefficient.

A 1.2 The Resonance Method

A 1.2.1 Radial Mode of a Thin Disc
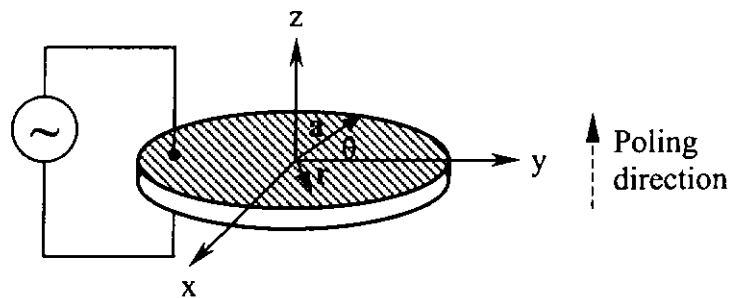
Figure A1.2 A thin disc with electric field parallel to its thickness.

A thin piezoelectric disc with electrodes normal to the poling direction as shown in Figure A1.2 can be used to determine k_p, σ^p, and s_{12}^E.

Assume the radius a is large than the thickness t (a/t > 20). Strong vibration exists in the plane normal to the poling direction and the thickness t is negligibly small, so $T_{33} = T_{r3} = T_{\theta 3} = 0$ and $\xi_\theta = \xi_3 = 0$, $T_{r\theta} = 0$ throughout the disc. Electric field is applied along the z direction so that $D_\theta = D_r = 0$. Constant T and E are then chosen as the independent variables, respectively. (Ikeda, 1990)

The constitutive equations of this system are given by:

$$S_{rr} = s_{11}^E T_{rr} + s_{12}^E T_{\theta\theta} + d_{31} E_3 \tag{A1.11}$$

$$S_{\theta\theta} = s_{12}^E T_{rr} + s_{11}^E T_{\theta\theta} + d_{31} E_3 \tag{A1.12}$$

$$D_3 = d_{31}(T_{rr} + T_{\theta\theta}) + \varepsilon_{33}^T E_3 \tag{A1.13}$$

The electrical impedance of the disc is given by:

$$Z = \frac{V}{I} = \frac{t}{j\omega\pi a^2 \varepsilon_{33}^T} \left(\frac{\Im(\frac{\omega a}{\upsilon^p}) + \sigma^p - 1}{(1 - k_p^2)\Im(\frac{\omega a}{\upsilon^p}) + \sigma^p - 1 + 2k_p^2} \right) \tag{A1.14}$$

where

$$\sigma^p = -\frac{s_{12}^E}{s_{11}^E} \tag{A1.15}$$

$$k_p^2 = \frac{2d_{31}^2}{(s_{11}^E + s_{12}^E)\varepsilon_{33}^T} \tag{A1.16}$$

where σ^p is the planar Poisson's ratio, k_p is the planar coupling coefficient, and $\Im$ is the modified quotient of Bessel functions which is defined by,

$$\Im(y) = \frac{y J_0(y)}{J_1(y)} \tag{A1.17}$$

where J_0 and J_1 are the zeroth and first order Bessel functions of the first kind given by:

$$J_0 = \sum_{n=0}^{\infty} \frac{(-1)^n}{n!\ n!}\left(\frac{y}{2}\right)^{2n} \tag{A1.18}$$

$$J_1 = \sum_{n=0}^{\infty} \frac{(-1)^n}{n!(n+1)!}\left(\frac{y}{2}\right)^{2n+1} \tag{A1.19}$$

Resonance frequencies of the planar mode are given by the roots of the transcendental equation:

$$\Im\left(\frac{\omega a}{\upsilon^p}\right) = 1 - \sigma^p \tag{A1.20}$$

Define η_1 as the lowest root of Equation (A1.20) and f_r as the fundamental resonance frequency of the radial mode, then

$$\eta_1 = \frac{2\pi f_r a}{\upsilon^p} \tag{A1.21}$$

Table A1.1 gives the variations of η_1 with σ^p. $f_r^{(2)}$ is the second lowest root of the Equation (A1.20) (first overtone frequency) which is the second harmonic resonance frequency. Thus, from a measurement of the fundamental resonance and second harmonic resonance frequencies, σ^p and η_1 can be calculated from Table A1.1.

At anti-resonance frequency f_a for a thin disc with no loss, the equation of electrical impedance Z becomes infinite, given by:

$$(1 - k_p^2)\Im\left\{\frac{\omega a}{(\upsilon^p)^{1/2}}\right\} + \sigma^p - 1 + 2k_p^2 = 0 \tag{A1.22}$$

y is defined as:

$$y = 2\pi f_a a / \upsilon^p = \eta_1 (1 + \frac{f_a - f_r}{f_r})$$ (A1.23)

k_p can be calculated by:

$$k_p^2 = \frac{\Im(y) + \sigma^p - 1}{\Im(y) - 2}$$ (A1.24)

Subsequently, s_{12}^E can be calculated by Equation (A1.15).

Table A1.1 Frequency constant of a disc resonator $\eta_1 = 2\pi f_r a / \upsilon^p$ and ratio of first overtone to fundamental resonance frequencies $f_r^{(2)} / f_r$ as a function of the planar Poisson's ratio σ^p. (ANSI/IEEE Std. 176-1987)

σ^p	η_1	$f_r^{(2)} / f_r$
0	1.84118	2.89566
0.05	1.87898	2.84258
0.10	1.91539	2.79360
0.15	1.95051	2.74826
0.20	1.98441	2.70617
0.25	2.01717	2.66699
0.30	2.04885	2.63043
0.35	2.07951	2.59625
0.40	2.10920	2.56423
0.45	2.13797	2.53416
0.50	2.16587	2.50589
0.55	2.19294	2.47926
0.60	2.21922	2.45414
0.65	2.24434	2.43040

Figure A1.3 shows the impedance spectrum of a BNBT-6 ceramic thin disc with 10.45 mm diameter and 0.565 mm thickness.
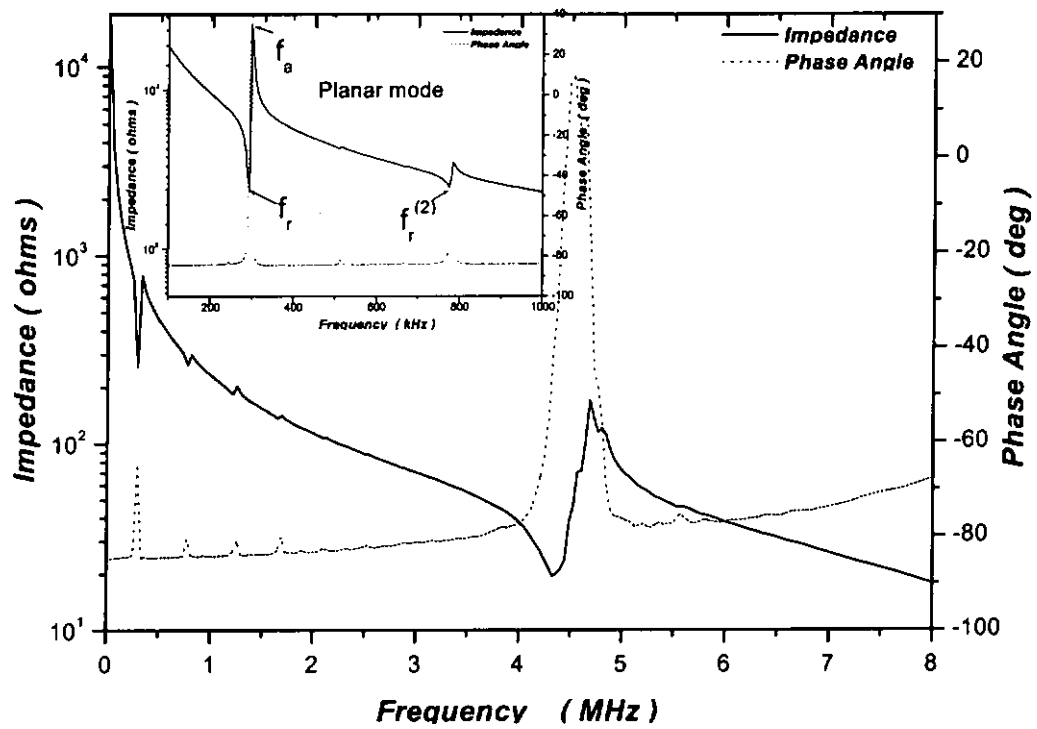
Figure A1.3 Electrical impedance and phase angle versus frequency spectra of a BNBT-6 ceramic thin disc.

A 1.2.2 Thickness Mode of a Thin Square Plate
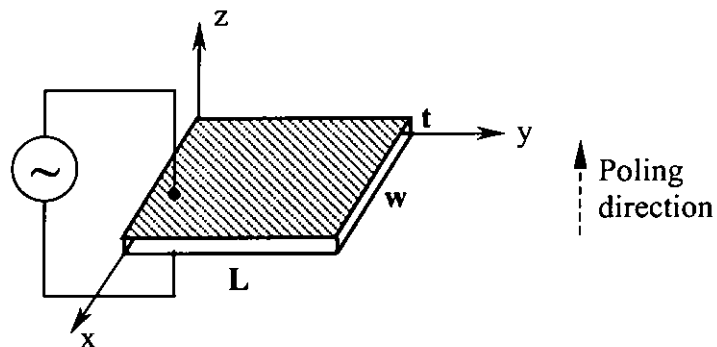
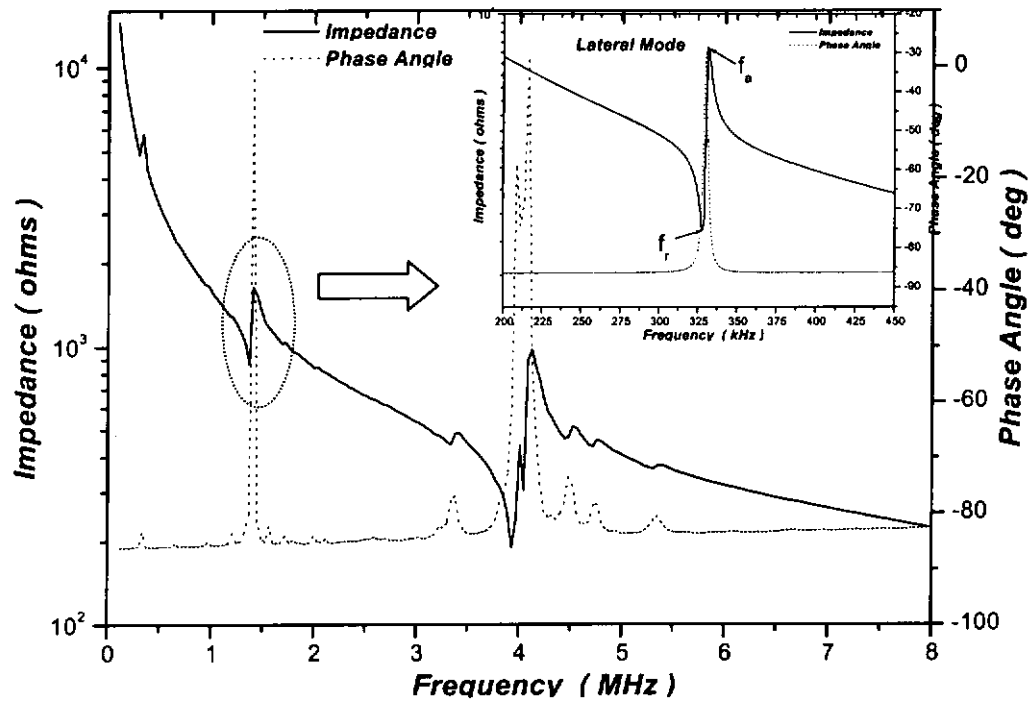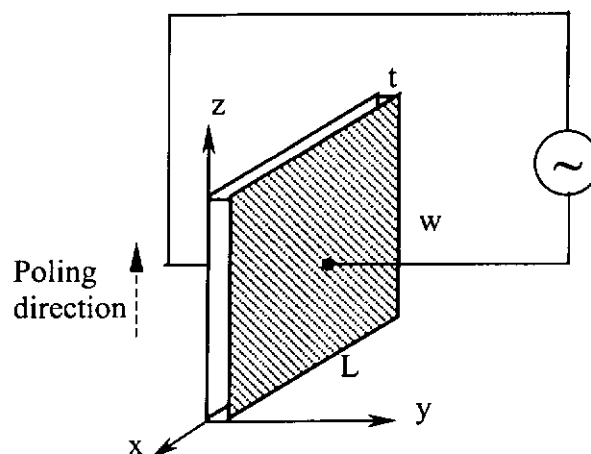Figure A1.4 A thin square plate with electric field parallel to its thickness.

A thin square piezoelectric plate with electrodes normal to the poling direction as shown in Figure A1.4 can be used to determine $k_t, c_{33}^E, c_{33}^D, \varepsilon_{33}^T$, and ε_{33}^S.

Assume the thickness t is much smaller than its length and width, L, w $>>$ t. The thin plate can be considered as laterally clamped ($S_1=S_2=S_4=S_5=S_6=0$) for plane wave propagation in the thickness direction. For an insulating dielectric medium with no electric flux leakage $D_1=D_2=0$ and $\partial D_3 / \partial z = 0$. Thus, D and S were chosen as independent variables and the constitutive equations of this system are given by:

$$T_3 = c_{33}^D S_3 + h_{33} D_3 \tag{A1.25}$$

$$E_3 = -h_{33} S_3 + \beta_{33}^S D_3 \tag{A1.26}$$

The electrical impedance of this system was given as: (Berlincourt, 1964)

$$Z = \frac{\int_0^t E_3 dz}{j\omega w D_3} = \frac{1}{j\omega C_c}[1 - k_t^2 \frac{\tan(\omega t / 2\upsilon_b^D)}{\omega t / 2\upsilon_b^D}] \tag{A1.27}$$

where $C_c = \dfrac{w}{t\beta_{33}^S}$ is the clamped capacitance of the plate. Assume the losses are negligible, the electromechanical coupling coefficient k_t can be calculated by

$$k_t^2 = \frac{\pi}{2}\frac{f_r}{f_a}\tan(\frac{\pi}{2}\frac{f_a - f_r}{f_a}) \tag{A1.28}$$

where f_r and f_a are the resonance and anti-resonance frequencies ,respectively.

The elastic stiffness coefficient c_{33}^D and c_{33}^E can be determined by

$$c_{33}^D = \rho(2tf_a)^2 \tag{A1.29}$$

$$c_{33}^E = c_{33}^D(1 - k_t^2)$$ (A1.30)

The free dielectric permittivity ε_{33}^T can be calculated from the measured capacitance C_0

at 1 kHz using the equation given by:

$$C_0 = \frac{\varepsilon_0 \varepsilon_{33}^T A}{t}$$ (A1.31)

where A is area of the electrode. The clamped dielectric permittivity ε_{33}^S can be obtained

by measuring the capacitance at twice the parallel resonance frequency f_r.

Figure A1.5 shows the impedance spectrum of a BNBT-6 ceramic thin square plate with

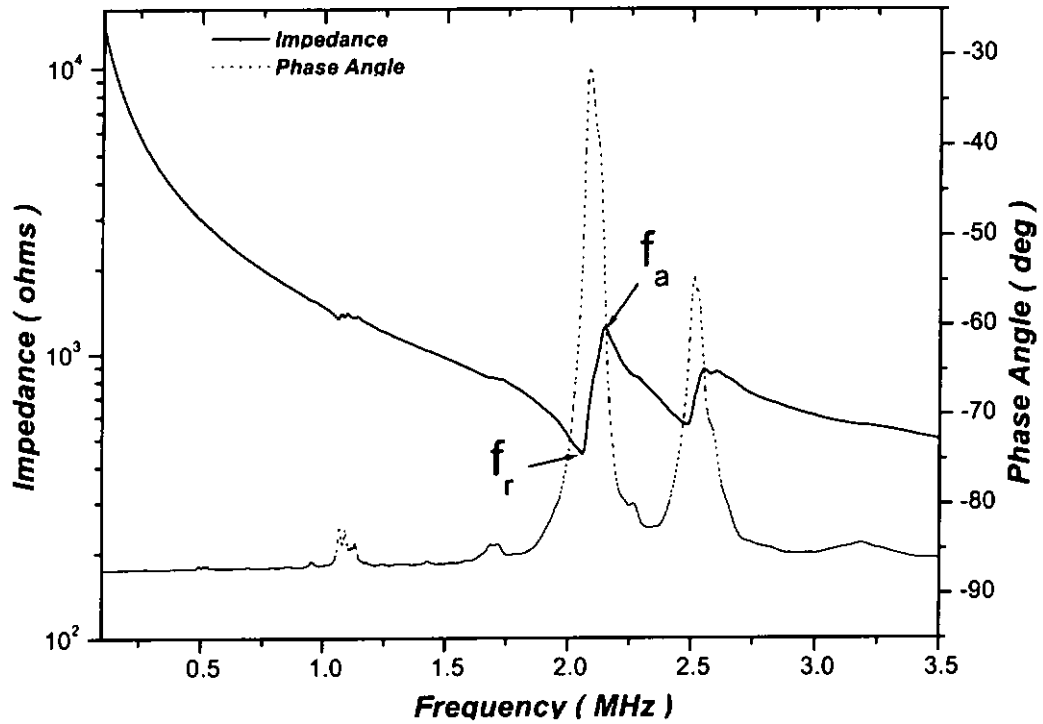7.25 mm length, 7.40 mm width and 0.61 mm thickness.
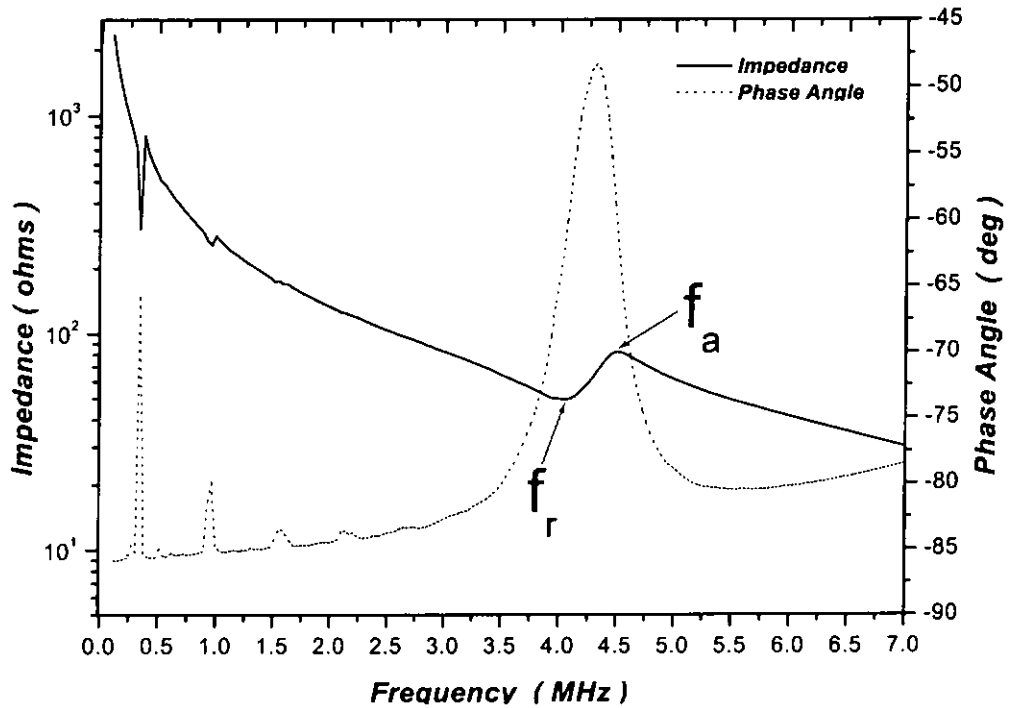
Figure A1.5 Electrical impedance and phase angle versus frequency spectra of a BNBT-6 ceramic thin square plate.

A 1.2.3 Lateral Extensional Mode of a Long Bar
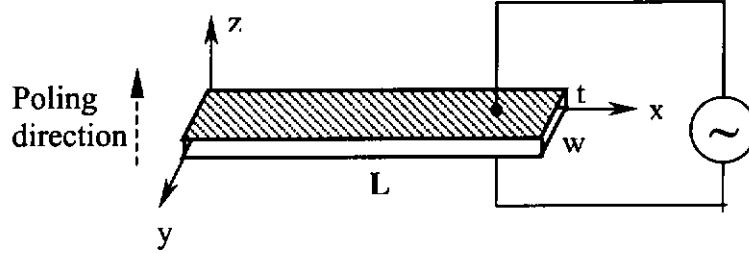
Figure A1.6 A length-expander bar with electric field parallel to its thickness.

A long piezoelectric bar with electrodes normal to the poling direction as shown in Figure A1.6 can be used to determine k_{31} and s_{11}^E.

Assume the length L is much larger than its width and thickness, L >> w, t.

Since the bar is free to vibrate in the x and y directions and its electroded surfaces form equipotential surfaces in the z direction, T and E are thus chosen as independent variables, respectively. Since thickness t is negligibly small, $E_1=E_2=0$ throughout the bar. Stress $T_2=T_3=T_4=T_5=T_6=0$ on the free surfaces and also throughout the bar. The constitutive equations of this system are given by (Berlincourt, 1964)

$$S_1 = s_{11}^E T_1 + d_{31} E_3 \tag{A1.32}$$

$$D_3 = d_{31} T_1 + \varepsilon_{33}^T E_3 \tag{A1.33}$$

The admittance of the vibrating bar can be obtained by:

$$Y = \frac{1}{Z} = j\omega \frac{L\omega}{t} \varepsilon_{33}^T \{(1 - k_{31}^2) + k_{31}^2 \frac{\tan(\omega L / 2\upsilon_b^E)}{\omega L / 2\upsilon_b^E}\} \tag{A1.34}$$

where υ_b^E is the acoustic velocity and the free relative permittivity ε_{33}^T can be determined from capacitance measured at 1 kHz. At resonance for an unloaded bar with no loss, the admittance becomes infinite,

$$\tan\frac{\omega L}{2\upsilon_b^E} = \infty \text{ and } f_r = \frac{\upsilon_b^E}{2L} \tag{A1.35}$$

This is followed by a zero of admittance at anti-resonance f_a given by:

$$\frac{\tan(\frac{\pi}{2}\frac{f_a}{f_r})}{\frac{\pi}{2}\frac{f_a}{f_r}} = \frac{k_{31}^2 - 1}{k_{31}^2} \tag{A1.36}$$

Conversely, electromechanical coupling coefficient k_{31} can be calculated from the measured f_r and f_a of the lateral mode. Elastic compliance s_{11}^E can be determined by:

$$s_{11}^E = \frac{1}{\rho(2Lf_r)^2} \tag{A1.37}$$

Figure A1.7 shows the impedance spectrum of a BNBT-6 ceramic long bar with 7.05 mm length, 1.71 mm width and 0.615 mm thickness.

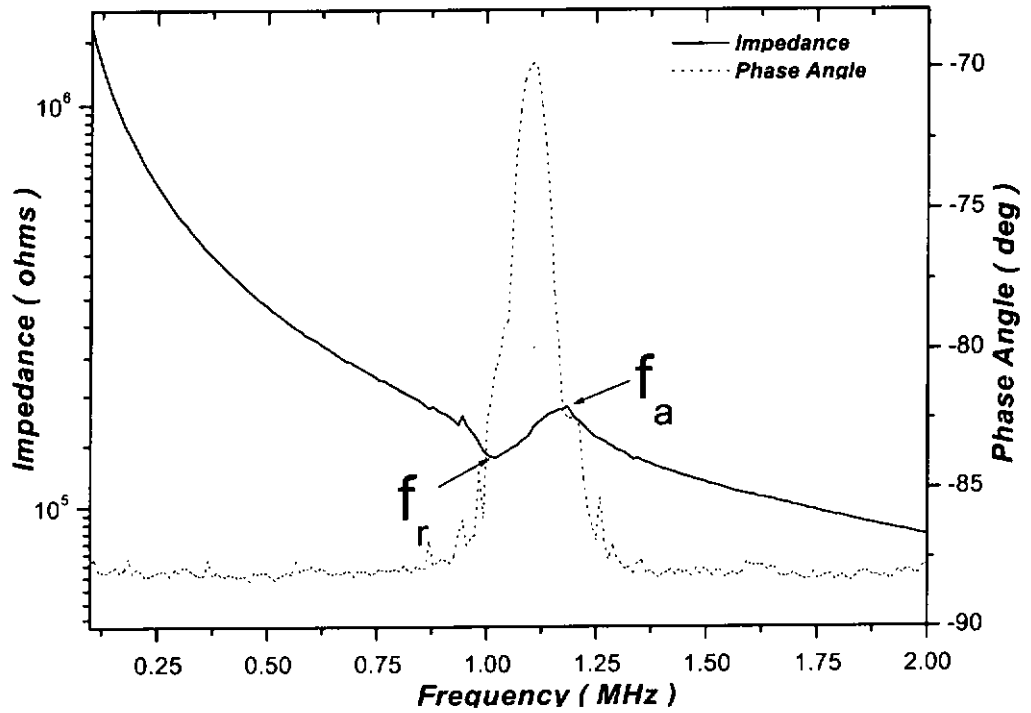Figure A1.7 Electrical impedance and phase angle versus frequency spectra of a BNBT-6 ceramic long bar.

A 1.2.4 Thickness Shear Mode of a Thin Plate

Figure A1.8 A thin shear plate with electric field parallel to its thickness.

A thin shear piezoelectric plate with electrodes parallel to the poling direction as shown in Figure A1.8 can be used to determine k_{15}, d_{15}, c_{44}^E, c_{44}^D, s_{44}^E, ε_{11}^T and ε_{11}^S.

Assume the thickness t of the plate is much smaller than its length and width, L, w >>t. The thin plate can be considered as laterally clamped ($S_1=S_2=S_3=S_4=S_6=0$) for shear wave propagation in the thickness direction. D and S can be chosen as independent variables and the constitutive equations of this system are given by:

$$T_5 = c_{55}^D S_5 + h_{15} D_1 \tag{A1.38}$$

$$E_1 = -h_{15} S_5 + \beta_{11}^S D_1 \tag{A1.39}$$

The behavior of thickness shear mode with electric field parallel to the direction of propagation can be described by equations similar to those in section A1.2.3. Thus,

$$k_{15}^2 = \frac{\pi}{2} \frac{f_r}{f_a} \tan(\frac{\pi}{2} \frac{f_a - f_r}{f_a}) \tag{A1.40}$$

$$c_{44}^D = \rho(2t f_a)^2 \tag{A1.41}$$

$$c_{44}^E = c_{44}^D (1 - k_{15}^2) \tag{A1.42}$$

$$s_{44}^E = \frac{1}{c_{44}^E} \tag{A1.43}$$

Relative permittivity ε_{11}^T and   can be obtained by the same way as that in the thickness mode. Subsequently, d_{15} can be calculated by:

$$d_{15} = k_{15} \sqrt{s_{44}^E \varepsilon_{11}^T} \tag{A1.44}$$

Figure A1.9 shows the impedance spectrum of a BNBT-6 ceramic thin shear plate with 7.87 mm length, 2.02 mm width and 0.71 mm thickness.

Figure A1.9 Electrical impedance and phase angle versus frequency spectra of a BNBT-6 ceramic thin shear plate.

A 1.2.5 Length Extensional Mode of a Tall Thin Rod
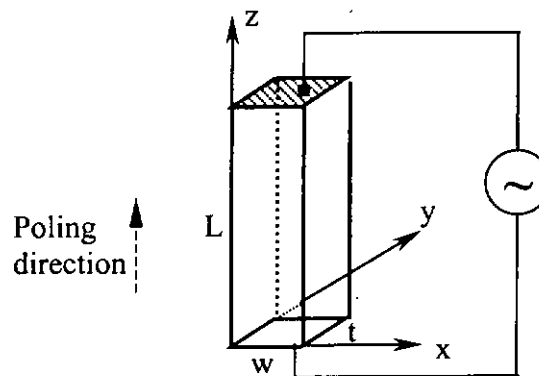
Figure A1.10 A tall thin rod with electric field parallel to its thickness.

A tall thin piezoelectric rod with electrodes normal to the poling direction as shown in Figure A1.10 can be used to determine k_{33}, s_{33}^E and s_{33}^D.

Assume the rod is long enough so that the permittivity of the rod is sufficiently greater than that of its surroundings to prevent fringing electric fields. If the cross-sectional dimensions w and t are small compared with its length L, $L > \sqrt{w}$ and $L > \sqrt{t}$, all stresses will be zero except T_3. Similarly, for an insulating dielectric medium with no electric flux leakage, $D_1=D_2=0$ and $\partial D_3 / \partial z = 0$. Hence, D and T are chosen as independent variables, giving (Berlincourt, 1964)

$$S_3 = s_{33}^D T_3 + g_{33} D_3 \tag{A1.45}$$

$$E_3 = -g_{33} T_3 + \beta_{33}^T D_3 \tag{A1.46}$$

The impedance of a tall thin rod vibrating along the z direction is given by:

$$Z = \frac{1}{j\omega C_s}[1 - k_{33}^2 \frac{\tan(\omega L / 2\upsilon_b^D)}{\omega L / 2\upsilon_b^D}] \tag{A1.47}$$

where

$$C_s = \frac{A}{L\beta_{33}^S} = \frac{A\varepsilon_{33}^s}{L} \tag{A1.48}$$

$$\beta_{33}^S = \beta_{33}^T(1 + \frac{g_{33}^2}{\beta_{33}^T s_{33}^D}) \tag{A1.49}$$

$$k_{33}^2 = \frac{g_{33}^2}{\beta_{33}^T s_{33}^D + g_{33}^2} \tag{A1.50}$$

$$\upsilon_b^D = (\frac{1}{\rho s_{33}^D})^{\frac{1}{2}} \tag{A1.51}$$

$$k_{33}^2 = \frac{d_{33}^2}{s_{33}^E \varepsilon_{33}^T} = \frac{\varepsilon_{33}^T g_{33}^2}{s_{33}^E} \qquad (A1.52)$$

where A is the cross-sectional area ($A = w \times t$), C_s is the clamped capacitance, s_{33}^D and

k_{33} can be calculated by:

$$s_{33}^D = \frac{1}{\rho(2Lf_a)^2} \qquad (A1.53)$$

$$k_{33}^2 = \frac{\pi}{2}\frac{f_r}{f_a} \tan(\frac{\pi}{2}\frac{f_a - f_r}{f_a}) \qquad (A1.54)$$

$$s_{33}^E = \frac{s_{33}^D}{(1 - k_{33}^2)} \qquad (A1.55)$$

Figure A1.11 shows the impedance spectrum of a BNBT-6 ceramic tall thin rod with 2.02 mm length, 0.65 mm width and 0.65 mm thickness.

Figure A1.11 Electrical impedance and phase angle versus frequency spectra of a BNBT-6 ceramic tall thin rod.

A 1.2.6 Calculations of Other Material Parameters

Using the calculated material parameters s_{11}^E, k_t, c_{33}^E, c_{33}^D, ε_{33}^T, ε_{33}^S, k_{15}, d_{15}, c_{44}^E, c_{44}^D, s_{44}^E, ε_{11}^T, ε_{11}^S, k_{33}, s_{33}^E and s_{33}^D and measured d_{33} and d_{31}, the following parameters can be calculated: (IEC Standards, 1976)

$$e_{33} = k_t \sqrt{c_{33}^D \varepsilon_{33}^S}$$ (A1.56)

$$e_{31} = (\varepsilon_{33}^T - \varepsilon_{33}^S - d_{33} e_{33}) / 2 d_{31}$$ (A1.57)

$$g_{33} = \frac{d_{33}}{\varepsilon_{33}^T}$$ (A1.58)

$$g_{31} = \frac{d_{31}}{\varepsilon_{33}^T}$$ (A1.59)

$$s_{13}^E = (d_{33} - e_{33} s_{33}^E) / 2 e_{31}$$ (A1.60)

$$s_{12}^E = -[s_{11}^E - \frac{2(s_{13}^E)^2}{s_{33}^E - 1/c_{33}^E}]$$ (A1.61)

$$c_{11}^E = \frac{s_{11}^E s_{33}^E - s_{13}^{E\,2}}{(s_{11}^E - s_{12}^E)[s_{33}^E(s_{11}^E + s_{12}^E) - 2s_{13}^{E\,2}]}$$ (A1.62)

$$c_{12}^E = \frac{-s_{12}^E s_{33}^E + s_{13}^{E\,2}}{(s_{11}^E - s_{12}^E)[s_{33}^E(s_{11}^E + s_{12}^E) - 2s_{13}^{E\,2}]}$$ (A1.63)

$$c_{13}^E = \frac{-s_{13}^E}{s_{33}^E(s_{11}^E + s_{12}^E) - 2s_{13}^{E\,2}}$$ (A1.64)

$$s_{11}^D = (1 - k_{31}^2) s_{11}^E$$ (A1.65)

$$s_{12}^D = s_{12}^E - d_{31}g_{31} \tag{A1.66}$$

$$s_{13}^D = s_{13}^E - d_{31}g_{33} \tag{A1.67}$$

$$c_{11}^D = \frac{s_{11}^D s_{33}^D - s_{13}^{D^2}}{(s_{11}^D - s_{12}^D)[s_{33}^D(s_{11}^D + s_{12}^D) - 2s_{13}^{D^2}]} \tag{A1.68}$$

$$c_{12}^D = \frac{-s_{12}^D s_{33}^D + s_{13}^{D^2}}{(s_{11}^D - s_{12}^D)[s_{33}^D(s_{11}^D + s_{12}^D) - 2s_{13}^{D^2}]} \tag{A1.69}$$

$$c_{13}^D = \frac{s_{13}^D}{s_{33}^D(s_{11}^D + s_{12}^D) - 2s_{13}^{D^2}} \tag{A1.70}$$

$$s_{44}^D = \frac{1}{c_{44}^D} \tag{A1.71}$$

$$c_{66}^D = \frac{1}{s_{66}^D} \tag{A1.72}$$

$$s_{66}^E = 2(s_{11}^E - s_{12}^E) \tag{A1.73}$$

$$s_{66}^D = s_{66}^E \tag{A1.74}$$

$$h_{33} = 2g_{31}c_{13}^D + g_{33}c_{33}^D \tag{A1.75}$$

$$h_{31} = g_{31}(c_{11}^D + c_{12}^D) + g_{33}c_{33}^D \tag{A1.76}$$

$$h_{15} = g_{15}c_{44}^D \tag{A1.77}$$

Frequency constant of N_p, N_{31}, N_{33} and N_{15} in cycle Hzm can be calculated by:

$$N_p = f_r a \tag{A1.78}$$

$$N_{31} = f_r t \tag{A1.79}$$

$$N_{33} = f_r L \tag{A1.80}$$

$$N_{15} = f_r t \tag{A1.81}$$

where a is the diameter of the thin disc, t is the thickness of the plate, L is the length of

the bar and f_r is the corresponding resonance frequency.

Young's modulus Y can be obtained by:

$$Y = \frac{1}{s_{33}^E} \tag{A1.82}$$

Calculation of mechanical quality coefficient Q_M and electrical quality coefficient Q_E

have been described in Chapter II.

APPENDIX II

SUPPLEMENTARY TO BNBT-6/EPOXY 1-3 COMPOSITE MATERIAL PARAMETERS

In Chapter III, a modified parallel and series model was used to evaluate the effective

material parameters of the BNBT-6/epoxy 1-3 composites. Some of the parameters have

been presented as functions of ceramic volume fraction ϕ in Chapter 3 and compared

with the measured results. The other effective composite parameters are given in this

appendix for completeness. These parameters include: the clamped relative permittivity

$\overline{\varepsilon_{33}^{S}}$, the electromechnical coupling coefficients $\overline{k_{31}}$ and $\overline{k_{33}}$, the piezoelectric

coefficients $\overline{e_{33}}$, $\overline{e_{31}}$, $\overline{g_{31}}$, $\overline{h_{33}}$ and $\overline{h_{31}}$, the elastic stiffness coefficients $\overline{c_{11}^{D}}$, $\overline{c_{12}^{D}}$, $\overline{c_{13}^{D}}$,

$\overline{c_{33}^{D}}$, $\overline{c_{11}^{E}}$, $\overline{c_{12}^{E}}$, $\overline{c_{13}^{E}}$ and $\overline{c_{33}^{E}}$, the elastic compliance coefficients $\overline{s_{11}^{D}}$, $\overline{s_{12}^{D}}$, $\overline{s_{13}^{D}}$, $\overline{s_{33}^{D}}$, $\overline{s_{11}^{E}}$,

$\overline{s_{12}^{E}}$, $\overline{s_{13}^{E}}$ and $\overline{s_{33}^{E}}$, the longitudinal wave velocities $\overline{\upsilon_{3t}^{D}}$, $\overline{\upsilon_{3t}^{E}}$, $\overline{\upsilon_{33}^{D}}$ and $\overline{\upsilon_{33}^{D}}$, the frequency

constants $\overline{N_{3t}^{D}}$, $\overline{N_{3t}^{E}}$, $\overline{N_{33}^{D}}$ and $\overline{N_{33}^{D}}$ and the acoustic impedance $\overline{z}$. They are plotted in

Figures A2.1 to A2.33.
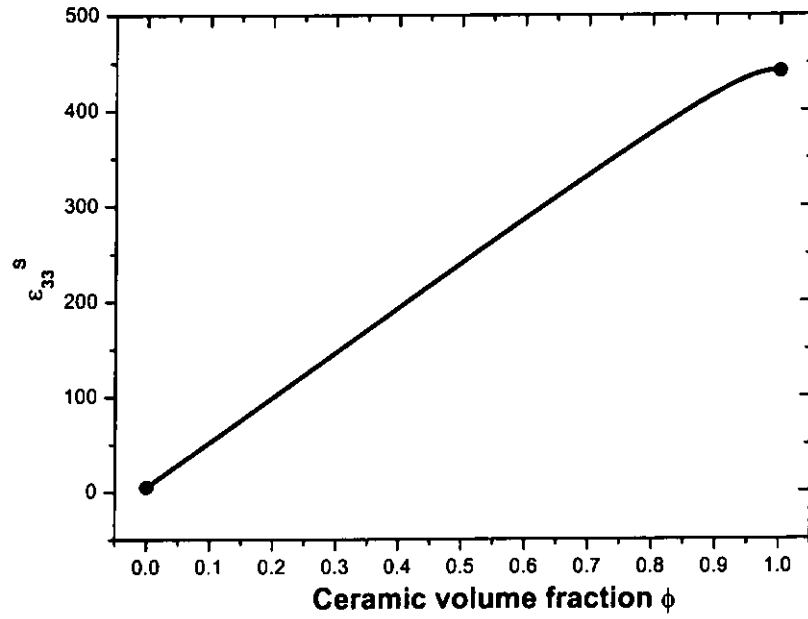
Figure A2.1 Variation of effective clamped relative permittivity $\overline{\varepsilon_{33}^S}$ of BNBT-6/epoxy 1-3 composites with the BNBT-6 volume fraction.
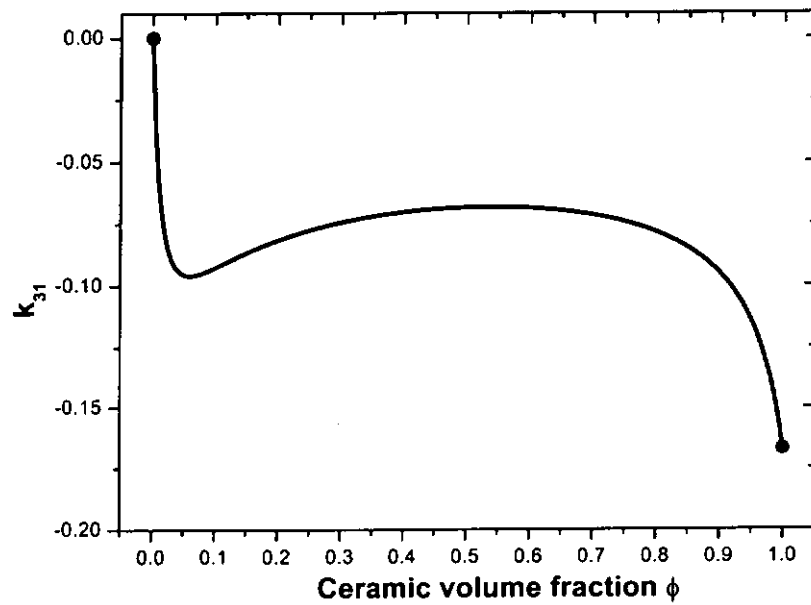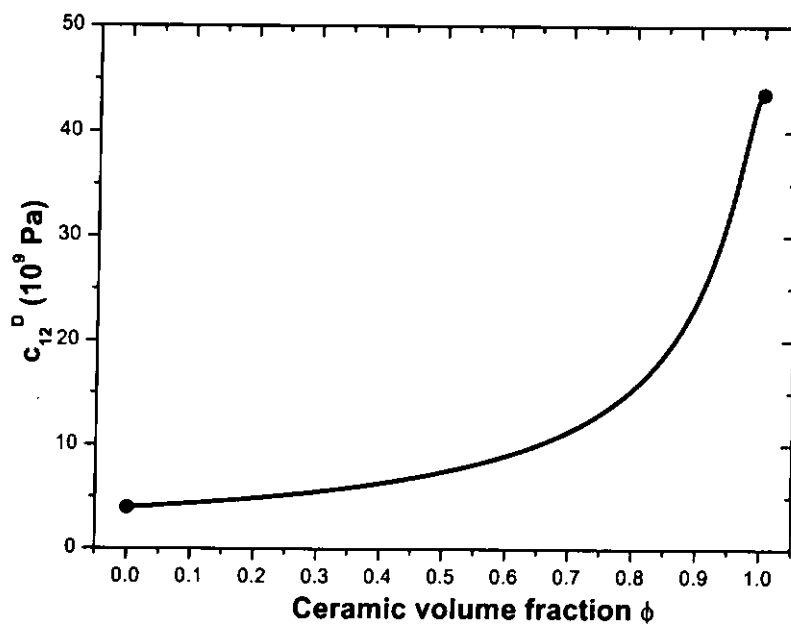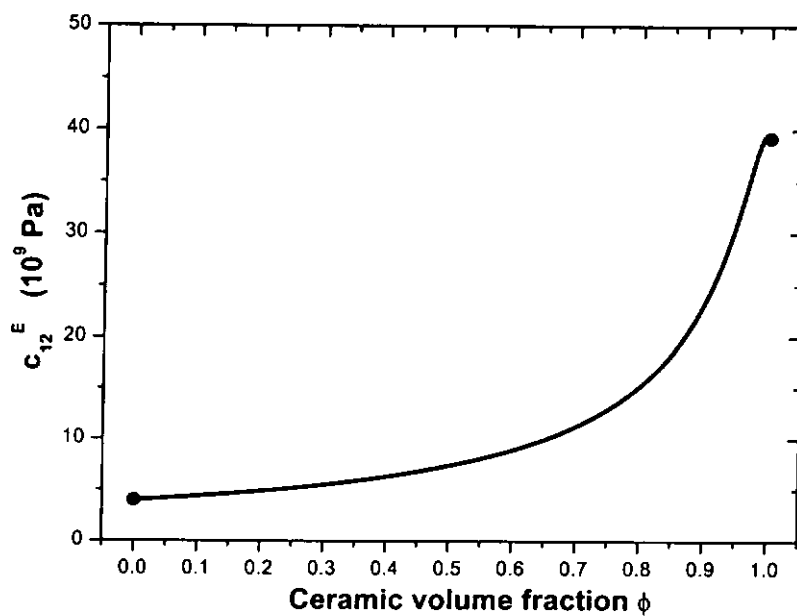

Figure A2.2 Variation of effective electromechanical coupling coefficient $\overline{k_{31}}$ of BNBT-6/epoxy 1-3 composites with the BNBT-6 volume fraction.
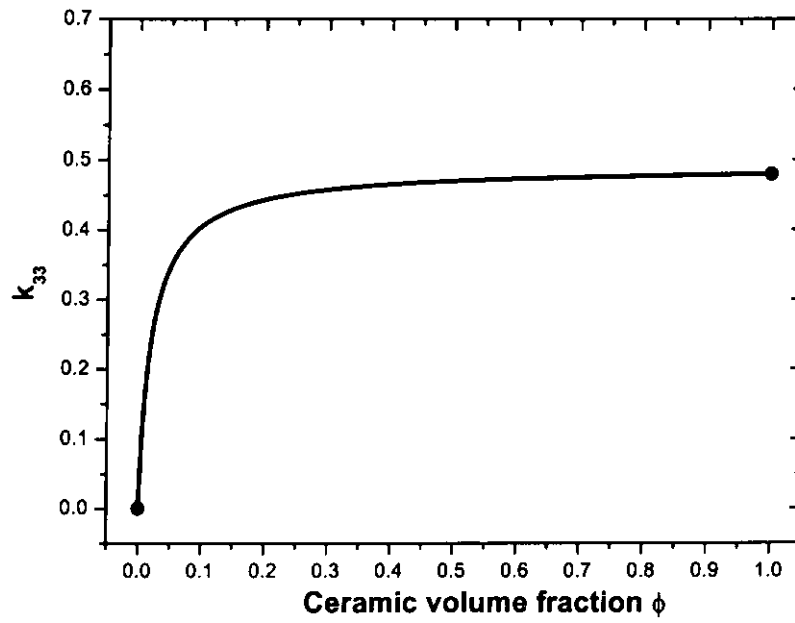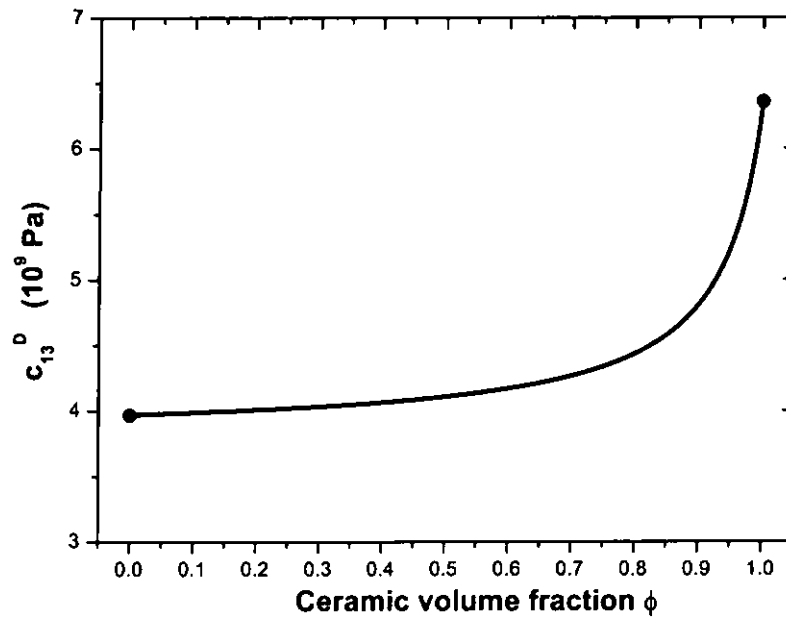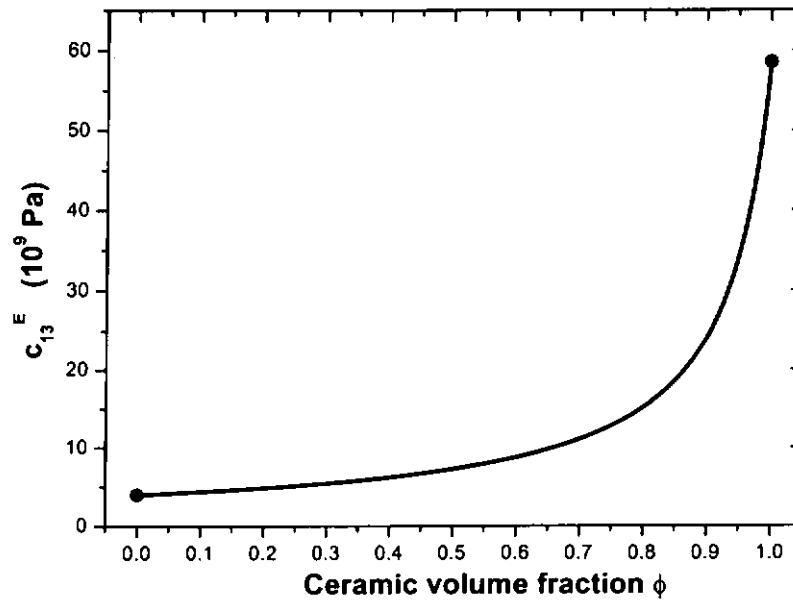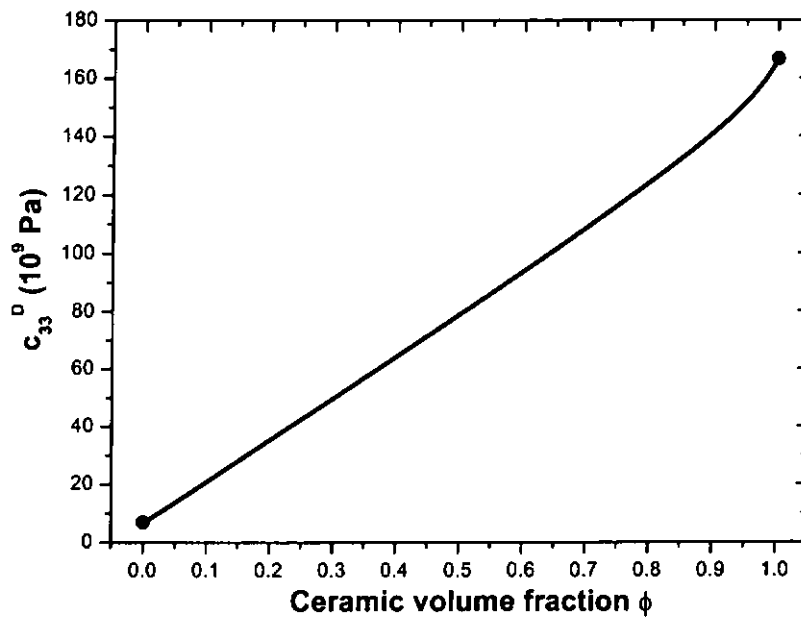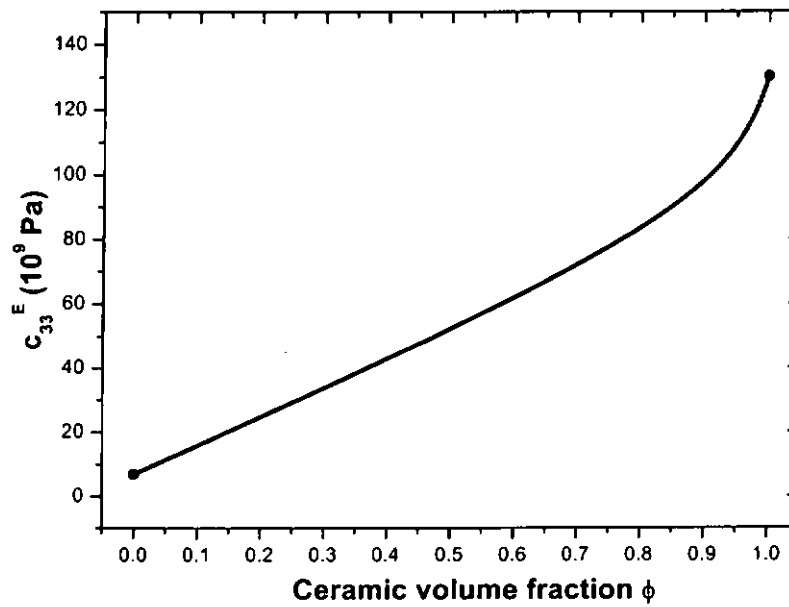
Figure A2.3 Variation of effective electromechanical coupling coefficient $\overline{k_{33}}$ of BNBT-6/epoxy 1-3 composites with the BNBT-6 volume fraction.
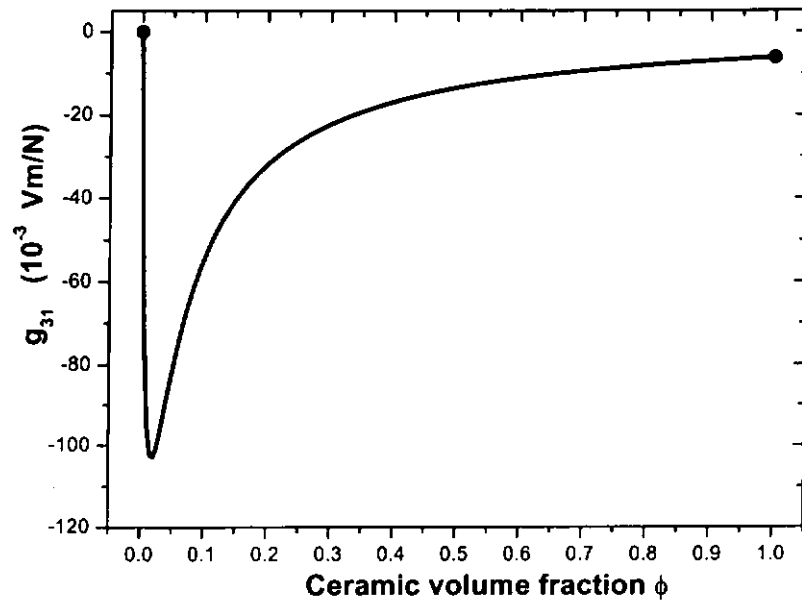
Figure A2.4 Variation of effective piezoelectric coefficient $\overline{g_{31}}$ of BNBT-6/epoxy 1-3 composites with the BNBT-6 volume fraction.
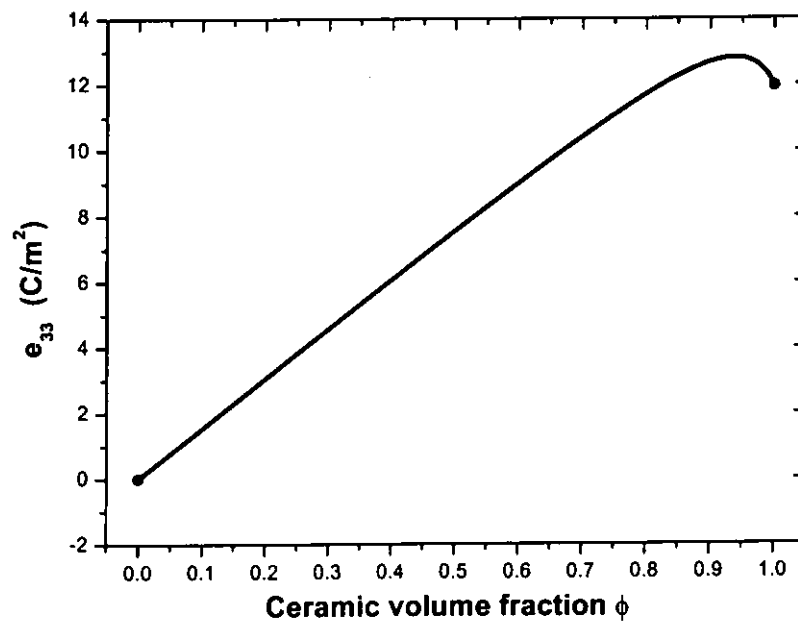
Figure A2.5 Variation of effective piezoelectric coefficient $\overline{e_{33}}$ of BNBT-6/epoxy 1-3 composites with the BNBT-6 volume fraction.
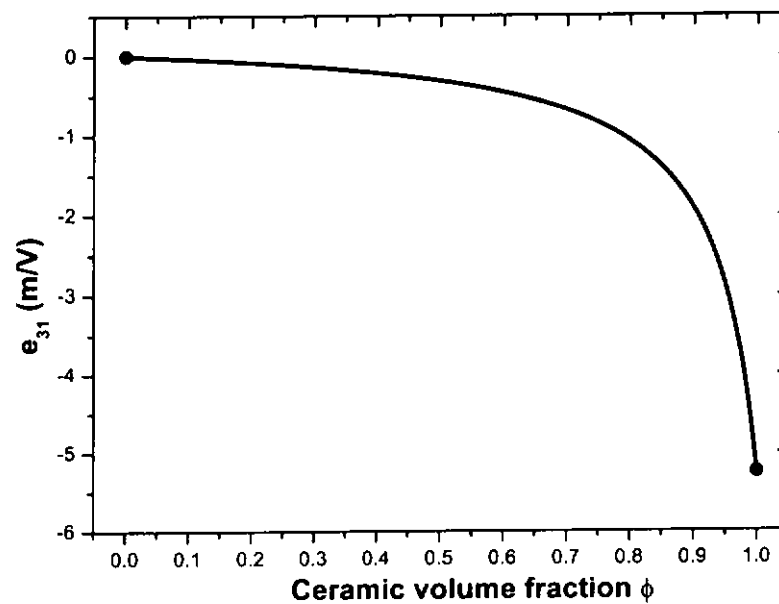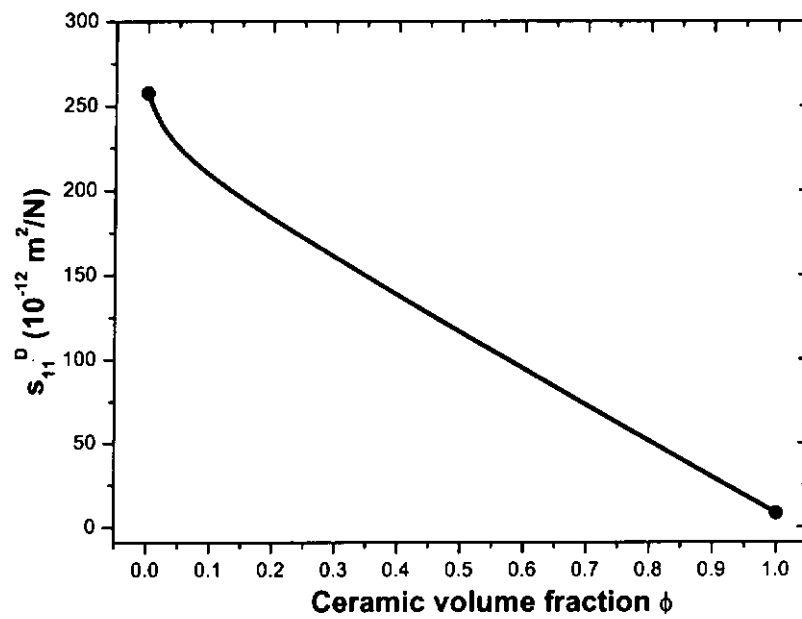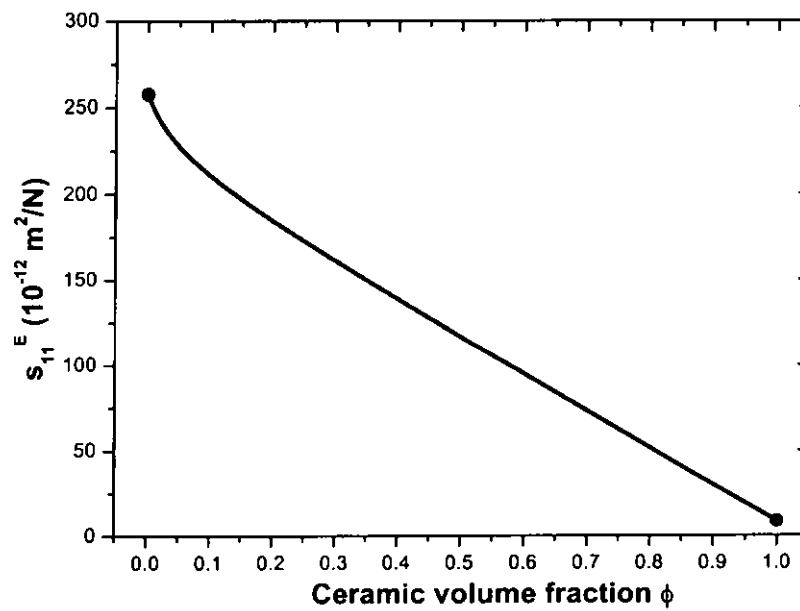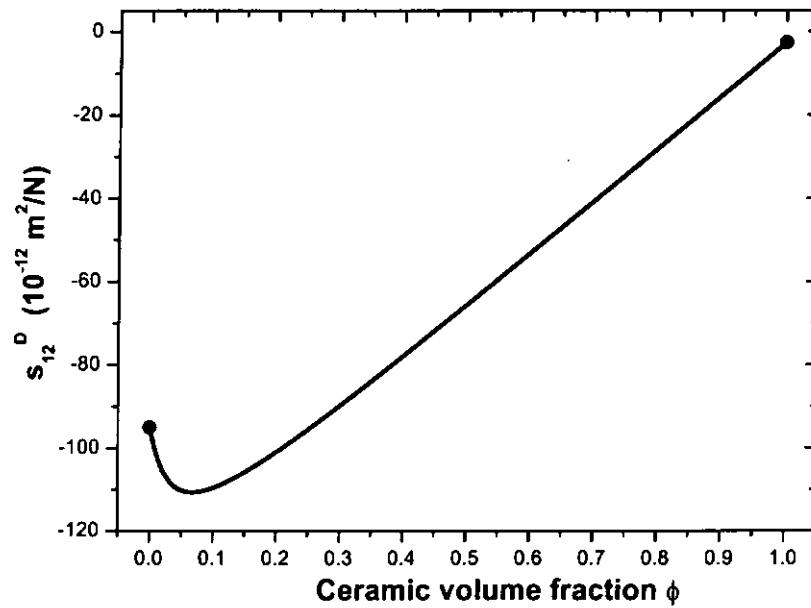

Figure A2.6 Variation of effective piezoelectric coefficient $\overline{e_{31}}$ of BNBT-6/epoxy 1-3 composites with the BNBT-6 volume fraction.
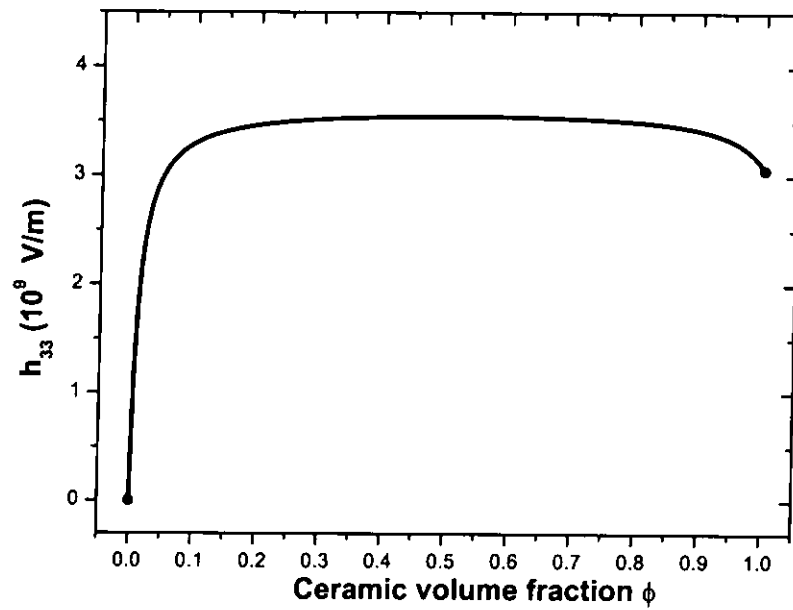
Figure A2.7 Variation of effective piezoelectric coefficient $\overline{h_{33}}$ of BNBT-6/epoxy 1-3 composites with the BNBT-6 volume fraction.
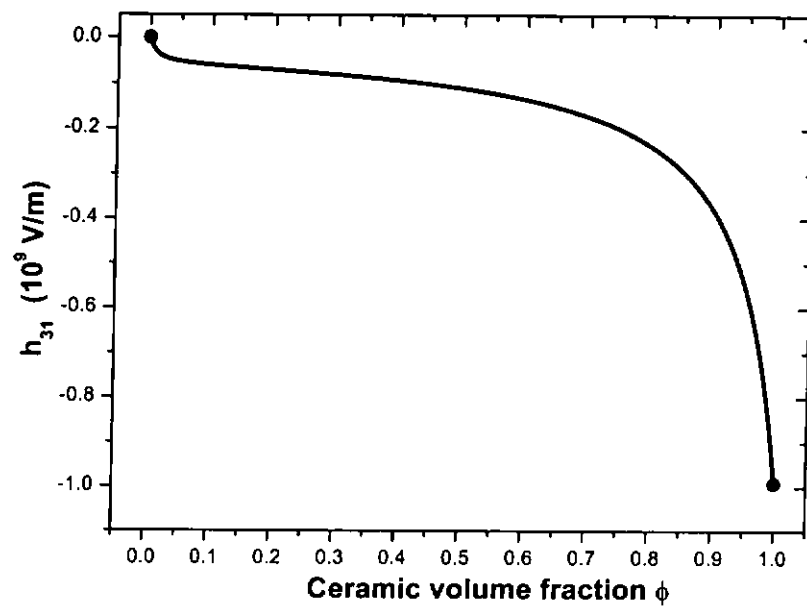
Figure A2.8 Variation of effective piezoelectric coefficient $\overline{h_{31}}$ of BNBT-6/epoxy 1-3 composites with the BNBT-6 volume fraction.
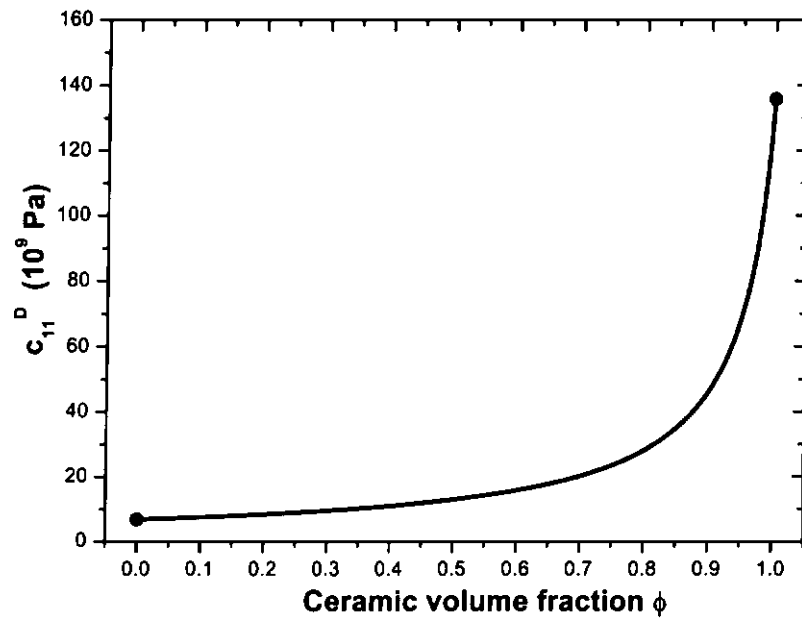
Figure A2.9 Variation of effective elastic stiffness coefficient $\overline{c_{11}^{D}}$ of BNBT-6/epoxy 1-3 composites with the BNBT-6 volume fraction.
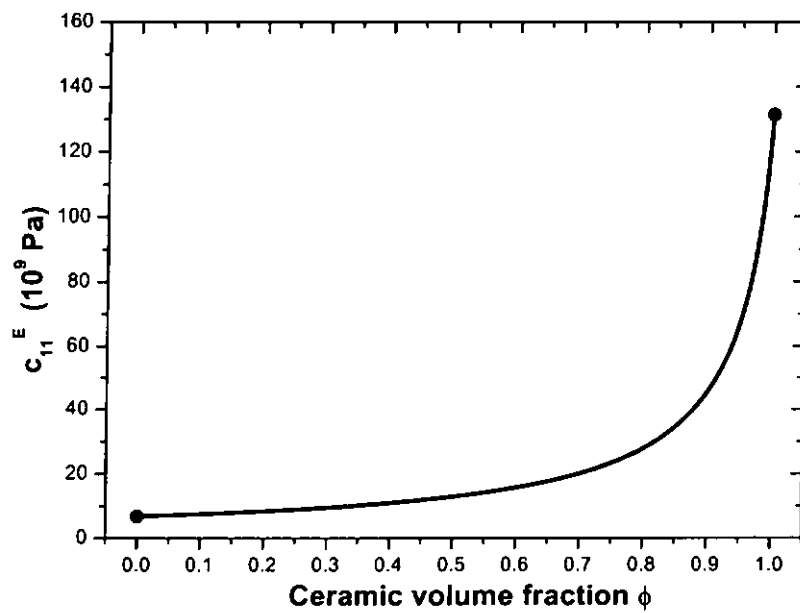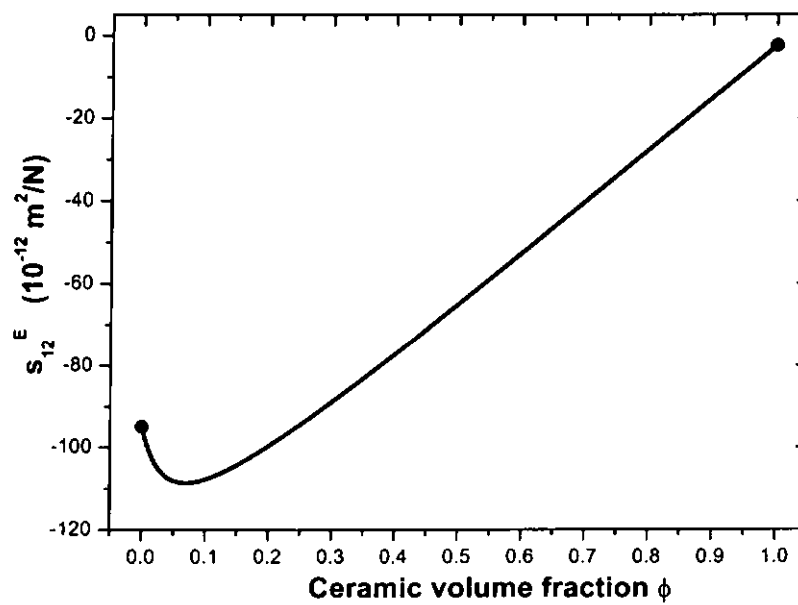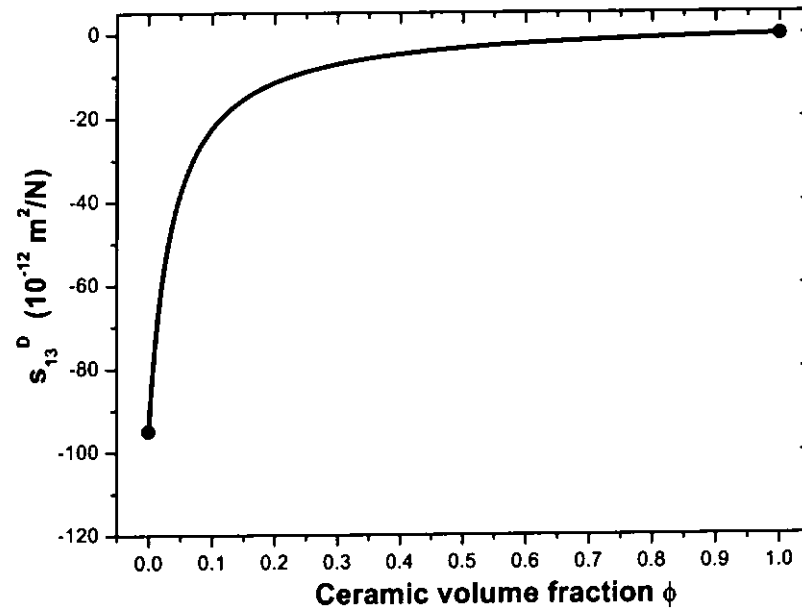

Figure A2.10 Variation of effective elastic stiffness coefficient $\overline{c_{11}^{E}}$ of BNBT-6/epoxy 1-3 composites with the BNBT-6 volume fraction.

Figure A2.11 Variation of effective elastic stiffness coefficient $\overline{c_{12}^D}$ of BNBT-6/epoxy 1-3 composites with the BNBT-6 volume fraction.
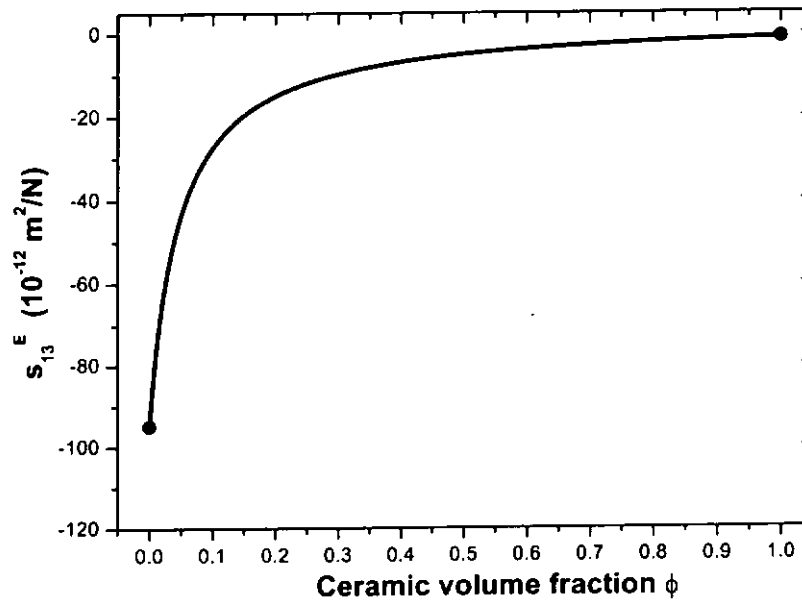

Figure A2.12 Variation of effective elastic stiffness coefficient $\overline{c_{12}^E}$ of BNBT-6/epoxy 1-3 composites with the BNBT-6 volume fraction.
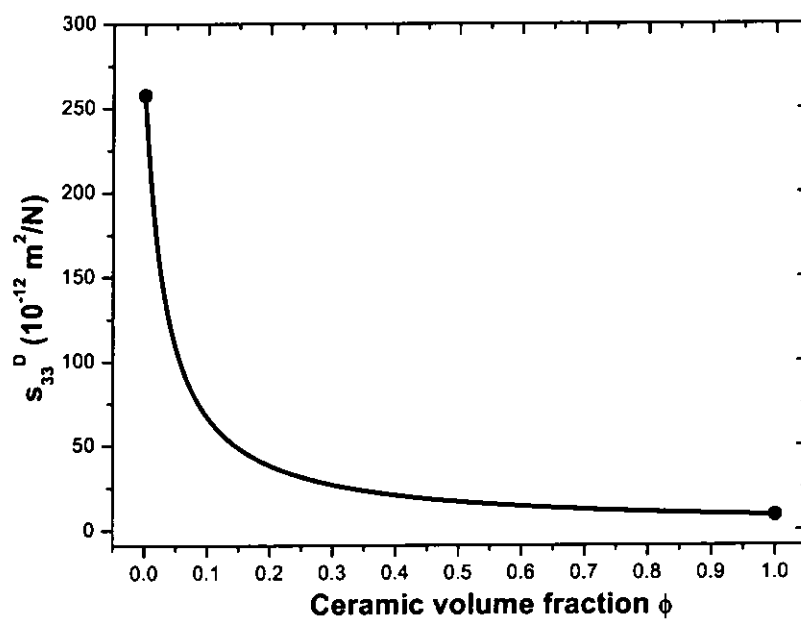
Figure A2.13 Variation of effective elastic stiffness coefficient $\overline{c_{13}^D}$ of BNBT-6/epoxy 1-3 composites with the BNBT-6 volume fraction.
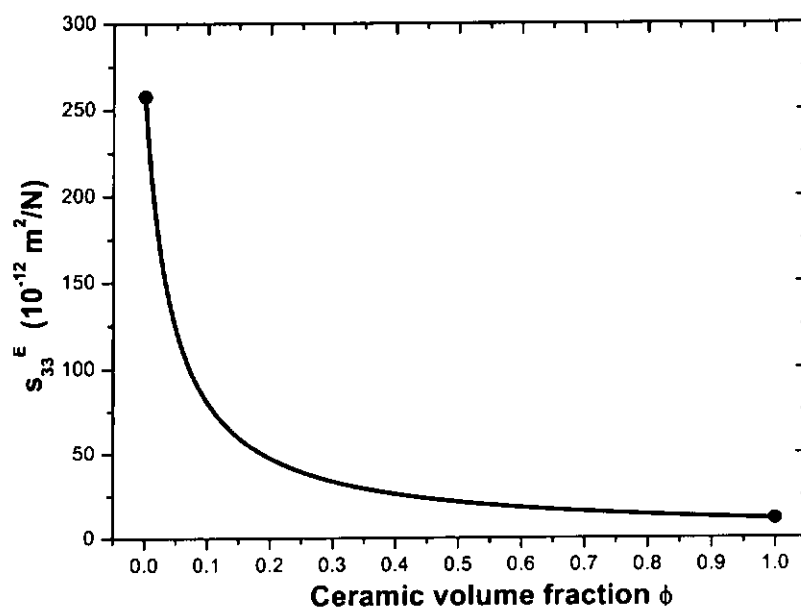

Figure A2.14 Variation of effective elastic stiffness coefficient $\overline{c_{13}^E}$ of BNBT-6/epoxy 1-3 composites with the BNBT-6 volume fraction.

Figure A2.15 Variation of effective elastic stiffness coefficient $\overline{c_{33}^{D}}$ of BNBT-6/epoxy 1-

3 composites with the BNBT-6 volume fraction.

Figure A2.16 Variation of effective elastic stiffness coefficient $\overline{c_{33}^{E}}$ of BNBT-6/epoxy 1-
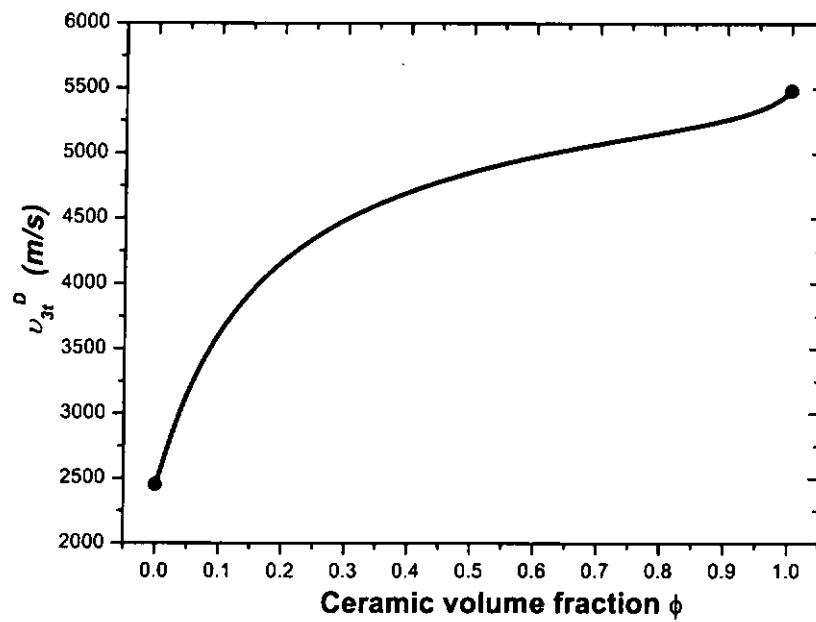
3 composites with the BNBT-6 volume fraction.

Figure A2.17 Variation of effective elastic compliance coefficient $\overline{s_{11}^{D}}$ of BNBT-6/epoxy 1-3 composites with the BNBT-6 volume fraction.

Figure A2.18 Variation of effective elastic compliance coefficient $\overline{s_{11}^{E}}$ of BNBT-6/epoxy 1-3 composites with the BNBT-6 volume fraction.

Figure A2.19 Variation of effective elastic compliance coefficient $\overline{s_{12}^{D}}$ of BNBT-6/epoxy

1-3 composites with the BNBT-6 volume fraction.

Figure A2.20 Variation of effective elastic compliance coefficient $\overline{s_{12}^{E}}$ of BNBT-6/epoxy

1-3 composites with the BNBT-6 volume fraction.

Figure A2.21 Variation of effective elastic compliance coefficient $\overline{s_{13}^{D}}$ of BNBT-6/epoxy

1-3 composites with the BNBT-6 volume fraction.

Figure A2.22 Variation of effective elastic compliance coefficient $\overline{s_{13}^{E}}$ of BNBT-6/epoxy

1-3 composites with the BNBT-6 volume fraction.

Figure A2.23 Variation of effective elastic compliance coefficient $\overline{s_{33}^{D}}$ of BNBT-6/epoxy

1-3 composites with the BNBT-6 volume fraction.

Figure A2.24 Variation of effective elastic compliance coefficient $\overline{s_{33}^{E}}$ of BNBT-6/epoxy

1-3 composites with the BNBT-6 volume fraction.

Figure A2.25 Variation of effective longitudinal wave velocity in a plate $\overline{v_{3t}^D}$ of BNBT-6/epoxy 1-3 composites with the BNBT-6 volume fraction.
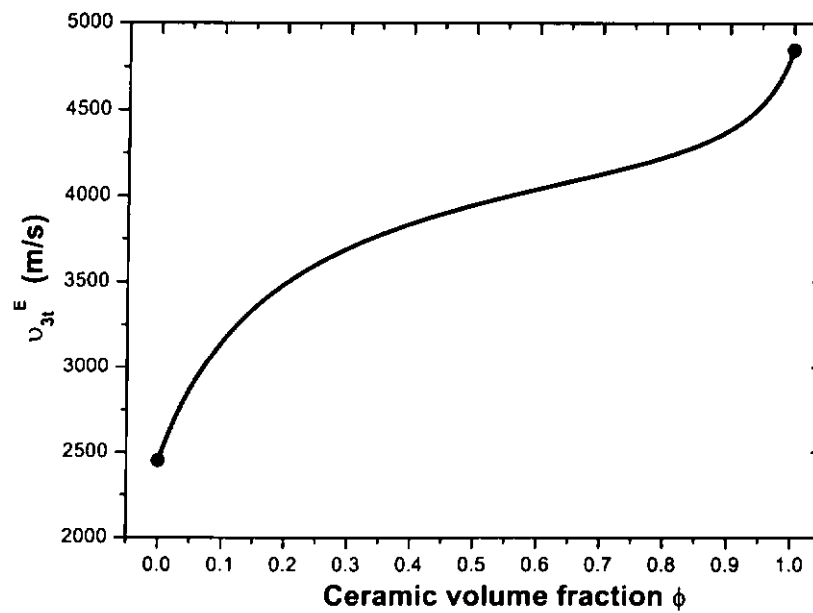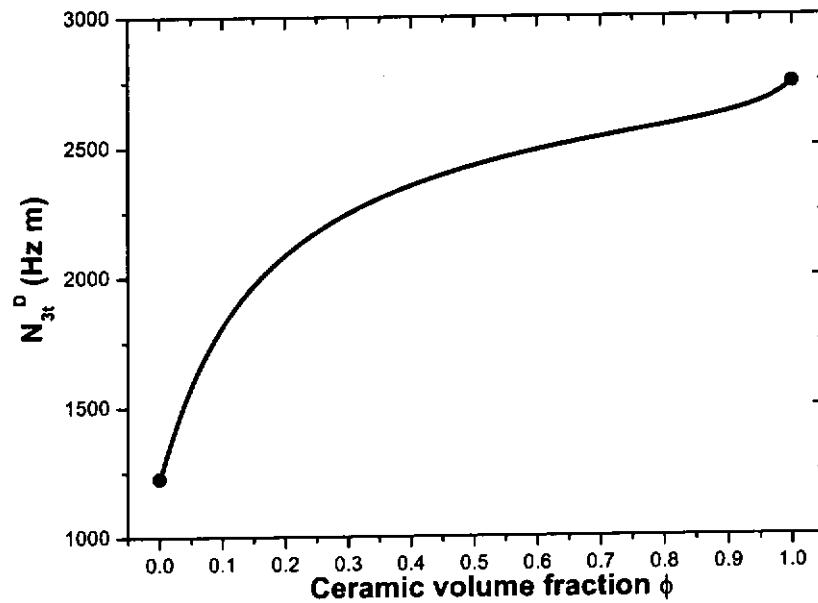

Figure A2.26 Variation of effective longitudinal wave velocity in a plate $\overline{v_{3t}^E}$ of BNBT-6/epoxy 1-3 composites with the BNBT-6 volume fraction.
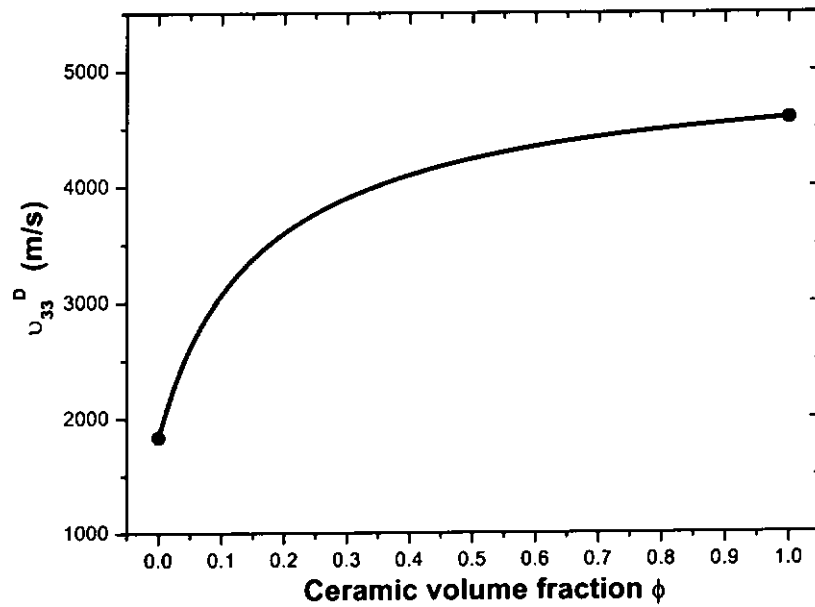
Figure A2.27 Variation of effective longitudinal wave velocity in a bar $\overline{v_{33}^D}$ of BNBT-6/epoxy 1-3 composites with the BNBT-6 volume fraction.
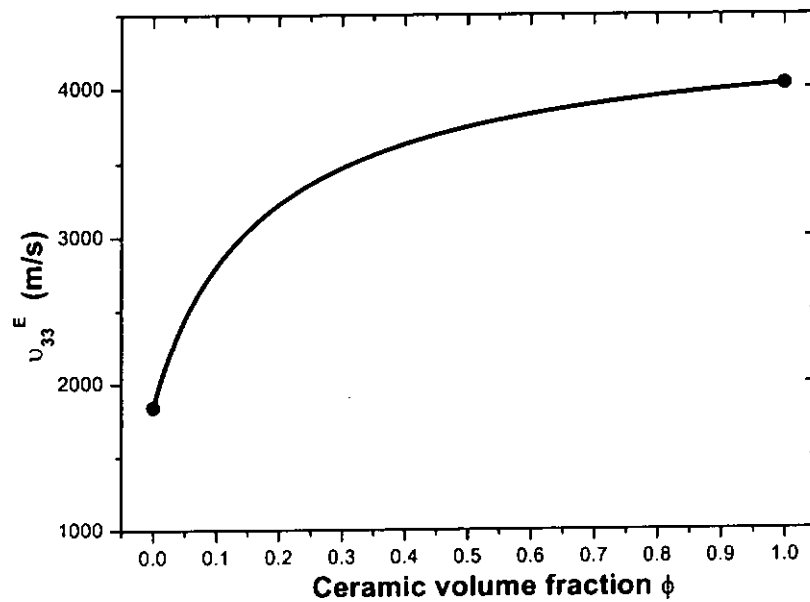
Figure A2.28 Variation of effective longitudinal wave velocity in a bar $\overline{v_{33}^E}$ of BNBT-6/epoxy 1-3 composites with the BNBT-6 volume fraction.

Figure A2.29 Variation of effective thickness frequency constant $\overline{N_{3t}^{D}}$ of BNBT-6/epoxy

1-3 composites with the BNBT-6 volume fraction.
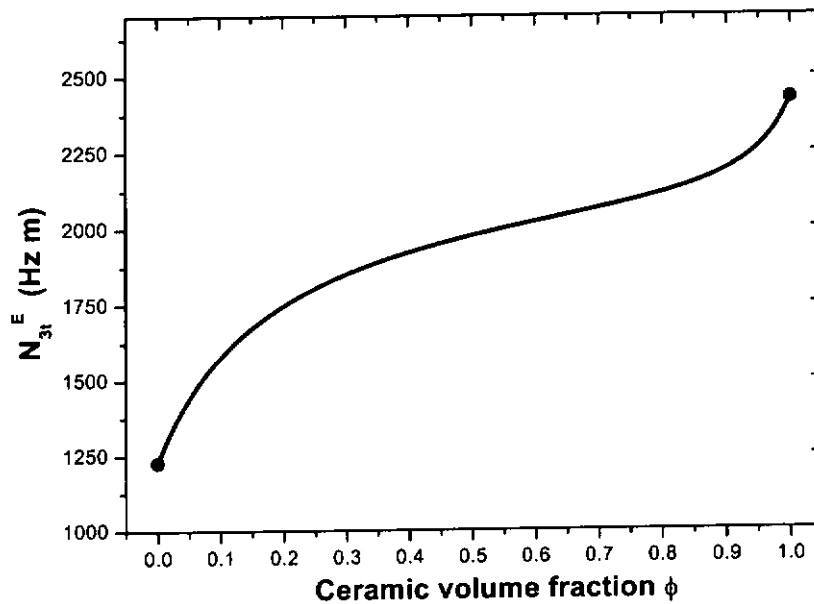
Figure A2.30 Variation of effective thickness frequency constant $\overline{N_{3t}^{E}}$ of BNBT-6/epoxy

1-3 composites with the BNBT-6 volume fraction.
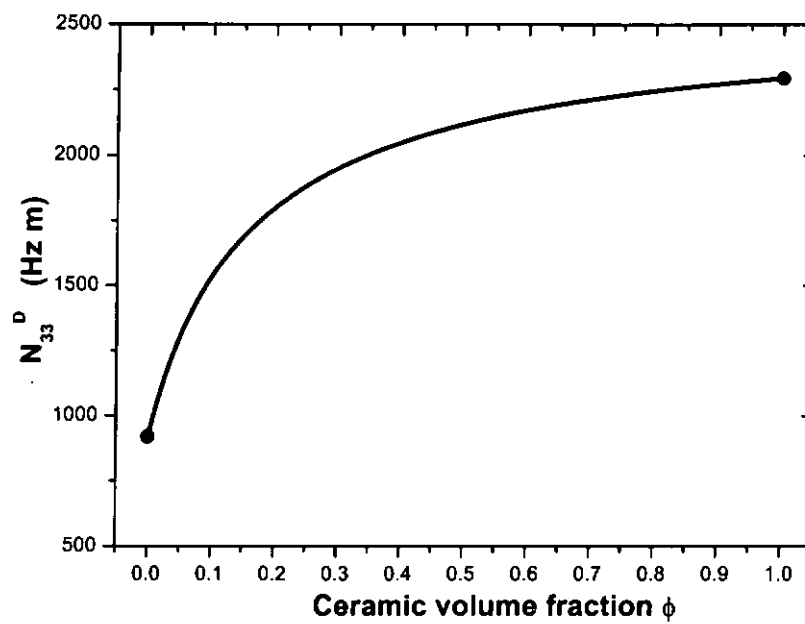
Figure A2.31 Variation of effective length frequency constant $\overline{N_{33}^{D}}$ of BNBT-6/epoxy 1-3 composites with the BNBT-6 volume fraction.
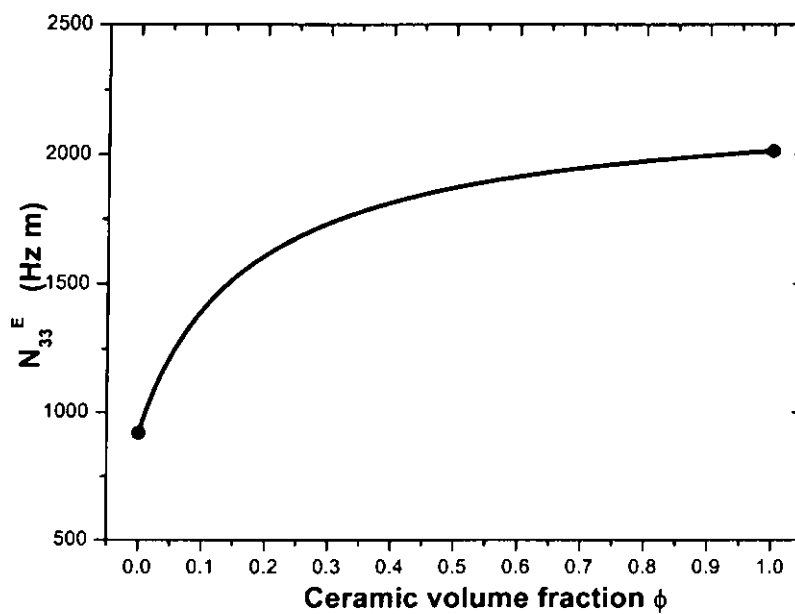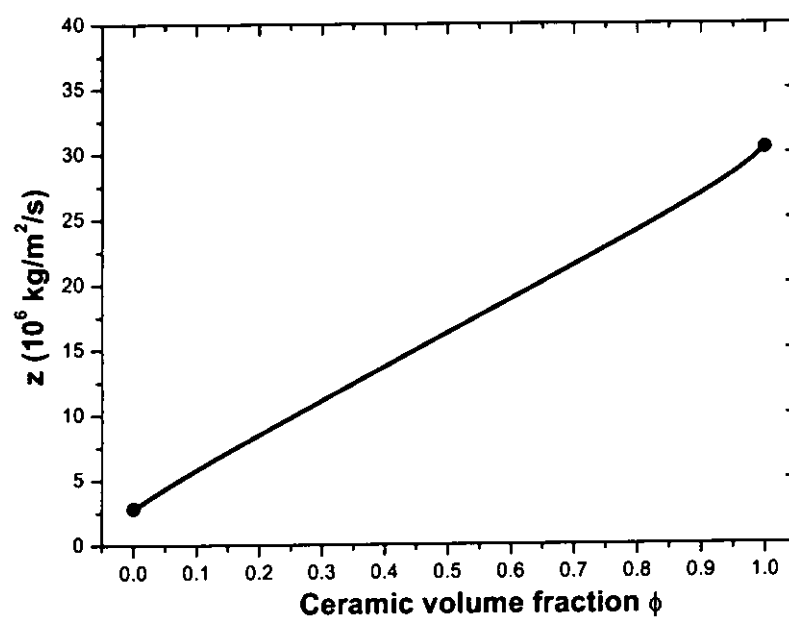

Figure A2.32 Variation of effective length frequency constant $\overline{N_{33}^{E}}$ of BNBT-6/epoxy 1-3 composites with the BNBT-6 volume fraction.

Figure A2.33 Variation of effective acoustic impedance $\bar{z}$ of BNBT-6/epoxy 1-3 composites with the BNBT-6 volume fraction.
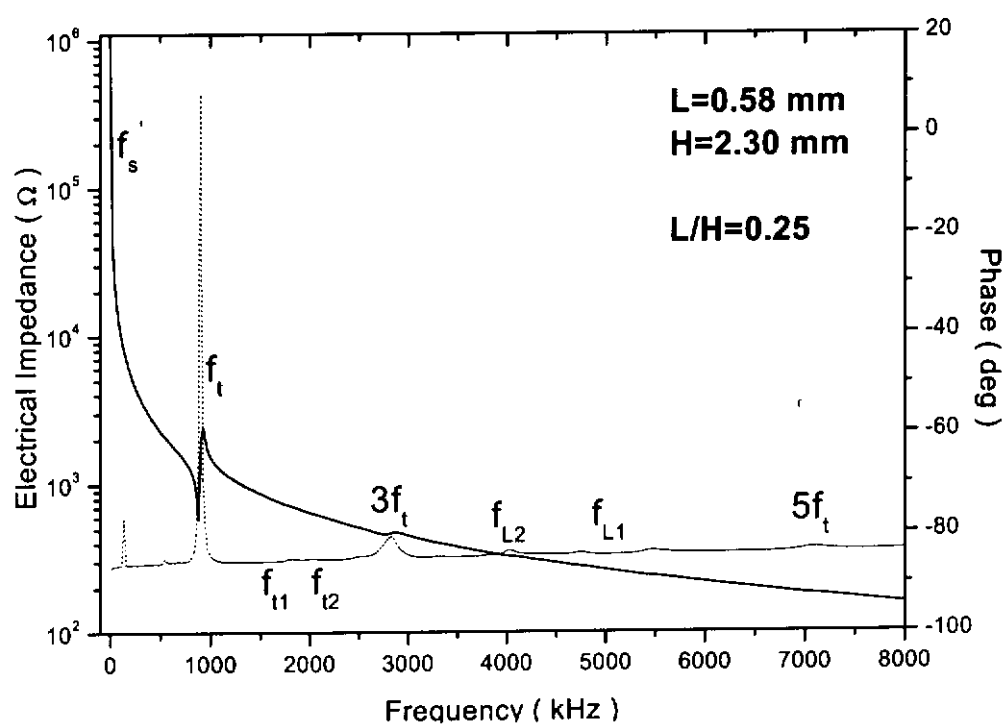
APPENDIX III

THINNING TEST RESULTS OF BNBT-6/EPOXY 1-3 COMPOSITES

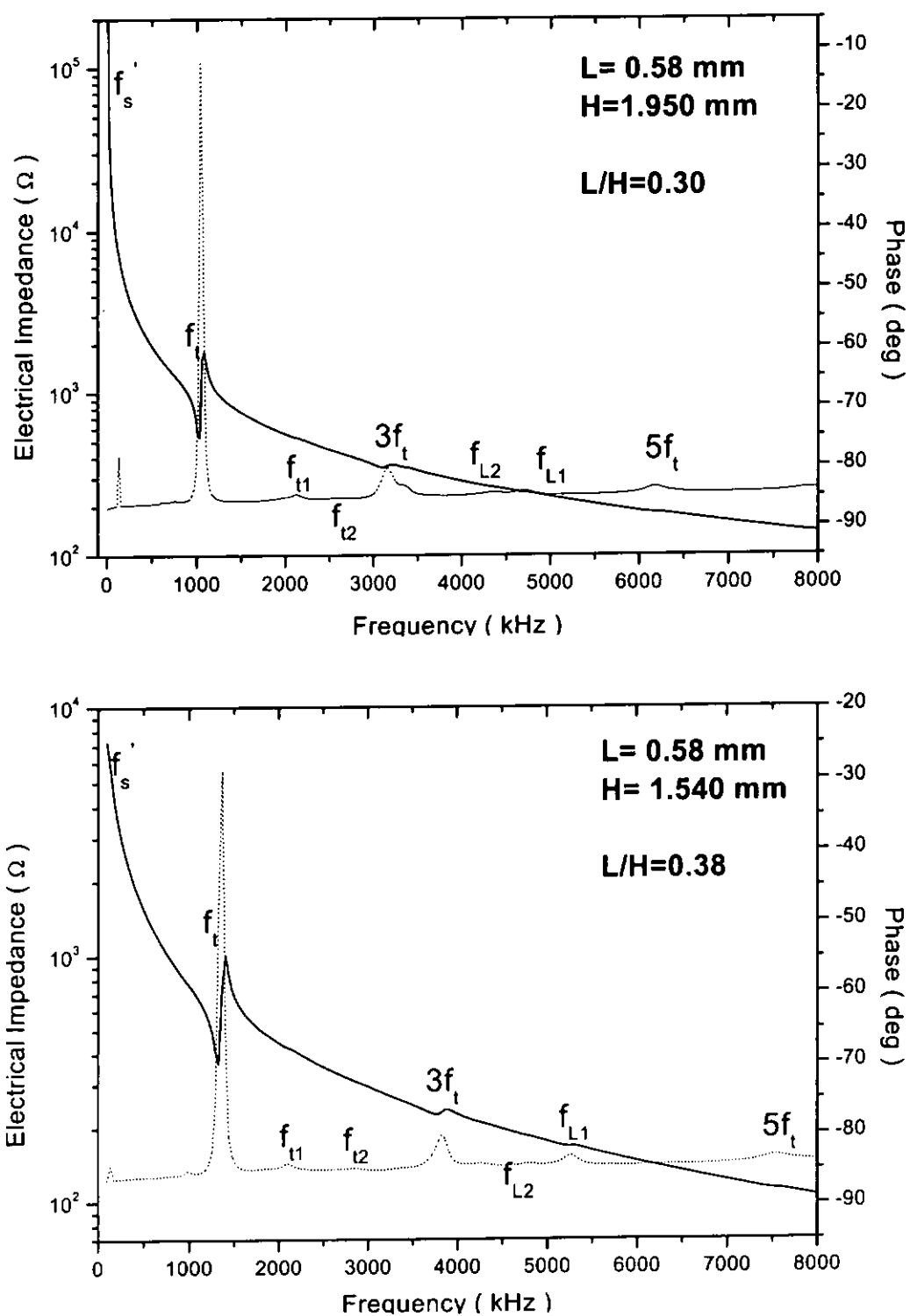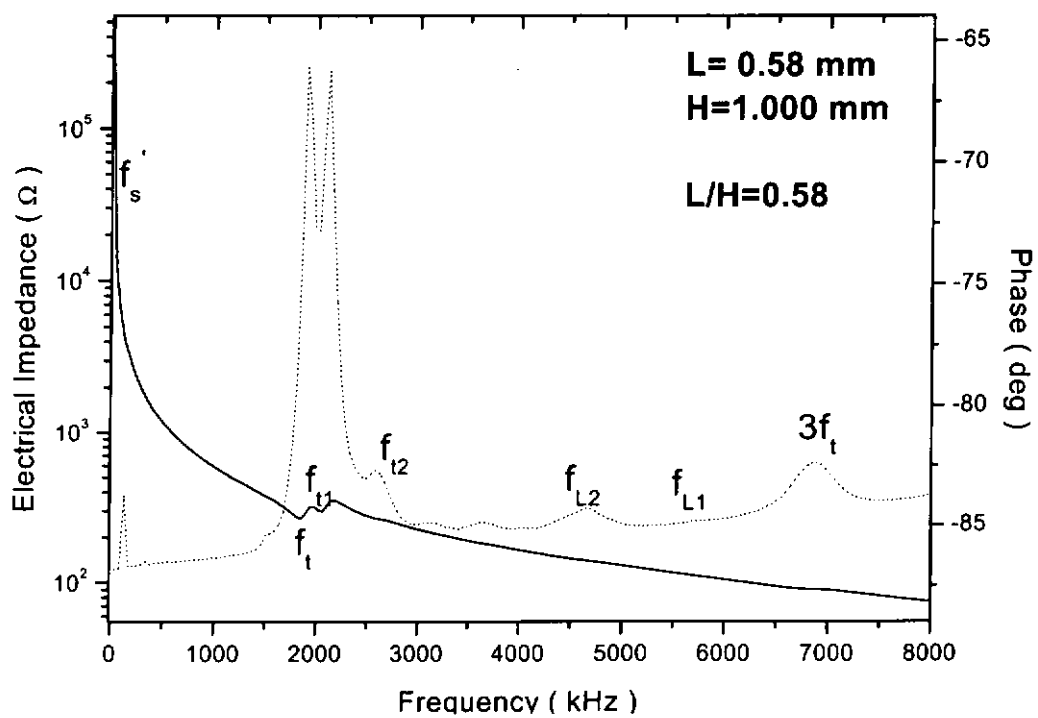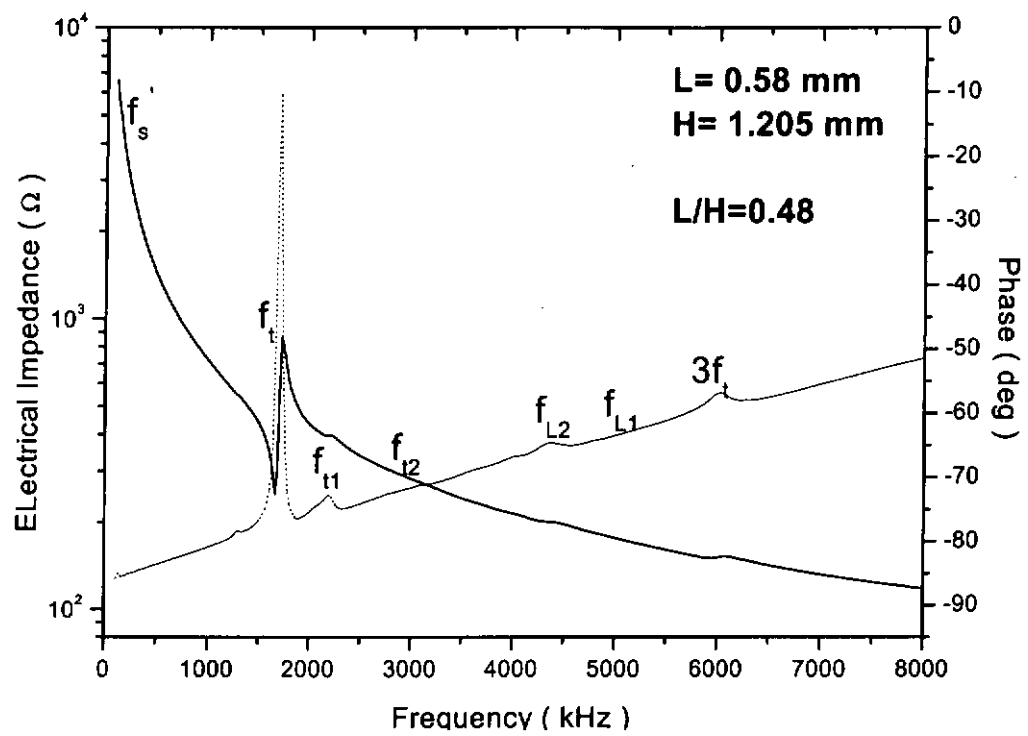Figure A3.1 Thinning test results of BNBT-6/epoxy 1-3 composite with ceramic volume fraction ϕ=0.52.
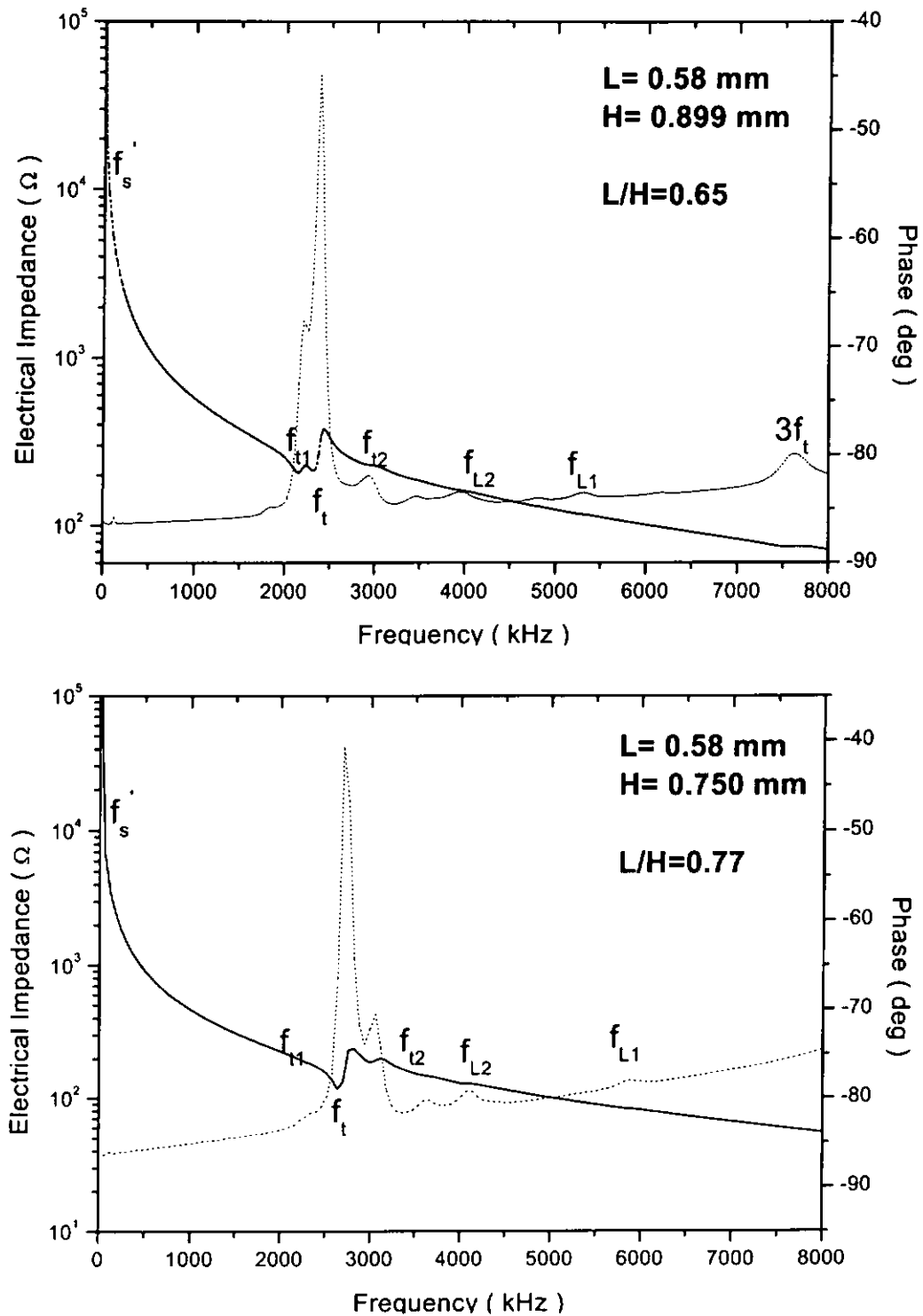
Fig. 3A.1 Cont.

Fig. 3A.1 Cont.

Fig. 3A.1 Cont.